

WESTERN AUSTRALIA SCHOOL OF MINES

**CHARACTERISATION OF PRIMARY COPPER ORE FOR
BLOCK CAVING AT THE EL TENIENTE MINE, CHILE**

ANDRES BRZOVIC

This thesis is presented as part of the requirements
for the award of the Degree of
Doctor of Philosophy of the
Curtin University of Technology

July 2010

To Gilda, Esteban, Sebastian and Natalia

DECLARATION

To the best of my knowledge and belief this thesis contains no material previously published by any other person except where due acknowledgment has been made.

This thesis contains no material which has been accepted for the award of any other degree or diploma in any university.

A handwritten signature in black ink, appearing to read "Andrew B.", written in a cursive style. The signature is enclosed within a large, thin, hand-drawn oval.

Signature:

Date: ...12th July 2010.....

ACKNOWLEDGEMENTS

The author would like to express his appreciation and gratitude to the individuals and organizations whose support and help made the completion of this study.

Professor E. Villaescusa, Industry Chair in Mining Rock Mechanics at the Western Australia School of Mines, not only for providing the opportunity to study this doctorate, but also for his invaluable help, guidance, patience, friendship and support during the course of this study.

Mr. P. Cepuritis, PhD student of the Western Australia School of Mines, for many things; his invaluable help through our discussion regarding rock mass characterisation, for providing a software program for seismic data analysis, for his help checking the written English, and his continuous friendship during all this time.

Mr. O. Araneda, Manager of Mining Resources and Development Department of the El Teniente Mine, for his continuous support to complete this study.

Mr. M. Didyk, Director of Technical Services of CODELCO, for his extraordinary help to persuade the right people in CODELCO to support this research.

Mr. P. Zuniga, Superintendent of Geological Department of the El Teniente Mine, for his help and support during the course of this study.

Mr. A. Thompson, Senior Research Fellow of the Western Australia School of Mines, for his help to correct the papers for publications and for providing the software to estimate the in-situ fragmentation.

Mr. C. Windsor, Associated Professor of the Western Australia School of Mines, for his teaching through the WASM's geomechanics master courses, which provided the initial guidance of this research.

Mr. D. Benado and Mr. J. Seguel, colleagues at the El Teniente mine, for their invaluable support and friendship throughout all this time, their help was an essential step to complete this research.

Mr. D. Beck, from Beck & Arndt Engineering Pty. Ltd., for his teaching regarding moment tensor and his invaluable contribution to use ABAQUS to model caving propagation.

Mr. G. Baird, Former Senior Research Fellow of the Western Australia School of Mines, for his teaching regarding the mathematic needed in rock mechanics.

Mrs. H. Morton and Mr. L. Machuca, colleagues at the Western Australia School of Mines, for their friendships and for making our stay in Kalgoorlie more enjoyable.

The staff and colleagues of the El Teniente Division, for their help and facilities during data collection. Special thanks to *Mr. C. Figueroa, Mr. E. Gonzales, Mr. C. Ordenes*, and *Mr. J. Zapata*.

The staff of the Western Australia School of Mines, for their help during the course of this study at WASM. Special thanks to *Mrs. M. Lavender* and *Mrs. W. Willingen*.

Finally, the author expresses his deepest gratitude to his family, especially to his wife, without her support, love, encouragement and companionship; this thesis certainly could not be completed.

ABSTRACT

This thesis investigated the rock mass geotechnical behaviour of primary copper ore at the El Teniente mine in Chile, which has been described as a massive and competent rock mass. The rock mass was characterised considering different structural data collection techniques and mapping scales. Modifications were made to the traditional sampling methodologies to better determine the observed geological discontinuities within primary copper ore. It was found that few open geological discontinuities, mainly the widely spaced large scale sub-vertical faults, are observed within primary ore, and this could be in agreement with the observed “*competent*” and “*massive*” rock mass behaviour at the mine site. The study also found a high frequency of small scale stockwork veins (cemented joints), which define at least three semi-orthogonal set orientations mine wide.

The faces of caved rock blocks found in the production level draw points were also characterised and an empirical criterion to define weak discontinuities that define caved blocks was established. From these observations, it can be concluded that the geological discontinuities (veins) having less than 1/3 of hard minerals as infill (*hard mineral means Mohs scale of hardness* ≥ 4) and thickness greater than or equal to 2mm may also be the weaker path where a competent rock mass fail under cave-induced stress conditions. This empirical definition was applied for the structural data collected from different geological units and mine sectors of the El Teniente mine. The results allowed a differentiation of several geotechnical units where traditional rock mass classifications schemes failed.

The observed rock mass behaviour during caving operations was back analysed to correlate with the new geotechnical units defined using that empirical definition. The back analysis studies included the rock damage as mine overbrake in mine drive at the undercut level, fragmentation performance, and mine seismicity recorded within a rock volume completely caved. A mine scale finite element numerical model was also built to assess the stress state around excavations during caving propagation. Damage orientation determination by seismic focal solutions was used to correlate against collected structural data to investigate the influence of weak discontinuities during block caving performance.

LIST OF PUBLICATIONS

Brzovic, A., Villaescusa, E. & Figueroa, C. (2006) Characterization of block-forming geological discontinuities during primary ore caving at El Teniente Mine, Chile. In *The Proceedings of the 41st U.S. Rock Mechanics Symposium*, Yale, D., Holtz, S., Breeds, C. & Ozbay, U. editors. ARMA/USRMS, Golden, Colorado 06-980, 1-9.

Brzovic, A. & Villaescusa, E. (2007) Rock mass characterization and assessment of block-forming geological discontinuities during caving of primary copper ore at the El Teniente mine, Chile. *Int. J. Rock Mech. Min. Sci. and Geomech. Abstr.*, 44, 565-83.

Brzovic, A. & Villaescusa, E. (2007) Rock mass characterization of primary copper ore for caving at the El Teniente mine. *The Proceedings of the International Workshop on Rock Mass Classification in Underground Mining*. Mark, C. & Pakalnis, R. editors. Vancouver. NIOSH, IC-9498:25-36.

Brzovic, A., Villaescusa, E. & Beck, D. (2008). Rock mass disassembly during caving propagation at the El Teniente Mine, Chile. *The Proceedings of International Conference and Exhibition on Mass Mining*. Schunnesson, H. & Nordlund, E. editors. University of Lulea, Lulea, Sweden, 1013-22.

Brzovic, A. (2009). Rock mass strength and seismicity during caving propagation at the El Teniente Mine, Chile. *The Proceedings of 7th International Symposium on Rockburst and Seismicity in Mines (RaSiM07)*. Tang, C.A. editor. Dalian University of Technology, Dalian, China, (2) 838-851.

CONTENTS

CHAPTER 1 INTRODUCTION.....	1
1.1 THE PROBLEM.....	1
1.1.1 <i>Research Hypothesis, Research Objectives and Data Collection Campaigns</i>	4
1.2 THESIS OUTLINE	6
1.3 THE EL TENIENTE MINE OVERVIEW	8
1.3.1 <i>Location and Brief Mine History</i>	8
1.3.2 <i>Resources and Size</i>	11
1.4 REGIONAL GEOLOGY	11
1.5 MINE SITE GEOLOGY	14
1.5.1 <i>El Teniente Mafic Intrusive Complex</i>	14
1.5.2 <i>Felsic Intrusions</i>	15
1.5.3 <i>Breccias</i>	16
1.5.4 <i>Alteration</i>	16
1.5.5 <i>Structures</i>	21
1.6 MINING METHODS	22
1.6.1 <i>Mining Methods History</i>	22
1.6.2 <i>In Situ Stress Field</i>	25
1.6.3 <i>Geotechnical Rock Mass Properties and Fragmentation</i>	26
1.6.4 <i>Current and Future Exploitation</i>	29
1.6.5 <i>Current Mine Method and Design</i>	31
CHAPTER 2 DATA COLLECTION TECHNIQUES.....	35
2.1 INTRODUCTION.....	35
2.1.1 <i>Goal</i>	36
2.2 DISCONTINUITY DEFINITIONS	36
2.2.1 <i>Classification of Structures at the El Teniente Mine</i>	38
2.3 DISCONTINUITY CHARACTERISTICS	40
2.4 GENERAL SAMPLING FEATURES AT THE RENO MINE SECTOR.....	40
2.5 SAMPLING BIAS.....	44
2.6 MEASUREMENTS AT EXPOSED ROCK FACES	45
2.6.1 <i>Drive Mapping</i>	46
2.6.2 <i>Line Mapping</i>	47
2.7 BOREHOLE LOGGING.....	53
2.7.1 <i>Oriented Core Logging</i>	53
2.7.2 <i>Un-Oriented Drill Cores</i>	55
2.8 FRAGMENTATION ASSESSMENT	57
2.8.1 <i>Characterisation of Caved Rock Blocks</i>	58
2.9 CONCLUSIONS.....	62

CHAPTER 3	FUNDAMENTALS OF ROCK STRUCTURE, ANALYSIS AND INTERPRETATION.....	63
3.1	INTRODUCTION.....	63
3.1.1	<i>Goal.....</i>	63
3.2	DISCONTINUITY ORIENTATION.....	64
3.2.1	<i>Background.....</i>	64
3.2.2	<i>Discontinuity Occurrence in Line Sampling.....</i>	66
3.2.3	<i>Set Definition.....</i>	68
3.2.4	<i>Orientations of Faults and Major Structures.....</i>	69
3.2.5	<i>Orientations of Veins.....</i>	71
3.2.6	<i>Comparison between Mapping Scales.....</i>	72
3.3	SPACING.....	73
3.3.1	<i>Background.....</i>	73
3.3.2	<i>Statistical Distribution of Discontinuity Spacing.....</i>	76
3.3.3	<i>Reliability of Mean Discontinuity Spacing Estimated.....</i>	77
3.3.4	<i>Normal Set Spacing of The El Teniente Discontinuities.....</i>	80
3.4	PERSISTENCE.....	87
3.4.1	<i>Background.....</i>	87
3.4.2	<i>Termination.....</i>	91
3.4.3	<i>Observed Trace Length of the El Teniente Discontinuities.....</i>	91
3.5	DISCONTINUITY INFILL.....	95
3.5.1	<i>Infill of the El Teniente Discontinuities.....</i>	96
3.6	APERTURE.....	99
3.6.1	<i>Thickness of the El Teniente Discontinuities.....</i>	99
3.7	ROUGHNESS.....	103
3.7.1	<i>Background.....</i>	103
3.7.2	<i>Roughness of El Teniente Discontinuities.....</i>	106
3.8	BLOCK SIZE.....	109
3.8.1	<i>Background.....</i>	109
3.8.2	<i>In Situ Block Size Estimations of the El Teniente Rock Structure....</i>	111
3.9	UN-ORIENTED CORE LOGGING DATA.....	112
3.9.1	<i>Background.....</i>	113
3.9.2	<i>Location and Orientation of Core Sections Studied.....</i>	115
3.9.3	<i>Estimates along the Same Core.....</i>	116
3.9.4	<i>Estimates from Multiple Core Orientations.....</i>	118
3.10	CONCLUSIONS.....	121
CHAPTER 4	CHARACTERISATION OF CAVED ROCK BLOCKS.....	123
4.1	INTRODUCTION.....	123
4.1.1	<i>Goal.....</i>	123
4.1.2	<i>Assumptions.....</i>	123
4.2	FEATURES OF CAVED ROCK BLOCK FORMING FACES.....	124

4.2.1	<i>Discontinuity Occurrence</i>	124
4.2.2	<i>Veins Infills</i>	125
4.2.3	<i>Failure mode</i>	126
4.2.4	<i>Vein thickness</i>	127
4.3	EMPIRICAL DEFINITION OF WEAK VEINS	130
4.3.1	<i>Relative vein infill strength</i>	131
4.3.2	<i>Data Analysis using relative vein infill strength</i>	132
4.3.3	<i>Interpretation</i>	135
4.4	CONCLUSIONS	136
CHAPTER 5 ANALYSIS OF WEAK DISCONTINUITY DATA		137
5.1	INTRODUCTION.....	137
5.1.1	<i>Goal</i>	137
5.2	WEAK DISCONTINUITY OCCURRENCE.....	137
5.2.1	<i>Discontinuity type</i>	139
5.3	SPACING.....	140
5.4	PERSISTENCE.....	143
5.5	ROUGHNESS	143
5.6	THICKNESS	144
5.7	BLOCK SIZE	148
5.7.1	<i>Block Size Distribution for Fragmentation</i>	149
5.7.2	<i>Fragmentation Model</i>	152
5.8	CONCLUSIONS	154
CHAPTER 6 ROCK MASS CLASSIFICATION SYSTEMS		155
6.1	INTRODUCTION.....	155
6.1.1	<i>Goal</i>	155
6.2	ROCK QUALITY DESIGNATION, RQD.....	156
6.2.1	<i>Applying RQD to the El Teniente Primary Copper Ore</i>	157
6.3	GEOMECHANICS CLASSIFICATION, RMR	158
6.3.1	<i>RMR_B Application to the El Teniente Primary Copper Ore</i>	160
6.4	Q-SYSTEM.....	161
6.4.1	<i>Q-System Application to the El Teniente Primary Copper Ore</i>	164
6.5	GEOLOGICAL STRENGTH INDEX, GSI.....	166
6.5.1	<i>GSI Application to the El Teniente Primary Copper Ore</i>	166
6.6	MINING ROCK MASS RATING, MRMR	167
6.6.1	<i>In-situ Rock Mass Rating, IRMR</i>	169
6.6.2	<i>Rock Mass Values</i>	173
6.6.3	<i>Scale Effects</i>	175
6.6.4	<i>MRMR Application to the El Teniente Primary Copper Ore</i>	176
6.7	CONCLUSION.....	178

CHAPTER 7	ESMERALDA MINE SECTOR.....	180
7.1	INTRODUCTION.....	180
7.1.1	<i>Goal.....</i>	<i>180</i>
7.2	ROCK MASS CHARACTERISATION	181
7.2.1	<i>Drive Mapping</i>	<i>184</i>
7.2.2	<i>Oriented Core Logging</i>	<i>187</i>
7.2.3	<i>Potential Fragmentation</i>	<i>189</i>
7.3	ROCK MASS RESPONSE	191
7.3.1	<i>Hydraulic Radius during Caving Propagation.....</i>	<i>191</i>
7.3.2	<i>Fragmentation.....</i>	<i>193</i>
7.3.3	<i>Rock Damage in Mine Drives of the Undercut Level</i>	<i>200</i>
7.4	CONCLUSIONS	207
CHAPTER 8	BACK ANALYSIS STUDIES.....	209
8.1	INTRODUCTION.....	209
8.1.1	<i>Goal.....</i>	<i>210</i>
8.2	BACKGROUND OF MINE SEISMOLOGY AND SEISMIC MONITORING AT THE EL TENIENTE MINE	210
8.2.1	<i>Seismic Moment and Moment Magnitude</i>	<i>213</i>
8.2.2	<i>The Gutenberg-Richter Distribution and Seismic Potential</i>	<i>214</i>
8.2.3	<i>Mine Production and Control of the Induced Seismicity</i>	<i>215</i>
8.2.4	<i>Moment Tensor</i>	<i>216</i>
8.2.5	<i>Focal Mechanism</i>	<i>218</i>
8.2.6	<i>Moment Tensor Inversion</i>	<i>220</i>
8.3	ANALYSIS OF RECORDED SEISMIC DATA DURING CAVING PROPAGATION	221
8.3.1	<i>Focal Mechanism at Reno Mine Sector</i>	<i>222</i>
8.3.2	<i>Focal Mechanism at Esmeralda Mine Sector</i>	<i>225</i>
8.3.3	<i>Seismicity during Caving Propagation</i>	<i>231</i>
8.4	MINE SCALE NUMERICAL MODEL.....	234
8.5	MODEL CHARACTERISTICS.....	235
8.5.1	<i>Model Package.....</i>	<i>235</i>
8.5.2	<i>Material Assumptions</i>	<i>235</i>
8.5.3	<i>In situ Stress Field.....</i>	<i>236</i>
8.5.4	<i>Model Geometry, Size and Model Steps.....</i>	<i>236</i>
8.5.5	<i>Model Calibration.....</i>	<i>240</i>
8.6	MODEL RESULTS.....	247
8.6.1	<i>Modelled Stress Path and Seismicity during Caving Propagation..</i>	<i>247</i>
8.6.2	<i>Modelled Stress Path and Rock Damage ahead of the Front Cave.</i>	<i>249</i>
8.7	DISCUSSION	250
8.8	CONCLUSIONS	252
CHAPTER 9	CONCLUSIONS	254

9.1	PREDICTING BEHAVIOUR OF ROCK MASSES OF PRIMARY COPPER ORE	254
9.2	ACHIEVEMENTS OF THE RESEARCH.....	254
9.2.1	<i>Structural Characterization of Primary Copper Ore</i>	255
9.2.2	<i>Cemented Joints as Controlling Rock Mass Failure</i>	255
9.2.3	<i>Characterising Rock Masses at the El Teniente Mine</i>	256
9.2.4	<i>Correlation with Rock Mass Response</i>	257
9.3	LIMITATIONS AND RECOMMENDATIONS FOR FUTURE WORK.....	258
REFERENCES.....		254
APPENDIX I Raw Structural Data.....		264
A.	Major Structures.....	265
B.	Drive Mapping.....	266
C.	Line Mapping.....	267
D.	Oriented Core Logging.....	268
E.	Un-Oriented Core Logging.....	269
F.	Caved Rock Block Data.....	270
APPENDIX II Additional Data Analysis.....		271
A.	Fault and Veins Orientation.....	272
B.	Set Definition for veins.....	276
C.	Infill of Faults and Veins.....	283
D.	Thicknesses of Faults and Veins.....	285
APPENDIX III Seismic and Numerical Model Data.....		288
A.	Seismic Source Parameters.....	289
B.	Recorded Seismicity.....	301
C.	Model Result Data.....	302
CD.....		303

LIST OF FIGURES

Figure 1.1. Photography sets of the massive and competent primary copper ore at the El Teniente mine containing healed veins (a & b). Core try with a typical recovery of the secondary copper ore (c).	3
Figure 1.2. Location of the El Teniente mine (red star) in Chile.....	9
Figure 1.3. Aerial photography and isometric view of El Teniente mine. Current exploitation area is delimited by white lines in the upper picture (both figures with mine grid).....	10
Figure 1.4. Geology of central Chile (after Skewes et al. 2002).....	12
Figure 1.5. Geology of the area surrounding the El Teniente copper deposit with true north (after Skewes et al. 2002).	13
Figure 1.6. Plainview with lithology and structures of the El Teniente ore body at the Ten-6 level (2165z). Red dashed lines indicating area of mine sectors studied in this research.	14
Figure 1.7. Stockwork intersected andesite rock type within primary copper ore. The white square (top photo) and the rock bolt plate (bottom photo) are 20x20 cm.	18
Figure 1.8. Typical late magmatic (LM) veins.....	19
Figure 1.9. Typical veins of the principal hydrothermal alteration stage (left side) and of the late hydrothermal alteration stage (right side).	19
Figure 1.10. East-West section at El Teniente mine showing the primary and secondary ore.	20
Figure 1.11. Faults at El Teniente mine within primary copper ore. Rock bolt plates are 20x20 cm.	21
Figure 1.12. Block caving mining method (Hamrin, 2001).	22
Figure 1.13. Panel caving method at El Teniente mine (Hamrin, 2001).....	23
Figure 1.14. Measurement of stress increase as a function of the distance to the caving front.	24
Figure 1.15.- Cross section showing Panel and pre-undercut caving methods at the El Teniente mine.	25
Figure 1.16.- Measurement of the in situ stress field at the mine site in mine coordinates (adapted from Villaescusa and Machuca, 2007).....	26
Figure 1.17. Cases histories in stability/instability diagram using Laubscher (1993).	28
Figure 1.18. Typical primary ore size distribution at El Teniente mine (Blondel et al., 1995).	28
Figure 1.19. Average measured productivity at Teniente 4 south mine sector (2354z) per unit type (Vasquez, 2003). Mine coordinates in meters.	30
Figure 1.20. Isometric view of El Teniente mine showing main current and future mine sectors.....	31
Figure 1.21. Stress state in the rock mass at the cave front.....	32
Figure 1.22. Plan view with layout of the undercut and production levels at the Esmeralda mine sector.	33
Figure 2.1. Scheme that illustrate the scale concept of the discontinuities (after Pusch 1995).....	38
Figure 2.2. Structure classification at the El Teniente mine according to the observed trace length into mine drives.	39
Figure 2.3. Schematic illustration of discontinuity properties (after Hudson and Harrison, 1997).	40
Figure 2.4. Different sample location at the undercut level of Reno mine sector.....	41

Figure 2.5. Different sample location at the production level of Reno mine sector.	42
Figure 2.6. Equal area lower hemisphere projection showing sample orientation for different data collection techniques used in this study.....	43
Figure 2.7. Mine wall at the El Teniente mine, showing how vein infill and alteration may cover the rock exposure, sometimes hiding structural data behind.....	45
Figure 2.8. Plan views showing rock types and intermediate structures (a) and interpreted major structures (b). The scale is 200m x 200m. Line colours represent different geological structures; LM veins as orange, PH veins as red, LH veins as green, and Faults as blue.	47
Figure 2.9. Mine drive cross-section showing some aspects of line mapping (modified after Villaescusa, 1991).....	49
Figure 2.10. Detail of drive mine wall showing some discontinuities with ‘open faces’ (exhibiting discontinuity wall surface) intersected by the tape (0.02 m width).	50
Figure 2.11. Data collection spreadsheet for scanline mapping (modified after Villaescusa 1991).....	50
Figure 2.12. Veins with exposed wall surface during scanline mapping.	52
Figure 2.13. Failure mode and thicknesses of discontinuities (Brzovic and Villaescusa, 2007).	52
Figure 2.14. Oriented drill core sample showing thin discontinuities, which were disregarded during data collection (within red square).....	54
Figure 2.15. Data collection spreadsheet for oriented drill cores.....	55
Figure 2.16. - Standard un-oriented core samples, prior it is split (a) and after that (b).	56
Figure 2.17. Data collection spreadsheet for standard non-oriented drill cores.....	57
Figure 2.18. Sectors studied for caved rock blocks characterisation at the Reno mine production level.....	59
Figure 2.19.- Caved rock block characterisation spreadsheet (adapted from Figueroa, 2003).	60
Figure 2.20.- Definition of rock block shapes and dimension (adapted from Figueroa, 2003).	61
Figure 2.21.- Characterised rock block showing trapezoidal prismatic shape in a draw point at the Reno mine sector (Figueroa, 2003).	61
Figure 3.1.- Lower hemispheric projection, modified after Hoek and Brown (1980).	64
Figure 3.2.- Angular relationship between linear survey and discontinuity set orientation.	65
Figure 3.3.- Application to the Poisson exponential binominal limit for sample data using stereonet plots (after Villaescusa 1985).	69
Figure 3.4.- Major discontinuity orientations per unit sector plotted in the lower hemispheric projection.	70
Figure 3.5.- Set definition for faults collected in mine drives (drive mapping). It is shown the main set orientation defined (set; s).....	70
Figure 3.6.- Set definition for veins collected using scanline mapping. It is shown the main set orientation defined (set; s).	71
Figure 3.7.- Set definition for veins collected using oriented core logging. It is shown the main set orientation defined (set; s).....	72
Figure 3.8.- Relationship between data collection thought set orientation per discontinuity types.	73
Figure 3.9. Direction cosines in a right-handed Cartesian system.	75

Figure 3.10.- Histogram of discontinuity spacing values, after Priest (1993).	76
Figure 3.11.- Sample number versus precision of the mean discontinuity spacing that follow a negative exponential <i>pdf</i> (after Priest and Hudson 1981).....	79
Figure 3.12.- Discontinuity frequency and truncation bias length.....	82
Figure 3.13.- Discontinuity frequency and truncation bias length per discontinuity type. (<i>Oc</i> ; oriented core logging. <i>Scl</i> ; line mapping, <i>Dm</i> ; drive mapping. <i>Ms</i> ; interpreted major structures).....	83
Figure 3.14.- 3D loci of discontinuity frequency diagram (data is from line mapping andesite Fw).....	84
Figure 3.15.- Observed spacing of discontinuity sets.....	86
Figure 3.16.- Discontinuities as circular disc a within rock mass (left), and their observed trace length (<i>l</i>) on a particular rock exposure (right), after Windsor (1977).	87
Figure 3.17.- Observed and corrected discontinuity size at the El Teniente mine (Villaescusa, 1991).....	90
Figure 3.18.- Influence of termination in rock block definition.....	91
Figure 3.19.- Observed trace length of major faults.....	92
Figure 3.20.- Probability distribution of the observed trace length with both ends exposed.....	94
Figure 3.21.- Observed veins discontinuity trace length distribution.....	95
Figure 3.22.- Chalcopyrite as infill distribution within PH veins observed in oriented cores logging (Fw sector.).....	97
Figure 3.23.- Schemes illustrated the suggested definitions of the aperture and the width, after ISRM (Brown, 1981).....	99
Figure 3.24.- Cumulative probability distribution of the observed thickness in major structures according to the mapping scale.....	100
Figure 3.25.- Observed thickness and trace length relationship for veins. (a) range of the scaling law relationship suggested by Vermilye and Scholz (1995). (b) range of the fractal relationship proposed by Johnston and McCaffrey (1996).....	102
Figure 3.26.- Relation between thicknesses and the mean of the mineralogical infill in veins observed at the andesite Fw sector. (<i>Oc</i> ; oriented core logging, <i>Scl</i> , scanline mapping).....	102
Figure 3.27.- Normalized aperture (thickness) distributions along single veins (after Vermilye and Scholz, 1995).....	103
Figure 3.28.- Roughness and shear strength.....	103
Figure 3.29.- Example of scale effect determining the discontinuity shear strength, after Barton et al. (1985).....	105
Figure 3.30.- Typical roughness profile and suggested nomenclature, after ISRM (Brown, 1981).....	106
Figure 3.31.- Roughness and Planarity observed in discontinuity types.....	108
Figure 3.32.- In situ block size distributions from rock structure simulation (<i>Oc</i> ; oriented drill core. <i>Scl</i> ; scaline mapping).....	112
Figure 3.33.- Plan view and section of Reno mine sector showing location of standard 6.1m long un-oriented drill core sections (grouped by similar orientation accord to Figure 3.34).....	115
Figure 3.34.- Orientation (trend/plunge) of standard 6.1m long un-oriented drill core sections including rock type. Cores sections are grouped by similar orientation. ...	116
Figure 3.35.- Discontinuity frequency along the drill cores. All data from andesite except magenta filled symbols (diorite).....	117
Figure 3.36.- Thickness distributions along drill cores for andesite rock type.....	118

Figure 3.37.- Mean values of discontinuity frequency observed in multiple core samples grouped by orientation.	119
Figure 3.38.- 3D loci diagram of simulated discontinuity frequency in the lower hemispheric projection.	120
Figure 3.39.- Mean values thickness distribution observed in multiple core samples grouped by orientation.	120
Figure 4.1.- Veins as faces of polyhedral caved rock blocks in draw points showing mineralogical infill such as chalcopyrite (yellow) and quartz (white).	125
Figure 4.2.- Distribution of hard infill observed within rock block forming veins from andesite and diorite rock types.	133
Figure 4.3.- Distribution of hard infill observed in veins considering failure mode.	134
Figure 4.4.- Distribution of hard infill observed in veins considering rock block volume.	134
Figure 4.5.- Distribution of hard infill observed in veins considering percentage of block caved column extraction.	134
Figure 4.6.- Plane of weakness theory applied to a rock mass having three discontinuity sets (Mohr-Coulomb parameters as reference).	135
Figure 5.1.- Cumulative frequency of veins collected in small scale sampling in term of the proportion of hard infill within veins. Oc; oriented core logging, Scl; scanline mapping.	138
Figure 5.2.- 3D loci of discontinuity frequency diagram for weak discontinuities (scanline Fw sector).	142
Figure 5.3.- Observed trace length in scanlines mapping, mean distribution for all sets.	145
Figure 5.4.- Mean distributions of roughness profiles observed in weak discontinuities collected by scanline mapping.	146
Figure 5.5.- Relationship between average thickness of discontinuity sets and truncation bias.	148
Figure 5.6.- Simulations of the mean unfractured distance for weak discontinuities. Scl; scanline mapping, Oc; oriented core logging, w; weak discontinuities.	148
Figure 5.7.- Discontinuity spacing and thickness of discontinuities. Scl; scanline mapping, Oc; oriented core logging, w; weak discontinuities, all; all discontinuities.	149
Figure 5.8.- Additional data points of the relationship between discontinuity spacing and thickness of discontinuities. Scl; scanline mapping, Oc; oriented core logging, w; weak discontinuities.	150
Figure 5.9.- Normalised increment of the discontinuity spacing and thickness of discontinuities. Scl; scanline mapping, Oc; oriented core logging.	151
Figure 5.10.- Rock structure simulations for data collected in oriented core logging, considering all discontinuities and only weak ones having thickness ≥ 2 mm.	152
Figure 5.11.- Conceptual framework of the fragmentation in the primary copper ore at the El Teniente mine.	153
Figure 6.1.- Procedure for measurement and calculation of RQD (Deere, 1968)...	156
Figure 6.2.- Typical core-recovery on core tray for andesite rock type at the El Teniente mine (Brzovic et al., 1998).	158
Figure 6.3.- The Q-support chart update for Sfr (instead of Smr), after Grimstad and Barton (1993). ESR= excavation support ratio, [2] $RMR_B=15LnQ+50$	164
Figure 6.4.- Geological strength index base on geological description (Marinos and Hoek, 2000).	167

Figure 6.5.- Flow sheet of the MRMR procedure (after Laubscher and Jakubec 2000).	168
Figure 6.6.- Structural definitions in IRMR/MRMR (Laubscher and Jakubec, 2001).	169
Figure 6.7.- Monogram for determining the corrected IRS value (Laubscher and Jakubec, 2001).	170
Figure 6.8.- The nomogram relating the <i>IRS</i> adjustment factor to the hardness index and vein frequency (Laubscher and Jakubec, 2001).	171
Figure 6.9.- RBS rating as a function of rock block strength (Laubscher and Jakubec, 2001).	171
Figure 6.10.- Joints spacing rating (Laubscher and Jakubec, 2001).	172
Figure 6.11.- Adjustment factor for cemented joints (Laubscher and Jakubec, 2001).	172
Figure 6.12.- Joints condition adjustment for multiple joint sets (Laubscher and Jakubec, 2001).	174
Figure 6.13.- Adjustment factor for major structure to <i>HR</i> (Laubscher and Jakubec, 2001)	176
Figure 7.1.- Main geological features of the Esmeralda mine sector (modified from Seguel 2005).	182
Figure 7.2.- Plan view of production level at the Esmeralda mine sector showing drive mapping line samples chosen for re-analysis of data according to different structural domain selection (different colours), and oriented drill core location (red arrows).	183
Figure 7.3.- Stereonets showing weak vein and fault orientations from <i>Cmet Fw1</i> structural domain.	185
Figure 7.4.- Set definition for weak veins and faults collected at mine drives accordingly to structural domain selection (red windows are only to identify main cluster, it is not the windows definition).	185
Figure 7.5.- Veins orientation, set definition (S_n) from the <i>Cmet Hw1</i> and core sample orientation (black line). Few structures are observed to the perpendicular of sample line (blind zone effect).	187
Figure 7.6.- Plot contour of veins collected by mine geologist using traditional scanline techniques in the Esmeralda mine sector (<i>Fw</i>).	188
Figure 7.7.- In situ rock block size distribution for weak discontinuities.	190
Figure 7.8.- In situ rock block size distributions for weak discontinuities considering vein thicknesses $\geq 2\text{mm}$ (with * in the chart). Oc; small diameter oriented cores from both sectors within Reno mine.	190
Figure 7.9.- Isometric view of the cave of Reno mine sector at the time of breakthrough to upper mine levels.	192
Figure 7.10.- Isometric view of the cave of the Esmeralda mine sector at the time of breakthrough to upper mine levels.	193
Figure 7.11.- Comparison between predicted (potential, feasibility studies) and observed (draw points and ore passes) fragmentation (adapted from Figure 7.8 and Table 7.5).	200
Figure 7.12.- Observed rock damage in mine drives as areas of high and low mine over-brake at the undercut level in June 1999 (adapted from Gaete et al., 2005). ..	201
Figure 7.13.- Observed rock damage in mine drives of the undercut level in August 1999 (adapted from Gaete et al., 2005).	201
Figure 7.14.- Observed rock damage in mine drives of the undercut level in December 1999 (adapted from Gaete et al., 2005).	202

Figure 7.15.- Observed rock damage in mine drives of the undercut level in April 2000 (adapted from Gaete et al., 2005).....	202
Figure 7.16.- Observed rock damage in mine drives of the undercut level in July 2000 (adapted from Gaete et al., 2005).....	203
Figure 7.17.- Observed rock damage in mine drives of the undercut level in September 2000 (adapted from Gaete et al., 2005).....	203
Figure 7.18.- Observed rock damage in mine drives of the undercut level in February 2001 (adapted from Gaete et al., 2005).....	204
Figure 7.19.- Observed rock damage in mine drives of the undercut level in July 2001 (adapted from Gaete et al., 2005).....	204
Figure 7.20.- Observed rock damage in mine drives of the undercut level in October 2001 (adapted from Gaete et al., 2005).....	205
Figure 7.21.- Observed rock damage in mine drives of the undercut level in October 2002 (adapted from Gaete et al., 2005).....	205
Figure 7.22.- Total rock damage observed at the undercut level of Esmeralda mine sector between 1999 and 2004 for H_w and F_w sectors. F_w sector has also being normalized by a factor of 2.	206
Figure 7.23.- Total rock damage observed in the undercut level of Esmeralda mine sector between 1999 and 2004 for H_w and F_w (normalised) sectors considering high and low rock damage.	206
Figure 8.1.- Seismogram recorded by a triaxial sensor at the El Teniente mine. ...	211
Figure 8.2.- Seismic events recorded per months at Esmeralda mine sector between 1996 and 2003.	212
Figure 8.3.- Isometric view of Esmeralda mine sector showing cave geometry, diorite rock and the recorded seismicity (crosses green and blues) between 1997 and 1999. For details see Figure 7.10.	213
Figure 8.4.- Equivalent body force description. Fault slip can be described by the superposition of either force couples M_{xy} and M_{yx} or force dipoles $M_{x'x'}$ and $-M_{y'y'}$. (Modified after Stein & Wysession 2003).	214
Figure 8.5.- The Gutenberg-Richter seismic event frequency-magnitude relation for different years at the studied mine sector.....	215
Figure 8.6.- Nine possible force couples M_{ij} of a moment tensor (after Aki & Richardson, 1980).	216
Figure 8.7.- Several possible source explanations for simultaneous non- double couple and double couple source mechanisms (from Mendecki, 1997).	219
Figure 8.8.- Focal mechanism and first motion (after Stein & Wysession 2003)...	219
Figure 8.9.- Faults plane solution and orientation of T, P and B axes for seismicity associated to the April 22 nd , 2003 event plotted in lower hemispheric projection (modified from Dunlop and Belmonte, 2005).	223
Figure 8.10.- Faults plane solution and orientation of T, P and B axes for major failures occurring between 2000-2005 plotted in lower hemispheric projection (modified after ISS, 2007)	223
Figure 8.11.- Source mechanism for major dynamic failures at the Reno mine sector.	225
Figure 8.12.- Plan view of Esmeralda mine sector showing event with moment tensor estimates (+; events. Blue coloured events were recorded prior to breakthrough to the upper levels and black ones after that).....	226
Figure 8.13.- Location of events with plane focal solution recorded from February to April 1999 indicating fault mechanisms; inverse-strike slip (red), normal-strike slip (black).	227

Figure 8.14.- Fault orientation from data collected by drive mapping (a) and fault plane solutions (b), both from diorite rock type at the Esmeralda mine sector.	228
Figure 8.15.- Isotropic component of moment tensor from interpreted discontinuities at the Reno mine sector (from Figure 8.11) and at the Esmeralda mine sector.	229
Figure 8.16.- Orientation of P, B and T axes for focal solutions interpreted in Figure 9.20b.....	230
Figure 8.17.- Studied areas at the Esmeralda mine sector showing the extraction front (30% of primary ore column height) and the undercutting by years.....	232
Figure 8.18.- Proportion of the cumulative seismicity recorded in Esmeralda mine sector per each location.....	232
Figure 8.19.- Isometric view of Esmeralda mine sector showing the recorded seismicity within <i>Cmet</i> rock type (above). Gutenberg-Richter curve for each studied unit type (below).	233
Figure 8.20.- Cumulative production (tonnes) for different mine sector considering up to 30% of primary ore column high.	234
Figure 8.21.- Initial geological equilibrium with the stress field and initial surface topology after hypothetical ranges erosion.	237
Figure 8.22.- Model size, boundary condition, and modelled mine levels.	238
Figure 8.23.- Detailed geometries of some mine model step in the numerical model.	239
Figure 8.24.- DPE plots and seismicity at the Esmeralda mine sector (Section 1120E).	242
Figure 8.25.- DPE plots at the Esmeralda mine sector during breakthrough to upper mine levels (Section 1120E).	243
Figure 8.26.- Different plan views (2240z) showing cumulative plastic strain reached for the rock mass at the model step before it is caved.	244
Figure 8.27.- Additional plan views (2240z) showing cumulative plastic strain reached for the rock mass at the model step before it is caved.	245
Figure 8.28.- Cumulative plastic strain at the plan view 2240z and the recorded seismicity between 1996 and 2002.	246
Figure 8.29.- Location of selected points where the stress path were analysed.....	247
Figure 8.30.- Modelled Stress paths (lines and arrows) at different structural domains as the result of cave geometries during caving propagation at the Esmeralda mine sector. Small circles indicate initial state of stresses (red circle from <i>Diorite</i> and <i>Cmet Hwl</i> in both graphs).	248
Figure 8.31.- Rock damage observed in mine drives at the undercut level, and shear stress path from the numerical model.	249

LIST OF TABLES

Table 1.1. Resources inventory 2003 using a Cut off by 0.5%Cu.	11
Table 1.2. Intact and rock mass properties of main rock types at the El Teniente mine.....	27
Table 2.1. Classification of discontinuities according to their size at the El Teniente mine.....	39
Table 2.2.- Censoring level, truncation bias and sample length applied to different line sampling techniques.....	45
Table 2.3. Summary of sample lines used and structures collected in drive mapping analysis.....	47
Table 2.4. Summary of sample lines used and structures collected in scanlines analysis.....	53
Table 2.5. Summary of sampling orientation used and structures collected in oriented core logging.....	55
Table 2.6. Summary of sampling orientation used and structures collected in un-oriented core logging.....	57
Table 2.7. Caved rock block blocks and faces characterised at the Reno mine production level.....	60
Table 3.1. Discontinuity occurrence per sampling technique.....	67
Table 3.2. Probability density distribution after Priest (1993).....	77
Table 3.3. Values of $\Phi(z)$ for the normal distribution, after Priest and Hudson (1981).....	79
Table 3.4. Arithmetic and Geometric mean normal set spacing for discontinuity type sets at the El Teniente primary copper ore.....	81
Table 3.5. Extreme values of discontinuity frequency and their orientations.....	83
Table 3.6. Arithmetic mean of the observed trace length in scanline mapping for discontinuity type sets.....	93
Table 3.7. Percentage of mineral species (more abundant ones) observed as infill within all veins, per data collection technique and sectors.....	97
Table 3.8. Mean of mineral species observed as vein infill per data collection technique and sectors.....	97
Table 3.9. Mean of mineral species observed as vein infill per family sets in line mapping.....	98
Table 3.10. Mean observed infill mineral assemblage per discontinuity type.....	98
Table 3.11. Vein thickness distribution per family sets observed in scanline mapping.....	100
Table 3.12. Vein thickness distribution occurrence observed in veins per data collection technique.....	101
Table 3.13. Roughness of discontinuities sets observed in scanlines mapping at the El Teniente mine.....	107
Table 3.14. Block size and volumetric joint count, after ISRM (Brown, 1981).....	110
Table 3.15. Mean discontinuity frequency along the drill cores.....	117
Table 3.16. Variation of mean thicknesses distribution along drill cores.....	117
Table 3.17. Summarised parameter features within rock mass.....	122
Table 4.1. Occurrence of the El Teniente discontinuities as rock block forming faces per rock type and mining methods.....	124
Table 4.2. Mean of mineral species observed as infill in veins forming caved rock block faces.....	126
Table 4.3. Modes of failure observed in veins forming caved rock block faces.....	126

Table 4.4. Apparent thickness (ae) observed in veins forming caved rock block faces.	127
Table 4.5. Thicknesses observed in veins forming caved rock block faces.	129
Table 4.6. Relative strength of the minerals at the El Teniente mine.	132
Table 5.1. Weak discontinuity occurrence for discontinuity sets observed in small scale sampling.	139
Table 5.2. Mean normal set spacing for data collected by drive mapping.	141
Table 5.3. Mean normal set spacing for weak discontinuities observed in small scale sampling.	141
Table 5.4. Extreme values of discontinuity frequency and their orientations of weak discontinuities.	142
Table 5.5. Observed trace length of weak discontinuity at the El Teniente mine.	145
Table 5.6. Roughness of weak discontinuity sets observed in scanlines mapping.	146
Table 5.7. Thickness of weak discontinuity sets.	147
Table 6.1. The Rock Mass Rating System (after Bieniawski 1989).	159
Table 6.2. Applicability of RMR_B to the El Teniente primary copper ore.	160
Table 6.3. Current Q-System description after Barton at al. (1974).	162
Table 6.4. Q -System for the El Teniente primary copper ore.	165
Table 6.5. Joints conditions adjustments (Laubscher and Jakubec, 2001).	173
Table 6.6. Parameters and rating values to major structures adjustments (Laubscher and Jakubec, 2001).	175
Table 6.7. Applying IRMR/RMRM to the El Teniente primary copper ore.	177
Table 7.1. Normal set spacing for weak discontinuities and faults from drive mapping at Esmeralda mine sector.	186
Table 7.2. Vein thickness distribution per family sets observed at <i>Cmet FwI</i> using drive mapping.	186
Table 7.3. Main set orientation and spacing for weak discontinuities using oriented drill core logging.	188
Table 7.4. Weak vein thickness distribution per family sets observed at <i>Cmet FwI</i> using oriented core logging.	189
Table 7.5. Fragmentation back analysis of Esmeralda mine sector (Pereira and Zamora, 1999).	195
Table 8.1. Main mine model steps and their descriptions.	238

LIST OF SIMBOLS

α	Angle, specifically azimuth angle of maximum dip, orientation of the mean joint set. Also trend of a line
α_n	Trend of a joint unit normal
α_s	Trend of a sampling line
β	Angle, specifically dip angle of the plane or plunge of a line
β_n	Plunge of a joint unit normal
β_s	Plunge of a sampling line
δ	Angle between the orientation of the sampling line and the joint unit normal
η	seismic efficiency
λ	Mean discontinuity frequency (= 1/S)
ρ	Density
σ_i	Principal stress, $i = 1, 2, 3$
σ_n	Normal stress
τ	Shear stress
τ_a	Apparent stress
φ	Diameter
ϕ	Friction angle
ae	Aparent thickness
Anh	Anhydrite
Ank	Ankerite
Ar	Argon
B	Null motion axes
Bo	Bornite
Bt	Biotite
c	Cohesion
C, C_i	Failure Mode, $i = 1, 2$
C.V.	Coefficient of variation
Ca	Calcite
Chl	Chlorite
cm	Centimeters
CODELCO	Corporacion Nacional del Cobre

Cpy	Chalcopyrite
Cs	Calcosine
Cu	Copper
DFN	Discrete Fracture Network
Dm	Drive mapping
DPE	Dissipated plastic energy
D_s	Potential fragmentation
e	Thickness
F	Fault
ff	Fracture frequency
F_w	Footwall
GSI	Geological Strength Index
Gyp	Gypsum
H	Failure Mode
H	Mohs Hardness scale
HR	Hydraulic Radius
H_w	Hangingwall
IR	Intact rock
ISRM	International Society of Rock Mechanics
J	Joint
J_v	Volumetric Joint Count
k	Dispersion parameter of joint orientation (Fischer's constant)
K	Plane
K	Potassium
Km	Kilometers
L	Trace length
LH	Late Hydrothermal
LM	Late Magmatic
m	Meters
m	Minor frequency
M	Moment tensor
Ma	Million of years
mm	Millimeters
Mo	Molybdenite

M_0	Seismic moment
Ms	Major structures
Mt	Magnetite
M_w	Moment magnitude
NML	New mine level
Oc	Oriented cores (referred as large diameter core samples, $\phi = 0.1-0.14$ m)
P	Force axes in pressure
pdf	density distribution function
PH	Principal Hydrothermal
Py	Pyrite
Q	Q-System of rock mass classification
Qtz	Quartz
RMC	Rock mass classification
RMR	Rock mass rating value
RQD	Rock Quality Designation
S	Spacing ($= 1/\lambda$)
s	Standard deviation (also as S.D.)
Scl	Scanline mapping
Se	Sericite
S_n	Normal discontinuity set spacing
T	Force axes in tension
T	Thickness
Te	Tenantite
tpd	Ton per day
tr	traces
Tu	Tourmaline
ucl	Undercut level
UCS	Uniaxial compressive strength
V	Veins
V_I	Failure Mode
V_{rb}	Rock block volume
w	Weak discontinuities
w	Weighting factor

WASM	Western Australia School of Mines
W_{comm}	Comminution process
$W_{\text{in situ}}$	In situ rock damage
z	Mine elevation, above sea level

CHAPTER 1 INTRODUCTION

1.1 The Problem

The characterisation of the rock mass, where any civil or mining excavation would be placed, is the most essential engineering activity to assure its stability and the economic performance. The discontinuities, their geometry and strength properties are likely the main controlling parameters of the behaviour of rock masses during and following excavation construction according to the principles of rock mechanics (Brown, 1981, Hudson and Harrison, 1997, Brady and Brown, 2003).

Characterising rock masses properly has been a main concern in the field of rock mechanics since the late 60's. Since then, the International Society of Rock Mechanics (ISRM) has suggested a method to more accurately perform this activity (Brown, 1981). Discontinuities to be characterized can be described by 10 basic parameters, which describe their geometry and strength properties. One important definition provided by the ISRM is about the term *discontinuity*. The most ample definition of the term geological discontinuity refers to any mechanical breaks or fractures in a rock mass having a zero or low tensile strength (Brown, 1981). This collective term includes most types of planes of weakness such as joints, faults, bedding planes, foliations, etc. That definition has guided the research in the field of rock mechanics during the last 30 years (Barton, 1976, Barton and Stephansson, 1990, Brown, 2003) and currently the rock structure characterisation is concerned with the assembly of rock blocks that comprise the rock mass.

In addition, the mining industry mainly characterizes the rock masses by applying Rock Mass Classification (RMC) systems. These RMC schemes breaks the rock mass into two main components; the properties of intact rock material and the geological discontinuities as define by the ISRM. Both combined rock mass properties are parameterised to determine a rock mass rating. By compiling case histories relative to performance, it has been possible to develop empirical relations for quantitative prediction of the strength characteristics between specific rock masses.

The problem investigated here is not about 'how to characterize' rock masses of the El Teniente mine, but to find out what are the main rock structure features

controlling rock mass behaviour. The following background reflects the nature of the problem or more precisely, the nature of the primary copper ore and its complexity behaviour during caving.

The El Teniente mine is the largest underground mine in the world, located in central Chile. The mine has been operating since 1906 and is currently mining out approximately 140,000 tons per day (tpd) using block caving methods. Rock masses of primary copper ore have been described as very competent and massive during caving operations (Rojas et al., 2001) as shown in Figure 1.1a,b. This is because caving performance has resulted in larger than expected fragmentation, and these rock masses have exhibited brittle, often violent failure under a high stress conditions (Dunlop and Gaete, 1997, Rojas et al., 2000a). Two mine sectors have been partially closed after severe damage in mine levels caused by some large magnitude dynamics failures. Furthermore, following the guidelines of the ISRM (Brown, 1981), very few, usually widely spaced discontinuities (mainly faults) are found within these rock masses, and this could be in agreement with the observed competent rock mass behaviour at the mine site. There is, however, a network of high frequency stockwork veins (healed and cemented joints in Figure 1.1a,b), which is characteristic of a porphyry copper ore deposit (Burnham, 1979).

Such competent rock masses have achieved caving with a small hydraulic radius of around 25m at two mine sub-sectors (Reno and Esmeralda mine sectors) within the El Teniente mine (Rojas et al., 2000a, Rojas et al., 2001). This suggests that the rock mass may also fail readily when is subjected to caving induced stress. It is interesting to note that rock masses of secondary ore, which are usually heavily fractured (Figure 1.1c), are achieved caving with a small hydraulic radius (around 22m), similar to that is supposedly the more competent primary ore. In addition, a significant proportion of fine fragmentation is usually observed in production level cave draw points of primary copper ore. This fine fragmentation allows high rates of underground caving primary copper ore production.

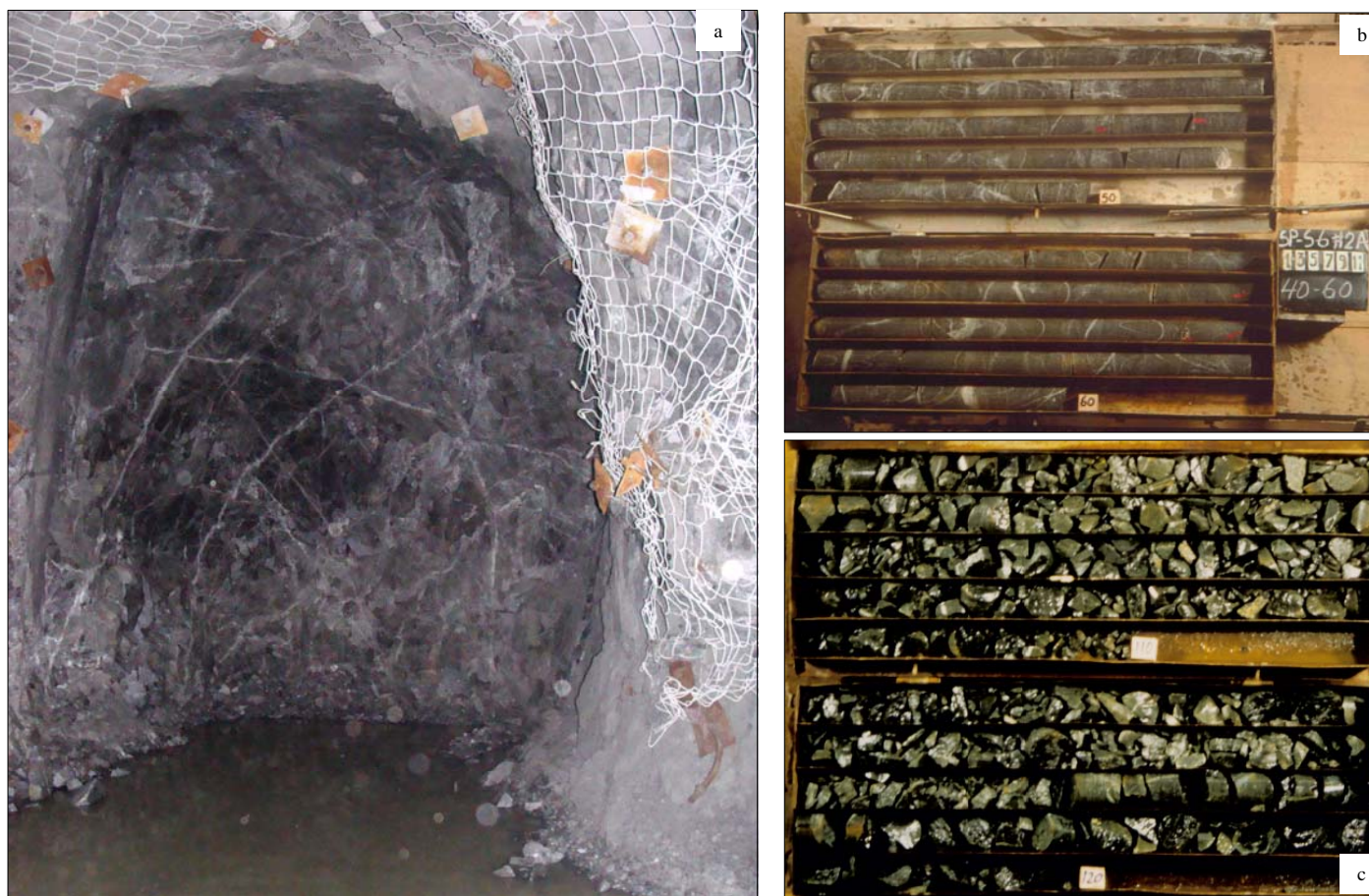


Figure 1.1. Photography sets of the massive and competent primary copper ore at the El Teniente mine containing healed veins (a & b). Core try with a typical recovery of the secondary copper ore (c).

The problem then is to understand this apparent inconsistency or this complex rock mass behaviour for a competent and massive rock mass. In other words, to find out what is the main rock structure features controlling rock mass behaviour at the El Teniente mine.

This apparent inconsistency has not been explained by applying current RMC systems. For instance, it has been found by a Geotechnical Committee Review Board that current RMC systems used at the mine site *'have failed to discriminate rock types that appear to have fundamentally different cavability and rock burst hazard characteristics'* (Goodman et al., 2000). It is believed that the reason for this failure may be due to the inability of these RMC systems to incorporate the proper rock structure features controlling rock mass behaviour. Moreover, it is currently believed at the mine site that the induced seismicity during caving operations *'has more relation to the rock mass characteristics (competence) rather than other factors'* (Araneda and Sougarret, 2007)¹.

Based on experience and observations, a research hypothesis is stated here as follow to guide this thesis and to understand the rock mass behaviour of primary copper ore. Like the strength of a granite rock sample under compressive load, which may be limited by the modest occurrence of weaker minerals (Tapponnier and Brace, 1976), it is believed that *"healed weaker veins may control the strength and behaviour of rock masses of the El Teniente mine"*. In other words, *"the rock mass strength of the massive and competent primary copper ore correlates with the abundance of weak healed veins (cemented joints) within such rock masses"*.

These types of geological structures are not strictly considered as *discontinuities* according to the ISRM because their high tensile strength (Brown, 1981), and these have not been properly included in these RMC systems as well.

1.1.1 *Research Hypothesis, Research Objectives and Data Collection Campaigns*

It is suggested here as the thesis hypothesis research that *"the abundance of healed weaker veins within the rock mass may control the strength and behaviour of rock masses of primary copper ore during caving process"*. Therefore, the main purpose

¹ Both authors currently act as mine operation managers of the El Teniente mine.

of this study is to determine the validity of this hypothesis and its implication for rock mass characterization at the mine site.

In order to achieve the main purpose of this thesis, the work is firstly carried out by applying the simple concept of a comparison between the input and the output of the caving phenomenon, i.e., a comparison between the geological features that compose the rock masses and the characteristics of caved rock block forming discontinuities found at production level draw points. From this work is expected to clarify how or through which, either *discontinuities* or *intact rock*, these rock masses are being disassembled during the caving process. Once the main characteristics that define the faces of caved rock blocks are established (expected to be the weaker path of the primary copper ore), these can be applied into the standard rock structure characterisation to investigate whether the occurrence of such weaker discontinuities may explain the observed differences in rock mass response to mining activities.

This research approach outlined a number of objectives that this thesis will examine. These are:

1. Based on rock structure characterisation and data analysis, develop a criterion to characterize rock masses of primary copper ore.
2. Validate this new criterion in another different mine environment.
3. Investigate whether the application of this new criterion can be used to understand the rock mass response to mining activities.

The field work for this thesis was carried out at the two different active areas within the El Teniente mine. The completeness of some data collection was influenced by ongoing production activities. Two main field work campaigns were organised in two stages, the first one was undertaken between 2002 and 2003, and the second one during 2006. The first field work campaign was conducted by task force team composed of mine geologists included and guided by the author of this thesis. The funds for this particular field work campaign were provided by a special the El Teniente investment funds classified as API T01M101 (Brzovic and Benado, 2003). The second field work campaign, which was considerably less extensive, was conducted by the author in 2006. Additional data sets collected by mine geologists and engineers as part of the production requirements were also re-analysed here

following the research hypothesis, these included: additional structural data, seismic and production records, and ground control information from several ongoing mine production sectors. This thesis also included an especial determination of moment tensors of the induced seismic events, and the development of a mine scale numerical modelling.

1.2 Thesis Outline

The present research was divided in two main parts. The first part was designed to develop the methodology to carry out rock mass characterization of the competent and massive primary copper ore. This was based on determining the main rock structure features that may control rock mass behaviour during caving. This first part was carried out at the Reno Mine Sector (former Ten Sub-6 mine sector) within the El Teniente mine and comprises Chapter 2 to 6. The objective 1 was achieved during this first part of the study.

The second part of the research was designed to validate the proposed methodology and to investigate how the new rock characterization methodology correlates with the real rock mass response to mining activities. This second part was completely undertaken at the Esmeralda mine sector within the El Teniente mine and comprises Chapter 7 and 8. Objectives 2 and 3 were achieved in this second part of this research.

In this thesis the literature review and fundamentals were undertaken considering the main subjects researched, and these are presented on a background subsection as a precursor to data analysis from El Teniente.

The chapters of this thesis have been summarised below:

Part I

Chapter 1 introduces the problem and the context of. The geological and geotechnical data and literature of ore deposit is reviewed. Location, history, stress field and mining methods are all described within this chapter.

Chapter 2 describes the data collection techniques used in this study and the location where the first field campaign was conducted. Literature review of conventional data

collections techniques, sampling bias, structure definitions are presented in this chapter. Simple modifications to current discontinuity collection techniques were implemented to better determine discontinuity characteristics within the primary copper ore.

Chapter 3 presents the analysis results of the rock mass characterisation undertaken during the first field work to describe the rock structure of the El Teniente primary copper ore. Discontinuity parameters are described following ISRM guidelines (Brown, 1981). In this chapter a literature review for main discontinuity parameters and for structural data analysis is also undertaken. Some data analysis is carried out considering the genetic origin of the geological discontinuities, from large scale faults to the small scale veins network (stockwork). A comparison between two structural domains of the Reno mine sector was also undertaken to investigate how discontinuity parameters vary throughout the rock mass.

Chapter 4 is an assessment of block forming geological discontinuities by mapping several caved rock blocks at the production level caving draw points. An empirical definition of weak discontinuities is defined in this chapter, and the discontinuities having these features are expected to be the weaker path for possible rock mass failures within primary copper ore.

Chapter 5 presents a re-analysis of data used in chapter 3, incorporating the established empirical definition of weak discontinuities gained in chapter 4. In this chapter the rock structure characterisation also follows the ISRM guidelines (Brown, 1981). A comparison between the two structural domains within the Reno mine sector was also undertaken, which included the stochastic simulation of the rock structure to obtain the in situ rock block distributions or the in situ fragmentation. The fragmentation model for the primary copper ore is also discussed in this chapter.

Chapter 6 describes an application of the current rock mass classification systems based on the data collected in previous chapters. The inability of these RMC systems to quantify actual differences between two structural domains of the Reno mine sector encountered in Chapters 3 and 5 is also discussed.

Part II

Chapter 7 describes a new data collection campaign undertaken at the Esmeralda mine sector to validate the proposed methodology discussed in chapter 4 and 5. Information of the rock mass response to mining activities at the mine sector for back analysis studies is also reviewed in this chapter. These included; caving propagation and hydraulic radius, fragmentation performance and rock damage at the undercut level.

Chapter 8 presents two back analysis studies undertaken at the Esmeralda mine sector to validate to hypothesis research. Seismicity during caving propagation and rock damage at the undercut level cause by stress redistribution were both as rock mass response to mining used in the back analysis. Differences between three structural domains within this mine sector were also assessed. Literature review of induced seismicity by caving process, and mine seismology, which included fault plane solutions and moment tensor to be compared with structural data, were reviewed in this chapter. This chapter also included a mine scale numerical modelling to assess the stress around excavation during caving propagation at the Esmeralda mine sector to complement the back analysis studies.

The concluding chapter highlights the main finding of this study, and the implication of rock mass cavability and fragmentation are discussed. The limitations of the methods and assumptions of the study are also addressed. Finally future research on this topic is proposed. The appendices include a detailed procedure used during data analysis, and list the raw data for each field site/data collection.

1.3 The El Teniente Mine Overview

1.3.1 Location and Brief Mine History

The El Teniente mine is located in Central Chile, latitude of approximately 34°South, and a longitude of approximately 70.3°West (Figure 1.2).

The ore body is located in the Andes range at 2,200 meters above sea level nearby a small mine town called Sewell. The mine site area is surrounding by severe

topography, where elevation difference greater than 1,000 meters over a kilometre are commonly observed (Figure 1.3).

The mine site is approximately 2 hours drive south direction from Santiago (90 kilometres), the Chilean's capital, and 44 km to west direction from Rancagua, the nearest large town. The relationship between mine coordinates and the Universal Transverse Mercator (UTM) coordinate system is as following:

$$\text{Mine North} = \text{True North} + 14^{\circ}19'34'' \quad (1.1)$$

$$\text{Mine Level (z)} = \text{Elevation above sea level} - 21.36\text{m} \quad (1.2)$$

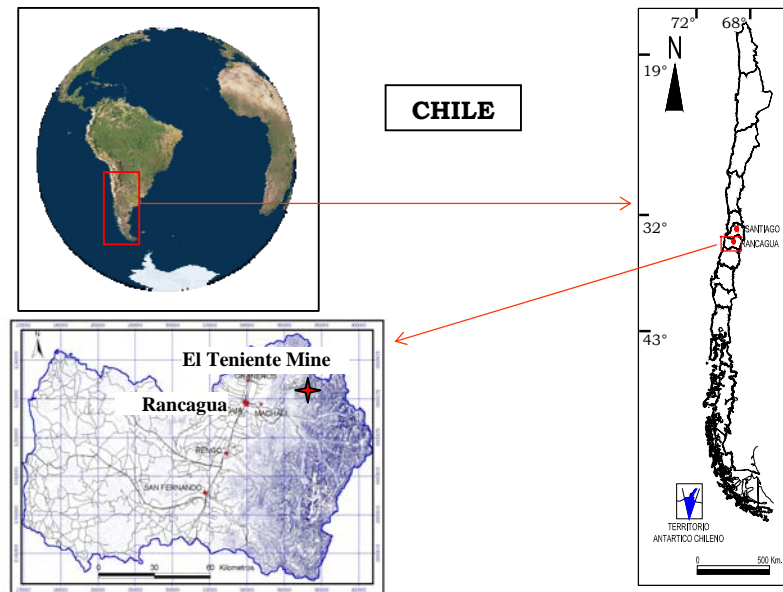


Figure 1.2. Location of the El Teniente mine (red star) in Chile

Mine layouts shown throughout this study use the mine coordinate systems.

A fugitive Spanish lieutenant apparently discovered the 'El Teniente' or 'The Lieutenant' ore body in 1706, however, aborigines of central Chile knew of this place before. Early mining production records date as far back as 1819, but, systematic underground exploitation began only in the early 20th century under the guidance of William Braden (Baros, 1995).

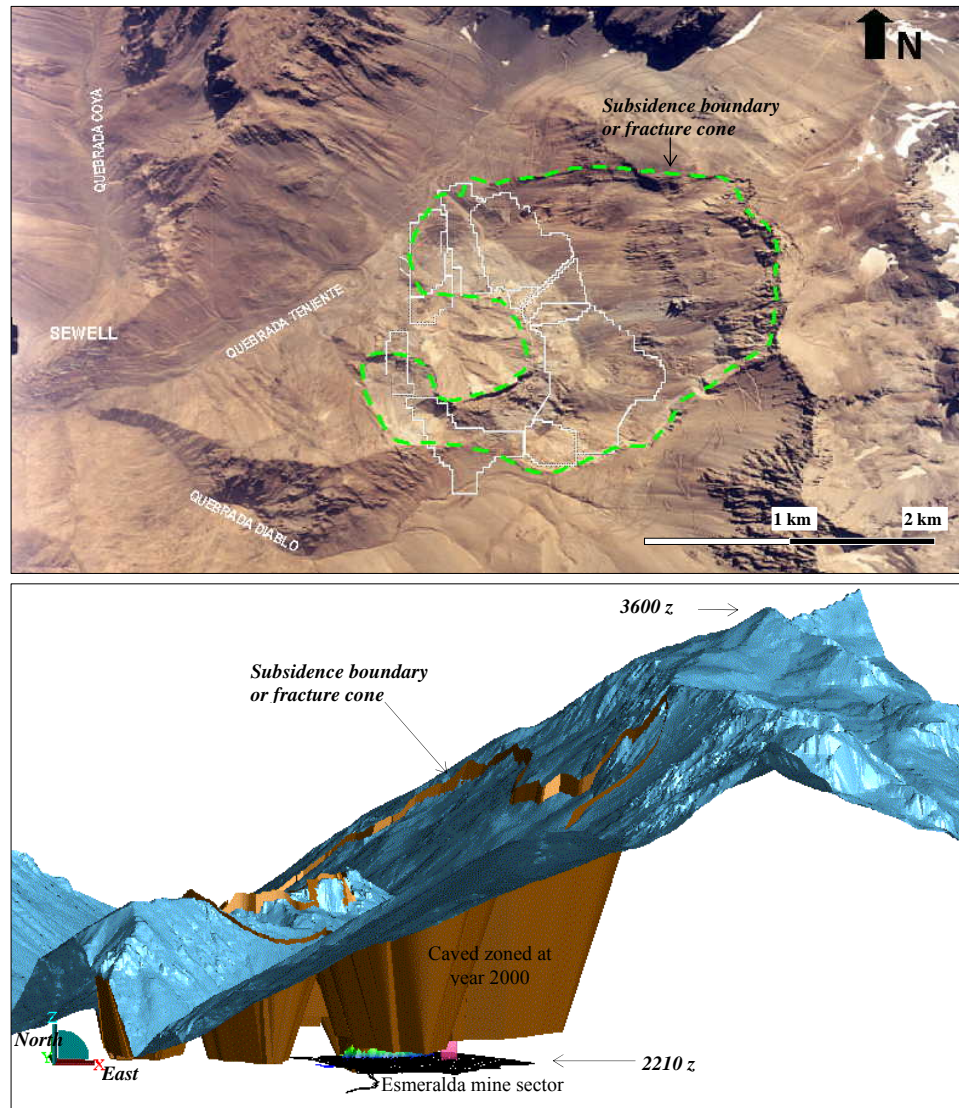


Figure 1.3. Aerial photography and isometric view of El Teniente mine. Current exploitation area is delimited by white lines in the upper picture (both figures with mine grid).

In 1904 W. Braden bought the property and formed the Braden Copper Company, a 250 tones per day (tpd) concentrator was built in Sewell at 2100 meters above sea level during this early beginning. In 1915 the company was acquired by the Kennecott company, which kept it until the government of Chile bought 51% of the property in 1967. Mine production in 1960 was 34,000 tpd of ore. In 1971 the El Teniente mine became a completely state-owned company, and in 1976 the Copper National Corporation (CODELCO) was created by the Chilean government. Currently CODELCO is the world's biggest copper producer owning five large

copper mine within the country; Chuquicacamatá mine, Radomiro Tomic mine, El Salvador mine, Río Blanco mine and the El Teniente mine.

Since 1906, more than 1,100 million tons have been mined out at the El Teniente mine. In 1975 the total copper production reached 500 million tons of ore, and between 1975 and 1995 another 500 million tons of ore were extracted. Currently, mine production is about 140,000 tpd, 80% of this within primary copper ore (Araneda and Sougarret, 2007). The secondary ore has been mined out since the beginning, but primary copper ore only started in 1982 (Rojas et al., 2001).

1.3.2 Resources and Size

El Teniente is the largest copper-molybdenum deposit known in the world. The actual depth to which the copper mineralization extends is unknown, it is known to be for more than 1.3 km deep (Skewes et al., 2002). The 0.5% Cu grade contour defines a shape in form of a pear that is roughly 2.8 km long and 1.9 km wide at the mine level Teniente 5 (2280z). The total resources of the in situ copper ore have been estimated to be more than 7,400 million of tons with an average grade greater than 0.82%Cu as shown Table 1.1. The hypogene or primary copper ore is chalcopyrite and bornite.

Table 1.1. Resources inventory 2003 using a Cut off by 0.5%Cu.

Categories	Million tons	Copper Grade, %Cu
Measured	1,128	0.985
Indicated	2,019	0.895
Inferred	4,288	0.753
Total	7,434	0.827

Note: In situ mineral, between surface and 360 meters below the current production level (2120z).

1.4 Regional Geology

The Andes Ranges, particularly in central Chile, have been formed from a crustal shortening, thickening and magmatic addition along the western continental margin of South America plate above the subducting Nazca plate (Ramos, 1988). The bulk of the Andes Range in central Chile consists of several kilometres of thick Mesozoic and Cenozoic sedimentary, intrusive and extrusive igneous rocks (Charrier et al.,

2002). The El Teniente ore deposit is located in a belt of tertiary volcanic rock in central Chile (Figure 1.4).

The El Teniente mine is hosted by the Farrelones Formation (Howell and Molloy, 1960), which consists of complex extrusive and intrusive igneous rocks dated from middle to late Miocene (Figure 1.5). It is a sequence of more than 2,500 meters thick lava flows, volcanolastics and piroclastics rocks, dykes and stocks of basaltic and rhyolitic composition (Vergara et al., 1998). The Farrelones Formation surrounding the mine site has been locally referred to as the Teniente Volcanic Complex (Skewes et al. 2002), which has been correlated with the upper part of this formation. The age of this volcanic complex has been dated between 7.2 and 15.2 millions of years (Cuadra, 1986), and its appearance seems to present a lower level of deformation.

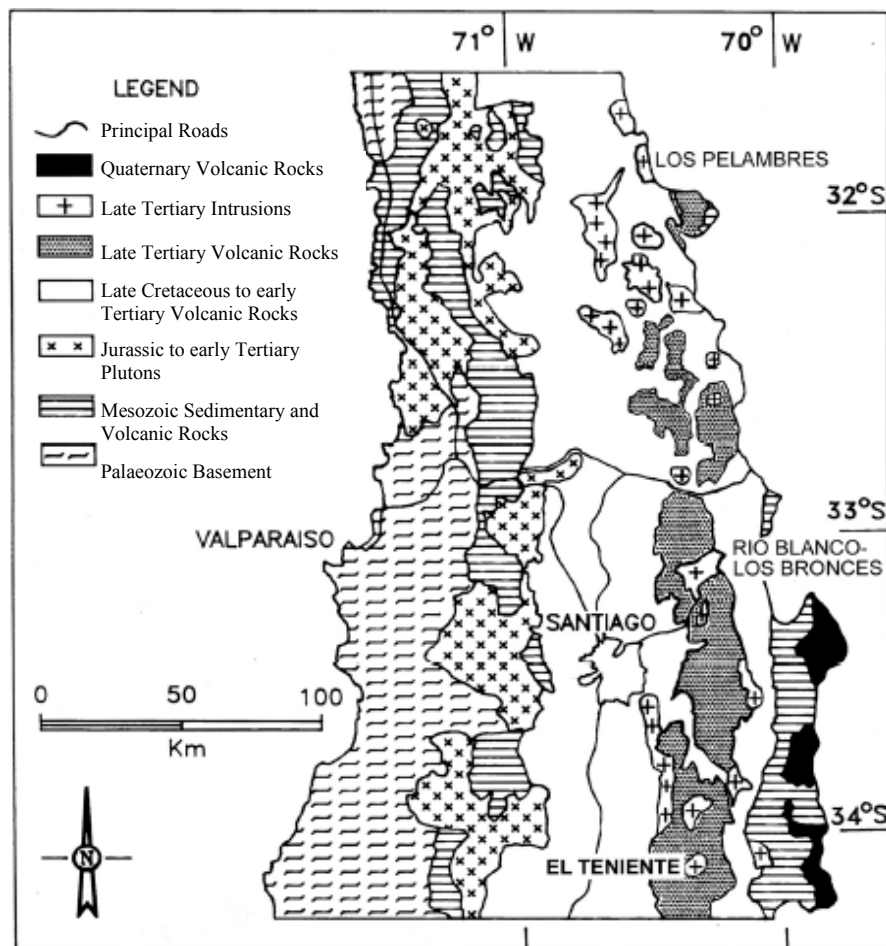


Figure 1.4. Geology of central Chile (after Skewes et al. 2002).

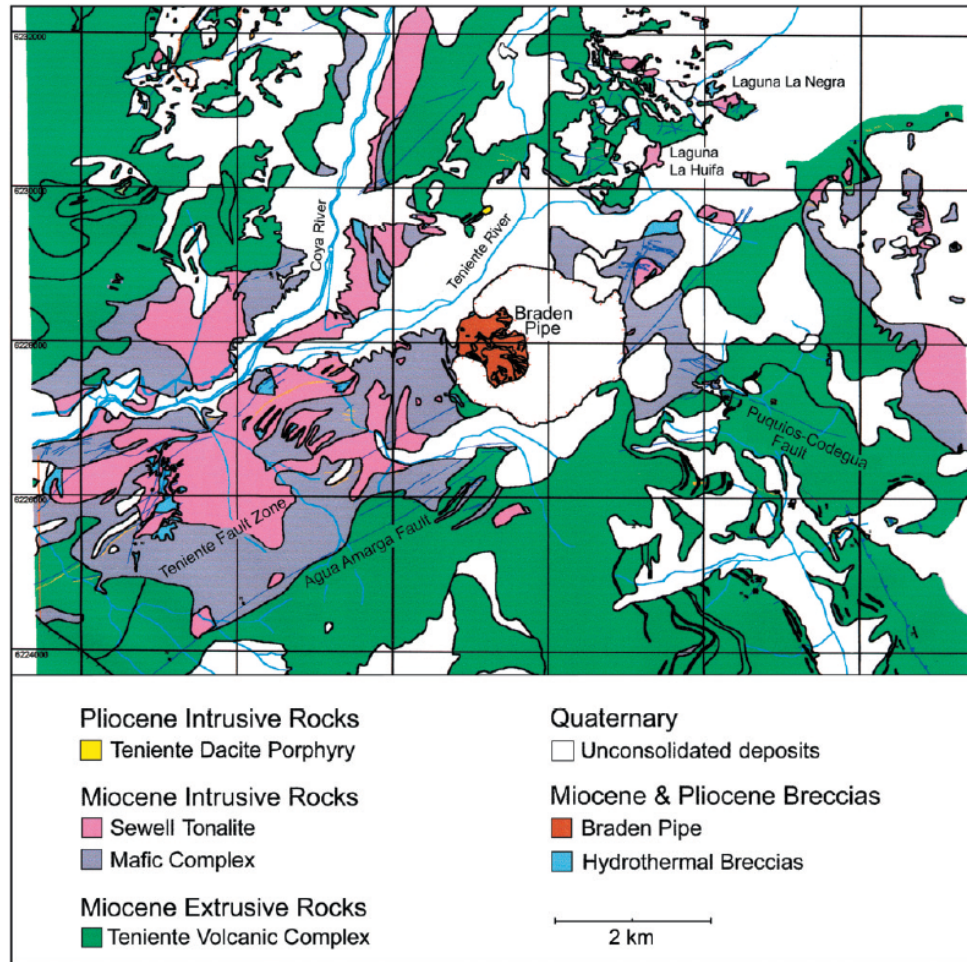


Figure 1.5. Geology of the area surrounding the El Teniente copper deposit with true north (after Skewes et al. 2002).

Despite the less deformed rock of the Teniente Volcanic Complex, Garrido et al. (1994) has suggested that the deposit is emplaced within the El Teniente Faults Zone (ETFZ), which is the most important feature at the district scale. The ETFZ consists of anastomosing strike-slip faults trending north-east 65° , within a 14 km long and 3 km wide block (Figure 1.5). Kinematics fault analysis and geological evidence from the regional and district area surrounding El Teniente indicates that a regional east-west shortening direction occurred during Pliocene, whereas a north-northeast shortening has prevailed during the quaternary (Garrido et al., 1994, Cladouhos, 1994).

² True north

1.5 Mine Site Geology

Several rock types can be identified within the ore body. Those have been described and referred to as the El Teniente Mafic Intrusive Complex, Felsic Intrusions and Breccias according to Skewes et al. (2002) in Figure 1.6.

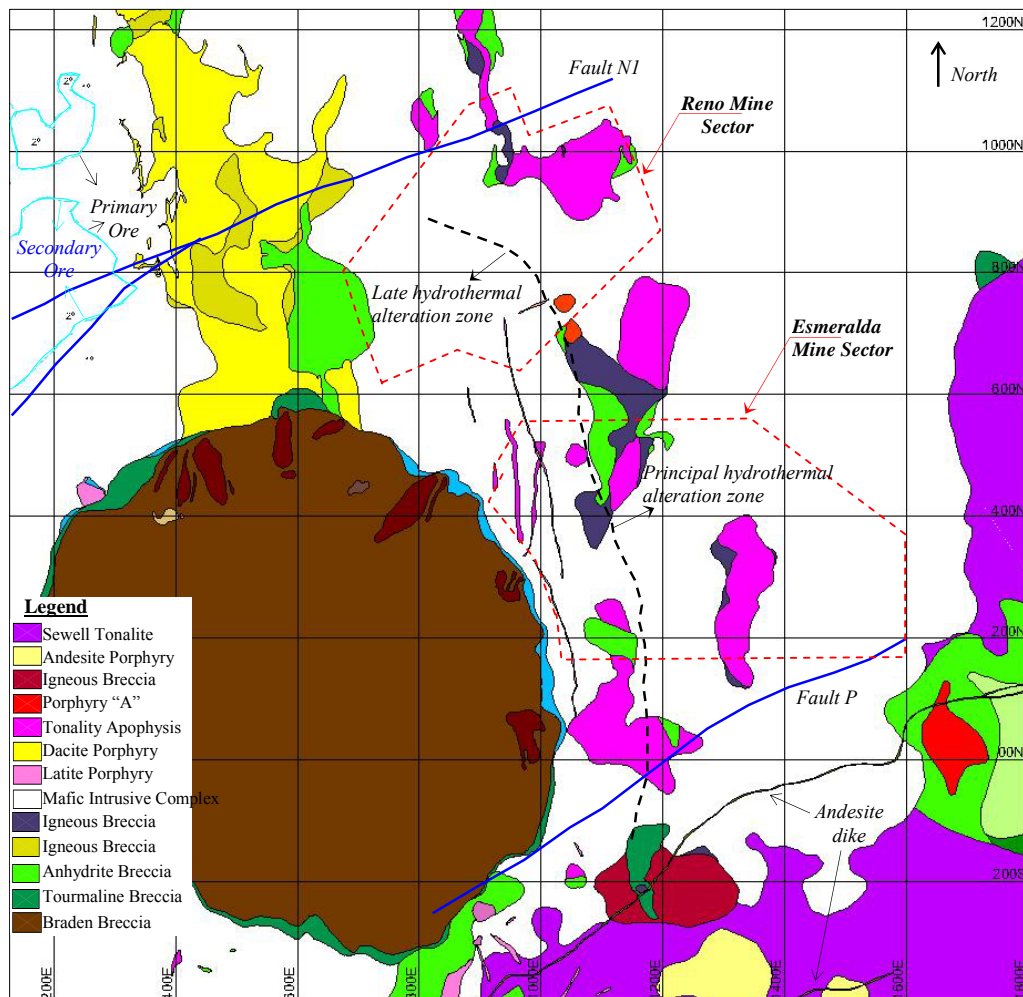


Figure 1.6. Plainview with lithology and structures of the El Teniente ore body at the Ten-6 level (2165z). Red dashed lines indicating area of mine sectors studied in this research.

1.5.1 El Teniente Mafic Intrusive Complex

The oldest and more abundant rocks within the mine have been called ‘andesite’ or ‘mine andesite’ (Skewes and Arevalo, 1997). This rock type, which is typically dark coloured, host 80% of the copper mineralization. Its original petrological features have been obscured by an intense and overlapping alteration stage (Skewes et al.,

2002). Although the name andesite suggests intermediate extrusive rocks, which have been correlated with the andesite extrusive of the Farellones Formation, it is a mafic intrusive rock. Recently studies have demonstrated that this mafic intrusive rock includes gabbros, diabases, basaltic and basaltic andesite porphyries, which have been denominated as the Mafic Intrusive Complex (Skewes and Arevalo, 1997, Skewes et al., 2002).

The Mafic Intrusive Complex has been interpreted as a form of laccoliths with a vertical extent of more than 2,000 meters in the mine area. At an inferred 8.9 million of years (Ma) ago, this complex intruded rocks of the El Teniente Volcanic Complex, according to Skewes et al. (2002).

1.5.2 *Felsic Intrusions*

Various individual felsic intrusive stocks and dykes have been recognised within the deposit. The most important are the Sewell Tonalite located south-east of the Braden Pipe, and the smaller Teniente Dacite Porphyry at north of the deposit (Figure 1.6). Other smaller felsic bodies appear mainly in the central part of the deposit to the East of the pipe.

The Sewell Tonalite, locally referred to as a ‘Diorite Porphyry’ (diorite in this study) occurs as a large stock to the south-east of the deposit. It is a light green to white equigranular to porphyritic rock. The Sewell Tonalite consists of abundant plagioclase (oligoclase), altered amphibole, biotite, quartz and minor potassium feldspar. This unit has been dated between 7.1 and 7.4 Ma by K-Ar (Cuadra, 1986).

The Teniente Dacite Porphyry, locally referred to as a ‘Dacite Porphyry’ (dacite in this study) is a tabular dyke up to 300 meters wide that strikes north (mine coordinates) over 1,500 meters. This unit is a light green to white porphyritic rock composed of 30-50% phenocrysts, such as abundant sub-euhedral plagioclase (oligoclase-andesine), occasional rounded quartz eyes and rare mafic crystals. The groundmass is composed mainly of granoblastic quartz and K-feldspar crystals (Skewes et al., 2002). Textural varieties have been observed within this body, which have been dated between 4.6 and 4.7 Ma (Cuadra, 1986).

Smaller felsic bodies have been recognized to the East of the Barden Pipe. The most relevant are the Tonalite Apophysis, locally called ‘Diorite’ or ‘Diorite Porphyry’ (similar to the Sewell Tonalite). Those units are light grey to light green intrusive rock, which form cylindrical apophyses. Their compositions are mainly of phenocrysts of abundant plagioclase (oligoclase-andesine), minor quartz eyes and remnant biotite phenocrysts, which have been replaced by chlorite. The groundmass is aplitic.

Other minor felsic intrusive bodies are the Latite Porphyry, sometimes in the form of thin dykes (1-2 meters wide) that appears surrounding the Braden Pipe, and the Andesite dykes located south of the deposit.

1.5.3 *Breccias*

A number of magmatic and hydrothermal breccias have been identified at the El Teniente mine; both mineralised and unmineralised have been described (Floody, 2000). The Braden Pipe is the largest breccia located close to the centre of the deposit. It is light grey, massive and essentially a post-mineralization polymict breccia pipe, which looks like concrete. The pipe’s shape is an inverted cone and is 1,200 meters wide at surface. The walls are inward dipping at 60-70°, except on the east side, which is sub-vertical. Within this unit several facies has been recognised, each one characterized by its own relationship matrix-clasts and alteration type. These facies have been interpreted as different stages of its own evolution. The matrix is typically rock flour material plus different minerals, and a typically tourmaline breccia ring of this body is known as Marginal Breccia (Figure 1.6).

Other less extensive breccias are described within the deposit. These are found mainly surrounding the felsic intrusive rocks and the Braden pipe. They are defined as hydrothermal breccia, where the matrix is principally mineralization such as anhydrite and tourmaline, among other minerals. Where the matrix is igneous rock, they are defined as igneous breccia.

1.5.4 *Alteration*

The main concept behind a genesis model for a porphyry copper deposit states that; as magmas (melts) rise through the upper crust, the confining pressure diminishes

and enriched solution called brine is separated from the melts by an exsolution process. This solution carries up metal that will be part of the ore. Because the volume of brine is greater than the volume of an equal mass of the enriched solution when it is part of the melts, its appearance by the exsolution process produces and transfers mechanical energy to the host rock due to expansion (Whitney, 1975, Burnham, 1979). The extent on which the mechanical energy is transferred to the host rock depends on the ambient pressure at the depth of emplacement. For example, at a confining pressure by 0.5 kilo-bars (around 2 kilometres deep), expansion could reach approximately 50 percent of the volume upon complete crystallization. This percentage decreases at increasing depth and vice versa. The mechanical energy generated is enormous, therefore an intense fracture system takes place in the roof of the host rock and is penetrated by the fluid phase, which further extends fractures by hydraulic fracturing. Fluid migration occurs into the network and the disequilibrium between hydrothermal fluid and host rock causes physical and chemical changes in the aqueous solution leading to metal precipitation (Cline, 1995). This process may occur several times; the occurrences are named 'first boiling', 'second boiling' and so on. Therefore, several fracturing stages can take place (Whitney, 1975, Burnham, 1979) and an intense vein network that has been called *stockwork* is generated (Figure 1.7).

Because the disequilibrium between hydrothermal fluid and host rock causes chemical changes in the host rock (Baene and Bodnar, 1995), an alteration halo is formed with each boiling. Furthermore, each boiling or event of alteration-mineralization may generate its own mineral assemblage vein systems, and the intensity of alteration may be related to the intensity of fracturing (Baene and Bodnar, 1995).

According to Cuadra (1986), four process or stages of hypogene mineralization-alteration have been described at El Teniente mine, which can be inferred as boiling stages. These are referred as; Late Magmatic (LM), Principal Hydrothermal (PH), Late Hydrothermal (LH), and 'Postuma' stage.

The Late Magmatic (LM) alteration has been characterized as potassic alteration. During this stage quartz, anhydrite and sulphide veins were formed, in association with, or preceded by a pervasive potassic alteration of the mafic rock (Zuniga, 1982).

The potassic alteration is characterised by abundant biotite, chalcopyrite, Fe-oxides, and anhydrite (Skewes et al., 2002). These authors suggest that this alteration resulted from an intense early biotite alteration through biotite veins. Therefore, the typically quartz anhydrite and sulphide veins in this stage do not alter the wall rock³, i.e., they do not generate alteration halos, such as the case observed (Figure 1.8). The LM alteration stage is mainly located surrounding the Braden Pipe breccia (Zuniga 1982, Cuadra 1986).

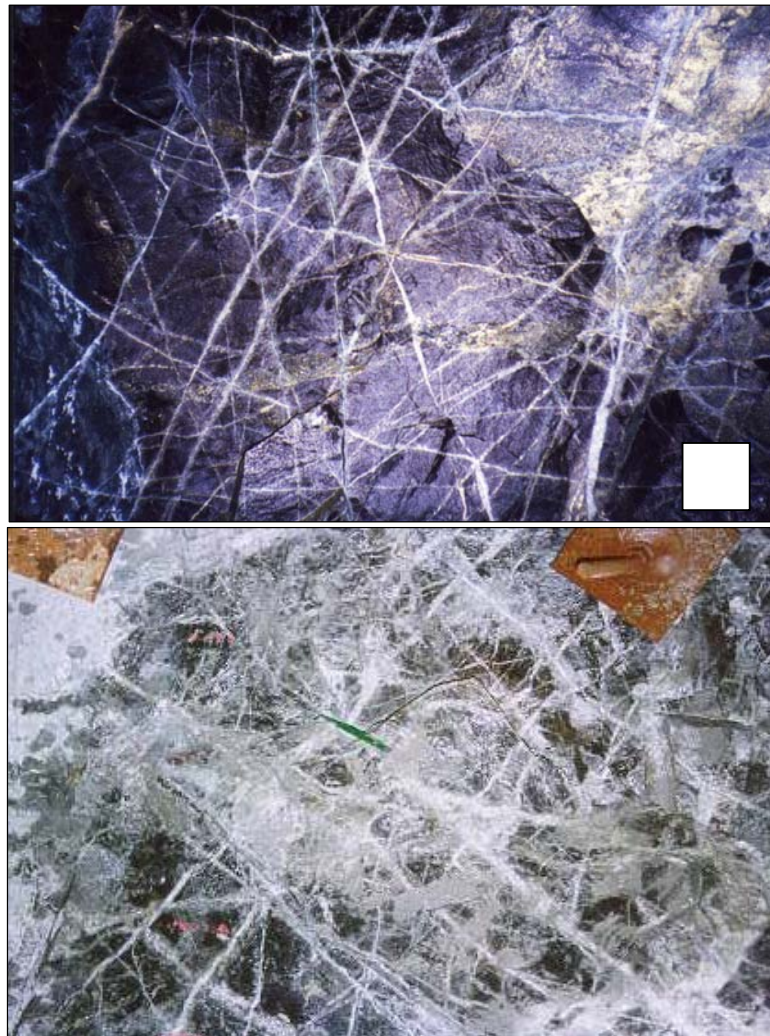


Figure 1.7. Stockwork intersected andesite rock type within primary copper ore. The white square (top photo) and the rock bolt plate (bottom photo) are 20x20 cm.

The Principal Hydrothermal (PH) alteration has been characterized as phyllic alteration. During this stage, chalcopyrite rich veins that also contain anhydrite,

³ Rock adjacent to the discontinuity surface.

pyrite, quartz and chlorite were developed (Zuniga 1982). Quartz sericite alteration is generated as alteration halos in the wall rock (Figure 1.9).

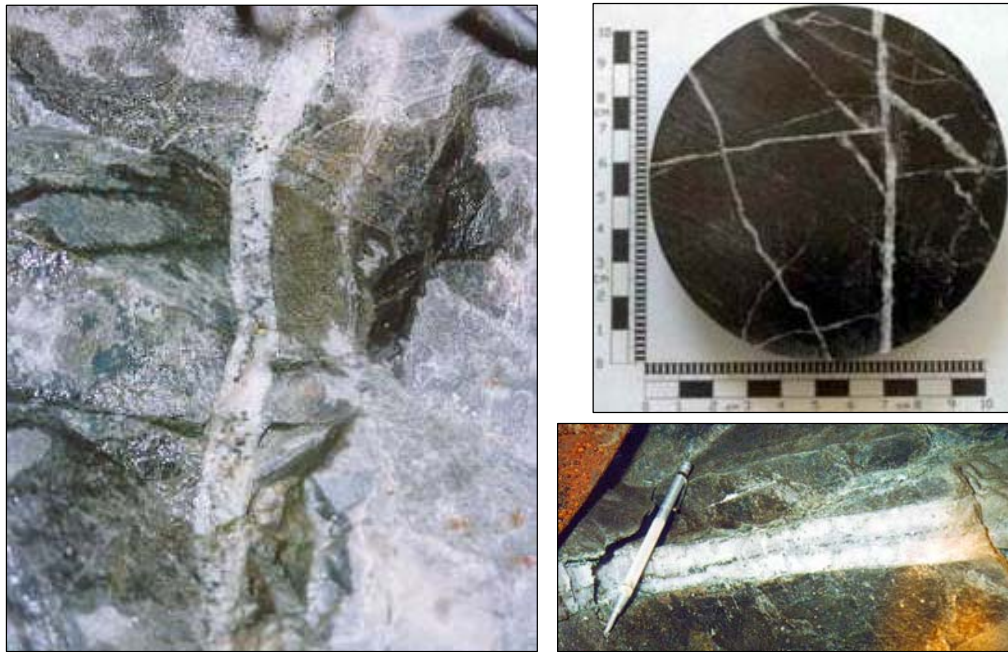


Figure 1.8. Typical late magmatic (LM) veins.

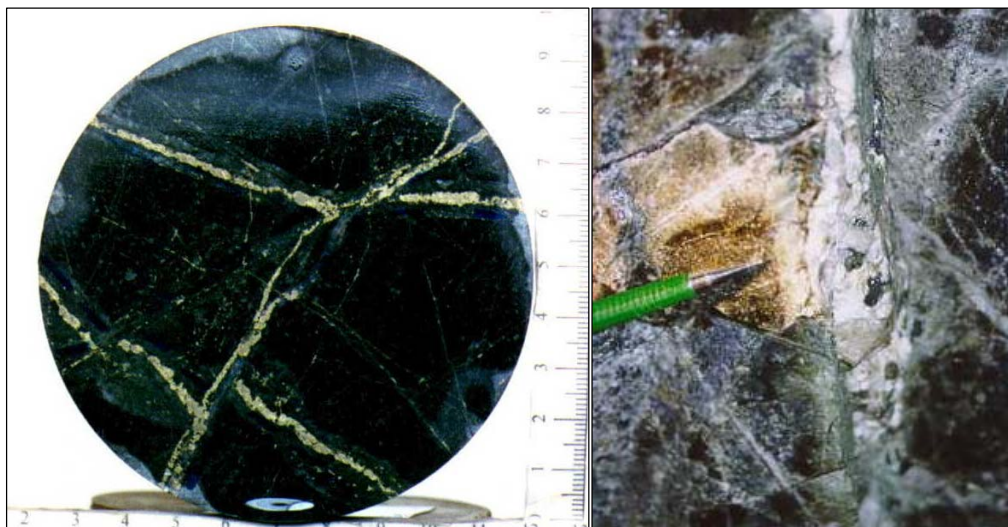


Figure 1.9. Typical veins of the principal hydrothermal alteration stage (left side) and of the late hydrothermal alteration stage (right side).

The Late Hydrothermal (LH) alteration has been characterized as a second stage of phyllic alteration. During this stage more diverse sulphide mineral assemblage veins

were formed, and included: bornite, chalcopyrite, anhydrite, pyrite, quartz, tennantite, gypsum, chlorite and molybdenite. Quartz sericite alteration is generated as alteration halos in the wall rock (Figure 1.9).

The Late Hydrothermal alteration has major intensity (vein frequency) surrounding the Braden pipe in a ring extending from 100 to 150 meters (Cuadra, 1986), whereas the Principal Hydrothermal alteration is more intense (vein frequency) surrounding the diorite apophyses. A boundary between both alterations zones has been defined, which is called the perimeter of hydrothermal alteration zone (Figure 1.6). Consequently at the mine site, the rock types have been named by a definitional hydrothermal alteration suffix, for example, andesite located within principal hydrothermal zone is called andesite PH.

The 'Postuma' alteration is considered the last stage of hypogene alteration. It is limited within the Braden pipe only (Floody, 2000). At this location, natural cavities contain giant euhedral gypsum crystals over 4 meters long as well as other minerals, which are related to this alteration stage.

Supergene alteration has also occurred, which is not a hypogene process, coinciding mainly with the complete leaching of anhydrite and the appearance of supergene chalcocite. Supergene alteration that defines the secondary ore has been recognised between 100 and 600 meters below the surface (Cuadra, 1986). Secondary ore is a heavily fractured rock mass (Figure 1.1c). The hypogene alteration zone, which is the original alteration without supergene alteration, is called primary ore (Figure 1.10).

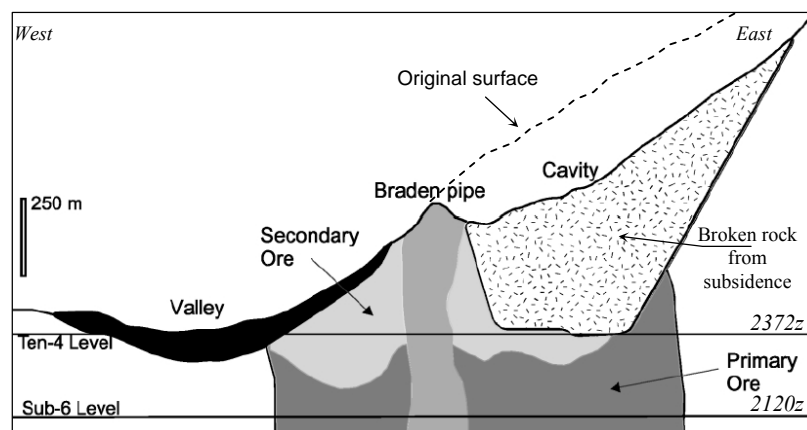


Figure 1.10. East-West section at El Teniente mine showing the primary and secondary ore.

1.5.5 Structures

In addition to the veins forming the stockwork, this section describes other structures recognised within the ore body such as faults or the fault systems according to Garrido et al. (1994) shows in Figure 1.11.

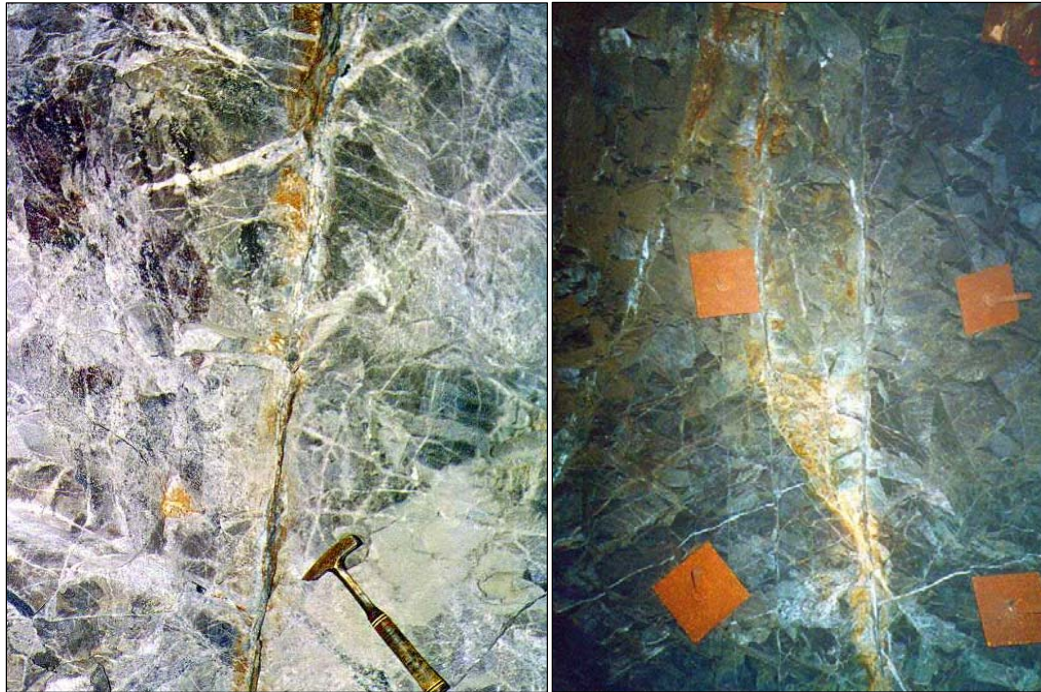


Figure 1.11. Faults at El Teniente mine within primary copper ore. Rock bolt plates are 20x20 cm.

Fault systems consist mainly in strike slip faults trending north-east and north-west (mine grid), which is associated with the late hydrothermal alteration stage. Late hydrothermal mineral assemblages appear in most faults (Brzovic, 2001). Two major faults have been recognized within the mine, these are called ‘Fault P’ located in the south part of deposit, and ‘Fault N1’ located in the north part (Figure 1.6). Both have been recognized with a horizontal trace length exceeding 800 meters and vertical trace length exceeding 400 meters. The gouge observed in both structures has an average thickness of 0.1 meters.

Faults are the only open discontinuities observed within the primary ore, which allow water flow through them. Copper and iron oxides may sometimes be recognised within the faults as shown Figure 1.11. Faults shown in this figure represent the

typical minor faults observed at the mine site, which may develop fault branches related to shear zones.

1.6 Mining Methods

1.6.1 Mining Methods History

The first applied mining method in the El Teniente was a combined shrinkage stoping and pillar caving method, which was used until the 1930's (Rojas et al., 2001). The experience gained in this period demonstrated that the secondary ore could be extracted using block caving methods (Chacon et al., 2004).

Block caving is the technique in which gravity is used in conjunction with rock mass features to disaggregate a rock mass. The caving of the rock mass is induced by undercutting the base of a block. Gravity induced instability produces the progressive rock mass failure leading rock blocks to falls, which are then handled by miners (Figure 1.12).

Block caving method applied for extracting secondary ore remained practically unchanged for many years (Chacon et al., 2004). The production level layout consisted of a 7.5x7.5 meters draw point grid with a 0.5 meters grizzly pass, manual extraction, and a vertical distance of 8 to 10 meters between production and undercut levels. The secondary ore began to deplete in the 1970's, however, a minor mine sector is currently being extracted within secondary ore.

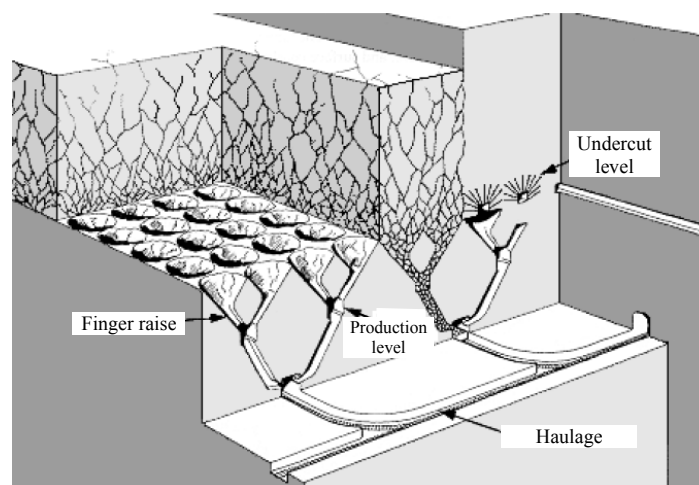


Figure 1.12. Block caving mining method (Hamrin, 2001).

Primary ore production started in 1982 in the Teniente 4 South mine sector (2243z), and continued to other sector within the mine. The physical and the mechanical properties of the primary ore differ significantly from the secondary ore. Primary ore was lower grade, stiffer, and harder. It resulted in coarser fragmentation than the secondary ore at caving draw points (Rojas et al., 2001). Consequently, a new caving method variant was applied; panel caving with a mechanized Load-Haul-Dump equipment system in production levels. Locally it is called the ‘conventional panel caving’ mining method (Rojas et al., 2001). The new method required more space between draw points, and the design involved a 17x15 meters draw point grid in the production level, a reduction level with picking hammer, and a 18 meters distance between production and undercut levels (Figure 1.13). Over 40,000 tpd has been mined in the Teniente 4 south mine sector using that mining method.

Experience and knowledge gained after 15 years of primary ore extraction using conventional panel caving (around 200 million tons extracted) showed that drive damage below the undercut level can occur with this method. This damage is caused by the abutment stress concentration ahead of front. A typical example of stress redistribution recorded by stress measurements at the undercut level are shown in Figure 1.14.

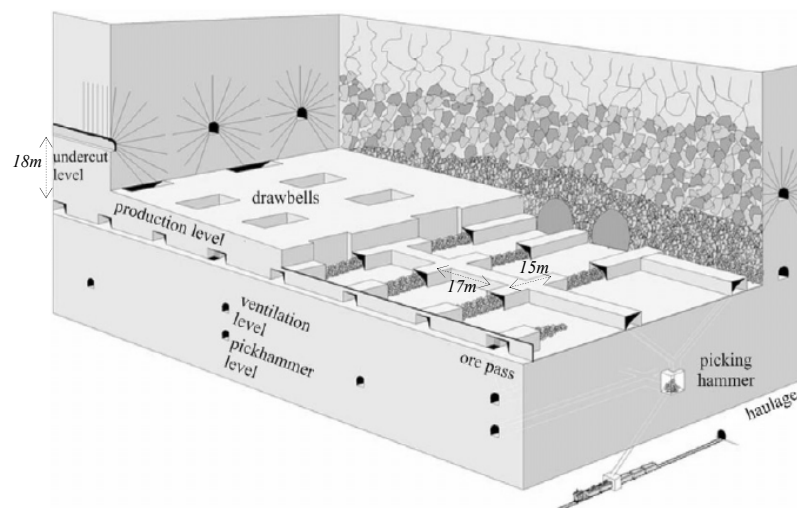


Figure 1.13. Panel caving method at El Teniente mine (Hamrin, 2001).

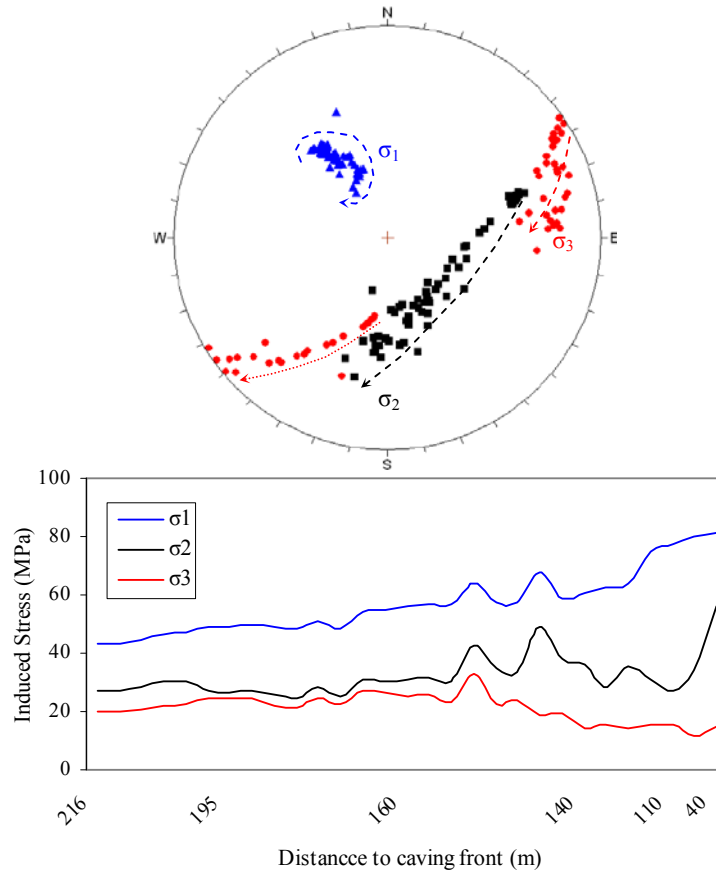


Figure 1.14. Measurement of stress increase as a function of the distance to the caving front.

Figure 1.14, which is from Esmeralda mine sector, shows how principal stress σ_1 almost doubling as a result of the abutment stress concentration due to the moving cave front. Data analysis of rock failures at the Teniente 4 south indicated that 18% of the area collapsed at the production level. This failure was attributed to the stress increase (Chacon et al., 2004). Based on this failure a new caving method variant was designed and implemented. This new method was called the pre-undercut caving method, which was firstly applied to the Esmeralda mine in 1994 (Rojas et al., 2001).

Pre-undercut mining differs from the conventional panel caving mining method with the development of the undercut. The pre-undercut variant consists of advancing the undercut ahead of all developments in the lower levels, i.e., all developments below the undercut level are excavated under the cave area and behind the cave front (Figure 1.15). This may reduce the effect of abutment stress at the production level. More details of this mining method are presented in Section 1.6.5.

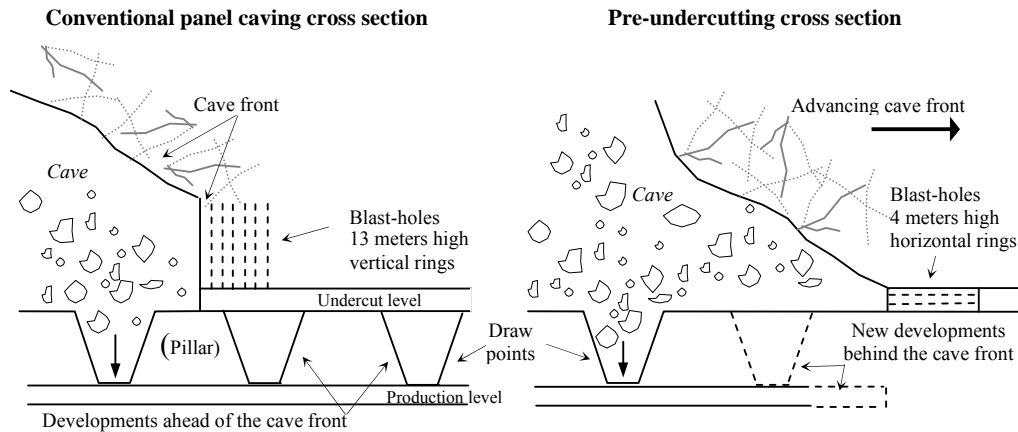


Figure 1.15.- Cross section showing Panel and pre-undercut caving methods at the El Teniente mine.

1.6.2 *In Situ Stress Field*

The stress tensor has been measured in more than 150 sites using different stress measurement techniques at the mine site. However, definition of the local and regional stress field is difficult due to both a complex configuration of old and current cavities formed by over 100 years of mining, and also due to the influence of the severe surface topography (Figure 1.3). Recently deeper stress measurements have been undertaken at the mine site using the Acoustic Emission (AE) technique, and the result are presented in Figure 1.16 (Villaescusa and Machuca, 2007).

These stress measurements have been reconciled with structural geology, surface displacements and seismicity on a regional scale, i.e., these stress measurement results are in agreement with paleo-strain field indications from fault slip vector analysis (Cladouhos, 1994), with contemporary strain field analysis from geodesic displacements, with local⁴ and regional seismic data (Windsor et al., 2006a). All these data sets were measured on a local scale surrounding the mine.

⁴ From the present research detailed in Section 8.3.1

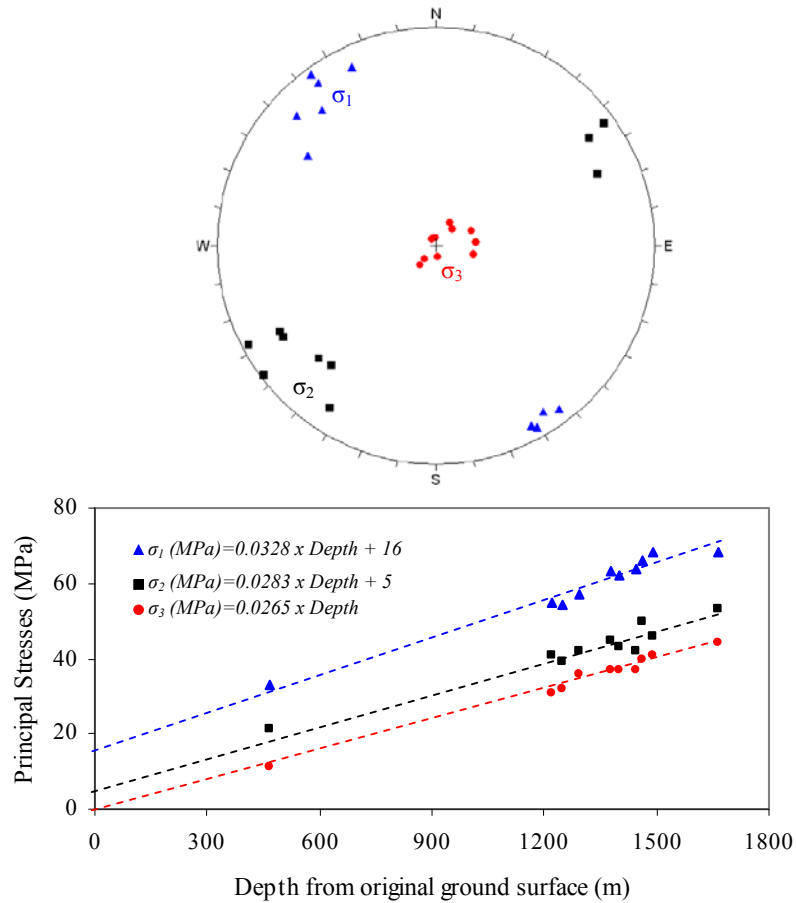


Figure 1.16.- Measurement of the in situ stress field at the mine site in mine coordinates (adapted from Villaescusa and Machuca, 2007).

1.6.3 Geotechnical Rock Mass Properties and Fragmentation

The El Teniente primary copper ore mass can be described as a massive, competent, and low permeable rock mass (Rojas et al., 2000b, Rojas et al., 2001). The geotechnical properties of the intact rock and the rock properties used at the mine site, which were obtained from hundred of lab test are presented in Table 1.2. In this table the rock mass quality ratings used currently in mine planning are also included; these were estimated by applying conventional Rock Mass Classification (RMC) systems to the data collected in mine drives (by using traditional scanline mapping described in Chapter 2).

Table 1.2. Intact and rock mass properties of main rock types at the El Teniente mine.

Parameters	Intact Rock Properties				Rock Mass Geotechnical Properties			
	Andesite	Dacite	Diorite	Braden Pipe	Andesite	Dacite	Diorite	Braden Pipe
E [GPa]	60	30	45	25	36	24	36	20
ν	0.16	0.18	0.21	0.23	0.21	0.20	0.26	0.28
B [GPa]	29.4	15.6	25.9	15.4	-	-	-	-
G [GPa]	25.9	12.7	18.6	10.2	-	-	-	-
γ [tonnes/m ³]	2.80	2.62	2.73	2.61	-	-	-	-
η [%]	4.40	3.00	4.70	7.70	-	-	-	-
UCS [MPa]	120	110	140	90	-	-	-	-
T_i [MPa]	14	12	15	6	-	-	-	-
E/UCS	500	273	321	278	-	-	-	-
UCS/ T_i	8.6	9.2	9.3	15	-	-	-	-
V_p [m/s]	6000	4800	5300	4300	-	-	-	-
V_s [m/s]	3200	2900	3000	2600	-	-	-	-
m_i/m_b	9.1	20.2	9.2	11.6	4.5	10.8	4.5	8.6
s	-	-	-	-	0.1	0.14	0.11	0.43
a	-	-	-	-	0.5	0.5	0.5	0.5
$\sigma_{ci/rm}$ [MPa]	118	112	125	72	49	60	42	50
$\sigma_{ti/rm}$ [MPa]	13	6	13	6	3	2	2	3
C [MPa]	23	19	23	10	9	9	8	9
Φ [°]	38	48	38	39	37	45	37	41
RMR _L	-	-	-	-	53-59	59-66	64-66	-
Q'	-	-	-	-	16-22	22-32	19	-
GSI	-	-	-	-	70-85	75-95	75-90	-

Note; E: Young Modulus. ν : Poisson ratio. B: Volumetric Deformation Modulus. G: Shear Modulus. γ : Density. η : Porosity. UCS: Uniaxial compression strength. T_i : Traction strength. V_p : P wave. V_s : S wave. $m_i/m_b/s/a$: Hoek and Brown failure criteria. $\sigma_{ci/rm}$: Traction in Hoek and Brown failure criteria. $\sigma_{ti/rm}$: Shear strength in Hoek and Brown failure criteria. C: Cohesion. Φ : internal friction angle. RMR_L: Laubscher 1993. Q': adapted from Barton et al. 1974. GSI: from Hoek et al. 1995.

Cavability at the mine site is usually determined by applying the Rock Mass Rating (RMR) methodology (Laubscher, 1993). Several case histories at the mine site using this method including these experiences with secondary ore are presented in Figure 1.17.

Figure 1.17 shows a worldwide case histories collected by Laubscher (1993) from different mines in Zimbabwe, Chile, Canada and USA are included. The failed caving experiences at the El Salvador mine (De Nicola and Fishwick, 2000), and at the North Parkes mine (Van As and Jeffrey, 2000) are also plotted in this figure.

The typical block size distribution in the El Teniente mine primary ore, which is used to define principal features of the mining design, is presented in Figure 1.18. In this figure andesite rock type from both alteration zones are plotted. These curves have been observed by size distribution measurements (visual inspection) undertaken continuously during 6 months in the production level draw points of Teniente 4 south mine sector in 1993 (Blondel et al., 1995). The relationship between main rock block

dimensions (large, a , intermediate, b , minor, c) and the volume of rock block is given by:

$$v_{rb} = 0.35b^3 \tag{1.3}$$

where v_{rb} is the volume of rock block, and b is the intermediate rock block dimension.

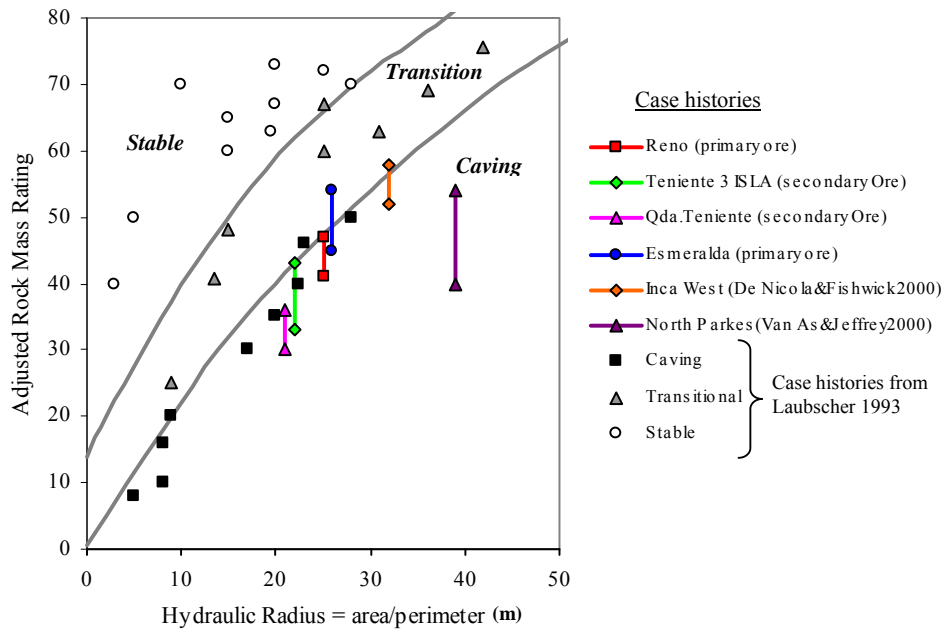


Figure 1.17. Cases histories in stability/instability diagram using Laubscher (1993).

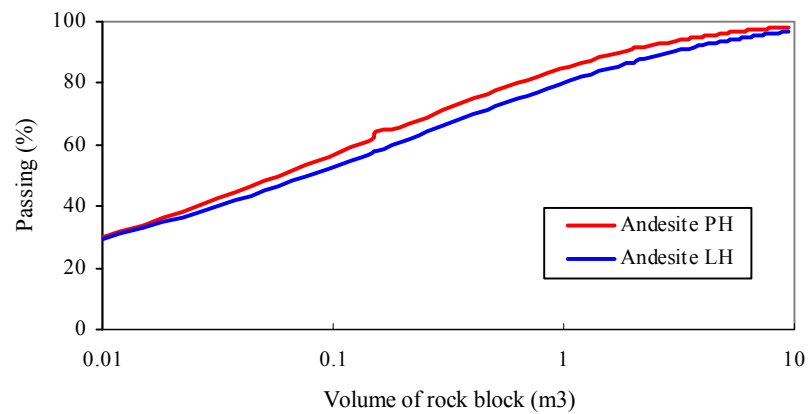


Figure 1.18. Typical primary ore size distribution at El Teniente mine (Blondel et al., 1995).

The typical rock block shape has the following rock block dimensions:

$$a = 0.7b = 0.5c \quad (1.4)$$

Mine experience shown in Figure 1.18 indicates that the andesite located at the east sector of the mine, within the principal hydrothermal (PH) alteration zone, has historically presented finer fragmentation than the same andesite from the late hydrothermal (LH) alteration zone. This is a good example of mine experience observed not only at the Teniente 4 south mine sector, but also observed at both Esmeralda and Reno mine sectors (Villegas, 2006). A real example of mine productivity measured in term of average tonnage extracted (Vasquez, 2003), shows different behaviour between rock unit types (by alteration zones and lithologies in Figure 1.19), which are in agreement with data presented in Figure 1.18.

A region east of the Braden Pipe (800E to 1400E mine coordinate) has been divided into two sections. The west part is called hangingwall (Hw) and the east part is called footwall (Fw) as shown in Figure 1.19. In both studied mine sectors the Hw and Fw sectors coincide with LH and PH alteration zones respectively. These typical mine nomenclature is widely used in this thesis.

1.6.4 *Current and Future Exploitation*

El Teniente mine is the biggest underground mine operation in the world, different sectors and levels are being extracted simultaneously using different mining methods, such as block caving, conventional panel caving, and pre-undercut variant methods. All mine sectors have been placed surrounding the Braden pipe as shown in Figure 1.20.

The main current mine sectors and the future New Mine Level (NML) are illustrated as an isometric view (Figure 1.20). Currently, the NML is in feasibility studies, the mine method selected is the pre-undercut variant, which may be placed at the Teniente 8 mine level (1890 z). This NML is expected to produce 140,000 tpd.

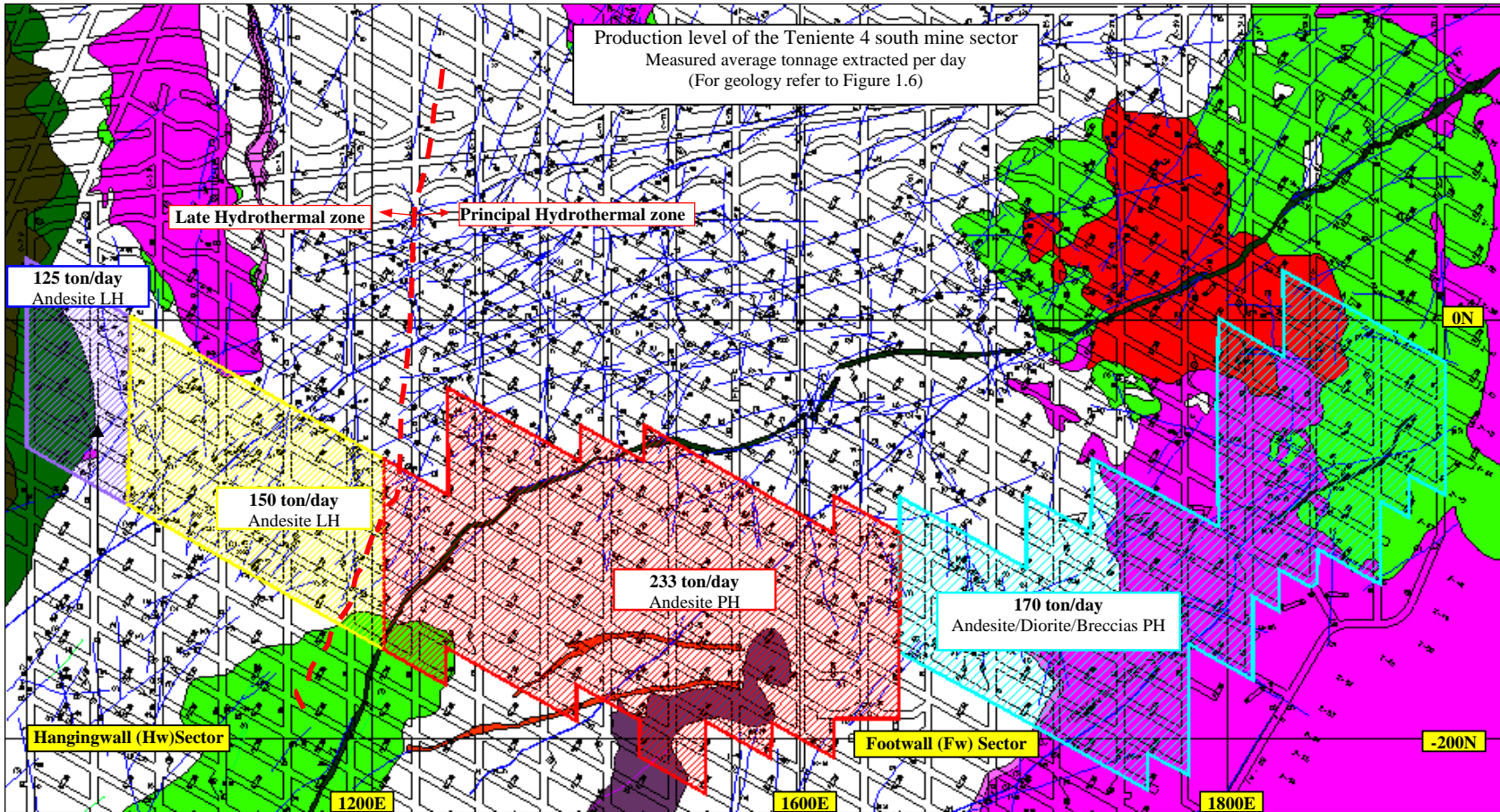


Figure 1.19. Average measured productivity at Teniente 4 south mine sector (2354z) per unit type (Vasquez, 2003). Mine coordinates in meters.

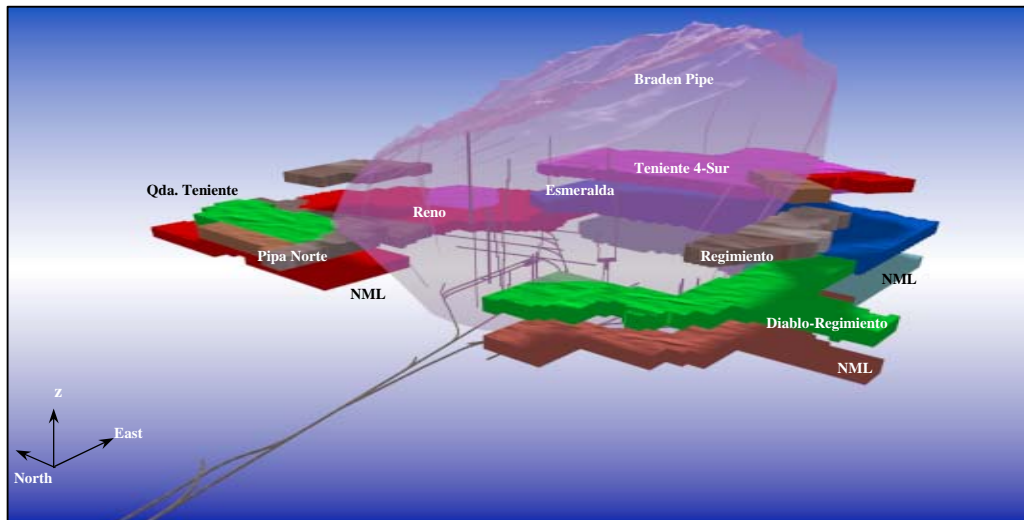


Figure 1.20. Isometric view of El Teniente mine showing main current and future mine sectors.

1.6.5 Current Mine Method and Design

The principal mine method used currently at the El Teniente mine is the panel caving method with pre-undercut variants. This mining method is used in the two mine sector being investigated here; Reno and Esmeralda mine sectors.

There is a conceptual frame work to the mine design for all mining activities when this method is applied, which is correlated with the stress state (Rojas et al., 2000a, Rojas et al., 2001). Mining by panel caving is characterized by a dynamic caving face that modifies the stress condition within the rock mass (Figure 1.14). Stress redistribution by the advancing cave front effectively defines three zones; (a) pre-mining, (b) transition and (c) relaxation zones (Figure 1.21).

- (a) Pre-mining zone. The in situ stresses and rock mass condition have not been affected by mining activity.
- (b) Transition zone. Stress redistribution occurs by mining activity (cave geometry). Because the cave front is continuously advancing, the stresses are continuously changing in magnitude and orientation (see Figure 1.14). Thus, the rock mass is being affected and may exhibit changing behaviour. This is a similar concept to the seismogenic zone in the cave back defined by Duplancic (2002).

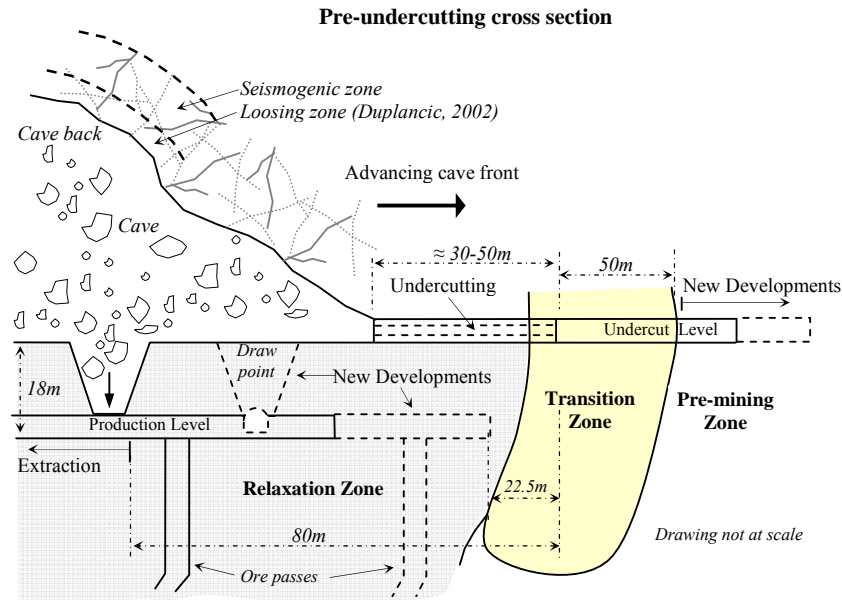


Figure 1.21. Stress state in the rock mass at the cave front.

- (c) Relaxation zone. The stresses have been modified, and there is a dramatic decrease in the magnitude of vertical stress. This area has been referred as ‘under shadow’.

Consequently with these definitions, the sequence of new development excavations adopted at the El Teniente mine is; (1) undercut level developing and blasting to generate caving, (2) development of a production level, excavation of draw points, draw bells and ore passes behind front cave, and (3) ore extraction. These operational aspects of the pre-undercut sequence define relevant distances between mayor development areas (also in Figure 1.21), which have been defined empirically (Rojas et al., 2000a, Rojas et al., 2001).

The Reno mine sector initiated its exploitation using traditional panel caving, but in 1999 the mine methods had changed to the pre-undercut variant. This means that for some production areas the developments at the production level have been excavated ahead of the undercutting process.

At least four typical levels are developed in this mining method; undercut level (ucl), production level (pl), ventilation level (vl), and transport level (tl). Additionally, the method may have an independent picking hammer level (phl) or this could be located in the production level next to an ore pass. According to the layouts used in

Esmeralda and Reno mine sectors, the standard distances between levels are; 18 meters in between ucl-pl, 40 to 50 meters in between pl-vl, 30 to 60 meters in between pl-phl (Barraza and Crokan, 2000).

The mine layout also considers drive spacing between 15 and 30 meters at the undercut and production levels, respectively (Figure 1.22).

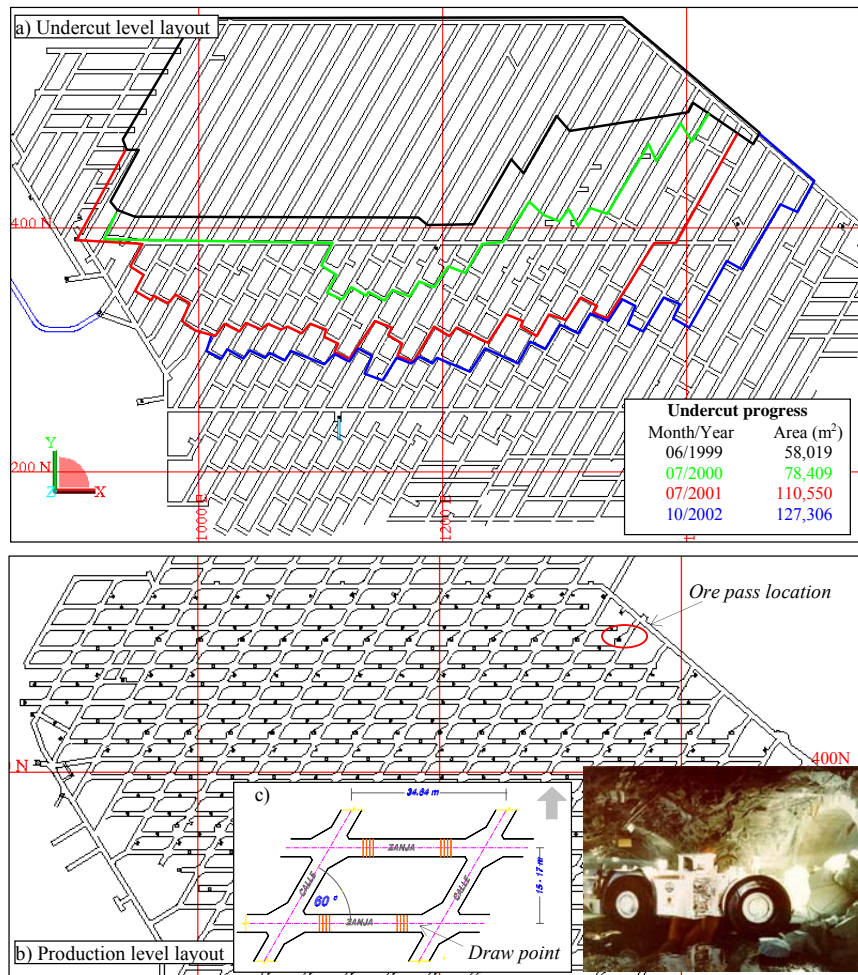


Figure 1.22. Plan view with layout of the undercut and production levels at the Esmeralda mine sector.

The drive orientation differs from place to place within the ore body as do the orientation of the major structures. The design layout at production level takes into account 60 degree intersecting drives to facilitate LHD equipment loading (Figure 1.22c). The drive design is set at 3.6x3.6 meters section in the undercut level, 4x4 meters section in the production level, and from 4x4 to 6x6 meters standard section

in the picking hammer level and/or transport level (Barraza and Crockan, 2000, Rojas et al., 2001).

The primary rock column height being exploited typically varies between 110 and 220 meters, and total mineral reserves being exploited may range between 250 -350 million tonnes. The caving may generate, in both the Esmeralda and Reno mine sectors, a cave front between 500 and 800 meters extent, and the cave area may increase an average of 20,000 m² a year (Figure 1.22a). The caved area at the undercut level shown in this Figure 1.22a is not the real hydraulic radius related to the rock mass cavability (Laubscher, 1990, Laubscher, 1993), because in this mining method an effective area (active footprint) is defined by active draw points at the production level (a detailed discussion about this topic is presented in Section 7.3.1).

CHAPTER 2 DATA COLLECTION TECHNIQUES**2.1 Introduction**

Rock mass characterisation is an essential step to understand and to predict the behaviour of rock masses during and following excavations. Rock mass characterisation is usually undertaken by implementing data collection techniques on rock exposures such as line mapping (scanlines) and borehole logging.

The rock mass can be thought of as composed of two main components; discontinuities and intact rock material. Discontinuities such as faults, joints, and bedding planes are the most likely features that influence and control the mechanical behaviour of the rock mass. Because discontinuities present within the rock mass are sometimes large in number, and also because considerable amount of detail is required to obtain average discontinuity properties, an objective (random sampling of a representative rock mass) and systematic approach during data collection are recommended (Brown, 1981).

Discontinuities in nature are a three dimensional (3D) entities, and their complete 3D structure within the rock mass are referred to as a discontinuity network or rock structure (Priest, 1993). To achieve a complete description of a discontinuity network is a difficult problem, because discontinuity characteristics cannot be completely observed. Observations of rock structure are usually one dimensional if bore hole logging is implemented, or at the best two dimensional, when outcrops or exposed mine wall are used during mapping. Furthermore, rock faces in outcrops, tunnels, and boreholes have a limited exposure; therefore sampling biases are introduced during rock structure characterisation. In order to determine the true nature of the rock structure, sampling biases to data collection must be corrected.

The scale of problem being analysed is another relevant issue during discontinuity network characterisation. The various scales of discontinuities may play different roles in rock mass mechanical behaviour, as suggested by Hoek and Brown (1980).

The rock structure characterisation undertaken in this study has considered these aspects. Sampling techniques used in this study include measurements at exposed rock faces, borehole logging and an assessment of block forming geological discontinuities at production level draw points.

2.1.1 Goal

The main objective of this chapter is to describe all data collection techniques used in this study to characterize the rock structure. In order to achieve this, a literature review of structure definition and characteristics, conventional data collection techniques and sampling bias was undertaken. The sampling descriptions also included detailed sampling location of data collected at the Reno mine sector.

2.2 Discontinuity Definitions

Rock mass discontinuities can be classified using a number of criteria, which are mainly based on their geological features such as the discontinuity genesis, occurrence and size (Hoobs, 1993). The most appropriate definition to the term geological discontinuity for engineering purpose has been proposed by the ISRM (Brown, 1981). The term geological discontinuity refers to any mechanical break or fracture in a rock mass having a zero or low tensile strength. This collective term includes most types of planes of weakness such as joints, faults, shear zones, bedding planes, foliations and/or schistosity planes, etc.

The ISRM (Brown, 1981) also defines **Faults** as a plane of fracture or fracture zones that divide the rock mass, showing an evident sign of shear displacements between both sides of the plane. **Joints** have been defined as a plane that divides a rock mass showing not signs of shear displacement. However, because shear displacements can be measured in micrometres, some authors have added '*extremely little or no movement*' to define a joint plane (Goodman, 1976). When a joint contains some mineral such as quartz, chalcopyrite, or epidote, which have healed and cemented the discontinuity, they are referred as **Veins** (David, 1984). Veins are not considered 'discontinuities' for engineering purposes according to the ISRM (Brown, 1981), due to their relative high tensile strength.

Bedding is known as a continuous plane that divides sedimentary rocks into beds or strata. **Schistosity or cleavage** is predominantly a planar rock fabric or foliation that is present in some metamorphic rock masses.

In the present study, the term **discontinuity** will be used as a general term to describe structures, such as faults, veins, joints, and fractures:

- **Fault** will refer to any discontinuity with an evident sign of shear displacement and/or the presence of gouge and/or slickensides.
 - **Veins** will refer to any discontinuity healed and/or cemented (low permeability) by a mineralogical assemblage of infill material.
 - **Joints** will refer to any discontinuity (permeable) without clear signs of shear displacements like gouge and/or slickensides, and with or without infill.
- Fracture** is used hereafter as its synonym.

Discontinuities have also been classified in terms of their size. For instance, Cruden (1977) has divided between major and minor discontinuities. **Major discontinuities** can be faults, dykes, contacts, and related features with a size of the same order of magnitude as the site being characterised. Major discontinuities should be analysed individually. **Minor discontinuities** are joint, minor shears, and bedding planes, which generally represent a large population. Their geometrical and strength properties must be estimated by measurement of a representative sampled population (Cruden, 1977). Based on that, a **Structural domain** could be defined as a zone in which the geometry and physical properties of the rock structure are statistically homogeneous (Brown, 2003).

Discontinuities present in the earth surface range in sizes from thousands of kilometres to microscopic measure (David, 1984, Pusch, 1995, Scholz, 2002). Consequently, the scale in which they are characterised may play a relevant role, as pointed out Cruden (1977). For instance, Hoek and Brown (1980) have demonstrated that there is a reduction in uniaxial compressive strength with increasing sample size (i.e., scale effect), which is mainly due to the presence and scale of discontinuities. Hudson and Harrison (1997) have discussed the scale effect related to the permeability of a jointed rock mass, which may vary depend on the scale of observation. These authors have addressed the concept of the Representative Elemental Volume (REV), which may be relevant during rock structure characterization. A REV is the volume at which the size of the sample tested to characterise it, is large enough to avoid the high variability encountered in small samples (Hudson and Harrison, 1997).

In this respect, Pusch (1995) has suggested a comprehensive classification of the discontinuities in relation to their sizes. His classification defines discontinuities

having seven orders of magnitude, from microscopic defects to a regional fracture zone. These magnitudes represent the scale at which the discontinuities are present within a rock mass. This concept is also related to the observed scaling law features of discontinuities parameters (lineal and fractal) discussed by the scientific community (Hoobs, 1993, Scholz, 2002). An example of the scale affect is presented in Figure 2.1.

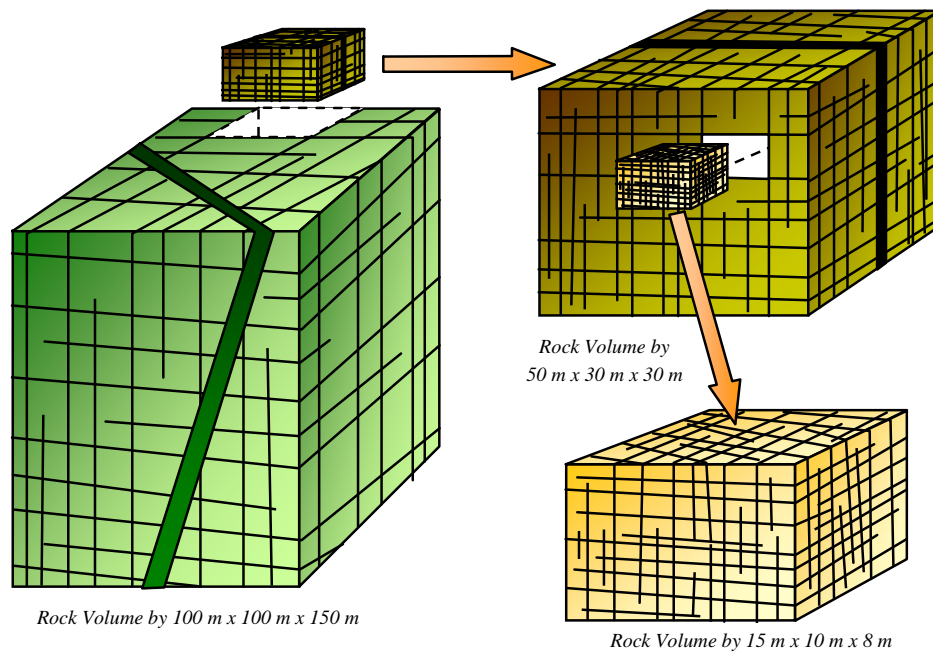


Figure 2.1. Scheme that illustrate the scale concept of the discontinuities (after Pusch 1995).

Therefore, for any given rock volume, discontinuities may be characterised at least by major and minor structures.

2.2.1 Classification of Structures at the El Teniente Mine

The discontinuities recognised at El Teniente mine have been classified in terms of their genetic nature and in terms of their size. Their genetic nature is discussed in Sections 1.5.4 and 1.5.5; in this study, the discontinuities have been classified as either veins or fault. Veins may represent numerous alteration stages recognized within the ore body, such as the consecutive sequence of; late magmatic (LM) veins, principal hydrothermal (PH) veins, and late hydrothermal (LH) veins. Faults have been interpreted to appear within the last alteration stage and subsequent geologic stages (Garrido et al., 1994, Brzovic, 2001).

These discontinuities have also been classified according to their apparent discontinuity size, which can be represented by their exposed trace length in mine drives as shows Figure 2.2 and Table 2.1. The structure size classification used in this study is defined as follows:

Minor structures: Structures that do not cross a standard drive, i.e., having an approximate observed trace length of less than 4 meters (blue lines in Figure 2.2).

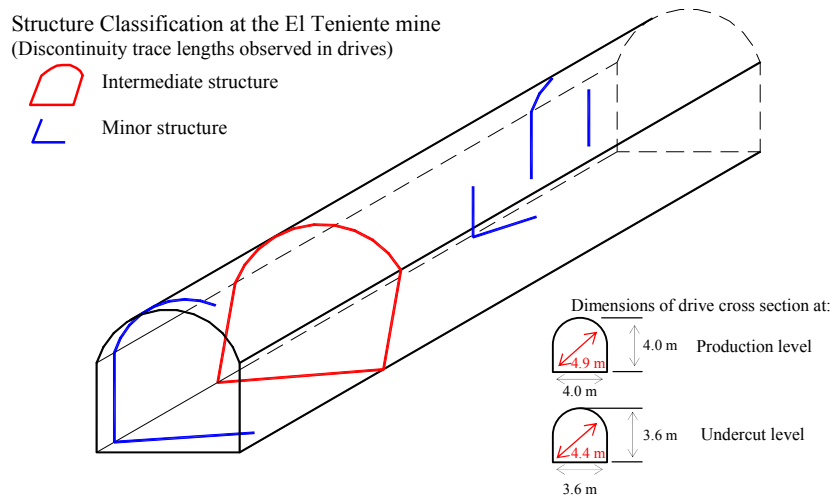


Figure 2.2. Structure classification at the El Teniente mine according to the observed trace length into mine drives.

Intermediate structures: Structures that cross a standard drive (typically 4 meters wide) or having an observed trace length greater than 4 meters when their strikes are semi-parallel to the drive orientation (red lines in Figure 2.2).

Major structures: When two intermediate structures are interpreted as being the same in two or more adjacent drives, i.e., having an observed trace length over 30 meters. At either the undercut or production level in conventional panel caving, two adjacent drives are 30 meters apart.

Table 2.1. Classification of discontinuities according to their size at the El Teniente mine.

Structure type	Discontinuity trace length observed in mine drives
Minor	< 4 meters
Intermediate	4-30 meters
Major	> 30 meters

2.3 Discontinuity Characteristics

In order to properly characterise the discontinuity characteristics, the International Society of Rock Mechanics has suggested to describe ten essential and basic parameters (Brown, 1981). These parameters represent the geometric and strength properties of discontinuities, which are schematically illustrated in Figure 2.3.

The geometric characteristics of the discontinuities can be described by five parameters: orientation, spacing, persistence, number of sets and block size. The other five parameters represent the strength of the discontinuity. These are roughness, aperture, filling, wall strength, and seepage. Such combined factors are likely to influence the rock mass quality and behaviour during and following excavation.

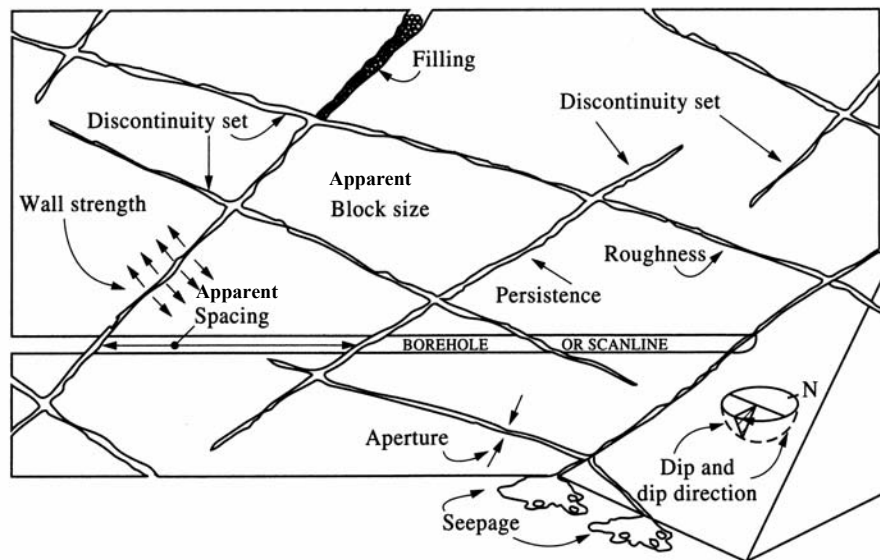


Figure 2.3. Schematic illustration of discontinuity properties (after Hudson and Harrison, 1997).

2.4 General Sampling Features at the Reno Mine Sector

Reno mine sector (formerly Ten Sub-6) within the El Teniente ore deposit was the place chosen to carry out the first part of this research. Line sampling techniques were implemented in mine drives to characterise the rock structure, and special data collection was used to determine the characteristics of block-forming discontinuities in the production level draw points. Line sampling techniques implemented were drive and line mapping (scanlines), as well as oriented and un-oriented borehole logging (Figure 2.4 and Figure 2.5).

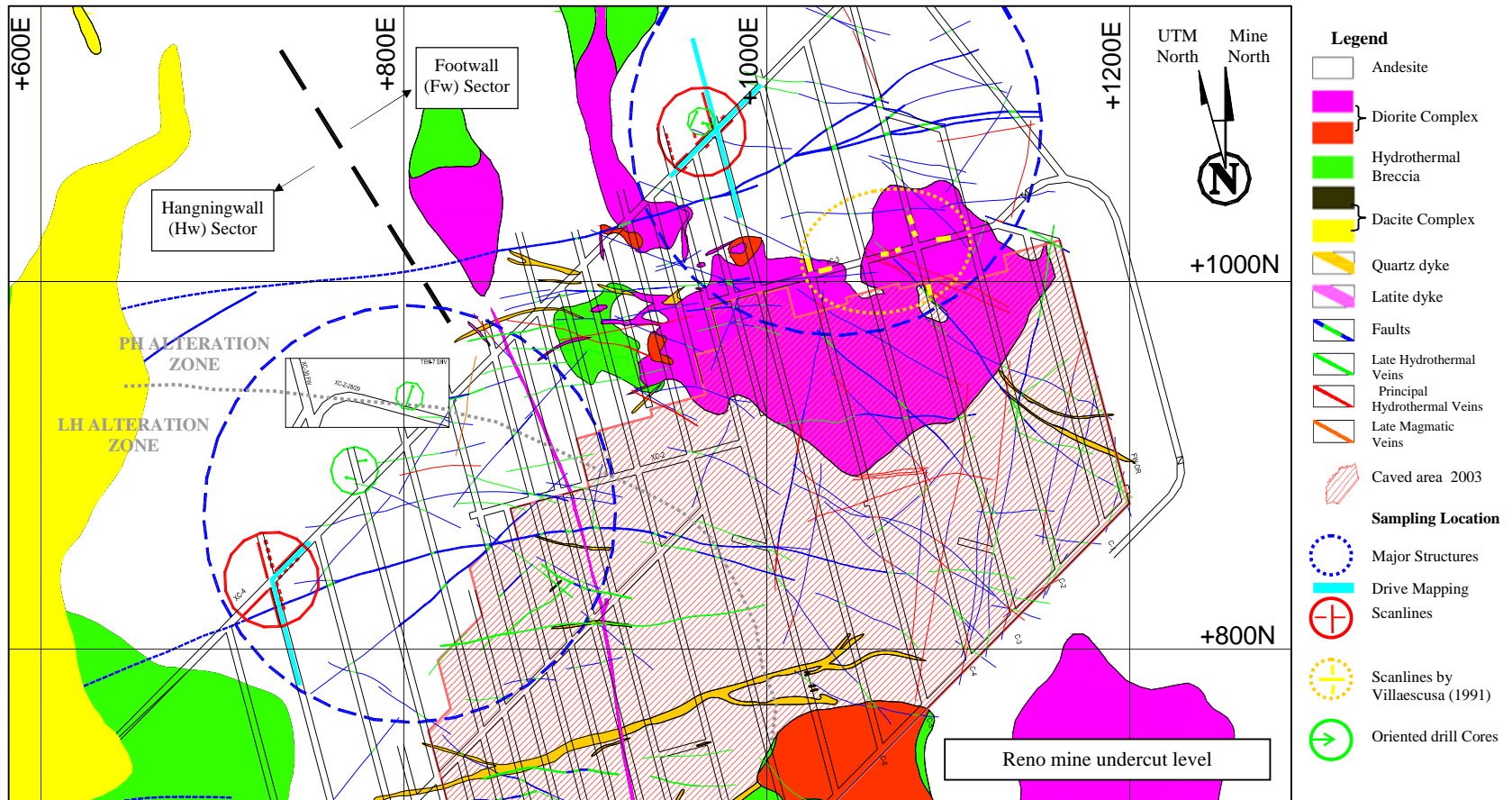


Figure 2.4. Different sample location at the undercut level of Reno mine sector.

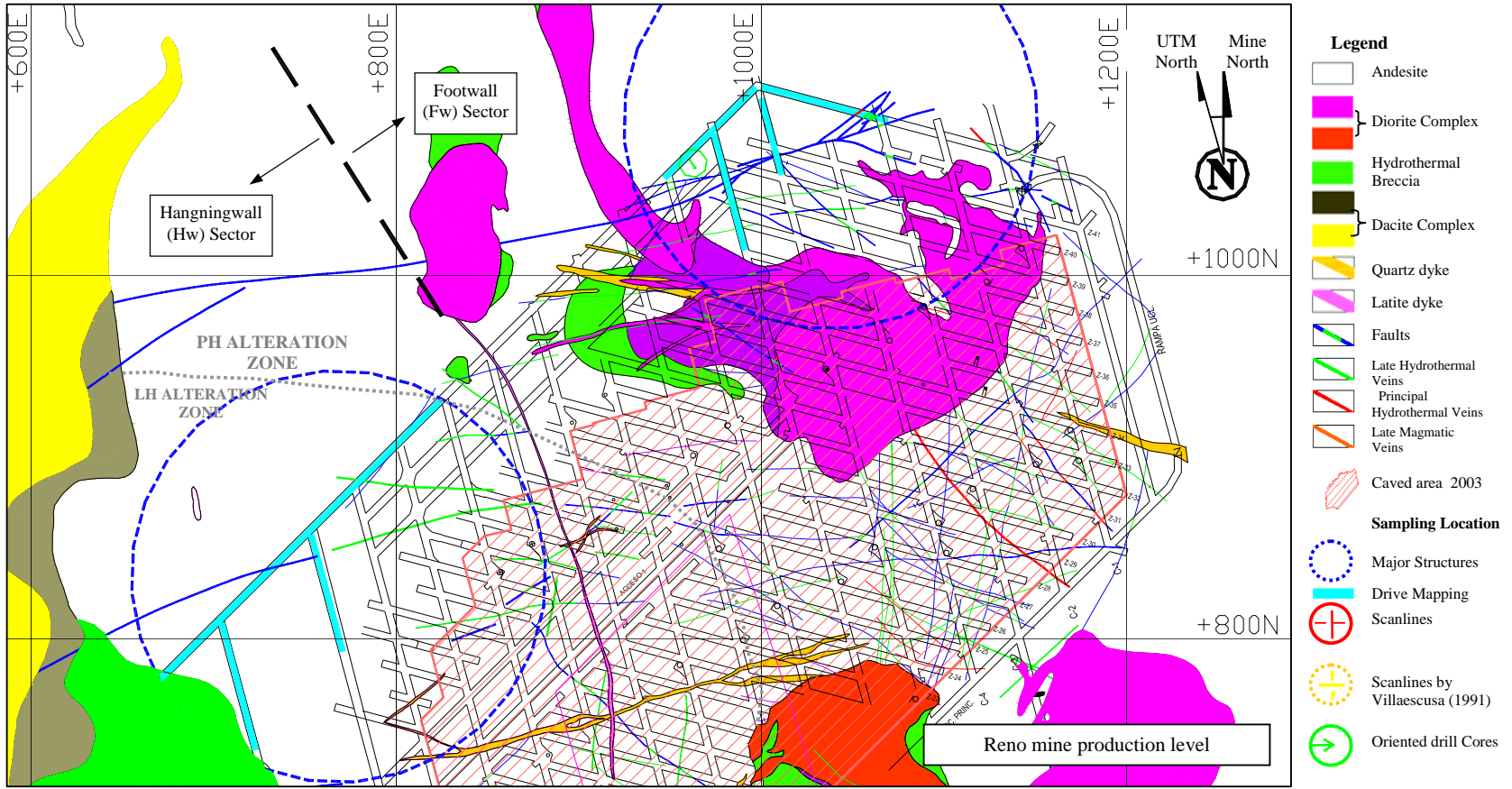


Figure 2.5. Different sample location at the production level of Reno mine sector.

Line sampling data collections were set-up within two caving sectors within both the undercut and the production levels of this mine sector. All sampling was performed in the andesite rock type (Figure 2.4 and Figure 2.5). The two sectors are referred to as andesite hanging-wall (H_w), and andesite foot-wall (F_w), and they represent two different alteration zones and two structural domains. The andesite H_w and F_w sectors are used throughout this research to compare structural data analysis. In Figure 2.4 and Figure 2.5 selected major structures were collected from an area of about 15,000 m².

Line sampling techniques considered different truncation biases and censoring levels (detailed in Section 2.4), which can be considered as different mapping scales.

Although line samplings were undertaken considering at least three semi-orthogonal orientations, the sample orientations were constrained by the actual mine layout. Line sampling orientations undertaken are presented in Figure 2.6.

Sample orientation and location for un-oriented drill core samples are presented in Section 2.5.2 and Chapter 3 respectively. Details of caved rock block samples collected at draw points are presented in Section 2.6.

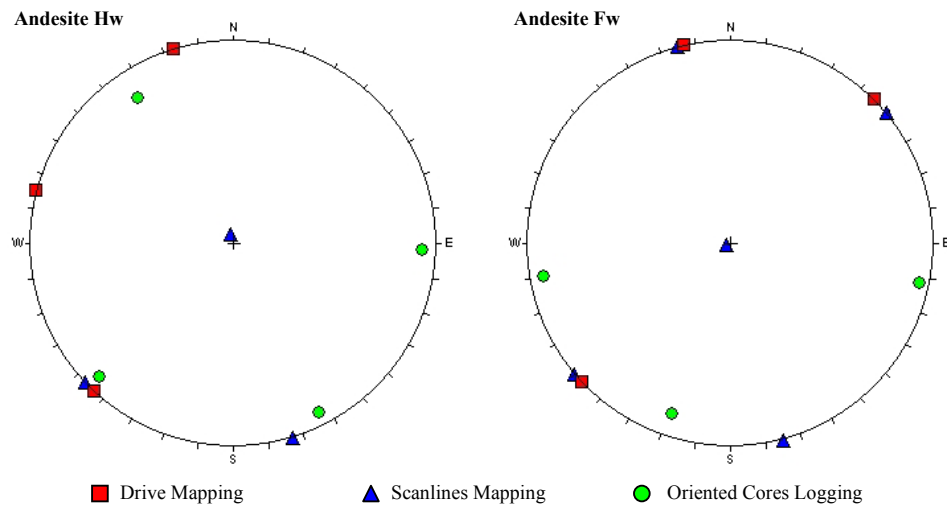


Figure 2.6. Equal area lower hemisphere projection showing sample orientation for different data collection techniques used in this study.

2.5 Sampling Bias

Since it is almost impossible to observe the complete discontinuity exposures during data collection due to the limited access for measuring techniques, sampling biases are introduced when discontinuity surveys are undertaken.

The main types of sampling bias introduced during data collection are described in following paragraphs. Some of these are explained in more details in Chapter 3.

Orientation bias: the number of discontinuity frequencies intersecting a sampling line will depend upon the angular relationship between the discontinuity set orientation and the sampling regime (Terzaghi, 1965). A discontinuity set parallel to the sampling directions will not be sampled. A quantitative correction of this sample bias is described by Priest (1993) and explained in Section 3.2.1. In the present research, in order to minimize the orientation bias during data collection, sampling lines were obtained considering at least three semi-orthogonal orientations, each one with a similar sample length to the other. However, the sampling line orientations were constrained by the actual mine layout, and only limited sampling was possible in the vertical direction (Figure 2.6). Therefore, biases and inaccuracy, primarily with respect to sub-horizontal discontinuity sets, would be expected (Hudson and Priest, 1983, Sen and Kazi, 1984).

Size biases: longer discontinuities are more likely to intersect a mapping line or borehole than shorter ones. This means the likelihood of a discontinuity being sampled is proportional to the discontinuity size (Warburton, 1980, Zhang and Einstein, 2000).

Truncation bias: the truncation value is the trace length below which discontinuities are not recorded (Villaescusa, 1991). It is usually an operator's decision to make. In the present study, different truncation biases were used during data collection, which are detailed in Table 2.2.

Censoring bias: this results when the artificial boundaries of the rock exposure are imposed on the sample, such as the core width or the wall mine height. If discontinuity sizes are longer than the rock exposure, the observed trace length will be biased to a shorter length and the end-points of the traces will be not observed (Villaescusa, 1991). In this study, different censoring levels were identified during

data collection, which are detailed in Table 2.2. Censoring levels and the truncation bias, applied during data collection, can be considered as different mapping scales.

Table 2.2.- Censoring level, truncation bias and sample length applied to different line sampling techniques.

Sampling method	Censoring level* (m)	Truncation bias (m)	Range of the horizontal sample length (m)
Major structure interpretation	-	30	150
Drive mapping	4.4-4.9	4	30-150
Line mapping	3.6-4	0.3**	7-22
Oriented drill core logging [‡]	0.1-0.14	0.1**	4-12
Un-oriented drill core logging	0.05	0.03 [†]	6-24

Note *: Censoring level only considers the maximum height/width of the observation window. **: Some discontinuities longer than the threshold value could not be sampled during data collection. ‡: Referred to large diameter drill core sample. †: Although a truncation bias threshold criterion was not implemented during drill core logging, the practical length threshold is estimated at around 0.03m based on the ability to visually identify discontinuity during core logging.

Covering exposure bias: this bias was observed when data collection was performed in mine drives. As the majority of the mine walls have a shape defined by discontinuity faces (discontinuity wall surface), some veins could not be observed. This unsystematic phenomenon occurs because the mineralogical infill and alteration features of a discontinuity faces sometimes hide other structural data (Figure 2.7).



Figure 2.7. Mine wall at the El Teniente mine, showing how vein infill and alteration may cover the rock exposure, sometimes hiding structural data behind.

2.6 Measurements at Exposed Rock Faces

Mapping of rock mass exposures, either outcrops or at underground mine walls has the advantage of gathering two-dimensional discontinuity data compared with one-

dimensional data obtained using borehole logging techniques. Discontinuity terminations, discontinuity sizes, and more reliable discontinuity orientation can be obtained from exposure mapping. Measurements of exposed rock faces used in this study include drive and line mapping.

2.6.1 Drive Mapping

At the El Teniente mine, drive mapping is routinely undertaken by geologists in most mine drives. Its aim is to determine the main rock mass geological features such as rock type, structures and alteration types. Only discontinuities having trace lengths greater than 4m long are collected (intermediate discontinuities). Most of these discontinuities intersect the mine drives, which have a typical cross section or area between 13m² and 16m² (Figure 2.2). An average of more than 20,000 meters of horizontal tunnels is mapped every year at the mine site.

The main geological features used to characterize each structure include; location referenced to mine coordinates, dip and dip direction, discontinuity type, alteration type, thickness, filling which consists of a qualitative description of the mineralogical infill assembly described as majority, abundant, moderate, and rare (for example, abundant chalcopyrite, moderate quartz, and rare anhydrite)¹, and kinematics indicators, when sense of movement is recognised.

Following the completion of mapping along several drives, the geologists undertake data interpretation to determine which discontinuities are continuous across several mine drives, thus forming a major structure. The minimum trace length interpreted for a major structure is 30m, which is the distance between two adjacent mine drives. The interpretation is based on geological features such as structure type, orientation, alteration type, mineralogical assemblage and thickness. Consequently, a plan view with only major structures is generated as shown Figure 2.8. The pattern of major structures is the main criteria defining the structural domains at the mine site.

In Figure 2.8, coloured areas and lines represent different rock and structure types. Blue lines are faults, green lines LH veins, red lines PH veins and orange lines LM veins. Almost no joints are found within primary copper ore.

¹ Usually by visual inspection helped by magnifying glasses (10x).

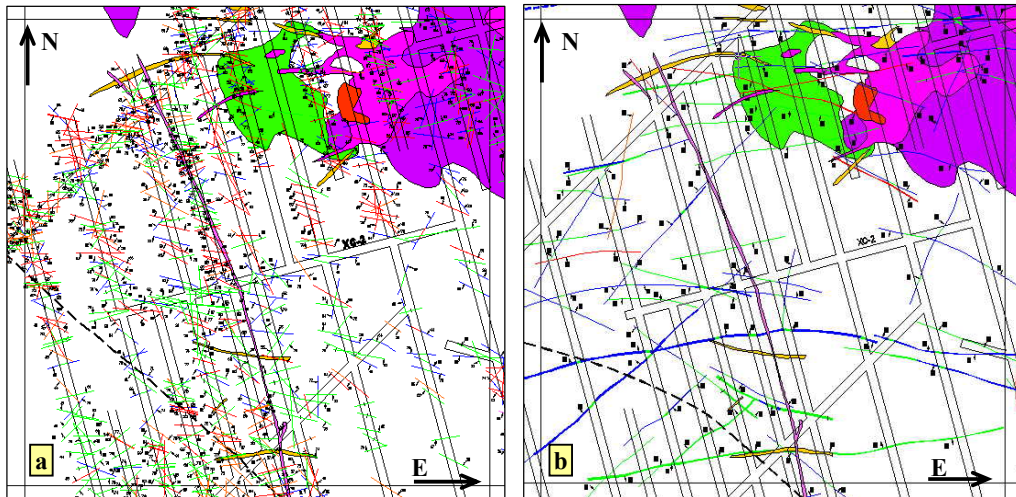


Figure 2.8. Plan views showing rock types and intermediate structures (a) and interpreted major structures (b). The scale is 200m x 200m. Line colours represent different geological structures; LM veins as orange, PH veins as red, LH veins as green, and Faults as blue.

In the present study, samplings of the intermediate structures were selected from available mine drives in undercut and production levels (in Figure 2.4 and Figure 2.5). Additional sampling information is presented in Figure 2.6 and Table 2.3.

Table 2.3. Summary of sample lines used and structures collected in drive mapping analysis.

Sample orientation	Andesite Hw			Andesite Fw		
	Number of Sample lines	Total Discontinuities	Total Meters	Number of Sample lines	Total Discontinuities	Total meters
N45°E	3	124	334	2	77	215
N15°W	6	115	376	6	101	263
N75°W	-	-	-	1	28	70
Total	9	239	710	9	206	548

2.6.2 Line Mapping

Line mapping, commonly referred as scanlines, is the most popular technique used to survey discontinuities on a rock exposure. Call et al. (1976), Villaescusa (1991), Priest (1993), and many others have suggested various form of scanline mapping. It involves measuring or recording all the discontinuities and their characteristic that intersect a given sample line. The scanlines may be placed at any orientation and inclination, but for practical purposes usually horizontal and vertical orientation are undertaken to minimise orientation bias.

The selection of the area to be mapped should consider the representativeness of a rock mass within a structural domain, but generally this is determined by availability

and accessibility to the rock exposure. Line mapping can provide significant amount of data, however, it also requires a significant amount of time to undertake. Villaescusa (1991) has estimated up to two days to choose an appropriate scanline-mapping site, set up the scanline, and record the data that are required. In an underground block caving mine production environment and based on experience, it may require twice the time suggested by Villaescusa (1991).

The length of the scanline is normally extended until a prerequisite number of observations are acquired. Priest (1993) suggests a sample size between 150 and 350 discontinuities. Savely (1972) suggested that at least 60 observations are required to stereographically define joints sets found along a particular sampled line. Villaescusa (1991) recommended at least 40 discontinuity observations per joint set to provide a sound database of a discontinuity set characteristic. Priest and Hudson (1981) proposed a method to estimate the number of observation required to determine the mean discontinuity spacing value for a negative exponential distribution at any desired precision (detailed in Section 3.2.3). More precision at high confidence level considerably increases the data required.

Conventional scanlines are routinely undertaken at the mine site to collect geotechnical data about minor structures, which are mainly used both to estimate the rock mass quality through the rock mass classification schemes, and also to assess fragmentation.

In the present study, modifications were made on the traditional line sampling methodologies to better determine veins characteristics within primary copper ore. The scanline scheme used here also considered as exposed drive wall as observation window (Figure 2.9).

At each selecting site, a tape is stretched on a previously washed wall rock and every discontinuity that intersects the tape and satisfies some pre-established requirement is recorded. These requirements are as follow:

1. Discontinuities with observed trace length equal to or greater than 0.3m were recorded (Truncation bias imposed).
2. The discontinuity must show a '*discontinuity wall surface*' or '*open face*' as shown in highlighted red circles in Figure 2.10. For veins or cemented joints,

it is more likely that some part of the discontinuity was ‘open’ by the effect of blasting during excavation.

- If point 2 is not satisfied, all discontinuities exhibiting weaker mineralogical infill should be recorded. Weaker mineralogical infills at the El Teniente mine are mainly gouge and/or slickenside, chalcopryrite, anhydrite and chlorite².

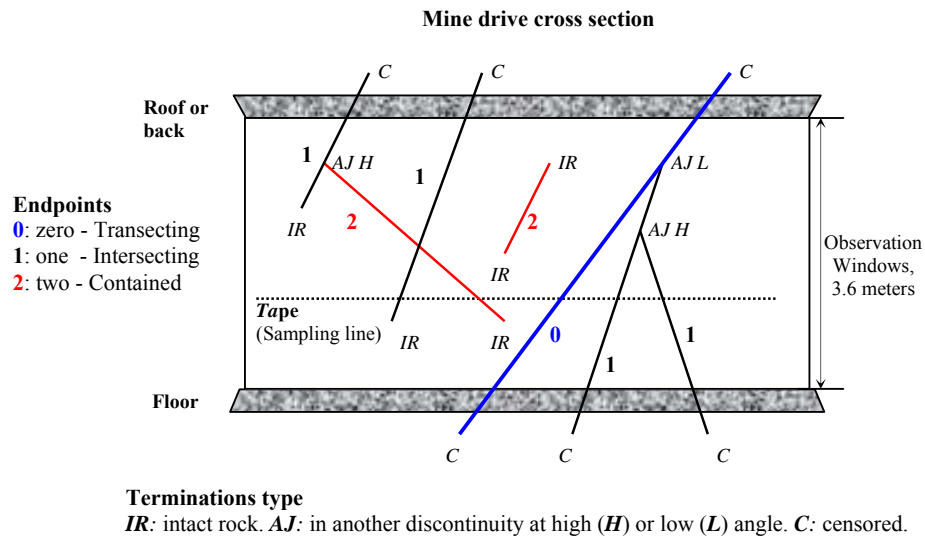


Figure 2.9. Mine drive cross-section showing some aspects of line mapping (modified after Villaescusa, 1991).

This study suggest that traditional scanline mapping undertaken at the mine site (i.e. including points 1 and 2 only) may not be able to characterise properly the primary copper ore at the El Teniente mine, or other rock masses with significant cemented rock block assemblages by stockwork veins. Hence, point 3 was introduced to minimize this bias by including discontinuities of intermediate and low strength that may not form a ‘discontinuity wall surface’ or ‘open face’. By including this criterion (point 3) line sampling will has bias to discontinuities of high strength. In order to evaluate how this bias may be affecting the discontinuity estimates, a data collection campaign using large diameter oriented drill cores was undertaken in the proximity of the scanlines sites (presented in detail in Section 2.6.1).

² These minerals are described as intermediate to weak strength infill in Chapter 4 (Table 4.6).

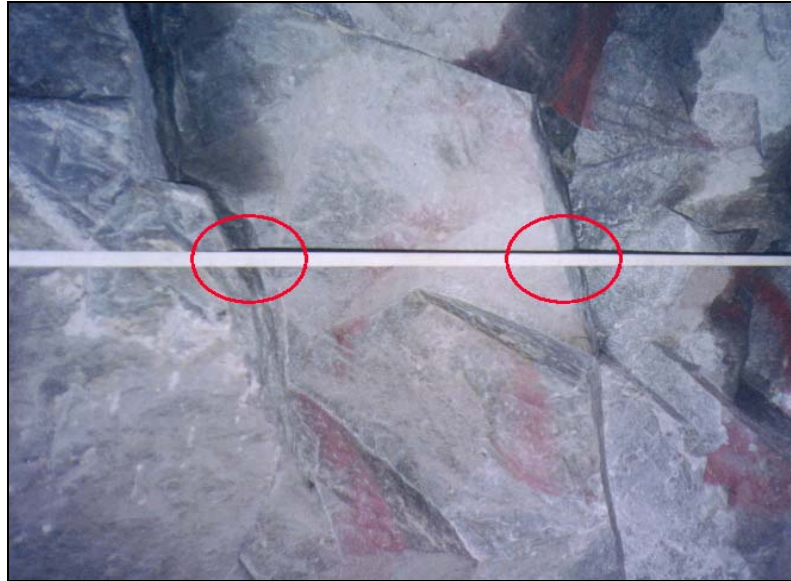


Figure 2.10. Detail of drive mine wall showing some discontinuities with ‘open faces’ (exhibiting discontinuity wall surface) intersected by the tape (0.02 m width).

The information collected by scanlines was recorded on a tabular data spreadsheet (Figure 2.11), which is suitable for subsequent data analysis using current software packages.

Line No:	North :	Wall Dip:	Page:	of:
Bearing:	East:	Wall DipDir:	By:	
Plunge:	Level:	Censoring levels (m): up down	Date:	
Elevation:	Location:	Rock Type	Start:	Finish:

Location		Discontinuity			Geometry						Infill features					Remarks			
					Small scale Roughness	Large scale Roughness	Above		Below		Face area (cm ²)	Filling or mineralogical infill	Vein Subtype	Halo			Thickness		Mode of Failure
Dist (m)	Endpoints	Type	DipDir	Dip			T1	T2	Trace length (m)	T1				T2	Type	Width (mm)	Max. (mm)	Min. (mm)	

Main notation used:

Endpoints	Discontinuity type		Small scale roughness	T1	Termination	T2		
0	Transsecting	J	Joint	1 to 9 Scale (ISRM 1981)	AJ	Another Joint	L	Low angle (< 20°)
1	Intersecting	V	Veins (LM, PH, LH)	Large scale roughness (Planarity)	IR	Intact rock	H	High angle (≥ 20°)
2	Contained	F	Faults	1 to 5 Scale (Laubscher 1990)	C	Censored	UN	Unknown

Figure 2.11. Data collection spreadsheet for scanline mapping (modified after Villaescusa 1991).

Basic information collected at each site included; the scanline number, location of the starting position in mine coordinates, scanline orientation, wall inclination, censoring level, date and personnel involved in the scanline mapping. A mnemonic system is adapted to the geological features of the El Teniente deposits. The discontinuity characteristics to be measured in the survey included (Figure 2.11):

1. Distance of discontinuity intersection along the tape.
2. Number of endpoints observed in between the window boundaries; **0** if the discontinuity transects the window boundaries, **1** if the discontinuity intersects one of the window boundaries and **2** if the discontinuity is contained within the window boundaries (in Figure 2.9).
3. Discontinuity type; joint, veins or fault. Veins include vein type descriptions such as LM veins, PH veins, and LH veins.
4. Orientation; dip direction and dip of the discontinuity.
5. Small scale roughness; by visual inspection to match the **1** to **9** scales from ISRM (Brown 1981, p.27) detailed in Section 3.7.
6. Large scale roughness; by visual inspection to match the **1** to **5** scales from Laubscher (1993, p.562) detailed in Section 3.7.
7. Trace length; length of the discontinuity measured as seen in the rock face.
8. Type of termination; according to Figure 2.9. These are; in another discontinuity at low ($< 20^\circ$) or high angle ($\geq 20^\circ$), intact rock, censored, and hidden.
9. Face's area; area of the exposed discontinuity wall surface (Figure 2.12).
10. Filling or infill features; in faults this may be gouge and/or slickenside. In veins or faults a quantitative mineralogical assemblage by visual inspection³ is described, for instance, 80% of chalcopyrite, 15% of anhydrite and 5% of chlorite (as shown Figure 2.12). The visual inspection is calibrated by using *comparison chart for estimating percentage composition* (Richard and Varos, 1955).
11. Vein Subtype; characterization of vein subclasses within major vein types (this parameter has been recorded for geological analysis, but it has not been used in this study).

³ Helped by magnifying glasses (10x)

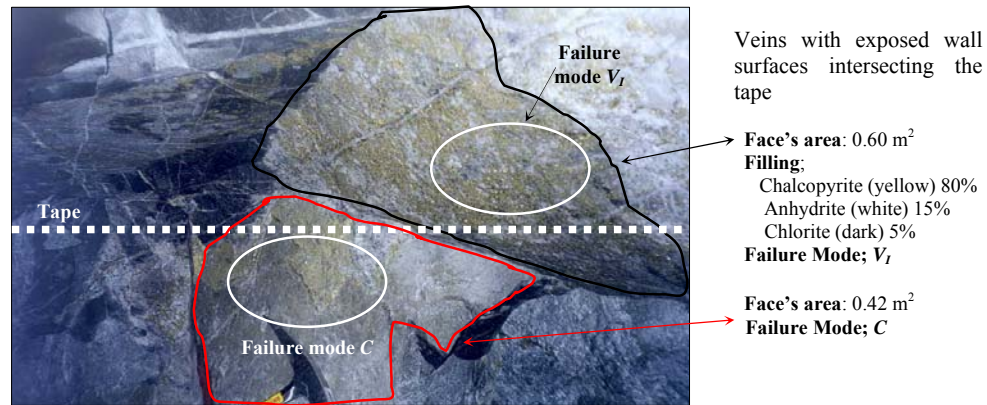


Figure 2.12. Veins with exposed wall surface during scanline mapping.

12. Halo; width and type of the alteration halo in the wall rock next to the veins as can be seen in Figure 2.13a (this parameter has been recorded for geological analysis, but it has not been used in this study).
13. Thickness; maximum and minimum thickness observed across the discontinuity trace length as can be seen in Figure 2.13a.

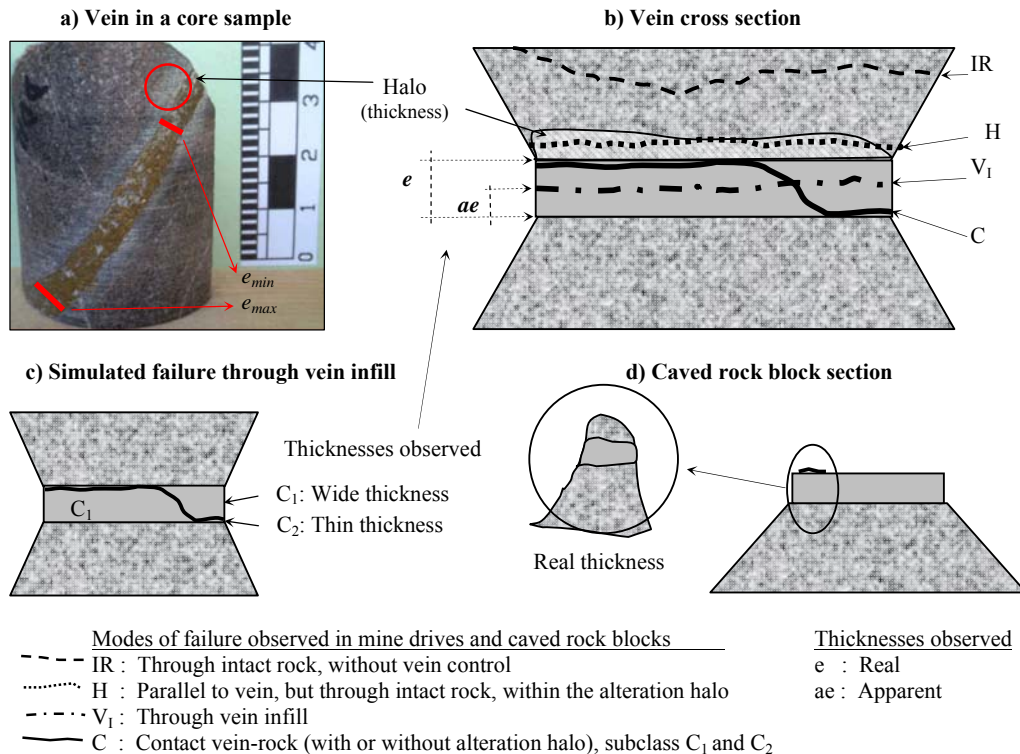


Figure 2.13. Failure mode and thicknesses of discontinuities (Brzovic and Villaescusa, 2007).

14. Mode of Failure; according to Figure 2.13 (Brzovic and Villaescusa, 2007).
 These are related to the rock mass disassembly and have been classified as; **C** if the failure is through the rock – veins contact, **V_I** if the failure is through the mineralogical infill assemblage, and **H** if the failure is through the intact rock, but parallel to the veins and within the alteration halo. Further detail is explained in Section 4.2.3.
15. Remarks; Special characteristic such as observed water condition, kinematics faults indicator, and others, etc.

In the present study, scanline samplings were selected from available mine drives in undercut and production levels (see Figure 2.4 and Figure 2.5). Additional sampling information is presented in Figure 2.6 and Table 2.4.

Table 2.4. Summary of sample lines used and structures collected in scanlines analysis.

Sample orientation	Andesite Hw sector			Andesite Fw sector		
	Number of Samples Lines	Total Discontinuities	Total meters	Number of Samples Lines	Total Discontinuities	Total meters
N45°E	2	145	40.0	3	115	24.9
N15°W	2	193	43.6	1	123	18.8
Vertical	16	183	32.4	9	81	15.3
Total	20	521	116	13	319	59

2.7 Borehole Logging

Examination of core samples obtained by diamond drilling techniques has been used for many years to characterise the rock mass conditions at depth. The method provides a relatively undisturbed sample of rock material which may contain ore and discontinuities. The information collected from drill cores can improve the knowledge of the ore deposits in a variety of ways, from geological modelling to hydrological information. In the current study, borehole logging has been used to collect discontinuity data, the techniques used include both oriented (mainly large diameter core samples) and un-oriented core logging (small diameter core samples).

2.7.1 Oriented Core Logging

Data collection using large diameter oriented core samples were undertaken at the two studied mine sectors. Core samples were obtained from large diameter (overcore) samples used to install Hollow Inclusion (HI) stress measurement cells and from over coring samples used for other purposes. This methodology had not

been applied at the El Teniente mine before. This type of core sample has the advantage of a larger (wide) rock exposure than standard drill core samples (small diameter), but usually has a short sample length. Samples from HI cells have core diameters of 140 mm and are up to 13-14 meters long. Other over coring samples have core diameter of 100 mm and a length up to 5-6 meters. These large diameter cores have also the advantage of reduced the risk of sample disturbance during drilling. A marking procedure was designed to orient each core sample with respect to the mine coordinate system.

Following a complete reconstruction and orientation of the core, a reference line was marked on the core. Each single discontinuity that both intersects the red line, and has enough trace length to measure the dip (“across the core”) is recorded. This means the truncation bias varies between 0.14 to 0.10 m, depending upon the core size used. Using this criterion, thin discontinuities that do not extend across the entire width of the core may be disregarded. An example of these thin discontinuities is shown in Figure 2.14 (within the red square).

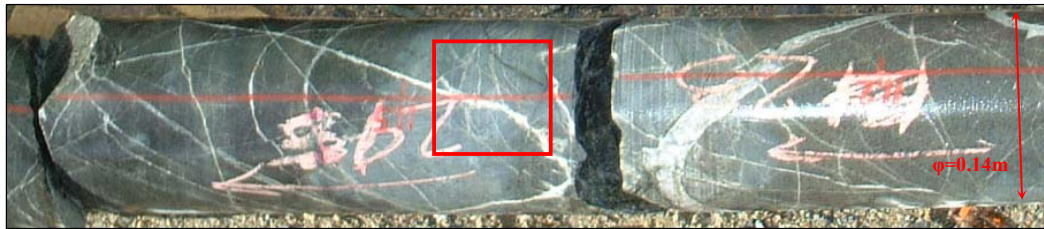


Figure 2.14. Oriented drill core sample showing thin discontinuities, which were disregarded during data collection (within red square).

The basic information collected at each oriented drill core sample included: Id core number, bearing, plunge, vertical reference, and location in mine coordinates. With these data, the discontinuities are automatically oriented in the Dips software package (Rocscience Inc, 1999). Discontinuity characteristics were described similar to the scanline methodology, which were recorded on a tabular data spreadsheet (Figure 2.15).

In the present study, large diameter oriented drill core sample were collected from mine drives in undercut and production levels (see Figure 2.4 and Figure 2.5). Additional sampling information is presented in Figure 2.6 and Table 2.5.

Core No: _____	North: _____	Angle orientation 1: _____	Page: _____	of: _____
Bearing: _____	East: _____	Core diameter: _____	By: _____	
Plunge: _____	Level: _____		Date: _____	
Elevation: _____	Location: _____	Rock Type _____	Start: _____	Finish: _____

Location		Structure					Infill features					Remarks	
Id	Dist. (m)	Type	DipDir	Dip	Roughness	Thickness	Filling (Infill)	Veins Subtype	Halo		Thickness (mm)		
									Type	Width	Max.	Min.	

Main notation used:

Structure type	J Joint	V Veins (LM, PH, LH)	F Faults	Roughness	1 to 9 Scale (ISRM 1981)
-----------------------	----------------	-----------------------------	-----------------	------------------	---------------------------------

Figure 2.15. Data collection spreadsheet for oriented drill cores.

Table 2.5. Summary of sampling orientation used and structures collected in oriented core logging.

Andesite Hw				Andesite Fw			
Id	Bearing /Plunge (Core diameter, m)	Total Discontinuities	Total Length (m)	Id	Bearing /Plunge (Core diameter, m)	Total Discontinuities	Total Length (m)
1	260/04 (Φ 0.10)	120	4.8	1	327/09 (Φ 0.10)	152	5.0
2	102/03 (Φ 0.10)	164	5.1	2	255/04 (Φ 0.14)	187	5.4
3	199/07 (Φ 0.14)	322	12.3	3	092/04 (Φ 0.10)	107	4.2
-	-	-	-	4	153/04 (Φ 0.14)	119	6.2
	Total	606	≈ 22			565	≈ 20

2.7.2 Un-Oriented Drill Cores

Un-oriented drill core logging is one of the main geologist's activities at the mine site, with more than 35,000 meters of logging every year. The main purpose of the drill core program is the development and continual improvement of the ore resource model, which consists of three-dimensional lithological and sulphide mineralogical models, however, little data is used for geotechnical characterisation

Typical drill core used at the mine site are drilled in 3.05 runs (10 feet core barrel length) with core diameter ranging from 48 to 64 mm (NQ⁴ and HQ diamond coring drills). These core samples are referred as standard or small diameter core samples. After drilling, the core is placed in a core tray (0.7 meters long) where measurements of fracture frequency (ff) is undertaken (Figure 2.16a). Following this, the core sample is photographed. Subsequently, the core sample is split into two parts along the core axis by a guillotine, which handles samples up to 0.4 meters long. One half is sent to the laboratory for assay analysis and the other is sent for geological logging. The geologists receive a half of the original drill core, which at this time has

⁴ Majority of cores samples used in this study.

been broken in many small pieces (Figure 2.16b), which makes the orientation reconstruction impossible. This is why this sampling technique is referred as un-oriented core logging.

Core logging undertaken at the mine site currently describes rock types, quantitative veins frequency, qualitative alteration and mineralogical veins infill assemblage, among other mineralogical parameters.



Figure 2.16. - Standard un-oriented core samples, prior it is split (a) and after that (b).

For this study, modifications to a quantitative description of vein features were introduced to log core properties such as infill features and thickness, and more accurate vein frequency estimates. Discontinuity characteristics were described similar to the scanlines, which were recorded on a tabular data spreadsheet (see Figure 2.17). The basic information collected included; Id core number, bearing and plunge, mine coordinate location of the hole collar, and section logged.

Id Core:		North:	Criterion:		Page:	of:
Bearing:		East:			By:	
Plunge:		Level:			Date:	
Section:		Location:		Rock Type	Start:	Finish:

Core section			Infill features						Remarks	
Id	From	To	Type	Filling (infill)	Veins Subtype	Halo		Thickness (mm)		
						Type	Width (mm)	Max.		Min.

Main notation used:

Structure type	J	Joint	V	Veins (LM, PH, LH)	F	Faults	
-----------------------	----------	-------	----------	--------------------	----------	--------	--

Figure 2.17. Data collection spreadsheet for standard non-oriented drill cores.

Although a truncation bias length threshold criterion was not introduced during un-oriented core logging (all discontinuities that can be seen were collected), the practical length threshold is estimated at around 0.03m based on the ability to visually identify discontinuities during core logging.

During un-oriented core logging the location of discontinuities was not recorded as was in Scanlines (distance of intersection a long a tape). The location of discontinuities was recorded as being within a non-overlapping segment of 1.02 meters long along of the selected core section. A core section for sample length was assumed to be 6.1 meters long, which coincide with core section selected for assay analysis.

Table 2.6. Summary of sampling orientation used and structures collected in un-oriented core logging.

Rock Type	Core sample 6.1 meter long		
	Number of samples	Total meters	Average frequency (m ⁻¹)
Andesite	108	658.8	53.4
Diorite	17	103.6	35.3
Dacite	8	48.8	36.4
Total	133	≈ 811	-

2.8 Fragmentation Assessment

The rock mass can be thought as an assemblage of potential blocks, which can be disassembled by the *excavation process* (Hudson and Harrison, 1997) or caving process (Laubscher, 2001). In block caving, the fragmentation is the size distribution of caved rock blocks measured in the production level mine draw points (i.e., after the excavation or caving process). The in situ fragmentation are the potential blocks, which assemble composed, the rock mass prior the excavation process. In block

caving the excavation process refers to the comminution process that occurs during flow through the caved zone to draw points.

In order to estimate the in situ fragmentation (in situ block size distribution), the determination of the three-dimensional nature of the rock structure is required. This is usually achieved by stochastically simulating the rock structure from data that have been collected from one or two-dimensional mapping. This implies a correction for the biases imposed by the sampling regime (see Villaescusa 1991, among others). Several software packages have been developed to perform this task, which include *Stereoblock* by Hadjigeorgiou et al. (1995), *Block Caving Fragmentation* (BCF) by Esterhuizen (1999), and a local methodology developed at the El Teniente mine (Blondel et al., 1995).

Determination of fragmentation may also be made by direct measurements in draw points. Several techniques may be used, ranging from visual inspection to sophisticated Digital Image Processing (DIP) methods, such as DIP technique described by Kemeny et al. (1993). However, none of these techniques have characterised the block forming geological discontinuities that actually define the caved rock block faces (fragmentation) in draw points as proposed in this study.

2.8.1 Characterisation of Caved Rock Blocks

Four important facts can be drawn from current observation of primary copper ore caving process at the El Teniente mine.

1. Practically no open joints can be observed within rock masses of the primary copper ore (Figure 1.1), which is in agreement with its described behaviour, as a competent and massive rock mass.
2. The rock mass has numerous of veins (Figure 1.7).
3. A significant proportion of fine fragmentation usually can be found within the draw points (Figure 1.18). This fine fragmentation allows high rates of underground primary copper ore production within block caving at the mine site.
4. Caving of primary copper ore has been obtained with a small radius hydraulic of 26m (Rojas et al., 2001), which may suggests a rock mass with poor to regular rock mass quality (Figure 1.16).

The conclusion from these facts is that the rock mass is being disassembled through either *weaker veins* or *intact rock* during caving process. In order to understand this process, caved rock blocks collected from draw points were characterised as part of this study (Brzovic et al., 2006).

The characterization of the caved rock blocks was based on a sampling objective (Brown, 1981) that required systematic observations and measurements of a number of selected rock blocks from a draw point. The same two alteration zones within the andesite rock type at the Reno mine sector were selected to perform this task (Figure 2.18). These zones included three-rock unit types: andesite *H_w*, andesite *F_w*, and diorite *F_w* (just diorite for this purpose). The andesite *H_w* sector is extracted by a variant of the pre-undercut variant method, and conventional panel caving is used to extract the andesite *F_w* and the diorite rock types.

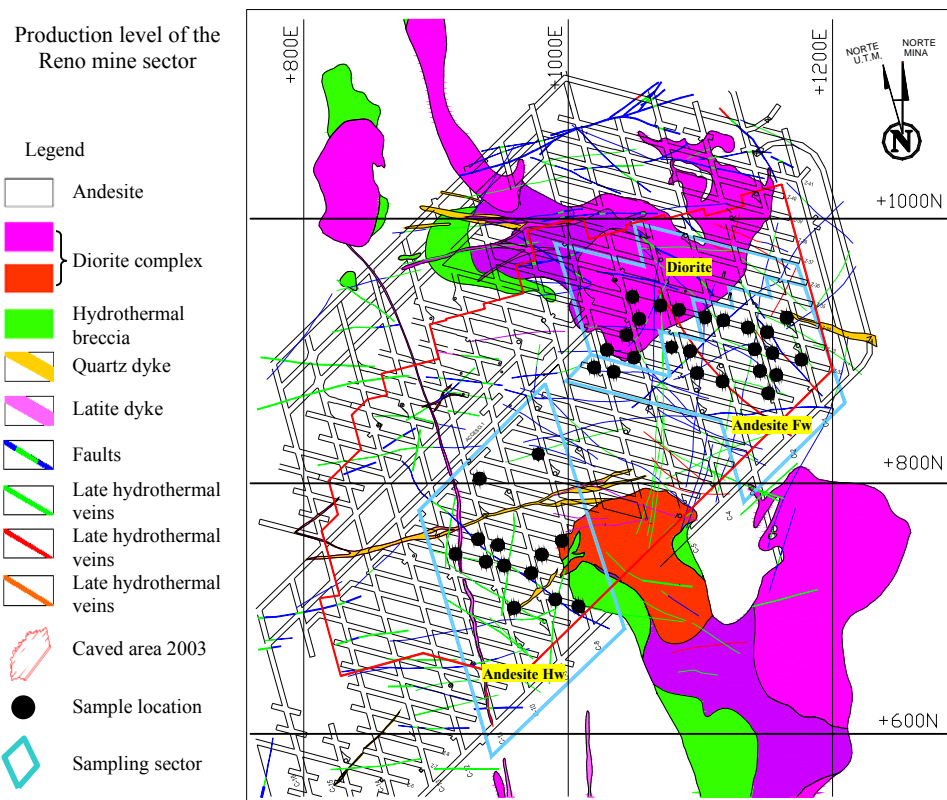


Figure 2.18. Sectors studied for caved rock blocks characterisation at the Reno mine production level.

Within the selected sectors, available draw points from the production area were chosen to collect rock blocks. The percentage of extraction from the extracted rock column height (production) at any selected draw point was chosen between 10% and

50%, in order to avoid secondary blasting effects and dilution. At any selected draw point, a rock block was randomly collected for detailed examination. The sampling aimed to collect similar numbers of rock blocks considering both, unit types and range of volume. However, the number and location of rock blocks selected was dependant upon production activities at this mine level (Table 2.7).

Table 2.7. Caved rock block blocks and faces characterised at the Reno mine production level.

Unit Type	Number of rock block per volume ranges				Number of characterised rock block faces
	< 0.05 m ³	0.05 – 0.5 m ³	> 0.5 m ³	Total	
Andesite Hw	12	13	4	29	242
Andesite Fw	13	11	6	30	225
Diorite	16	8	4	28	257
Total	41	32	14	87	724

The main caved rock block description included location, geometrical and face characteristics similar to those established during line mapping (Figure 2.19). Data collected included volume, shape, number of faces, edge (length), and dihedral angle between pairs of rock block faces.

Rock block geometrical characteristics										
Rock Block Number:			Location:			Drawpoint:		Date:		
Number of Faces:			Unit Type			Extraction %:		By:		
3D Shapes:		Dimensions: B:		(m)	B2:	(m)	Length:	(m)	Height:	(m)
Structure defining rock block faces					Infill features					
Face Id	Structure Type	Thickness (mm)			Roughness	Failure mode	Filling or infill	Veins Subtype	Halo	
		Max	Min	Real					Type	Width

Main notation used:

Structure type				Geometric figure		TpP		Roughness	
IR	Intact rock	J	Joint	SP	Square Pyramid	TrP	Triangular Prism	1 to 9 Scale (ISRM 1981)	
F	Faults	V	Veins (LM, PH, LH)	CR	Cuboid Regular	CI	Cuboid Irregular		

Figure 2.19.- Caved rock block characterisation spreadsheet (adapted from Figueroa, 2003).

The parameters descriptions presented in Figure 2.19, which were not described in Section 2.5.2 (line mapping) are detailed as follow:

1. Shape and dimensions of rock block. A general shape classification was created and the main rock dimensions were defined according to Figure 2.20.

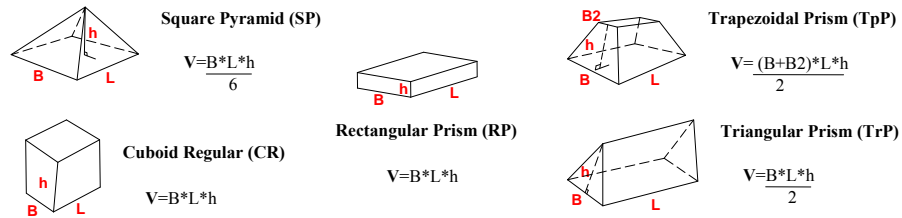


Figure 2.20.- Definition of rock block shapes and dimension (adapted from Figueroa, 2003).

- Edge (length) and dihedral angle between every pair of faces combination were measured. The dihedral angle is the acute angle measured in the plane perpendicular to the edge.
- Apparent and real thicknesses and failure mode according to Figure 2.13 (Additional explanation of failure mode is presented in Section 4.2.3).

An example of a caved rock block characterisation is illustrated in Figure 2.21.



Figure 2.21.- Characterised rock block showing trapezoidal prismatic shape in a draw point at the Reno mine sector (Figueroa, 2003).

2.9 Conclusions

In this chapter a review of main aspect in data collection has been undertaken. These are referred as discontinuity definition and characteristics, scale effect, sampling bias and sampling techniques.

The general term ‘discontinuity’ define by ISRM (Brown, 1981) used here also included geological structures having high tensile strength such as healed veins, cemented with a mineralogical infill assemblage.

Data collection design used in this study has been planned considered these factors. The rock structure characterisation was undertaken including different sampling techniques, which can be classified as; measurement at exposed rock faces, borehole logging and an assessment of block forming geological discontinuities at production level draw points.

Different truncation biases and censoring levels were identified and implemented during data collection. The sampling techniques can then be used to characterise the rock structure at different mapping scales, from major structures on a mine scale, detailed face mapping scales to drill core logging.

Modifications were made on the traditional line sampling methodologies (Villaescusa, 1991, Priest, 1993) to better determine the vein characteristics observed within primary copper ore. These were applied to all sampling techniques.

Major sampling features undertaken at Reno mine sector such as sample location and orientation are also documented in this chapter.

3 FUNDAMENTAL OF ROCK STRUCTURE, ANALYSIS AND INTERPRETATION

3.1 Introduction

Rock mass strength and deformability are strongly influenced by the geometric and strength characteristics of the geological discontinuities. The International Society of Rock Mechanics (Brown, 1981) has suggested an objective and systematic methodology to characterise discontinuities in rock masses, which included ten essentials parameters.

The degree of fracturing or the in situ block size distribution within rock mass can be determined by deterministic and probabilistic methods. These methods such as the simplest Volumetric Joint count J_v (Pasmtron, 1985) and the more complex Discrete Fracture Network (DFN) modelling, are based on characterisation of discontinuity parameters such as orientation, spacing, persistence, and number of sets. Rock block interlocking and strength properties are determined by the interaction between discontinuities, which are based on the characterisation of discontinuity parameters such as roughness, aperture, filling, wall strength, and seepage features of discontinuities. Such combined factors are likely to influence the mechanical behaviour during and following excavations.

In this research, a data collection campaign has been undertaken at the Reno mine sector to characterise the rock structure of primary copper ore. Sampling techniques described in Chapter 2 were used to collect structural data from mine drives in two different structural domains.

3.1.1 Goal

The main objective of this Chapter is to characterise the rock structure of the El Teniente primary copper ore following ISRM guidelines, i.e., by a detailed description of suggested discontinuity parameters (Brown, 1981). In order to achieve this goal, a literature review on the main discontinuity parameters for structural data analysis was undertaken. In this chapter the literature review and fundamentals are presented on a background subsection as a precursor to data analysis from El Teniente.

A second objective of this chapter is to examine the differences between two structural domains within Reno mine sectors (named as *Hw* and *Fw* sectors) to investigate how discontinuity parameters vary throughout the rock mass. Correlation and/or agreement of data between data collection techniques are also discussed.

3.2 Discontinuity Orientation

3.2.1 Background

In rock mechanics and rock engineering, the most accepted way to represent the orientation of structural data is using the hemispherical projection methods. Sometimes this method is referred as the spherical projection technique (Priest, 1993). A plane *K* to be found in three dimensional space is graphically represented with respect to the surface of a reference sphere projected on a two-dimensional horizontal plane (Figure 3.1).

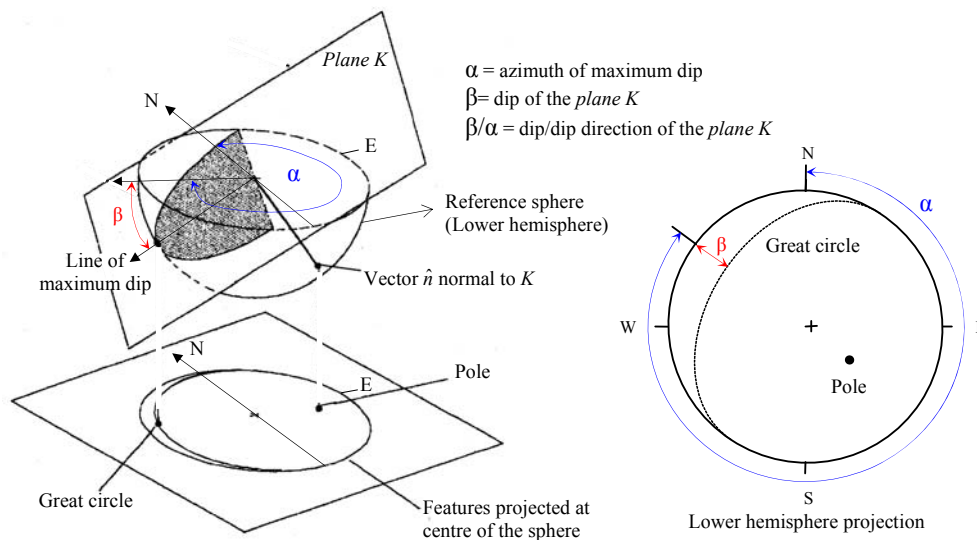


Figure 3.1.- Lower hemispheric projection, modified after Hoek and Brown (1980).

In this case, the lower hemisphere intersected by the plane *K* form a semi-circular arc called *great circle*, which is projected at the horizontal plane of the sphere centre. In addition, the lower hemisphere intersected by a unit vector \hat{n} normal to plane *K* define a point called *pole*, which is also projected at the horizontal plane of the sphere centre. Then, either the *great circle* or the *pole* may be recorded in polar

coordinates using two angles, the trend α , and the plunge β , which finally represent the spatial orientation of the plane K in a two dimensional plane, in this case defined as the lower hemisphere projection¹. In this research all structural data analysis as illustrations uses the lower hemispheric projection.

Linear sampling introduces orientation bias to the sample data (Terzaghi 1965). For particular discontinuity spacing, the number of observations from one discontinuity set is a function of the angle of intersection between the set and the sampling line (scanline or borehole). Parallel discontinuity to the sampling line will not be sampled. Figure 3.2 illustrates the angular relationship δ between the orientation of the sample line L and the true spacing of set S_n (normal to the set).

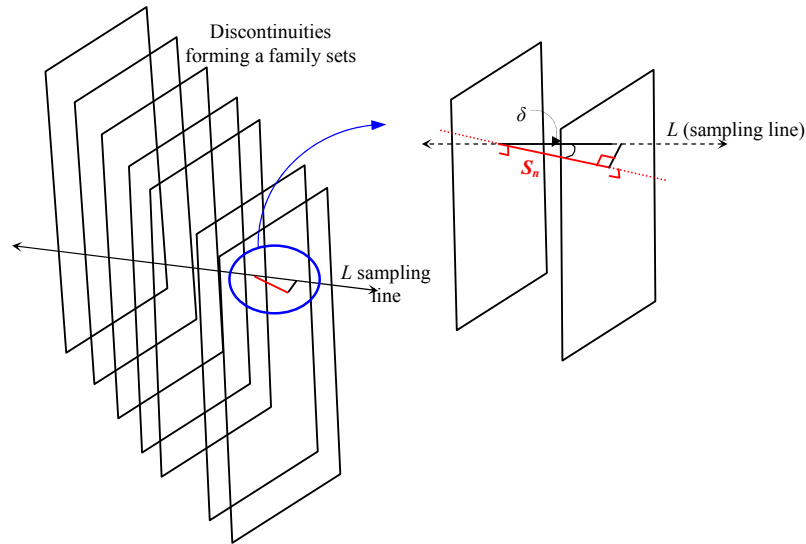


Figure 3.2.- Angular relationship between linear survey and discontinuity set orientation.

The number of discontinuities N_δ that interested by the linear survey is given by (Terzaghi, 1965):

$$N_\delta = \frac{L \cos \delta}{S_n} \quad (3.1)$$

and therefore the mean spacing is given by:

¹ The great circle and the pole could be intersected on the upper hemisphere, which lead to define the upper hemisphere projection.

$$\bar{S}_n = \frac{L \cos \delta}{N_\delta} \quad (3.2)$$

To minimize this orientation bias a weighting factor, w , can be applied (Priest, 1993). This weighting factor is calculated from the expression:

$$w = \frac{1}{\cos \delta} \quad (\delta < 90^\circ) \quad (3.3)$$

where δ is the acute angle between the sampling line and the normal to the mean orientation of the discontinuity set (Figure 3.2).

The angle δ can be determined either from the hemispherical projection, by vector algebra methods (in Section 3.3), or from the following expression (Priest, 1993):

$$\cos \delta = |\cos(\alpha_n - \alpha_s) \cos \beta_n \cos \beta_s + \sin \beta_n \sin \beta_s| \quad (3.4)$$

where α_n/β_n is trend and plunge of the normal to the discontinuity set and α_s/β_s is trend and plunge of the sampling line.

When δ approaches 90° , w became very large, and therefore a single data point could dominate the distribution pattern. To avoid this problem a maximum value of 10 could be adopted suggested Priest (1993).

A practical way to minimise orientation bias, which was try to adopted here, is the use of three mutually orthogonal equal lengths for each sampling site.

This study utilised Dips software package (Rocscience Inc, 1999), which provides stereographic projection and other tools to simplify and speed up the structural data analysis. Using Dips, correction weighting for orientation bias and mean discontinuity set estimates for Fisher distribution k (Fischer, 1953) can be automatically obtained.

3.2.2 Discontinuity Occurrence in Line Sampling

Before proceeding with the rock structure characterization and considering the fact that different truncation bias and censoring levels were introduced during data

collection, the occurrence of discontinuity types through mapping scales and sectors was examined (Table 3.1).

Although the occurrence of discontinuities in this particular survey have not been analysed considering the natural anisotropy of the rock structure, some relevant aspects can be deduced from data shown in Table 3.1. Firstly, excluding faults, open joints were not found within the primary copper ore; a large number of veins were recognized instead. A second relevant aspect is that faults were better characterized using large scale sampling. In contrast, veins were better characterized using small scale sampling. In other words, faults and veins are present within the primary copper ore at different scales. Even different vein types appeared when different scales were considered. In the next sections it is shown that, in most cases, a similar sampling line orientation with respect to mean discontinuity orientation was used for all the mapping scales, therefore, the information gathered, and the conclusions reached, may be not depend upon the sampling regime.

Table 3.1. Discontinuity occurrence per sampling technique.

Sampling Methods (Truncation bias)	Sector	Data	Occurrence of Discontinuity Types (%)				
			Faults	Veins			
				Total	Individual estimates		
				LH Veins	PH Veins	LM Veins	
Major Structures Plan view (≥ 30 m)	Hw	21	57.1	42.9	38.1	4.8	-
	Fw	22	77.3	22.7	13.6	9.1	-
Drive Mapping (≥ 4m)	Hw	239	16.7	83.3	38.1	15.1	30.1
	Fw	206	30.5	69.5	27.7	37.4	4.4
Scanlines Mapping (≥ 0.3m)	Hw	521	1.9	98.1	2.9	5.4	89.8
	Fw	319	7.2	92.8	3.5	23.2	66.1
Oriented Cores Logging (≥ 0.1m)*	Hw	606	0.3	99.7	4.8	6.9	88.0
	Fw	565	1.9	98.1	3.4	24.1	70.6

* Note: Some discontinuities longer than this threshold value could be disregarded during data collection (see Section 2.6.1).

In addition, Table 3.1 shows that the occurrences of PH veins in sampling lines are in agreement with the definition of alteration zone boundaries suggested by Cuadra (1986). PH veins are more abundant at in the *Fw* sector (within the PH alteration zone). Next, LM veins tend to be better characterised using small scale sampling than other vein types.

The structural data analysis that follows in next section was carried out considering main discontinuity types, i.e., faults and veins. In some cases a detailed analysis was also undertaken considering vein types separately.

3.2.3 Set Definition

Historically, joint sets have been defined by two main approaches. In the first instance, sets have been defined through the visual recognition of cluster on the hemispheric projection and in the field, taking advantage of human capabilities to recognise a pattern (Call et al., 1976, p.69; Einstein and Beacher 1983, p.45; Villaescusa 1991, p.42). The second method applies cluster-analysis techniques to identify sets, such as the algorithm developed by Shanley and Mahtab (1976) and Mahtab and Yegulalp (1982), and the proposal methodology by Bridges (1990). These cluster analysis techniques used stochastic analysis to define the angular relationship between discontinuities.

Human capabilities to recognise patterns have been debated, because it could be 'entirely subjective and therefore susceptible to personal bias and inconsistency' (Priest, 1993, p.77). Also, joint cluster recognition is difficult when there are complex and overlapping clusters of discontinuity orientation (Bridges, 1990). The option of statistical models are merely numerical, rigid, and do not include the any engineering judgment (Call et al., 1976).

Cluster-analysis technique, such as the Mahtab's algorithms (Mahtab and Yegulalp, 1982) do not offer a unique solution to define a number of discontinuity sets. Consequently engineering judgment and personal experience is required to arrive at realistic solution, as has been mentioned by Priest (1993, p.82), and Kulatilake et al. (2004, p.188).

In the present study, traditional clustering and contouring on the equal-angle lower hemispheric projection were utilised to discriminate sets. This approach has been statistically matched by applying the Poisson Exponential Binomial Limit, as suggested by Pincus (1951, p.101; 1953, p.502). Statistically, the likely occurrence of a discontinuity set can be gauged using this test of significance (Figure 3.3).

This methodology provides the probability of obtaining a concentration on a stereographic projection, which deviates from a random distribution (Villaescusa, 1985). The confidence limited desired can be calculated from a given number of poles in the entire sample.

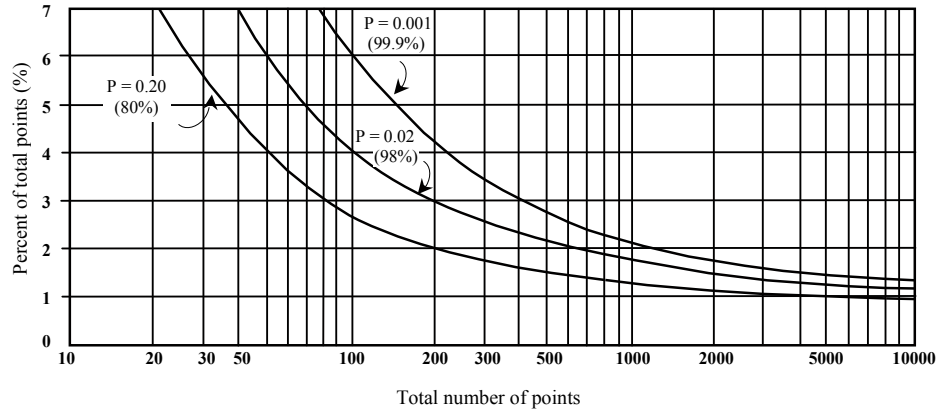


Figure 3.3.- Application to the Poisson exponential binominal limit for sample data using stereonet plots (after Villaescusa 1985).

For example, in Figure 3.3, if a 98% confidence level contour is reached, there is 98% confidence that the joint set is real and not a result of chance or error. Conversely, if the sample has 200 poles, to assure with 98% confident that a joint set is real and is not a product of chance or error, it has to be defined by at least a 3% of concentration contour in the stereo plot (Villaescusa, 1985). During this study the 98% confidence levels was adopted to define discontinuity set.

3.2.4 Orientations of Faults and Major Structures

Some researchers have suggested treating major discontinuities as individual entities, because they usually play a relevant role in the stability analysis (Call et al., 1976, Cruden, 1977). Nevertheless, the mining method utilised at El Teniente mine allows the collection of enough major structures to be statistically analysed. Discontinuity orientation for major structures is presented in Figure 3.4.

Figure 3.4 illustrates that the majority of the major discontinuities have sub-vertical orientation in both sectors of the mine, and the differences between sectors are minor. Table 3.1 shows that faults are the main component of the major structures (over 60% of the data), with the second group of discontinuities being the LH veins.

The fault set orientations observed from data collected in mine drive (drive mapping) are presented in Figure 3.5. This figure shows that two sub-vertical set of faults were found in both sectors, with one set similar in both sectors.

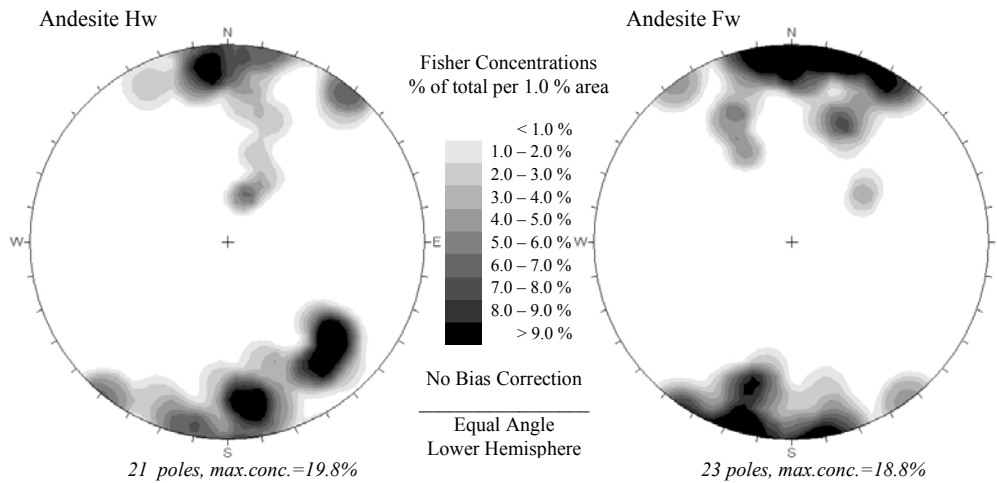


Figure 3.4.- Major discontinuity orientations per unit sector plotted in the lower hemispheric projection.

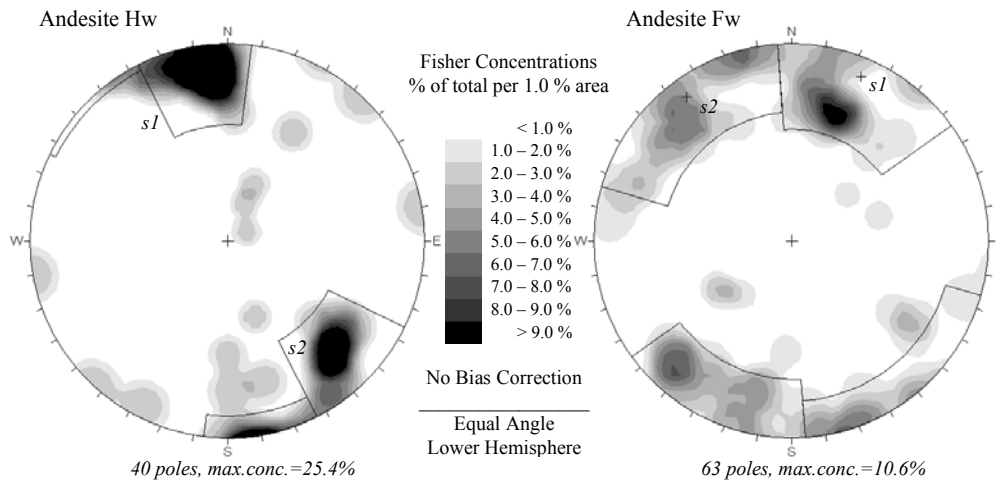


Figure 3.5.- Set definition for faults collected in mine drives (drive mapping). It is shown the main set orientation defined (set; s).

Although, sub-horizontal discontinuities were not entirely defined by large scale sampling, the fault orientation data is in agreement in Figure 3.5 with the strike-slip faults characteristics described at the mine scale (Garrido et al., 1994). The fault system has been associated with an approximately northwest compression (shortening direction) during ore formation within the El Teniente Shear Zone (Garrido et al., 1994). This is also in agreement with paleo strain field indications from fault slip vector analysis (Cladouhos, 1994) and with contemporary strain field from geodesic displacements (Windsor et al., 2006). Both data sets were measured on a local scale surrounding the mine. Therefore, despite of bias against to sub-

horizontal discontinuities during current data collection, the data suggest a rare occurrence or small likelihood of sub-horizontal faults within the primary copper ore at the studied mine sector.

Additional fault orientation data were collected during the review of this thesis using small diameter vertical oriented and no-oriented cores² at the Reno mine sector, which is detailed in the Appendix II.A. This additional data analyses suggests that faults tend to have sub-vertical orientations, which agree with the concept of a small likelihood of faults as having horizontal orientations. In addition, it is observed that the same average orientation is observed between major structures and faults recognised in drive mapping.

3.2.5 Orientations of Veins

Since veins were better characterized using small scale sampling, their orientations and definition of sets are examined from small scale sampling, i.e., from line mapping and oriented core logging (Figure 3.6 and Figure 3.7).

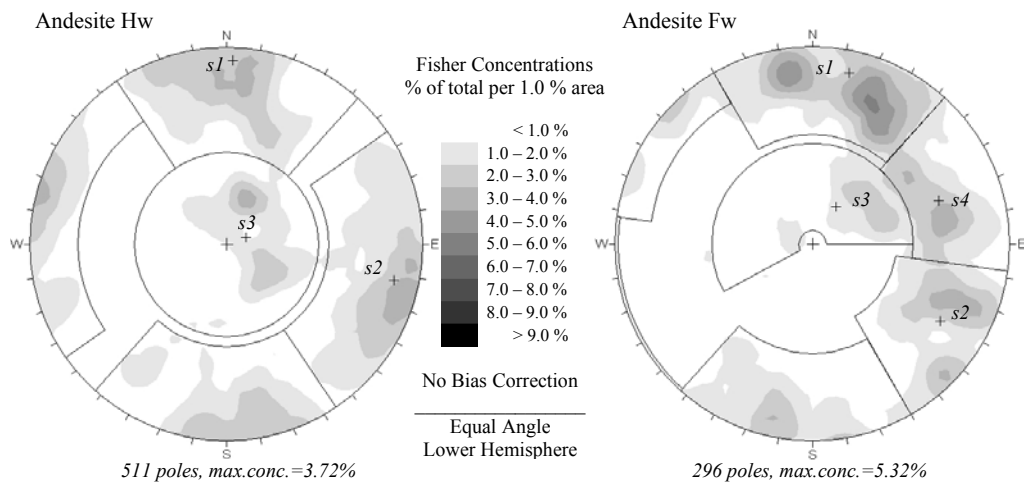


Figure 3.6.- Set definition for veins collected using scanline mapping. It is shown the main set orientation defined (set; s).

Although oriented core logging is more biased to sub-horizontal discontinuities and scanline mapping is affected by an exposure bias, Figure 3.6 and Figure 3.7 show clearly that at any sector, veins comprise at least 3 semi-orthogonal discontinuity sets. These figures also reveal that data collected using both sampling techniques

from each sector, have similar discontinuity orientations, i.e., only slight differences can be observed between sectors and mapping scales.

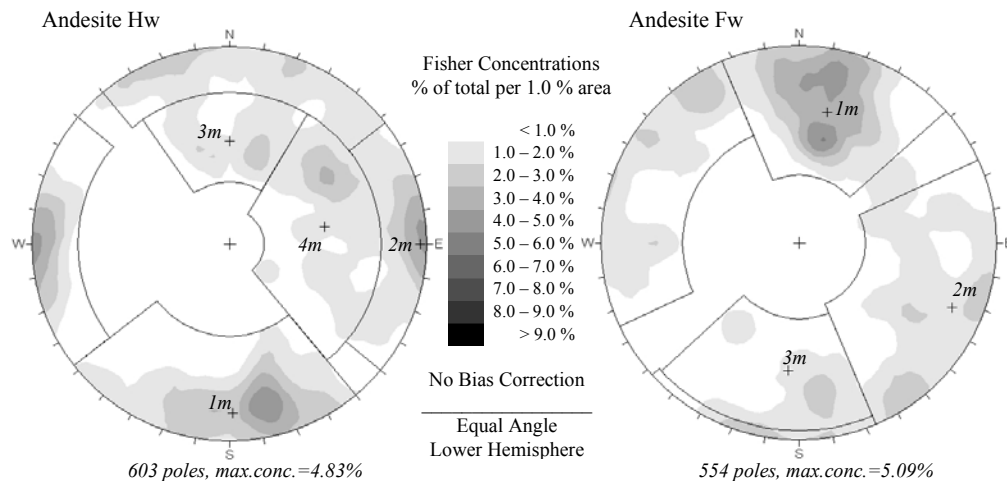


Figure 3.7.- Set definition for veins collected using oriented core logging. It is shown the main set orientation defined (set; s).

3.2.6 Comparison between Mapping Scales

The relationship between data collection techniques was also tested through data analysis of discontinuity types as shown in Figure 3.8. In this figure discontinuity set orientation per discontinuity types at each location is compared based on mapping scales. Set definitions for each discontinuity type were defined based on Figure 3.3, the stereo plots and set definition are shown in Appendix II.B.

Data presented in Figure 3.8 lead to conclude the following:

1. When a discontinuity type appears at more than one mapping scale, the discontinuity orientation is consistent. This may suggest that sampling bias have not been strongly affected.
2. In term of the average orientation, only TM veins seem to show slight variations between the two studied sectors.
3. The average orientation of faults and LH veins are very similar as would be expected based on their close genesis during ore formation.

² It is not a common practice to drill oriented core samples, these analysed here are the only ones existing at the mine site so far.

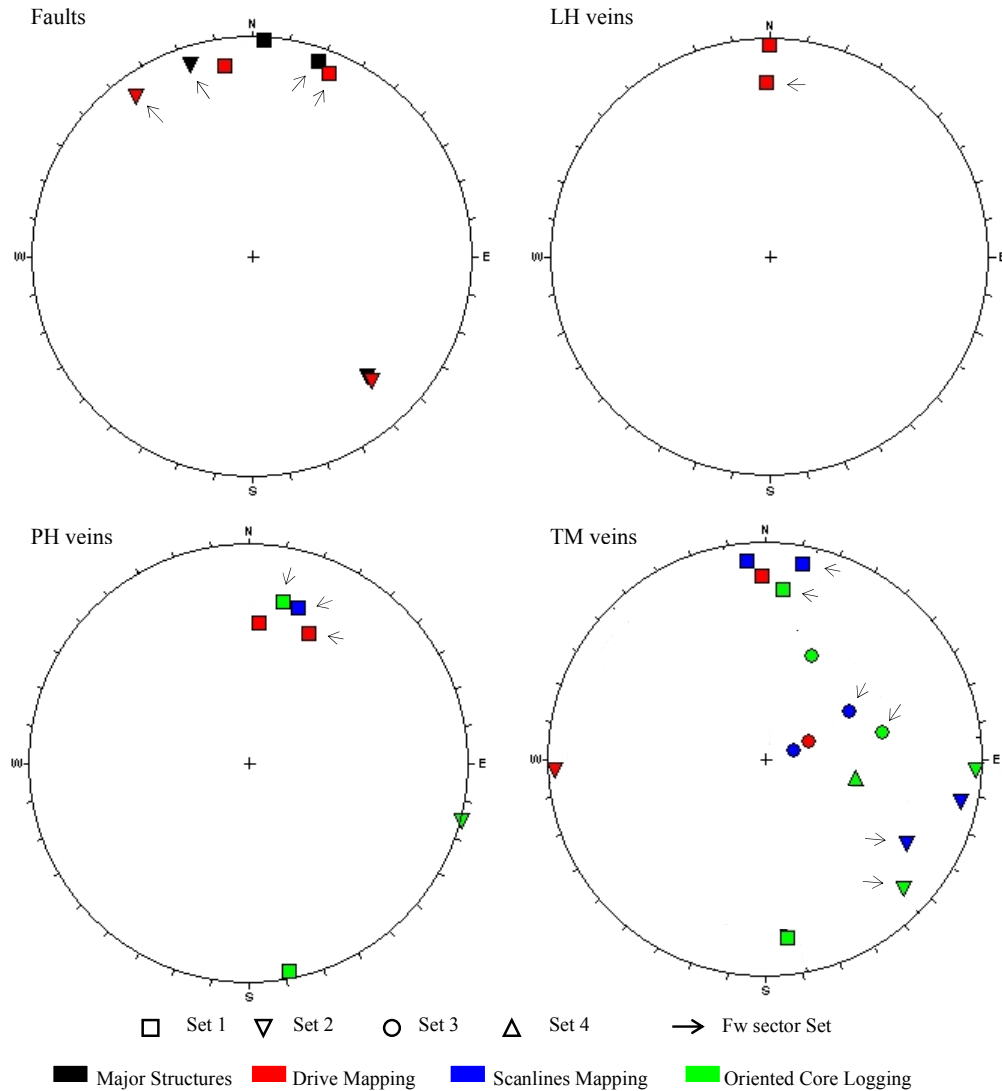


Figure 3.8.- Relationship between data collection thought set orientation per discontinuity types.

3.3 Spacing

3.3.1 Background

Spacing (S) is the perpendicular distance between adjacent discontinuities, according to the ISRM (Brown 1981, p.5). Its inverse is called frequency (λ). Priest (1993) provides one more formal and complete definition of spacing. Priest distinguishes three types of spacing: total spacing, set spacing and normal set spacing. In the same way three types of frequency can be defined; total frequency, set frequency and normal set frequency. These definitions are as follow.

Total Spacing: This is the distance S_t between a pair of immediately adjacent discontinuities measured along a particular line sampling within rock mass. Its inverse is the total frequency (λ_t), also referred as linear frequency (Priest 1993).

Set Spacing: This is the distance S_s between a pair of immediately adjacent discontinuities from the same set, measured along a particular line sampling within rock mass. Its inverse is the set frequency (λ_s). Set spacing has been called apparent set spacing, either to the apparent set frequency.

Normal Set Spacing: This is the perpendicular distance S_n between a pair of immediately adjacent discontinuities from the same set, measured along a particular line sampling within rock mass. Its inverse is the normal set frequency (λ_n). Normal set spacing has been called true set spacing, either to the true set frequency. Normal set spacing assumes that all the observations are parallel to the mean orientation of the set.

The two first 'spacing' can be estimated directly from a linear discontinuity survey such as a scanline or oriented drill cores. To estimate the true spacing between a pair of immediately adjacent discontinuities from the same set a long the sampling line is the following equation required:

$$S_n = S_s \cos \delta \quad (3.5)$$

where S_s is the measured distance on the sampling line and δ is the acute angle between orientation of the sample and the vector normal to the mean orientation of the discontinuity joint set (Figure 3.2). From equation 3.1 is clear that $S_s = L/N_\delta$.

The angle δ can be calculated using equation 3.4 or from vector algebra methods as follow. Let define the direction cosines lx_n, ly_n, lz_n of a unit vector \hat{n} normal to the plane K , and the direction cosines lx_s, ly_s, lz_s of a unit vector \hat{s} of the sampling line.

The direction cosines of a unit vector of orientation α_n/β_n can be estimated as (Figure 3.9):

$$lx_n = \cos \alpha_n \cos \beta_n \quad (3.6)$$

$$ly_n = \sin \alpha_n \cos \beta_n \quad (3.7)$$

$$l_y n = \sin \beta n \quad (3.8)$$

where α_n is the dip direction (or bearing) and β_n is the dip (plunge) of the unit vector.

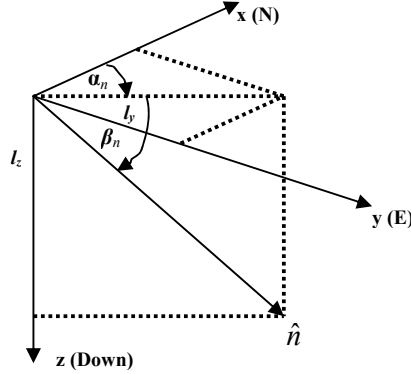


Figure 3.9. Direction cosines in a right-handed Cartesian system.

Then, the dot product of the two unit vectors can be calculated as follow:

$$\cos \delta = \hat{n} \cdot \hat{s} \quad (\delta < 90^\circ)$$

$$\cos \delta = | (l_x l_{x_n}) + (l_y l_{y_n}) + (l_z l_{z_n}) | \quad (3.9)$$

and the true spacing S_n is given by:

$$S_n = (l_2 - l_1) \cos \delta \quad (3.10)$$

where l_1 and l_2 are the consecutive intersection distance (measured on the tape) of the two discontinuities from the same set, and where $l_2 > l_1$ and $l_1 \geq 0$.

There are two methods to calculate the mean normal set spacing. These are referred to the 'arithmetic' and 'geometric' mean spacing values (Windsor, 1997). The arithmetic mean is determined by simply summing all calculated normal set spacing for a particular discontinuity set and dividing this value by the total number of spacing in the sample, as follow:

$$\overline{S}_n = \frac{1}{n} \sum_{i=1}^n S_{ni} \quad (3.11)$$

where \bar{S}_n is the mean normal set spacing, n is the number of spacing values on the sample, and S_{ni} is individual normal spacing between two consecutive discontinuities from the same set. To estimate the variability of this mean value is given by the variance s^2 , as follow:

$$s^2 = \frac{1}{n-1} \sum_{i=1}^n (S_{ni} - \bar{S}_n)^2 \quad (3.12)$$

note that s is also the standard deviation (S.D.) of the sample.

The geometric mean spacing involves finding the probability density distribution function of the normal set spacing data.

3.3.2 Statistical Distribution of Discontinuity Spacing

The geometric mean spacing is calculated following the determination of the density distribution function (*pdf*) of the data set by fitting the best curve on the plotted frequency histogram (Figure 3.10). Based upon field measurements, most workers have supported fitting either the exponential *pdf* (Priest and Hudson, 1976, Call et al., 1976, Wallis and King, 1980, Einstein and Beacher, 1983, Villaescusa and Brown, 1992) or the lognormal *pdf* (Bridges, 1975, Sen and Kazi, 1984) on a variety of igneous, sedimentary and metamorphic rocks. These two probability density functions are presented in Table 3.2.

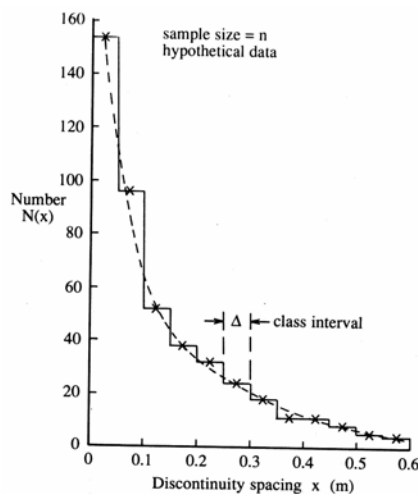


Figure 3.10.- Histogram of discontinuity spacing values, after Priest (1993).

Table 3.2. Probability density distribution after Priest (1993).

Name	Function	Range	Mean	Variance
Negative exponential	$f(x) = \lambda e^{-\lambda x}$	$0 \leq x < \infty$	$1/\lambda$	$1/\lambda^2$
Lognormal	$f(x) = \frac{1}{x\sigma\sqrt{2\pi}} e^{-0.5\left(\frac{\ln(x)-\mu}{\sigma}\right)^2}$	$0 \leq x < \infty$	$\mu l = e^{\left[\mu + 0.5\sigma^2\right]}$	$\mu l^2 \left\{ e^{\left[\frac{\sigma^2}{1}\right]} - 1 \right\}$

If the occurrence of a discontinuity along a linear survey is entirely random, then the location of one discontinuity has no influence upon the location of any others. In this case the discontinuity intersection obeys a one-dimensional Poisson process (Priest, 1993). When this occurs the probability density distribution of total discontinuities spacing is a negative exponential. A negative exponential *pdf* for discontinuity spacing might suggest, but does not prove, that discontinuity intersection along a sampling is a purely random event.

Hudson and Harrison (1997) emphasise the fact that discontinuities are not random events. Even though the Poisson process of random events can be expected to apply to field data, ‘fracturing is deterministic and occurs as result of direct mechanical causes’ (Hudson and Harrison, 1997). In other words, the occurrence of a negative exponential distribution ‘is expected as a result of a suite of superimposed geological events, each of which produces fracturing of a given distribution’ (Hudson and Harrison, 1997). In this respect, Hudson and Priest (1979) have demonstrated that a negative exponential distribution of *total spacing* may be obtained from the combination of non-exponential distributions of set spacing.

Whether a discontinuity spacing distribution follows a negative exponential *pdf* or a lognormal *pdf* may depend on the sampling regime adopted. If a truncation level is adopted, then small discontinuity spacings will be lost and spacing will be overestimated. In this case, a negative exponential distribution would appear as a lognormal distribution.

3.3.3 Reliability of Mean Discontinuity Spacing Estimated

Priest (1993) described two separate criteria by which the reliability of mean discontinuity spacing can be assessed:

1. Inaccuracy: the estimated mean is consistently biased by some persistent factor. Inaccuracy may be produced by a short sampling line when the mean spacing value is longer than the length of the sampling line.
2. Imprecision: is caused by the tendency of small samples to produce mean spacing values that exhibit inconsistent random deviations from the true value.

Inaccuracy is a type of bias that generally affects vertical sampling lines, particularly in mine drives or tunnels where limited rock exposure in the vertical direction is found. Sen and Kazi (1984) have produced graphs that illustrated the effect of scanline length on the calculation of mean discontinuity spacing values, when the mean discontinuity spacing can be described by either a negative exponential distribution or a lognormal distribution. Those graphs can be used to estimate the population means spacing from the sample mean, length of scanline and type of distribution. According to this work, if the scanline's length is at least 20 times of the mean normal set spacing, then will not be any difference between the estimated mean value and the population mean value, for the case where normal set spacing follows a negative exponential distribution. If this scanlines length is less than $20\lambda^{-1}$, then the estimated normal set mean spacing value will be underestimated.

Applying standard methods based on the central limit theorem Priest and Hudson (1981) have proposed a method of calculating the precision of the mean spacing value from a sample of size n . The theorem states that the mean value \bar{x} of the random samples of size n , taken from a population that follow any distribution, has some defined but unknown mean value μ_x , and variance σ_x^2 , which will tend to be normally distributed with a mean μ_x and standard deviation of the σ_x/\sqrt{n} . The term σ_x/\sqrt{n} is referred as the standard error of the mean. For a normal distribution, some proportion $\Phi(z)$ of the various sampling lines will yield a mean value within the range:

$$\Phi(z) \text{ range} = \bar{X} \pm \frac{zs}{\sqrt{n}} \quad (3.13)$$

where s is the standard deviation, z is a standard variable associated with a particular confidence level (given in Table 3.3).

Table 3.3. Values of $\Phi(z)$ for the normal distribution, after Priest and Hudson (1981).

z	$\Phi(z)$
0.675	0.50
0.842	0.60
1.036	0.70
1.282	0.80
1.645	0.90
1.960	0.95
2.567	0.99
∞	1.00

If the discontinuity spacing follows a negative exponential probability distribution, the mean spacing and standard deviation are theoretically the same ($1/\lambda$), and then equation 3.13 can be reduced to:

$$n = \left(\frac{z}{\varepsilon} \right)^2 \quad (3.14)$$

where ε is the allowable error.

This equation can be used to determine the sample size required to achieve a given error bandwidth. Priest and Hudson (1981) have reproduced curves that summarise the relation of equation 3.14 (Figure 3.11).

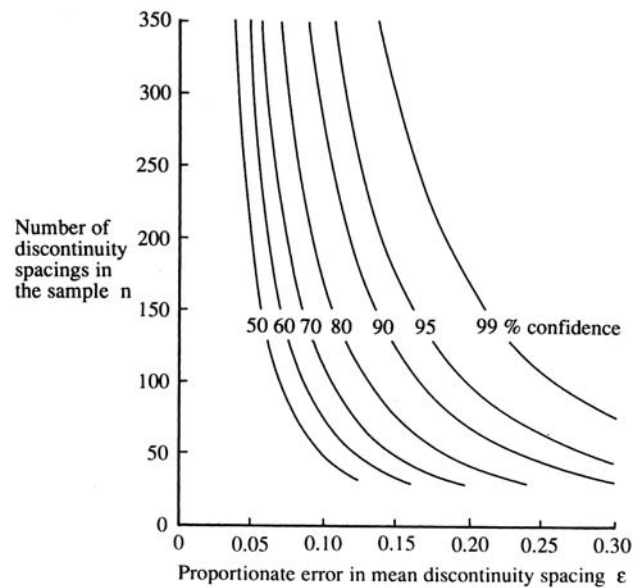


Figure 3.11.- Sample number versus precision of the mean discontinuity spacing that follow a negative exponential *pdf* (after Priest and Hudson 1981).

Following their graph, for instance, if we require estimating the normal set mean spacing within an error bandwidth of $\pm 20\%$ at the 80% confidence level, the samples will need at least 41 data points. For the case of an error bandwidth of $\pm 10\%$ at the 90% confidence level, at least 271 data of the set will be needed

3.3.4 Normal Set Spacing of The El Teniente Discontinuities

The mean normal discontinuity set spacing, arithmetic and geometric, considering all discontinuities, was estimated for all mapping scales and sectors (Table 3.4). As an example, in order to reduce size effect of class interval width and its effect on calculations (class interval width Δ in Figure 3.10), the geometric mean spacing was estimated fitting the negative exponential function on the cumulative probability distribution (Einstein and Beacher, 1983). The equation used was:

$$F(x) = 1 - e^{-\lambda x} \quad \text{For } x > 0 \text{ and } \lambda > 0 \quad (3.15)$$

where x is the observed spacing and λ is the mean discontinuity frequency.

The mean normal set spacing for faults could be estimated only using data from drive mapping and interpreted major structures. The results from drive mapping presented in Table 3.4 are consistent with previous and current analyses in other mine sectors (see Brzovic, 2001, and new data in Section 7.2.1), and with the published data of 9.7 meters as the mean of the *total spacing*³ obtained from several (differently oriented) scanlines within mine drives at the El Teniente mine (Brooks et al., 1996).

In addition, the spacing data are strongly influenced by the truncation level used, as shown Figure 3.12. This figure includes the mean normal discontinuity set frequency⁴ (all sets) estimated for all data collected by all line sampling techniques. The frequency is plotted against the truncation bias length used on each sampling technique.

³ see Spacing definition in section 3.3.1.

⁴ Inverse of mean normal discontinuity set.

Table 3.4. Arithmetic and Geometric mean normal set spacing for discontinuity type sets at the El Teniente primary copper ore.

Discontinuity type	Sectors Studied	Mapping scale	Set number	Dip/Dipdir	Poles	Arithmetic		Poles used	Max-Min (m)	Poles in vertical lines	Negative Exponential Distribution
						Mean (m)	S.D. (m)				Mean (m)
FAULTS	Hw	Major Structure*	Set 1	89/183	13	22.2	14.3	8	50.0-6.0	-	-
			Set 2	74/316	6	29.8	11.4	6	50.9-20.2	-	-
		Drive Mapping	Set 1	82/174	18	3.0	4.9	12	15.5-0.05	-	-
			Set 2	76/316	11	23.4	8.8	6	33.7-9.0	-	-
	Fw	Major Structure*	Set 1	86/199	13	28.1	12.9	10	49.9-7.0	-	-
			Set 2	85/162	9	20.7	9.7	5	36.9-12.0	-	-
		Drive Mapping	Set 1	84/203	31	8.9	10.7	23	47.3-0.04	-	7.73
			Set 2	84/144	22	5.6	4.4	15	12.3-0.4	-	5.46
VEINS[†]	Hw	Scanline Mapping	Set 1	86/182	178	0.419	0.594	159	3.872-0.007	12	0.308
			Set 2	82/282	145	0.330	0.362	128	2.622-0.009	10	0.319
			Set 3	12/251	168	0.230	0.241	147	1.456-0.001	106	0.218
		Oriented Core Logging	Set 1	81/359	208	0.062	0.070	204	0.505-0.001	-	0.057
			Set 2	89/270	110	0.125	0.139	103	0.911-0.010	-	0.118
			Set 3	55/180	81	0.145	0.151	78	0.931-0.002	-	0.140
	Fw	Scanline Mapping	Set 4	52/260	150	0.088	0.088	145	0.530-0.005	-	0.087
			Set 1	83/192	119	0.326	0.311	108	1.423-0.011	5	0.327
			Set 2	68/251	63	0.329	0.318	56	1.231-0.014	1	0.319
			Set 3	25/212	67	0.353	0.313	54	1.335-0.024	34	0.365
		Oriented Core Logging	Set 4	74/301	51	0.320	0.466	41	1.525-0.005	6	0.200
			Set 1	68/192	204	0.059	0.050	195	0.297-0.006	-	0.064
			Set 2	80/293	221	0.069	0.061	206	0.350-0.004	-	0.073
			Set 3	66/005	71	0.151	0.270	67	1.410-0.007	-	0.091

Notes *: from interpreted mayor structures. S.D.; standard deviation. †; fault were included in this calculation, but since these only represent a few amount, it does not change the estimates.

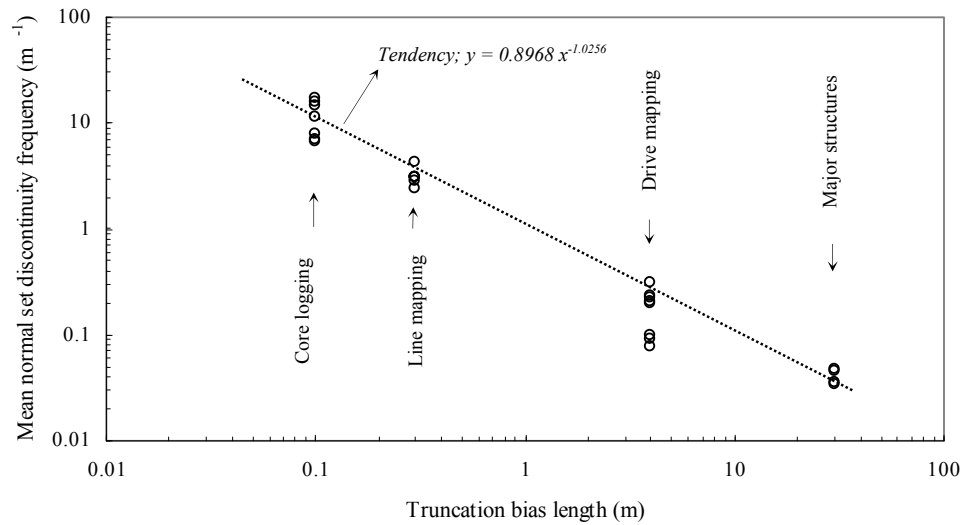


Figure 3.12.- Discontinuity frequency and truncation bias length.

It appears that the normal discontinuity set spacing increased considerably as the sampled discontinuity trace length was increased. Data collected using small core diameter presented in Section 3.9 confirms this relationship between the sampling regime and the estimated frequency. Additionally, assuming that each truncation level applied represents a mapping scale; the mean normal discontinuity set frequency may be represented as a fractal feature within the rock mass.

A fractal set can be defined as (Hoobs, 1993):

$$N_i = c r_i^{-D} \quad (3.16)$$

where N_i is the number of lineal objects with a linear dimension r_i , and D is the fractal dimension by definition, and c is a constant of proportionality. This fractal feature can be represented by a constant of proportionality $c=0.8968$, and a fractal dimension $D= -1.0256$ (Figure 3.12).

Scaling law properties (fractal and lineal) for the spacing on other parameters of the geological discontinuities have been proposed by several authors (Hoobs, 1993, Gillespie et al., 1993, Cladouhos and Marret, 1996, Scholz, 2002), and these are consistent with this finding. Although it is not argued whether the Poisson or the fractal process better describes the nature of fractures within the rock mass, for

practical purposes in rock mass characterization at the mine site, is important to recognize that the truncation bias used during data collection plays a relevant role in the results obtained.

A similar graph was created using data for each discontinuity type (Figure 3.13), which also shows a similar trend for discontinuity spacing.

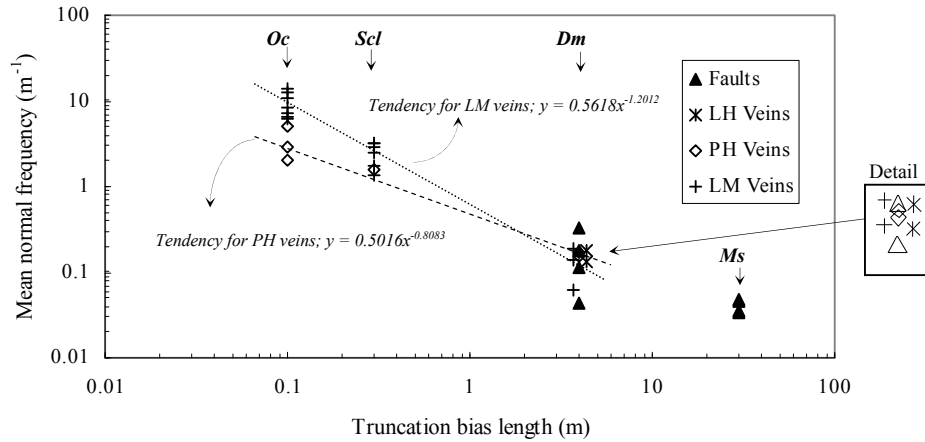


Figure 3.13.- Discontinuity frequency and truncation bias length per discontinuity type. (*Oc*; oriented core logging. *Scl*; line mapping, *Dm*; drive mapping. *Ms*; interpreted major structures).

Furthermore, using the proposed discontinuity frequency diagram, the three-dimensional loci (Hudson and Priest, 1983), the global maxima and minima and their orientations for discontinuity frequencies were estimated for both sectors (Table 3.5).

Table 3.5. Extreme values of discontinuity frequency and their orientations.

Sampling method	Global type	Andesite Hw		Andesite Fw	
		Discontinuity frequency (m ⁻¹)	Trend/Plunge	Discontinuity frequency (m ⁻¹)	Trend/Plunge
Line mapping	Maxima	6.53	062/48	8.82	064/34
	Minima	2.34	197/07	2.23	257/68
	Mean	4.97		5.74	
	Coef. of variation	17%		25%	
Oriented Core logging	Maxima	29.70	036/17	28.56	342/02
	Minima	8.69	280/05	4.61	225/65
	Mean	19.32		16.90	
	Coef. of variation	26%		32%	

This table also includes the mean discontinuity frequency as the average values obtained from more than 8000 equidistant directions (or points⁵) in the stereonet. This mean value would represent the discontinuity frequency normalized with respect to the orientation at this location. The true three-dimensional loci diagram using data collected in scanline mapping from *Fw* sector is presented in Figure 3.14

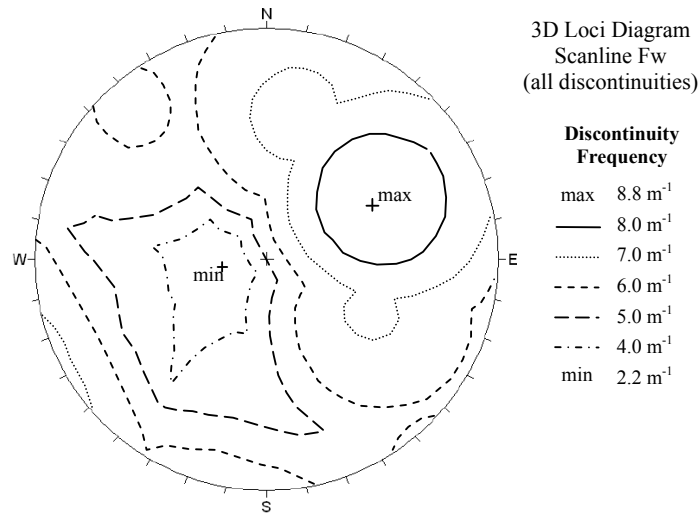


Figure 3.14.- 3D loci of discontinuity frequency diagram (data is from line mapping andesite Fw).

The data presented in Table 3.5 confirms the strong influence that the truncation bias plays in the discontinuity frequency gathered from a rock mass. It also shows that, in terms of average orientations, both sectors are quite similar when considering the same mapping scale, but minor differences appear when comparing the same sectors at different mapping scales. Although real, appreciable differences in ground behaviour are experienced within the two sectors, the data in Table 3.5 show negligible differences between the andesite sectors when all discontinuity types are considered.

As an illustration, some histograms with normal set discontinuity spacing distributions for different veins types and mapping scales are presented in Figure 3.15.

⁵ The maximum and the minimum represent two single orientations or point in this diagram.

Because the data suggests a fractal characteristic for discontinuity spacing, reliability of the estimates following either approaches of Sen and Kazi (1984) nor Priest and Hudson (1981) could not be readily applied. However, the practical rule of 20 times the mean spacing for the sample length (Sen and Kazi, 1984) has been satisfied for most sampling populations used, specially for the small scale sampling (line mapping and oriented core logging).

In addition, using traditional scanlines at the mine site (i.e., using the pre-established mapping approach to collect data that ignore tightly healed veins, in Section 2.6.2) the *total spacing* measured at the same structural domain ranged from 0.9 to 4.8 (Brzovic, 2001). These measurement could be affected by the degree of the overbrake that mine wall drives presented after excavations. In the present research, using the enhanced scanline method, the measurement of *total spacing* ranged from 3.6 to 6.5, which may represent an increment of 40% on data collected using traditional scanlines.

The observed spacing data suggests that rock masses of primary copper ore at the El Teniente mine consist of assemblage of thousands of small intact rock blocks bounded by veins (LM and HP veins at a scale approximately of 0,1 to 5 meters, and LH veins at a scale of approximately 1 to 5 meters) and widely space faults contact. This rock mass feature is consistent with both its strong competence and its high grade ore resources.

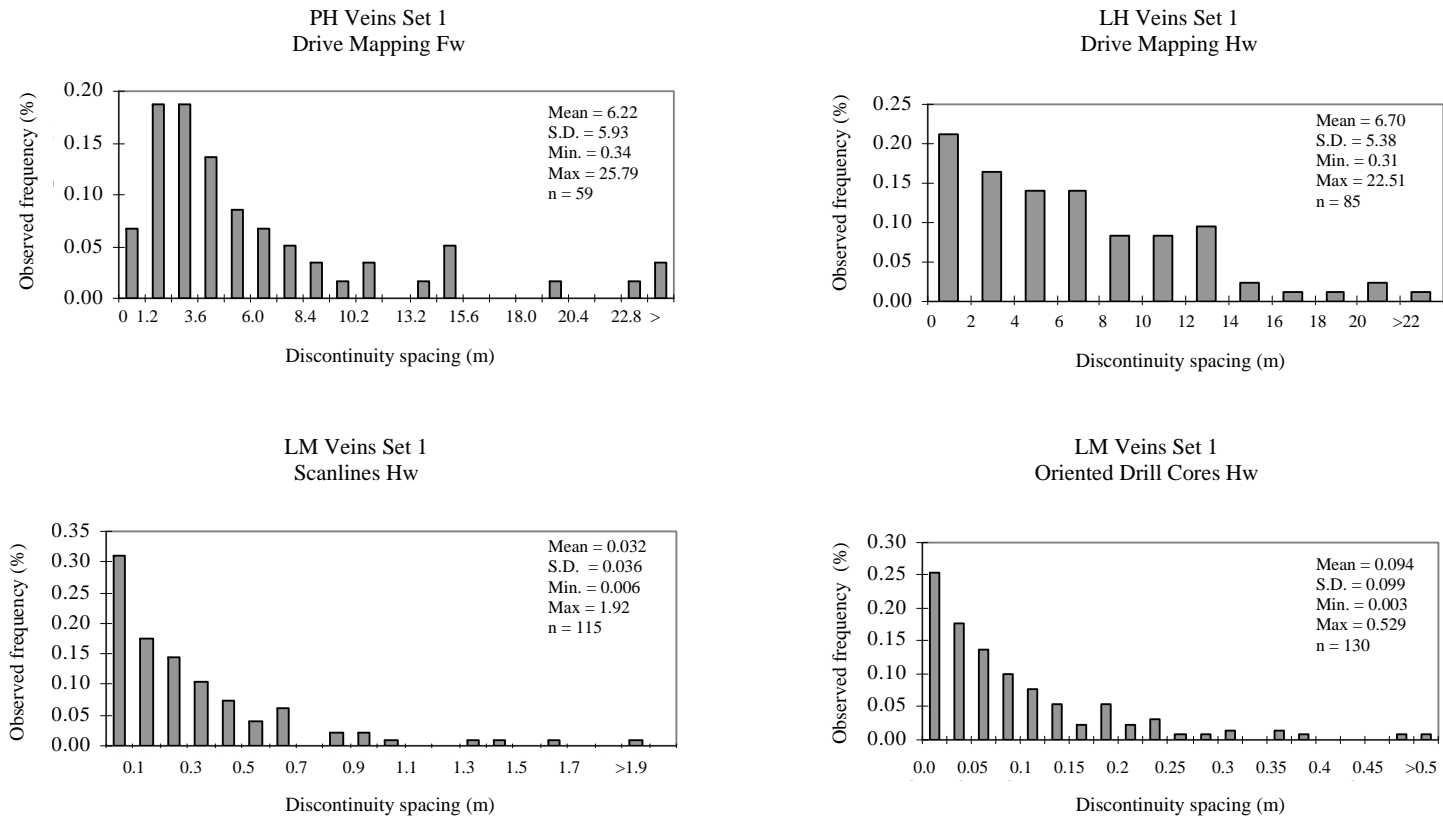


Figure 3.15.- Observed spacing of discontinuity sets.

3.4 Persistence

Persistence is sometimes referred to as continuity or discontinuity size, according to the ISRM (Brown 1981, p.5). It is the discontinuity trace length observed in a rock exposure, or the measurable length of the linear trace formed by the intersection of the discontinuity with the planar excavation in rock (Figure 3.16). Persistence is also referred as the areal extent of the discontinuity plane, however complete areal exposure rarely can be observed. Discontinuity size is one of the most difficult rock mass parameter to determine, because it is a three-dimensional entity, whereas observations of trace length in outcrops or excavation wall are made at best two dimensions. Therefore, sampling biases are introduced during data collection.

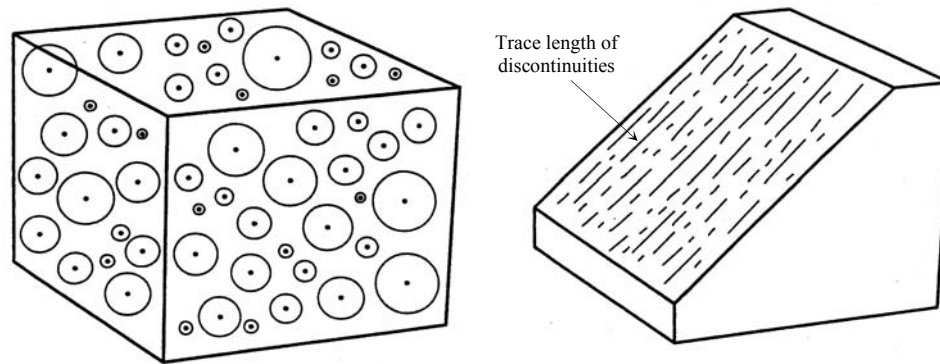


Figure 3.16.- Discontinuities as circular disc a within rock mass (left), and their observed trace length (l) on a particular rock exposure (right), after Windsor (1977).

3.4.1 Background

The simple estimation of the mean discontinuity trace length of a discontinuity set is the arithmetic mean of the all trace lengths sampled. The arithmetic mean trace length, \bar{l} , is given by (Priest and Hudson 1981):

$$\bar{l} = \sum_{i=1}^n \frac{l_i}{n} \quad (3.17)$$

where l_i is the i^{th} discontinuity trace length sampled on a planar surface, and n is the total number of sampled trace length.

Unfortunately, this arithmetic mean is not an accurate reflection of the true mean value of the discontinuity size, basically because both the bias associated with the sampling regime adopted during data collection (discussed in Section 2.4) and the assumption of the discontinuity model. A hypothetical model of discontinuities embodies a number of assumptions such as the topology, shape and sizes of the discontinuities.

The topology of a discontinuity concerns the equation of its surface. It has been generally assumed to be planar for most researchers (Warburton, 1980, Priest and Hudson, 1981, Kulatilake and Wu, 1984, Villaescusa and Brown, 1992, Priest, 1993, Mauldon and Mauldon, 1997, Zhang and Einstein, 2000), but in the reality it is not necessarily true (see Pollard and Aydin, 1988). The shape of the discontinuity has also been assumed as a circular disc of negligible thickness in order to simplify its analysis.

The assumptions regarding topology and shape of discontinuities are related to each individual discontinuity; however the size of the discontinuities and their spatial distribution is concerned with their population. The discontinuity size can be an expression of its probability density distribution, which can follow, for example, either a negative exponential or a lognormal *pdf*. These models of size distribution assume that the centres of areas of the discontinuities are distributed volumetrically within the rock mass in a particular fashion, which for simplicity is usually assumed to obey a three dimensional Poisson process. In this respect and for area sampling, the size distribution of discontinuities, which are assumed to be flat circular disc of negligible thickness, parallel to each other with centre location randomly and independently distributed in space (Poisson process), can be estimated as (Warburton, 1980):

$$f(l) = \frac{1}{\mu_D} \int_l^{\infty} \frac{g(D)dD}{\sqrt{D^2 - l^2}} \quad (3.18)$$

where D is the diameter of discontinuities, l is the trace length observed on a planar surface of infinite size, $g(D)$ is the *pdf* of the diameter of discontinuities with a mean value μ_D , $f(l)$ is the *pdf* of the true trace length of discontinuities with a mean value

μ_l . In other words, the observed discontinuity trace length on the sample surface depends on their size distribution.

In order to use equation 3.18 to estimate the joint diameter distribution $g(D)$, the true trace length distribution $f(l)$ should be known first. However, the sampling regime only allow to determine the *pdf* of the measured trace length on a finite exposure $g(l)$ (with a mean value $\bar{l} = \mu$), which is subjected to sampling bias. For example, truncation bias and censoring level may exclude small and large discontinuities of the true $f(l)$ respectively, large discontinuities are more likely to intersect both the rock exposure and the line sampling as well.

Therefore, in order to estimate $g(D)$, it is necessary to infer $f(l)$ from the $g(l)$. Several researcher have assumed and inferred properties of $f(l)$ based on the observed characteristic of $g(l)$. For instance Kulatilake (1993) assume that $f(l)$ and $g(l)$ have the same form and the same standard deviation ($\sigma_l = \sigma$). Zhang and Einstein (2000) not only assume that $f(l)$ and $g(l)$ have the same form, but also the same covariance ($\sigma_l/\mu_l = \sigma/\mu$). Villaescusa and Brown (1992) have proposed a method to estimate $f(l)$ from the $g(l)$ (using scanline sampling) by solving the maximum likelihood estimator (Laslett, 1982) for discontinuity size. Zhang and Einstein (2000) have extended this estimator to be used with data collected using finite circular windows.

Alternative methods to estimate the mean trace length μ_l of $f(l)$ are described by Priest and Hudson (1981), Pahl (1981) and Kulatilake and Wu (1984). Priest and Hudson (1981) proposed a method for estimating the distribution of the trace length, the distribution of the semi-trace length, and the distribution of the censored semi-trace length that intercept a randomly located linear survey. This methodology is applicable to censored discontinuities measured at exposures with limited extent.

Pahl (1981) have proposed a technique for the estimation of mean trace length where knowledge of both the actual trace lengths and the trace length function distribution is not required. Based on the assumption of topology, shape and size of discontinuities, the author has derived an expression to determine μ_l using data collected in window mapping, where censored and truncation are applied. Kulatilake and Wu (1984) extended the Pahl's method to a set whose orientation is described by a probabilistic distribution.

Finally, $g(D)$ is estimated from $f(l)$ based on analytical relations between the mean μ_l and the standard deviation σ_l of $f(l)$, and the mean μ_D and the standard deviation σ_D of $g(D)$ (see Villaescusa, 1991, Zhang and Einstein, 2000).

An example of the corrected discontinuity size estimated from observed, censored discontinuity trace length $g(l)$ at the El Teniente mine is presented in Figure 3.17 (from Villaescusa, 1991).

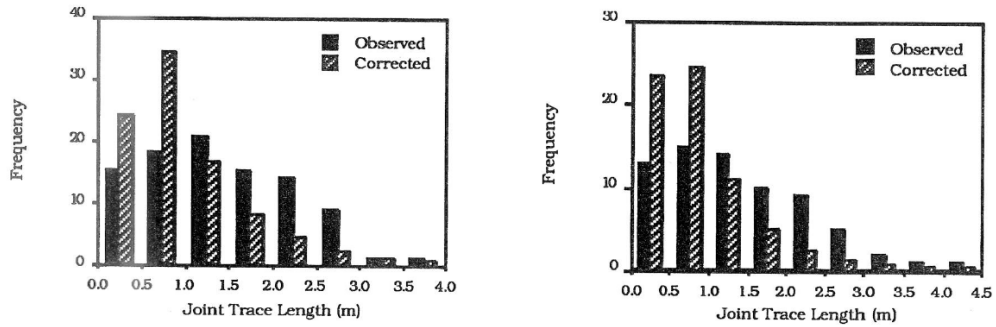


Figure 3.17.- Observed and corrected discontinuity size at the El Teniente mine (Villaescusa, 1991)

Assuming a volumetric Poisson distribution process for the discontinuity centre location, λ_{vi} (volumetric joint density), the observed joint density, λ_{Li} , or discontinuity occurrence of set i for impersistent discontinuities in a line sampling is estimated as follow (Warburton, 1980);

$$\lambda_{Li} = \frac{1}{4} \lambda_{vi} \pi \cos \delta_i \mu_2 \quad (3.19)$$

where δ_i is the angle between the orientation of the sampling line and the unit normal to the mean set i , and μ_2 is the second moment of the joint diameter distribution $g(D)$. It is interesting to note that covering exposure bias observed at the El Teniente mine drive may affect measurement of λ_{Li} , and calculations of both $g(D)$ and λ_{vi} .

In the current research, no specific bias corrections were made to estimate the true trace length of the discontinuities. Yet, data analysis of the measured trace length distribution on a finite exposure $g(l)$ is presented. For most joint size distributions, the mean value μ of $g(l)$ is always greater than the mean μ_l or μ_D (Priest and Hudson, 1981). Then, the mean value μ may be considered the upper bound or the true mean size.

3.4.2 Termination

In defining a rock block within the rock mass, the type of discontinuity termination may be very important. The ISRM (Brown, 1981) has suggested a *termination index* T_r , which is given by:

$$T_r = \frac{100N_r}{N_r + N_o + N_j} \% \quad (3.20)$$

where the N_r is when the discontinuity end in intact rock, N_o in another discontinuity, and N_j when the termination cannot be observed (obscured). A similar notation is presented in Figure 2.9.

A large value of T_r indicates that most discontinuities terminate in intact rock, and the rock blocks within the rock mass contain many intact rock bridges resulting in different block interlocking, perhaps a in different rock mass quality (Figure 3.18).

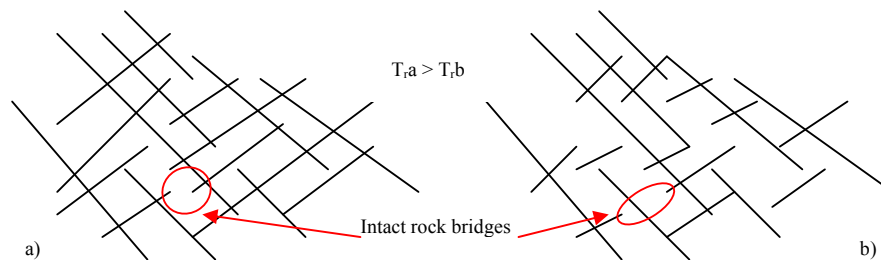


Figure 3.18.- Influence of termination in rock block definition.

Although termination data were collected during scanline mapping, the termination index has not been calculated. It is believed that the high discontinuity occurrence of veins within the rock mass, lead to a low probability of intact rock bridges in the rock block definition during fragmentation, which was observed in caved rock blocks studied in Chapter 4.

3.4.3 Observed Trace Length of the El Teniente Discontinuities

The trace lengths of discontinuities were mainly measured during line mapping, which used a truncation bias of 0.3m. The exposed trace length of the interpreted major discontinuities was also measured and is presented in Figure 3.19. Data

presented in this figure were measured only in faults, and reflect their size characteristics as the longest discontinuities observed at the mine site.

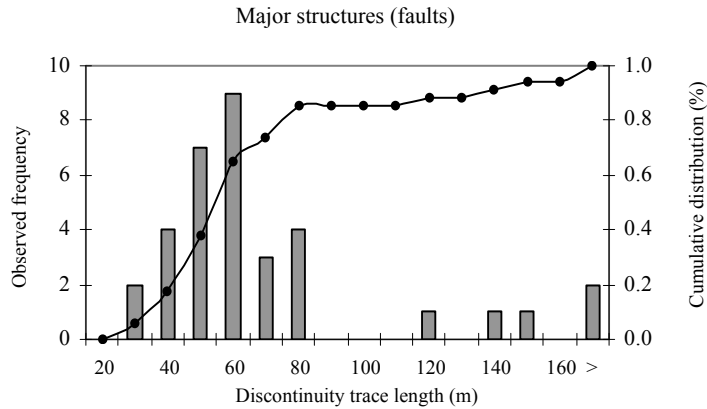


Figure 3.19.- Observed trace length of major faults.

A more detailed data analysis of the observed trace length per discontinuity type considering discontinuity endpoint features is presented in Table 3.6 and in Figure 3.20.

Prior to discussing data from Table 3.6 and in Figure 3.20, some conclusions regarding discontinuity trace length can be drawn from the discontinuity occurrence and spacing data presented in Table 3.1, Figure 3.8 and Figure 3.13. These figures show that the occurrences of discontinuities types vary substantially based on the truncation bias length used during sampling design, even for a same discontinuity orientation set. The data suggest different size characteristics for vein types and faults. In this respect fault and LH veins may represent the longer discontinuities.

Data presented in Table 3.6 and in Figure 3.20 also suggest that PH veins tend to be statistically longer than LM veins. For both vein types, the data were affected by the same sampling biases, but PH veins have lower abundance of both shorter trace length (< 1.5m) and contained discontinuities than LM veins.

Table 3.6. Arithmetic mean of the observed trace length in scanline mapping for discontinuity type sets.

Discontinuity type	Set number	Sectors Studied	Dip/ Dipdir	n	Observed Trace length for endpoint types						
					Contained (type 2)			Intersecting (type 1)			Transecting (type 0)
					n (%)	mean (m)	S.D. (m)	n (%)	mean (m)	S.D. (m)	n (%)
Faults	Not defined	Hw		10	3 (30%)	2.47	2.23	2 (20%)	7.00	1.41	5 (50%)
		Fw		23	6 (26%)	1.50	0.91	6 (26%)	2.15	0.43	11 (48%)
	Total & Mean			33	9 (27%)	1.82	1.31	8 (24%)	3.36	2.34	16 (49%)
LH Veins	Not defined	Hw		11	4 (36%)	0.60	0.14	5 (45%)	2.52	1.22	2 (18%)
		Fw		15	4 (27%)	1.88	0.53	9 (60%)	2.42	1.45	2 (13%)
	Total & Mean			26	8 (31%)	1.24	0.77	14 (54%)	2.46	1.33	4 (15%)
PH Veins	Set 1	Fw	73/198	39	12 (31%)	1.59	0.62	26 (67%)	2.23	0.75	1 (3%)
	Not defined	Hw		26	12 (43%)	2.62	1.11	14 (50%)	2.46	1.21	2 (7%)
		Fw		35	18 (51%)	1.49	0.70	15 (43%)	2.22	1.09	2 (6%)
	Total & Mean			102	42 (41%)	1.84	0.94	55 (54%)	2.29	0.96	5 (5%)
LM Veins	Set 1	Hw	85/175	115	54 (47%)	1.28	0.87	60 (52%)	2.06	0.86	1 (1%)
		Fw	85/191	50	25 (50%)	1.02	0.43	22 (44%)	1.85	0.45	3 (6%)
	Set 2	Hw	85/282	121	78 (64%)	1.01	0.76	39 (33%)	1.78	0.84	4 (3%)
		Fw	74/301	58	33 (57%)	1.20	0.59	24 (41%)	1.92	0.69	1 (2%)
	Set 3	Hw	16/252	117	88 (75%)	1.41	1.02	26 (22%)	3.03	2.35	3 (3%)
		Fw	48/244	61	40 (66%)	1.57	1.73	19 (31%)	2.08	0.90	2 (3%)
	Not defined	Hw		111	62 (56%)	1.00	0.55	44 (40%)	1.93	1.18	5 (5%)
		Fw		42	27 (64%)	0.76	0.37	14 (33%)	1.96	0.89	1 (2%)
Total & Mean			675	407(60%)	1.19	0.93	248(37%)	2.06	1.17	20 (3%)	

Note; there was not set definition in several cases with either few or scatter data. S.D.; standard deviation.

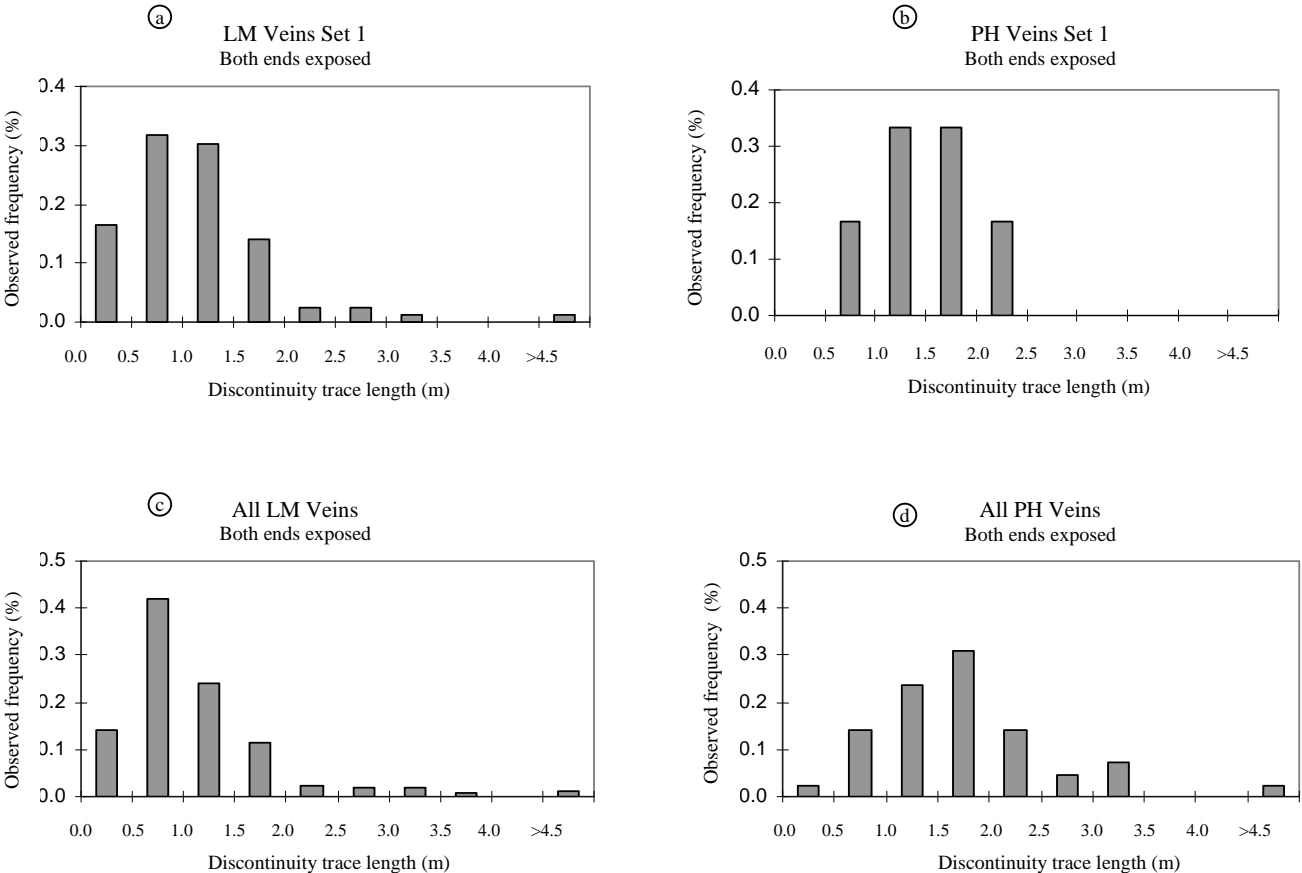


Figure 3.20.- Probability distribution of the observed trace length with both ends exposed.

The observed trace length distributions of all sets of LM have similar mean value, even between sampling sectors, and similar to the mean of all veins collected. Again, although sampling biases has not been corrected, data may suggest that the all LM veins have the same discontinuity size properties throughout the mine sector. Villaescusa (1991, p.181) has suggested a lognormal distribution for discontinuity size for most discontinuity sets at the Reno mine sector (sample line location in Figure 2.4), where the most likely mean trace length σ_D was also estimated. These values ranged between 0.10 and 0.36 meters for all discontinuity sets. Vein types were not differentiated in Villaescusa's work, but according to Table 3.1, it is believed that most discontinuity collected in that study were LM veins.

If all discontinuity sets have similar discontinuity size characteristics for an assumed circular disc shape (Warburton, 1980), then an average value of their observed trace length distribution might be a good representation of the $g(l)$ as presents Figure 3.21.

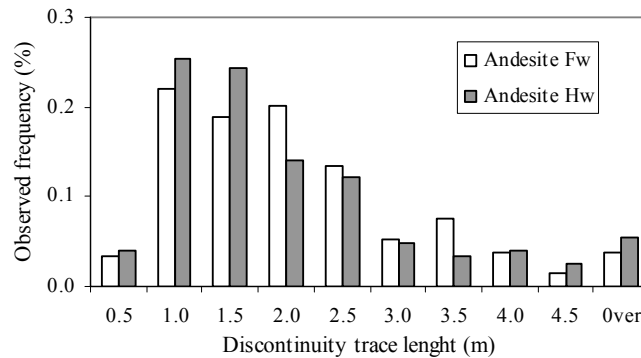


Figure 3.21.- Observed veins discontinuity trace length distribution.

The data found in the present research may suggest that the discontinuities observed within rock masses of primary copper ore at the El Teniente mine have a small true mean discontinuity size and/or a very high volumetric joint density.

3.5 Discontinuity Infill

The material that separates adjacent rock wall of the discontinuity is called filling according to ISRM (Brown 1981, p.6). This material is usually weaker than the

parent, adjacent rock. The parallel distance between these adjacent rock walls is termed the width of the filled discontinuities.

At the El Teniente mine, most discontinuities within the primary rock mass are healed veins filled with a mineralogical assemblage. Consequently, veins are not pathways (impermeable). The faults are also discontinuities filled with a mineralogical assemblage, but they are not healed, because their most recent movements occurred after and/or simultaneously with the mineralisation process. All faults have slickensides and/or gouge, and some major faults have signs of water percolation in form of deposition of copper and iron oxides (Figure 1.11). In the current study the filling is referred as infill.

The infill observed in veins was studied by a quantitative estimation of their mineral composition. For instance, a vein could be described as containing 25% of quartz, 50% of chalcopyrite and 25% of anhydrite. This quantitative infill description was only undertaken at the small sampling scales, i.e., during line mapping and oriented drill core logging.

3.5.1 Infill of the El Teniente Discontinuities

The results show that more than 9 mineral species were present as vein infill. Rarely was one mineral present in all veins, and rarely did this mineral maintain the same proportion of abundance as infill throughout all veins. In fact, some particular mineral composition and associated alteration halos have been used to classify vein types at the El Teniente ore deposit (Cuadra, 1986). For instance, the occurrence of chalcopyrite observed in PH veins from oriented core logging is presented in Figure 3.22. It is clear that the occurrence of chalcopyrite as infill varies from 0 to 100% in HP veins.

However, four main mineral species were found to be the most common and abundant in all veins recognized during this study; chlorite, anhydrite, chalcopyrite and quartz (Table 3.7 and Table 3.8).

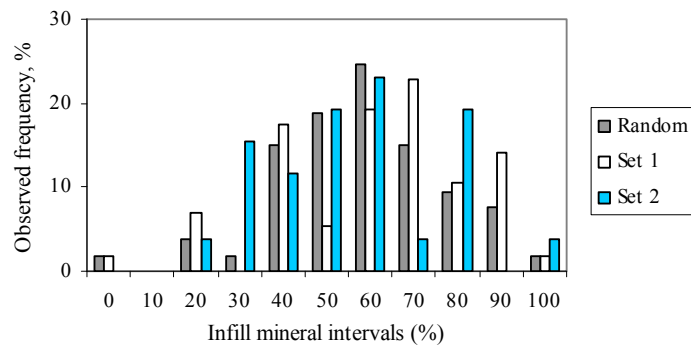


Figure 3.22.- Chalcopyrite as infill distribution within PH veins observed in oriented cores logging (Fw sector.)

Table 3.7. Percentage of mineral species (more abundant ones) observed as infill within all veins, per data collection technique and sectors

Sampling method	Sector	Data	Proportion of veins having the mineral specie as infill (%)						
			Molybdenite	Chlorite	Biotite	Anhydrite	Chalcopyrite	Pyrite	Quartz
Line mapping	Hw	511	6.5	52.8	12.3	71.2	80.2	3.1	91.8
	Fw	296	6.4	58.4	12.8	84.8	94.6	17.9	86.8
Drill core logging	Hw	604	5.6	38.1	22.5	18.7	80.0	2.5	94.9
	Fw	554	3.1	67.5	25.4	70.6	96.6	31.9	86.3

Table 3.8. Mean of mineral species observed as vein infill per data collection technique and sectors.

Sampling method	Sector	Data	Mean of mineral specie observed as vein infill (%)						
			Chlorite	Biotite	Anhydrite	Chalcopyrite	Pyrite	Quartz	Other
Line mapping	Hw	511	6.8	1.7	17.4	13.0	0.2	56.5	4.4
	Fw	296	10.0	1.6	21.7	29.7	2.8	31.5	2.7
Drill core logging	Hw	604	5.5	5.0	2.6	13.0	0.3	68.9	4.7
	Fw	554	13.2	3.7	16.5	26.8	3.9	32.4	3.5

In term of the vein infill (Table 3.8), no substantial differences could be observed between veins from the same mapping sector (*Hw* and *Fw*) but from different mapping scale. These results, as should be expected according to the main alteration zones (LH and HP), suggest that the visual estimates of the mineralogical infill have been undertaken with enough accuracy to achieve repeatable results.

In addition, variability of the vein infill between veins sets can be observed from Table 3.9 (sets showed in Figure 3.6). In this table, it shows that similar infill mineralogy with little variability is observed for all sets, and the individual values are

similar to the mean of the sector. However, as should be expected according to the main alteration zones (LH and HP), the mineralogical composition was found to have some particular differences between andesite sectors (*H_w* and *F_w*).

Table 3.9. Mean of mineral species observed as vein infill per family sets in line mapping.

Sector	Set	Data	Mean of mineral specie observed as veins infill (%)						
			Chlorite	Biotite	Anhydrite	Chalcopyrite	Pyrite	Quartz	Others
<i>H_w</i>	Random	30	5.2	2.3	16.7	8.2	0.6	61.5	5.5
	Set 1	173	6.1	1.5	17.0	13.6	0.2	55.8	5.8
	Set 2	142	8.8	2.5	23.9	13.1	0.4	48.3	3.0
	Set 3	166	6.2	1.0	12.4	13.2	0.2	63.3	3.7
	Total & mean	511	6.8	1.7	17.4	13.0	0.2	56.5	4.4
<i>F_w</i>	Random	17	15.0	0.6	30.3	18.6	0.6	32.4	2.5
	Set 1	104	7.6	2.1	21.9	31.4	4.2	30.2	2.6
	Set 2	62	14.0	1.3	25.3	25.2	2.0	30.9	1.3
	Set 3	65	9.1	1.3	18.5	33.6	0.2	35.1	2.3
	Set 4	48	9.4	1.7	17.8	30.6	5.3	30.1	5.0
	Total & mean	296	10.0	1.6	21.7	29.7	2.8	31.5	2.6

One important fact can be deduced from these tables. Assuming a representative sample size, the observed average infill assemblage does not vary significantly within the same sector, then it can be said that the average infill assemblage can be considered to have an isotropic characteristic within the rock mass. In others words, a linear sampling scheme will define the same average infill distributions at any discontinuity orientation. Furthermore, the infill features observed for each vein types, which are detailed in Appendix III.C confirm that finding. A summary of the infill characteristics per vein type are presented in Table 3.10.

Table 3.10. Mean observed infill mineral assemblage per discontinuity type.

Discontinuity type	Sector studied	Observed mineralogical assemblage as infill in discontinuities (%) (Range of mean percentage observed from oriented cores logging and scanline mapping)							
		Biotite	Chlorite	Anhydrite	Bornite	Chalcopyrite	Pyrite	Quartz	Molybdenite
LM Veins	<i>H_w</i>	2-6	5-7	3-18	2-3	8-9	1<	60-75	1<
	<i>F_w</i>	2-5	13-16	17-24	1<	17-20	1-2	38-40	1<
PH Veins	<i>H_w</i>	-	1	1-7	-	74-75	1-2	17-22	-
	<i>F_w</i>	1<	2-5	14-15	-	57-60	8-9	14-15	1<
		Gypsum	Chlorite	Anhydrite	Bornite	Chalcopyrite	Pyrite	Quartz	Ankerite
LH Veins	<i>All</i>	3-6	6-23	2-18	2-16	10-26	1-30	11-19	7-35
Faults	<i>All</i>	5-11	10-20	12-15	1-4	7-16	1<	5-14	4-21

Note; Chlorite includes sericite in faults.

Data in Table 3.10 confirms that vein types have a different mineralogical assemblage as infill (Cuadra, 1986), which in term of mean values may vary substantially between andesite sectors or hydrothermal alteration zones.

3.6 Aperture

Aperture is the perpendicular distance between adjacent rock walls of an open discontinuity, in which the intervening space is air or water filled (ISRM 1981, p.6). The ISRM has distinguished aperture from the term width in the case of filled discontinuities (Figure 3.23). At the El Teniente mine the majority of discontinuities are filled structures, therefore the term thickness will be used to describe the width of these discontinuities hereafter.

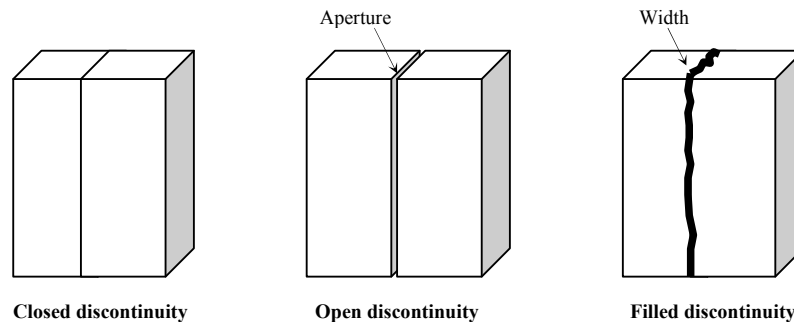


Figure 3.23.- Schemes illustrated the suggested definitions of the aperture and the width, after ISRM (Brown, 1981)

The thicknesses of the discontinuities were measured in all measurement techniques, and the data analysis is carried out with the mean value of two field observations, the maximum and minimum values (see Figure 2.13a).

3.6.1 Thickness of the El Teniente Discontinuities

Data analysis of observed thicknesses in faults from interpreted major structure and drive mapping considering all mine sectors is presented in Figure 3.24. It seems that the El Teniente's fault thicknesses observed in Figure 3.24 may follow a similar trend suggested by the literature, which proposed scaling law properties for fault parameters such as length, displacement and thicknesses of the gouge zone (Scholz,

2002). It is clear from Figure 3.24 that large faults at the El Teniente mine tend to exhibit large thicknesses.

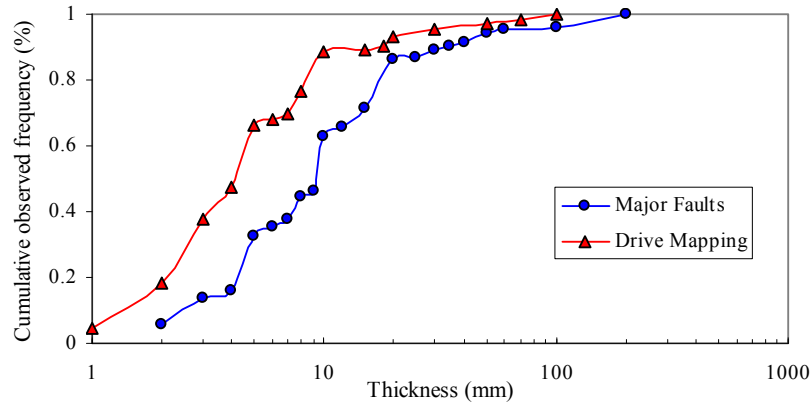


Figure 3.24.- Cumulative probability distribution of the observed thickness in major structures according to the mapping scale.

Data analysis of the vein thickness distributions showed that no appreciable differences between discontinuity sets in a sector mapped at the same scale. Similarly to veins infill, Table 3.11 shows almost the same vein thickness distributions for all set and between andesite sectors. The data in Table 3.11 are from scanline mapping and set definitions are presented in Figure 3.6. Discontinuity set thickness distributions considering each genetic type does not vary significantly within each sector, and between *Hw* and *Fw* sectors as well (see also Appendix II.D).

Table 3.11. Vein thickness distribution per family sets observed in scanline mapping.

Sector	Sets	Data	Thickness distribution observed (%)						Mean (mm)
			<1mm	1- <2mm	2- <3mm	3- <5mm	5- <10mm	≥10mm	
<i>Hw</i>	Random	30	16.7	56.7	10.0	6.7	3.3	6.7	1.9
	Set 1	172	13.4	40.1	19.8	18.6	7.0	1.2	2.0
	Set 2	139	10.1	61.9	10.1	8.6	5.8	3.6	1.9
	Set 3	165	12.7	45.5	15.2	12.7	6.1	7.9	2.5
	Total & mean	506	12.5	48.8	15.0	13.2	6.1	4.3	2.1
<i>Fw</i>	Random	17	23.5	58.8	11.8	0.0	0.0	5.9	1.5
	Set 1	104	14.4	51.9	14.4	13.5	4.8	1.0	1.7
	Set 2	62	19.4	51.6	16.1	11.3	1.6	0.0	1.4
	Set 3	65	4.6	50.8	21.5	15.4	6.2	1.5	2.1
	Set 4	48	20.8	33.3	20.8	18.8	4.2	2.1	1.9
	Total & mean	296	14.9	49.0	17.2	13.5	4.1	1.4	1.8

Similarly to discontinuity spacing, data in Table 3.12 suggest that the distribution of veins' thicknesses observed in line sampling was strongly affected by the truncation

level applied. Additional (thinner) discontinuities appeared as the truncation length value was decreased. In this table, data collected by small diameter un-oriented core logging (discussed in detail in Section 3.9.3 and 3.9.4) are included, and confirm this finding. These vein characteristics are in agreement with scaling law relationship between length and aperture (thickness) observed in vein systems in several different geological environments (Vermilye and Scholz, 1995, Johnston and McCaffrey, 1996).

Table 3.12. Vein thickness distribution occurrence observed in veins per data collection technique.

Sampling method	Truncation bias length	Data	Thickness distribution observed (%)					
			<1mm	1- <2mm	2- <3mm	3- <5mm	5- <10mm	≥ 10mm
Drive mapping	4m	342	-	5.5	11.7	41.9	25.4	15.5
Lines mapping	0.3m	802	13.3	48.9	15.8	14.9	4.2	2.9
Oriented core logging	0.1 m	1126	26.3	44.2	13.6	11.7	2.6	1.6
Un-oriented core logging	0.03m*	Many**	64.0	21.5	7.7	4.3	1.8	0.7

Note *: Mean obtained from 108 core section samples 6.1 metres long collected from multiple directions (in Section 3.9.3 and 3.9.4)

Furthermore, it has been suggested that the relationship between vein thicknesses (T or e) and trace length (L) may be represented as;

$$T=10^{-3} - 8*10^{-3}L \text{ (Vermilye and Scholz, 1995)} \quad (3.21)$$

or as;

$$L=10^2-2*10^2T^{0.8} \text{ (Johnston and McCaffrey, 1996)} \quad (3.22)$$

The veins data observed in scanlines mapping for these two parameters, when both discontinuity ends were exposed, are presented in Figure 3.25. In this figure veins interpreted as major structures are also included. Although, the data do not fit in to the proposed ranges, these suggest a relationship of this kind.

Two important facts can be deduced from all the data presented on veins thickness (Table 3.11 and Table 3.12, Figure 3.25, and data in Appendix II.D). Firstly, assuming a representative sample size, the observed vein thickness distributions can be considered to have an isotropic characteristic within the rock mass. That is, a linear sampling scheme will define the same thickness distributions at any discontinuity orientation. Secondly, longer discontinuities recognized at the El Teniente mine tend to be statistically thicker than shorter ones.

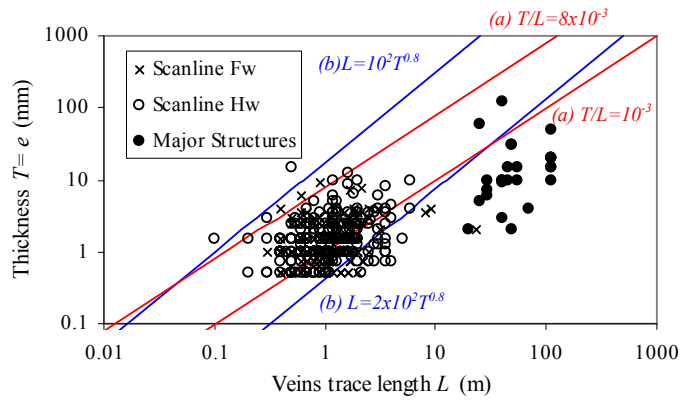


Figure 3.25.- Observed thickness and trace length relationship for veins. (a) range of the scaling law relationship suggested by Vermilye and Scholz (1995). (b) range of the fractal relationship proposed by Johnston and McCaffrey (1996).

In addition, the relationship between thicknesses and the mean of the infill in veins observed in data collected at the *Fw* sector is shown in Figure 3.26. It is shown that the average vein infill does not appear to vary with vein thickness. This finding suggests that sampling bias did not affect the mineralogical infill, and both sampling techniques may represent this feature with similar results.

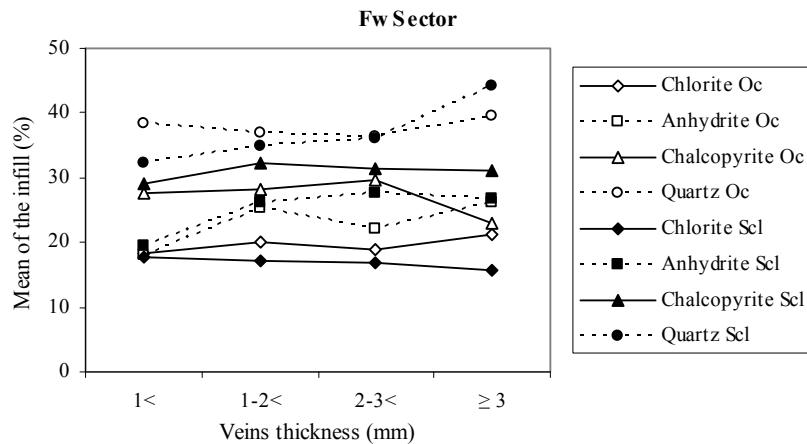


Figure 3.26.- Relation between thicknesses and the mean of the mineralogical infill in veins observed at the andesite *Fw* sector. (Oc; oriented core logging, Scl, scanline mapping).

Furthermore, the thickness profile along single veins normalized with respect to its observed trace length is presented in Figure 3.27 (Vermilye and Scholz, 1995). This figure shows that for over 70% of observed vein trace length the thickness profile is almost the same (assumed here as the “representative thickness value”), and only at

the vein tips the thickness abruptly decrease. Assuming this geometry to the El Teniente veins, the thickness observed of a single vein that cross a small diameter core sample has more likelihood to show this “representative thickness value (0.7)” than thickness of the tip (0.3).

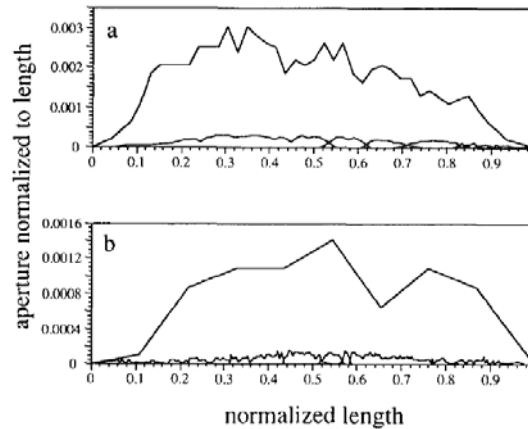


Figure 3.27.- Normalized aperture (thickness) distributions along single veins (after Vermilye and Scholz, 1995).

3.7 Roughness

Roughness is the inherent surfaces roughness and waviness relative to the mean plane of a discontinuity, according to the ISRM (Brown 1981, p.5).

3.7.1 Background

The discontinuity wall roughness is an important component of its shear strength (Figure 3.28), particularly when the discontinuity has not experienced any shear displacement or when both sides of the discontinuity are locked tightly together.

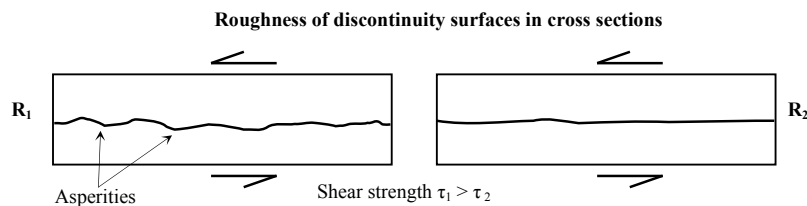


Figure 3.28.- Roughness and shear strength.

The importance of wall roughness decreases when the aperture, infill, thickness increases or when displacement has occurred (Brown, 1981). This is because:

- With increased aperture, the interlock between walls of discontinuities tends to disappear, and the small-scale asperities no longer provide any resistance to shear.
- With increased thickness of fill material, the shear strength then becomes an expression of the shear strength of the fill material itself.
- Previous displacements could have polished or damaged small asperities, and then a reduced resistance to shear could have resulted.

The term roughness of the discontinuity wall can be characterised by waviness or large-scale undulation, and by the unevenness or small-scale asperities. While the first one generally may affect the initial direction of the shear displacement, the unevenness may affect the initial shear strength of the discontinuity. In the last case the normal stress applied to the discontinuity orientation (effective normal stress) will affect the initial shear strength of the discontinuity by a dilation phenomenon. Dilation is a deviation of the horizontal displacement vector from the mean direction of the applied force, due to the overriding of surface irregularities (Bandis, 1990). In other words, during initial movements, re-accommodating of surfaces asperities occurs, which in some case may tighten the discontinuity.

Orientation and scale effect are important factors to consider with roughness profiles. The nature of roughness on the discontinuity surface may be different at different orientations. Consequently, it is important to characterise its orientation variations. In addition, Barton and Choubey (1977), and Barton et al. (1985) have demonstrated that the scale in which the roughness profile is measured is also a relevant factor in the discontinuity shear strength (Figure 3.29).

Different methods are available to measure surface roughness, such as the impression method, and the linear profile method, among others (see Brown, 1981). But the most common is the use of a simple descriptive method. The ISRM (Brown, 1981) has suggested nine descriptive terms to characterise the roughness of the

discontinuity surfaces (Figure 3.30), which can be used based on two scales of observation: Small scale (several centimetres) and large scale (several metres).

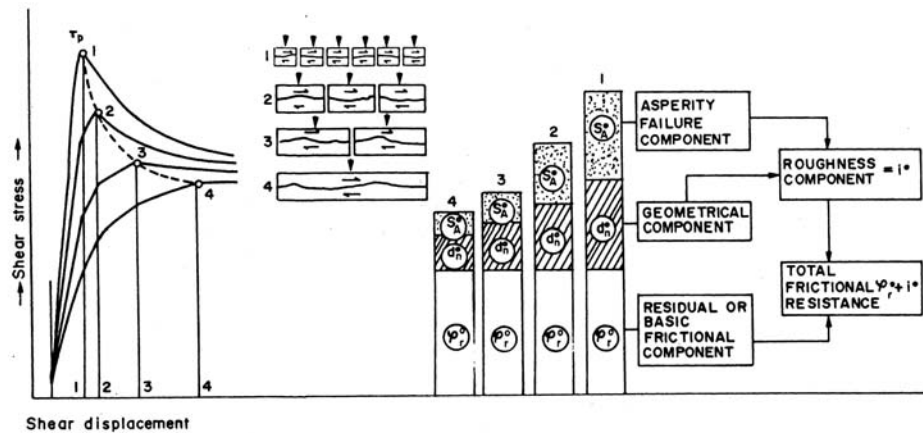


Figure 3.29.- Example of scale effect determining the discontinuity shear strength, after Barton et al. (1985).

The main objective during characterisation of a roughness profile is to facilitate the estimation of discontinuity shear strength. For example, Barton and Choubey (1977), and Barton et al. (1985) have proposed an empirical relation for the strength of rock joints based on roughness of surfaces and strength of the asperities, as follow:

$$\tau = \sigma_n \tan[JRC \log_{10}(JCS / \sigma) + \phi_r] \quad [\text{Pa}] \quad (3.23)$$

where τ is the shear stress, σ_n is the normal stress, JRC is the Barton's Joint Roughness Coefficient, which is a roughness profile that may be considered similar to this shown in Figure 3.30. JCS is the joint wall compressive strength, and ϕ_r is the residual friction angle (in Figure 3.29).

However, it is important to note that the discontinuity definition by ISRM (Brown, 1981) imply zero or low tensile strength (i.e., rock joints), which is not applicable to the majority discontinuities at the El Teniente mine. Most of them are healed veins cemented with strength infill mineral, therefore, the strength of these discontinuities would depend more of its infill features rather than to its roughness.

In the present study the suggested profile by ISRM has been utilised to characterise the small scale of roughness (20 centimetres). To characterise the large scale of

roughness (up to 4 meters), the five terms proposed by Laubsher (1990, 1993) have been used.

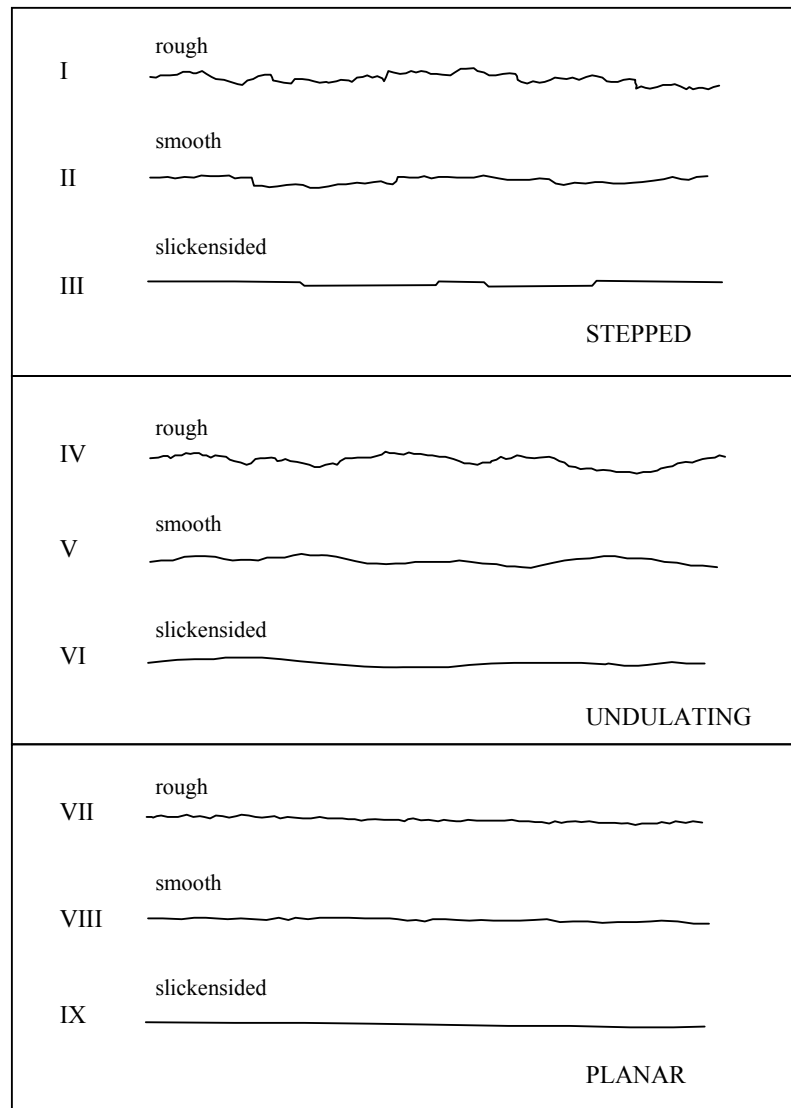


Figure 3.30.- Typical roughness profile and suggested nomenclature, after ISRM (Brown, 1981).

3.7.2 Roughness of El Teniente Discontinuities

Larger discontinuity surface exposure exists in mine drives compared to drill core, so roughness profile are from scanline mapping. The roughness profile was measured by visual inspection of the discontinuity surface using Figure 3.30. The results are presented in Table 3.13 and in Figure 3.31.

Table 3.13. Roughness of discontinuities sets observed in scanlines mapping at the El Teniente mine.

Discontinuity type	Set number	Sectors Studied	Dip / Dipdir	n	Small scale of Roughness by ISRM (Brown 1981), percentage of observations (%)									Large scale of Roughness (Laubscher 1993, p562), %				
					Planar			Undulating			Stepped			Straight	Slight undulation	Curved	Wavy	
					Polished	Smooth	Rough	Polished	Smooth	Rough	Polished	Smooth	Rough				One-dir.	All-dir.
Faults	Random	Hw		10	-	-	10.0	-	-	60.0	20.0	10.0	-	-	20.0	70.0	10.0	-
		Fw		23	-	-	13.0	39.1	4.3	34.8	4.3	-	4.3	13.0	39.1	39.1	4.3	4.3
	Total & Mean				33	-	-	12.1	27.3	3.0	42.4	9.1	3.0	3.0	9.1	33.3	48.5	6.1
LH Veins	Random	Hw		11	-	-	36.4	54.5	0.0	9.1	-	-	-	36.4	45.5	18.2	-	-
		Fw		15	-	7.1	7.1	42.9	7.1	35.7	-	-	-	6.7	53.3	40.0	-	-
	Total & Mean				26	-	4.0	20.0	48.0	4.0	24.0	-	-	-	19.2	50.0	30.8	-
PH Veins	Set 1	Fw	73/198	39	-	-	17.9	56.4	5.1	12.8	5.1	-	2.6	17.9	48.7	25.6	7.7	0.0
	Random	Hw		26	-	3.8	15.4	38.5	15.4	19.2	-	3.8	3.8	10.7	46.4	28.6	7.1	7.1
		Fw		35	-	-	17.1	62.9	8.6	11.4	-	-	-	17.6	50.0	32.4	-	-
	Total & Mean				100	-	1.0	17.0	54.0	9.0	14.0	2.0	1.0	2.0	15.8	48.5	28.7	5.0
LM Veins	Set 1	Hw	85/175	115	0.9	3.4	27.6	35.3	10.3	11.2	10.3	0.9	-	19.5	46.9	15.9	16.8	0.9
		Fw	85/191	49	2.0	-	22.4	42.9	12.2	12.2	6.1	2.0	-	22.9	47.9	20.8	8.3	-
	Set 2	Hw	85/282	122	1.6	7.4	20.5	21.3	17.2	21.3	9.0	1.6	-	17.2	40.2	29.5	13.1	-
		Fw	74/301	58	-	-	18.6	45.8	3.4	16.9	10.2	-	5.1	19.0	43.1	20.7	13.8	3.4
	Set 3	Hw	16/252	116	0.9	-	15.5	37.9	10.3	19.8	11.2	1.7	2.6	16.2	41.9	27.4	12.8	1.7
		Fw	48/244	61	-	1.6	14.8	45.9	9.8	19.7	6.6	1.6	0.0	20.0	40.0	33.3	6.7	-
	Random	Hw		110	-	4.5	25.5	36.4	7.3	10.0	11.8	1.8	2.7	20.7	46.8	15.3	14.4	2.7
		Fw		41	-	-	19.5	34.1	9.8	22.0	12.2	2.4	-	19.0	28.6	38.1	14.3	-
Total & Mean				672	0.7	2.8	21.1	35.8	10.5	16.3	9.9	1.5	1.3	18.8	42.6	23.9	13.1	1.2

Note: The term polished has been used instead slickenside in the roughness profile, as ISRM (Brown 1981) recommend. The term slickenside have to be used only when evidence of previous shear displacement has been observed.

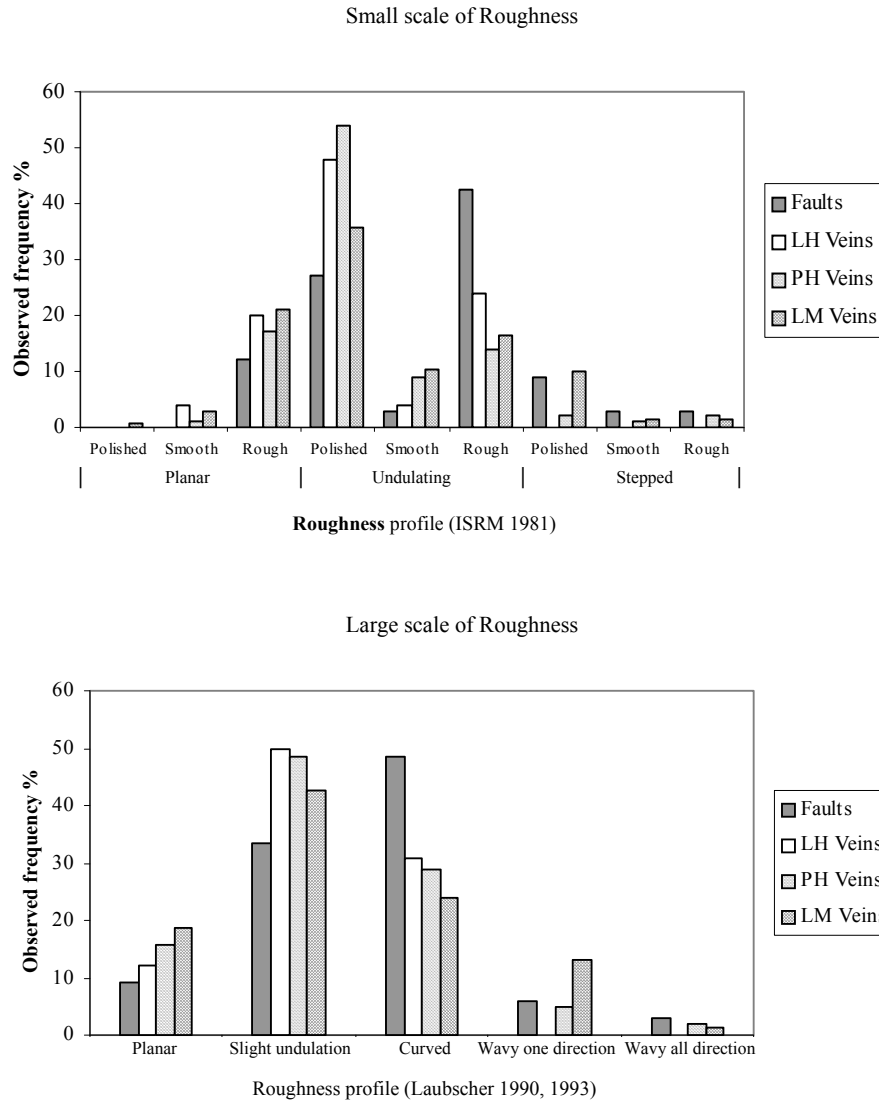


Figure 3.31.- Roughness and Planarity observed in discontinuity types.

These figures reveal clearly that for all discontinuity type at any sector, the small and large scale of roughness profile is practically the same. That is, undulating at small scale roughness and slight undulation at large scale roughness as main topologies of the discontinuities at the studied mine sectors.

3.8 Block Size

3.8.1 Background

Block size is one of the most important indicators of rock mass quality because it represents the degree of rock mass fracturing. The number of discontinuity sets, their spatial orientations, spacing, and persistence will determine the dimensions and shape of the rock blocks, which is usually referred as the in situ fragmentation. Block size coupled with shear strength characteristics of discontinuities will determine the strength of the rock assemble, and its mechanical behaviour during and following excavation. Block size may be defined by volume, surface area, or by a representative linear dimension.

Two main methods have been proposed to estimate the in situ block size; these may be described as deterministic and probabilistic methods. The first one estimates only an average size of rock blocks, and the second ones determine its size distributions.

The ratio RQD/J_n from the Q-System (Barton et al., 1974) has been used as an early approach to determine the block size. RQD is the rock quality designation (Deere, 1964) and J_n is the joint set number (both parameters are described in detail in Chapter 6).

The ISRM (Brown, 1981) has suggested describing the block size either by means of the average of the typical block, referred as *Block size index* (I_b), or by the total of number of discontinuities intersecting a unit volume of rock mass, referred as *Volumetric joint count* (J_v).

The Block Size Index I_b can be estimated by a simple observation in the field of the average dimension of block, or in some cases using the following equation:

$$I_b = \frac{S_1 + S_2 + S_3}{3} \text{ [m]} \quad (3.24)$$

where S_i is the i^{th} average modal set spacing (in meters). This equation, however may not give a realistic value of I_b when more than three discontinuity sets are present.

The Volumetric Joint Count J_v is defined as the sum of the number of joints per meter for each joint set present within rock mass. It is measured along the joint set perpendicular, and it is estimated as follows:

$$J_v = \frac{n_1}{L_1} + \frac{n_2}{L_2} + \dots + \frac{n_n}{L_n} \text{ [Joints/m}^3\text{]} \quad (3.25)$$

where n_i is number of joints along the sampling length L for each of n joints sets. Finally, J_v is linked to a descriptive term, which give an impression of the corresponding block size (Table 3.14).

Table 3.14. Block size and volumetric joint count, after ISRM (Brown, 1981).

Description	J_v (joints/m ³)
Very large blocks	<1.0
Large blocks	1-3
Medium-sized blocks	3-10
Small blocks	10-30
Very small blocks	>30

Note; Values of $J_v > 60$ would represent crushed rock.

Palmstron (1985) has linked the J_v with the RQD by an empirical equation as follow:

$$RQD = 115 - 3.3 J_v \quad (3.26)$$

From his work, he has developed a chart that quantifies the block size based on J_v for different block shapes. The volume of rock blocks is corrected by the angular relationship between discontinuity sets, for the general case when three semi-orthogonal discontinuity sets are present with rock mass. The equation is given by:

$$V = V_o x \frac{1}{\sin \alpha} x \frac{1}{\sin \beta} x \frac{1}{\sin \gamma} \text{ [meters}^3\text{]} \quad (3.27)$$

where V_o is the volume of rock when the discontinuity sets are orthogonally oriented, and α , β , and γ are the angles between discontinuity sets.

Assuming that the length of the intact rock between adjacent joints follows a logarithmic normal *pdf*, Sen and Eissa (1991) have demonstrated that RQD is not related to J_v linearly, i.e., Palmstron's equation 3.26 is applicable only for moderate values of RQD . Their work proposes determining block size using J_v and the *linear frequency* (λ_i) for each discontinuity sets, as follow:

$$V = \frac{1}{J_v} \left(\frac{1}{\lambda_{\tau 1} \lambda_{\tau 2}} + \frac{1}{\lambda_{\tau 1} \lambda_{\tau 3}} + \frac{1}{\lambda_{\tau 2} \lambda_{\tau 3}} \right) \quad [\text{meters}^3] \quad (3.28)$$

where J_v has particularly the dimension of m^{-1} . $\lambda_{\tau i}$ with $i=1$ to 3 represents the joint frequency measured in more or less orthogonal directions.

Equation 3.28 does not depend of the probability density distribution of the intact length. The Sen and Eissa's work also present charts that link the J_v , RQD and block volume for three main categories of rock block shapes.

Although deterministic methods may provide an early approach of the average block size, these estimates may be considered no reliable enough because the natural characteristics of the rock structure are not being taken into account in these calculations. A more accurate approach to assess the in situ fragmentation is to simulate the rock structure, which is currently referred as Discrete Fracture Network (DFN) modelling method.

In recent years, several discontinuity models and software packages have been developed to predict the size distributions of rock blocks. By simplicity, some software packages have been developed assuming infinite discontinuity size, such as the software packages *Simblock* (Maerz and Germain, 1992) and BCF (Esterhuizen, 1999). Increasing complexity in the simulations has been made by including discontinuity size as an *impersistent* or *persistence factor* of an imaginary infinite joint. The imaginary continuous joint is divided in segment (areas) of joint rock and rock bridges by a suggested proportion. Examples using this discontinuity model are the *IBSD* software package (Lu and Lhatam, 1999) and *Makeblock* software package (Wang et al., 2003). More complex and complete DFN modelling, which include joint size distribution estimates applying stereological methods (Warburton, 1980), are the software packages *Joints* (Villaescusa, 1991), *Stereblock* (Hadjigeorgiou et al., 1995) and *FracMan* (Dershowitz et al., 1998)

In this study, block size distributions of the mine sectors being studied were estimated by simulating the rock structure using a software program. This program assumes a Fisher distribution for orientation, negative exponential distribution for spacing and infinite trace length for discontinuities (Thompson, 2002). This software package was the only one available during the development of this study. Due to the

lack of discontinuity size limits, simulations may be considered as illustrative results only.

3.8.2 In Situ Block Size Estimations of the El Teniente Rock Structure

Simulations of the rock structure were based on orientation and spacing data gathered from the smaller scale sampling techniques, i.e., line mapping and oriented core logging. In situ block distributions considering sampling methods and mine sectors are presented in Figure 3.32.

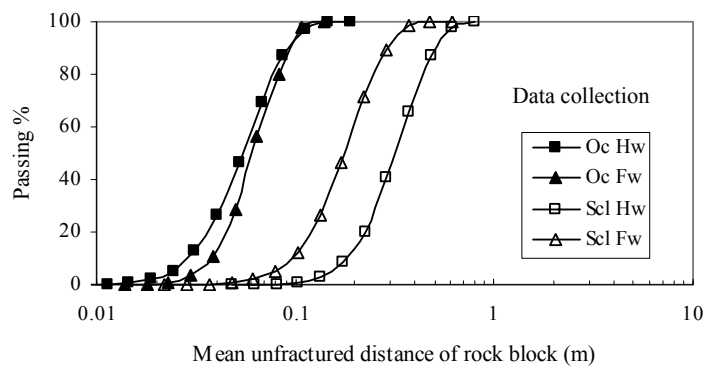


Figure 3.32.- In situ block size distributions from rock structure simulation (Oc; oriented drill core. Scl; scaline mapping).

Similarly to other discontinuity parameters, Figure 3.32 shows that the in situ rock block size distributions is also affected by the truncation bias length adopted during data collection. Moreover, considering only data collected by oriented core logging, the same degree of 'fracturing' (by healed veins) is observed between the two andesite sectors (*Hw* and *Fw*), whereas some differences appear when scanline mapping data is taken in to account.

3.9 Un-Oriented Core Logging Data

Un-oriented cores logging is one of the geologists' main activities at the mine site, with more than 35,000 meters of core logged every year. The main purpose of the drill core program is the development and continual improvement of the ore resource model, which consists of three-dimensional lithological and sulphide mineralogical models, however, few data is used for geotechnical characterisation.

Since core logging is essentially a heavily censored one dimensional characterisation method, it can be considered less detailed and comprehensive than a scanline placed at a mine wall. Core logging has the advantage that it provides data, not only prior to excavations, but also can access the rock mass beyond an excavation. Therefore, the relationship between both data collection techniques (scanlines and oriented core logging) needs to be understood in order to maximise utilisation of the information involved in rock mass characterisation and definition of the rock mass structure. This has not been included in the current research. However, small diameter core (diameter of 48 mm, see Section 2.6.2) data was used in this study as a complimentary data in the rock structure characterisation of the primary copper ore at the El Teniente mine.

In addition, the standard core logging practice undertaken at the mine site constrains the geotechnical characterisation in one important way. The core samples are not oriented⁶, subsequently discontinuity frequency estimates only represents the direction in which the core sample is oriented (Hudson and Priest, 1983). Therefore, the data may not be reliable for comparison of discontinuity frequency estimates between different core orientations. Even, if the real discontinuity frequency is obtained using such small diameter oriented drill cores, the truncation bias length corrections are required in order to compare results with other line mapping techniques (see Figure 3.12).

In this section, structural data collected using several un-oriented cores from Reno mine sector are presented to complement the rock structure characterisation of the primary copper ore.

3.9.1 Background

According to Warburton (1981), equation 3.19 says that for a similar orientation the observed discontinuity frequency in a sampling line depend on the size characteristics and the density of centre point locations.

In addition, for discontinuity sizes greater than a core diameter contained in a large enough volume, the probability to sample an impersistent discontinuity by a drill

⁶ It is also broken in many small pieces prior the geological logging (see Section 2.6.2)

core of radius c and length L , can be estimated as follow (Mauldon and Mauldon, 1997):

$$P(X) = \frac{\pi D^2 \cos \delta i + cL + \pi c^2}{\pi s^2} \quad (3.29)$$

where D is the discontinuity diameter, and s is the radius of a coaxial cylinder to the drill core that define the large volume. δi is the acute angle between the core orientation and the vector normal to the mean discontinuity joint set _{i} .

Assuming a three-dimensional Poisson process for joint centre location (randomly and independently distribute in space) the discontinuity occurrence for a given set, N_i , observed in a drill core can be obtained as (Zhang and Einstein, 2000);

$$N_i = N_T P(X_i) \quad (3.30)$$

where N_T is the mean of the stochastic variable within the large volume, and $P(X_i)$ for a set i from equation 3.29. Equation 3.29 is similar to equation 3.19. In both equations, the observe discontinuity frequency in drill cores essentially depends on the discontinuity size and the stochastic parameter.

For other discontinuity sets, the discontinuity occurrence in drill core can also be estimated as above. The total linear frequency observed in a drill core, λ_t (Priest, 1993) can be described as;

$$\lambda_t = \sum_i^n N_{Ti} P(X_i) \quad (3.31)$$

where n represent the number of sets within the rock mass. If all sets have the same size characteristics, Equation 3.31 can be written as;

$$\lambda_t = P(X) \sum_i^n N_{Ti} \quad (3.32)$$

Based on the assumption that the discontinuity occurrence within a rock mass follows a stochastic process, the total discontinuity frequency (λ_t) observed in a core sample will then depend essentially on the discontinuity size characteristics of sets and their stochastic parameters.

Accordingly, the nature of vein occurrence within rock masses of the primary copper at the El Teniente mine was examined by the analysing several un-oriented core sections located throughout Reno mine sector.

3.9.2 Location and Orientation of Core Sections Studied

Analyses of the data observed in drill core sections were divided in two main groups. Firstly, data analysis was carried out for estimates along the same drill core (adjacent samples). This was undertaken only on a few drill cores. Secondly, data analysis was undertaken for isolated core sections from multiple orientations and locations. The location of all 6.1m long core samples used in the analysis are shown in Figure 3.33. These samples were also grouped by orientation as shown Figure 3.34.

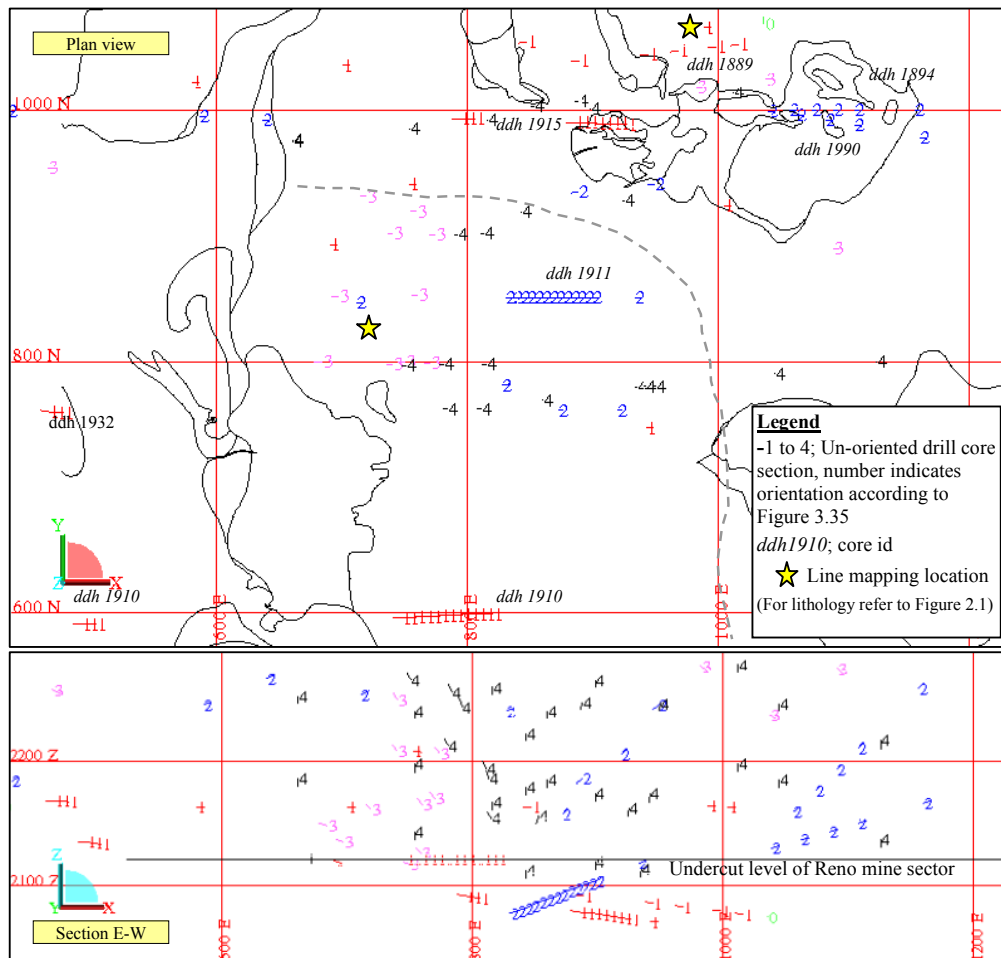


Figure 3.33.- Plan view and section of Reno mine sector showing location of standard 6.1m long un-oriented drill core sections (grouped by similar orientation accord to Figure 3.34).

Fault occurrences in all drill core sections represent less than 0.1 percent of all discontinuities sampled. Fault spacing observed in drill core oriented north-south, which trends approximately normal to the fault system in this mine sector, ranged between 5 to 10 meters irrespective of location and lithology. These values are similar to what was observed at mine drive mapping (Table 3.4) and also in previous measurements (Brzovic, 2001).

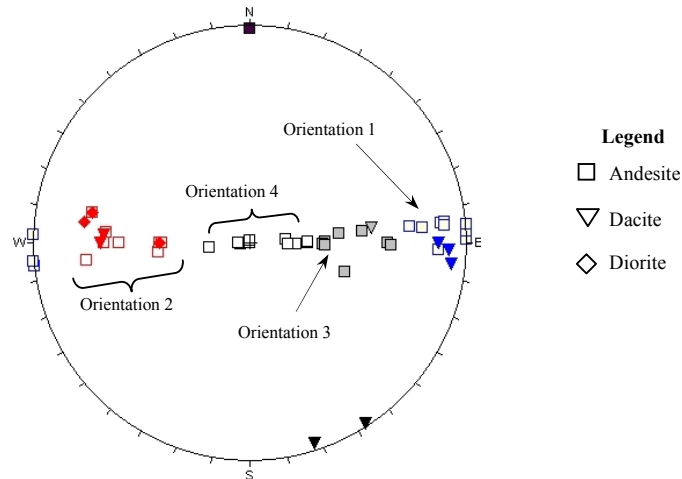


Figure 3.34.- Orientation (trend/plunge) of standard 6.1m long un-oriented drill core sections including rock type. Cores sections are grouped by similar orientation.

3.9.3 Estimates along the Same Core

Only a few cores included continuous measurements along their core axis, i.e., multiple adjacent or alternating core sections. Data analysis for several drill cores containing adjacent and alternating core sections are presented in Figure 3.35 and Table 3.15. The locations of these cores are shown in Figure 3.33.

Discontinuity frequencies observed along the same core in andesite rock type, which were measured for adjacent and alternating core sections, seem to exhibit some form of “*rock structure homogeneity*” as shown in both Figure 3.35 and Table 3.15. This is because, apart from core ddh1889 which is located near to the edge of the ore body, the discontinuity frequency is over 40 m^{-1} in all core sections from andesite rock type, with less than 15% of coefficient of variation. In addition, the discontinuity frequency observed in both ddh1911 and ddh1915 is practically the same, even when the holes are 400 meters apart each other. These results are

independent of type of alteration and core orientation. In dacite and diorite rock types, lower discontinuity frequency is observed compared to andesite. However, this result is not conclusive since orientation bias may have influenced these estimates.

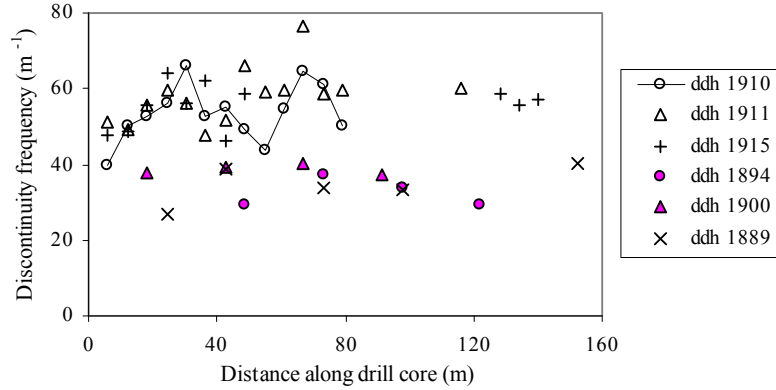


Figure 3.35.- Discontinuity frequency along the drill cores. All data from andesite except magenta filled symbols (diorite).

Table 3.15. Mean discontinuity frequency along the drill cores.

Rock Type	Id Drill core	Plunge / Bearing	Sample number	Observed discontinuity frequency (m ⁻¹)			
				Mean	Maximum	Minimum	Coeff. Variation
Andesite Hw	ddh 1910*	00/089	13	53.6	65.9	39.9	14%
	ddh 1911	22/270	14	58.0	76.4	47.9	13%
Andesite Fw	ddh 1915*	08/092	11	55.5	64.1	46.1	10%
	ddh 1889	06/085	5	34.5	40.0	26.7	15%
Diorite	ddh 1894	45/270	4	32.4	37.1	29.2	12%
	ddh 1900	15/277	4	38.5	40.1	37.2	4%
Dacite	ddh 1910*	00/089	3	23.4	28.1	20.5	18%
	ddh 1732*	04/096	3	54.1	63.3	45.1	17%

Note *; these drill cores have approximately the same orientation, and are around 300-400 meters from each other (see Figure 3.33).

The thickness distributions observed along the drill cores (only for andesite rock type) are examined in Table 3.16 and Figure 3.36.

Table 3.16. Variation of mean thicknesses distribution along drill cores.

Rock Type	Id Drill core	Sample number	Mean of the observed discontinuity frequency (%)					
			1mm<	C.V.	1-2mm	C.V.	>2mm	C.V.
Andesite Hw	ddh 1910*	13	76.0	3%	12.9	12%	11.1	22%
	ddh 1911	14	67.9	7%	16.7	24%	15.4	21%
Andesite Fw	ddh 1915*	11	69.7	6%	15.7	29%	14.6	18%

Note *; Both drill cores have approximately the same orientation, and are around 400 meters from each other. C.V.; Coefficient of variation.

The thickness distributions presented in Figure 3.36 show similar values along the drill cores, with a very high percentage of thin discontinuities (<1mm). These data may be another indication of some kind of “*rock structure homogeneity*” at the El Teniente stockwork.

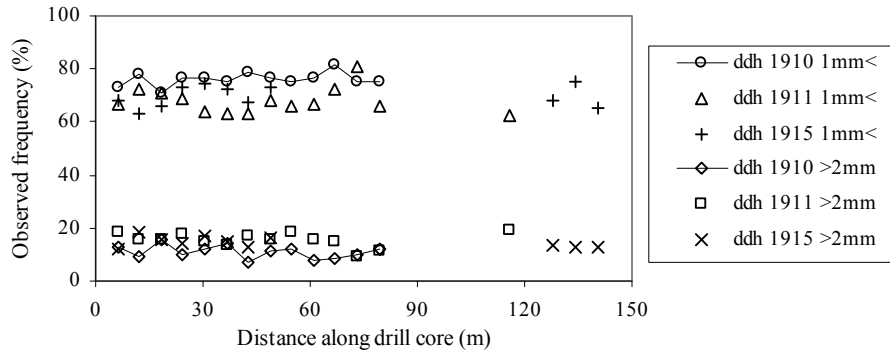


Figure 3.36.- Thickness distributions along drill cores for andesite rock type.

Although a truncation bias length threshold was not set during data collection on un-oriented drill cores, the practical truncation length threshold is estimated at around 2-3 centimetres. This is based on the ability to visually identify discontinuities during core logging. Therefore, data plotted in all these Figure 3.36 and Figure 3.37, Table 3.15 and Table 3.16, not only confirms the strong influence of truncation bias length in the spacing results, but also confirms that shorter discontinuities tend to be statistically thin. This last conclusion can be seen from a comparison between Figure 3.36 and Figure 5.5 (in Section 5.6.)

3.9.4 Estimates from Multiple Core Orientations

Similar data analyses were carried out based on multiple core sections with different orientations. In this case, the analysed samples were grouped by similar orientation according to Figure 3.34. The results for different orientations and rock types are presented in Figure 3.37 and Figure 3.38 for discontinuity frequency, and in Figure 3.39 for thickness distributions.

In this case, the core sections studied for andesite rock type were divided by the alteration zones rather than by sector *Hw* or *Fw*. For most core sections, the selection by alteration zone also coincides with the one made by sectors *Hw* and *Fw*.

According to Figure 3.37, in more than 85% of core samples (92 samples) from andesite rock type the observed discontinuity frequency is over 40m^{-1} , irrespective of the core orientation. The mean value for andesite rock type is 54.9m^{-1} . Most core sections having discontinuity frequencies less than 40m^{-1} are located in the principal hydrothermal zone within the andesite.

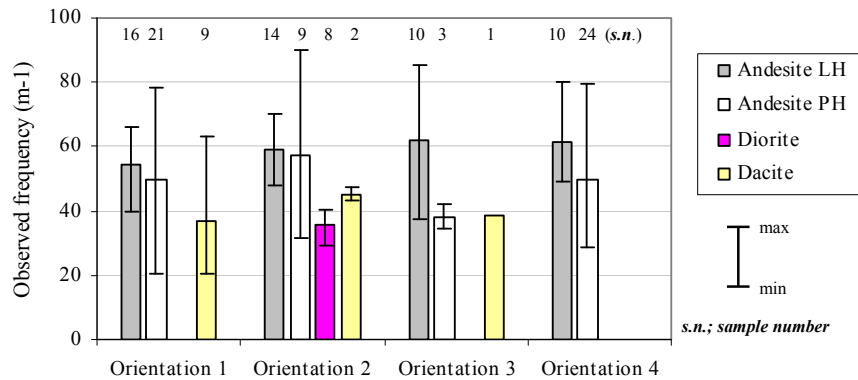


Figure 3.37.- Mean values of discontinuity frequency observed in multiple core samples grouped by orientation.

The observed variability in discontinuity frequency (Figure 3.37) may be expected due to the natural anisotropic characteristics of the rock structure. The natural anisotropic characteristics of the rock structure can be evaluated by simulating a three-dimensional loci of the discontinuity frequency diagram (Hudson and Priest, 1983) as shown Figure 3.38. In this figure three sets have been reproduced. The normal mean set spacing values used were; S_1 of 0.017m , S_2 of 0.038m and S_3 of 0.044m , which were obtained from data analysis of a detailed structural log of three orthogonal small diameter oriented cores⁷ (Harrison, 2009). These obtained spacing values are in agreement to the trend found in Figure 3.12 (Section 3.3.4). Although the discontinuity size is assumed infinite in this discontinuity frequency diagram, this illustrates that despite the apparent variability of the discontinuity frequency observed in data from un-oriented core sections (Figure 3.37), the rock mass may be considered to have some kind of “structural homogeneity” (at least through the andesite rock type). In other words, despite of the orientations bias, apparently the discontinuity frequency in core section from andesite look all similar having high veins frequency.

The thickness distributions observed in core samples from andesite rock type (Figure 3.39), are practically the same for each of the core directions shown in Figure 3.34. The data shows that, independently of the core orientations, for over 93% of the core samples thin discontinuities represent over 50% of the data. The mean percentage value of thin discontinuities for andesite rock type is 64%. It is clear that additional thin discontinuities appear when the truncation length threshold values used in line mapping is decreased (see Table 3.12). Both these analyses suggest that shorter discontinuities tend to be statistically thin.

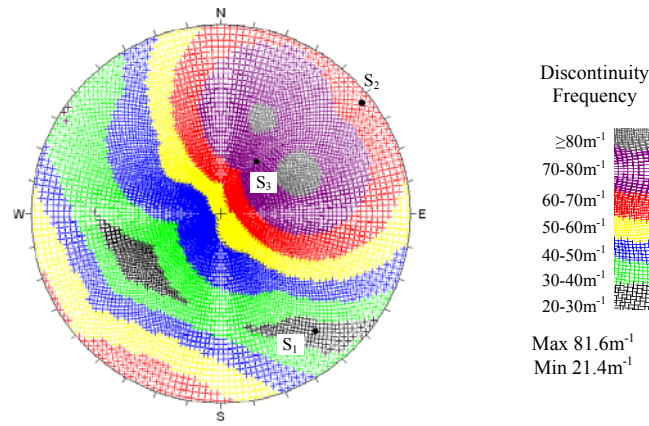


Figure 3.38.- 3D loci diagram of simulated discontinuity frequency in the lower hemispheric projection.

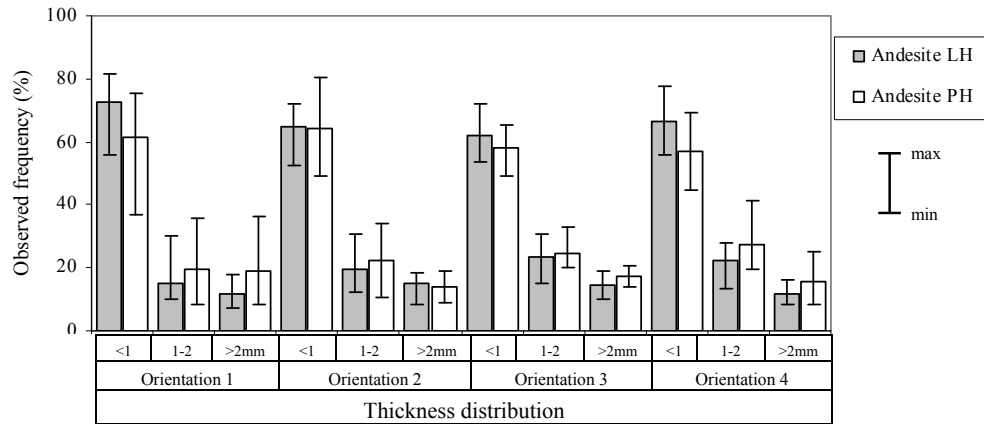


Figure 3.39.- Mean values thickness distribution observed in multiple core samples grouped by orientation.

⁷ See also Appendix II.A for core location and orientation.

The data shown in Figure 3.39 indicates that the discontinuity thickness distribution, observed in 6.1 m long core samples, is essentially isotropic within the stockwork at the El Teniente mine.

3.10 Conclusions

The result of rock structure characterization indicated that mainly faults and veins are present within the rock mass under consideration. Sub-vertical faults were defined as widely spaced, while veins were present in high frequencies in at least three semi-orthogonal set orientations. Almost no joints were found within the rock mass. Moreover, negligible differences were observed in terms rock mass '*fracturing*' (vein frequency) and in term of in situ rock block distributions between the two studied sectors, particularly using data from oriented core logging.

Truncation biases applied during data collection strongly affected the discontinuity set parameters such as spacing and distribution of thicknesses, and the in situ block size distributions. These characteristics indicate scaling law properties for discontinuity parameters, which are in agreement with observed characteristics in other geological environments. However, for practical purposes in rock mass characterisation at the mine site, it is important to recognise that truncation bias length adopted during data collection play a relevant role in the results obtained.

Some discontinuity parameters such as roughness, thicknesses and maybe discontinuity size have been found to have an isotropic characteristic within the rock mass. The infill features have also been found to have an isotropic characteristic, but at their own location, because the mineralogical infill in veins changes between locations and/or between hydrothermal alteration zones.

It has also been found that longer discontinuities are statistically thicker than shorter ones, which is in agreement with observed discontinuity features in other geological environments. Furthermore, the mean infill compositions in veins do not change with their thicknesses.

Although sampling biases have affected data collection, there is a good observed correlation between sampling techniques at different mapping scales.

A summary of the relationship between sampling techniques, sets and structural domains is presented in Table 3.15. The main difference observed between sectors is given by the infill features in veins.

Table 3.17. Summarised parameter features within rock mass.

Discontinuity Parameter	Comparison between		
	Mapping Scales	Sets (Same sector)	Structural Domain
Orientation	Observed similarities for discontinuity types	-	Only LM veins seem to vary between sectors. For all discontinuities slight differences seem to appear
Spacing	fractal relationship with truncation bias	Anisotropy	Practically the same
Persistence	n/o	May be isotropic	May be Isotropic (?)
Filling	Similar	Isotropy	Anisotropy
Roughness	n/o	Isotropic	Isotropic
Thickness	Scaling law relationship with truncation bias	Isotropic	Isotropic
Block Size	Affected by truncation bias	-	The same in data from oriented core logging, but slight differences in scanline mapping

Note: n/o not observed.

Rock masses of primary copper ore at the El Teniente mine can be thought as an assemblage of thousands of small blocks, which are cemented each other by the mineralogical vein infill. This rock mass feature is in agreement with both its strong competence and massive aspect, and with its high grade ore resources. This is also in concordance with a suggested true mean discontinuity size very small (<1m) and/or a very high volumetric joint density.

The data analyses presented so far included all discontinuities recognized within the rock mass. However, it is not expected that veins having intermediate or high tensile strength (for example, veins having abundant quartz as infill) would be dominant during rock mass disassembly by caving. Consequently, it is required to find a criterion to assess the relevance of hard and weak discontinuities within the raw data, which is discussed in next Chapter 4.

CHAPTER 4 CHARACTERISATION OF CAVED ROCK BLOCKS**4.1 Introduction**

In block caving mining methods, the size distribution of rock blocks found in production level draw points is called fragmentation, which is the result of rock mass disassembly during caving and comminution process. It is expected that these caved block forming discontinuity faces will be mostly defined by the geological discontinuities found within the rock mass. It is also expected that either existing geological discontinuities will propagate or new intact rock fractures will be created during this process. In fact, the predictions of potential fragmentation size are based on stochastic simulations of the rock structure that is based on structural data collected using mainly line mapping techniques undertaken in mine drives (see Villaescusa 1991, among others).

Previous chapters have shown that few joints have been found within the primary copper ore. Instead, there is a high frequency network of small scale veins coupled with widely spaced faults. These features agree with the description of a competent and massive rock mass. Accordingly, it is expected that either faults or veins, or even new intact rock fractures appear in faces of caved rock block in production level draw points. These geological features would be the weaker path where the competent and massive rock mass of primary copper ore fail during caving.

4.1.1 Goal

The main objective of this chapter is to assess the caved rock block forming discontinuities as being either intact rock fractures or existing geological discontinuities. In order to achieve this goal, several caved rock blocks were characterised at the production level caving draw points of Reno mine sector.

4.1.2 Assumptions

It is assumed that the discontinuity characteristic found using small scale sampling (line mapping and oriented drill core) can be considered representative of the sectors where rock blocks were extracted. This is a reasonable assumption considering the nature of the discontinuity characteristics described in Chapter 3. In this regards,

only the vein infill varies throughout the rock masses, and that feature agree with geological definition of the hydrothermal alteration zones. In this chapter, the studied caved rock block was carried out accordingly to this definition, which also coincides with the division of *Hw* and *Fw* sectors.

4.2 Features of Caved Rock Block Forming Faces

4.2.1 Discontinuity Occurrence

Most faces from the 87 caved rock blocks studied here were characterized based on the discontinuity definition provided in Section 2.2 (data base detail in Appendix I.F). The general results with respect to the types of discontinuities and the mine method being used are presented in Table 4.1.

Table 4.1. Occurrence of the El Teniente discontinuities as rock block forming faces per rock type and mining methods.

Mining Method	Lithology/Sectors	Data number	Discontinuity Occurrences (%)		
			New Fractures*	Faults	Veins
Pre-Undercut	Andesite Hw	242	6.2	3.7	90.1
Panel Caving	Andesite Fw	257	8.6	5.8	85.6
	Diorite	225	6.2	4.4	89.4
Total & Mean		724	7.0	4.7	88.3

Note *: new (fresh) intact rock fracture.

The data in Table 4.1 show that irrespective of the caving method and rock type, over 91% of the caved rock block faces are discontinuities observed within the primary ore; such as stockwork veins and faults (Figure 4.1). Significant differences in the undercut procedure and geometries are being used at the Reno mine sector. Conventional panel caving uses 13 metres high rings with subsequent block caving extraction. In contrast, pre-undercut uses 4 metres high horizontal slices followed by a delayed block caving extraction (see Section 1.6.1 and Figure 1.15).

Table 4.1 also shows that few caved rock block faces were formed by new intact rock fractures, which, when identified, usually had very rough and fresh surfaces. In addition, few faults were present as caved rock block faces; this was expected given their observed wide spacing and low occurrence within the rock mass. The spacing between faults is large compared to a typical rock block scale (mainly up to 2 metres long). In contrast, veins were fully forming the faces of the rock blocks. Again this in

agreement with their high frequency of occurrence observed within the rock masses of primary copper ore.

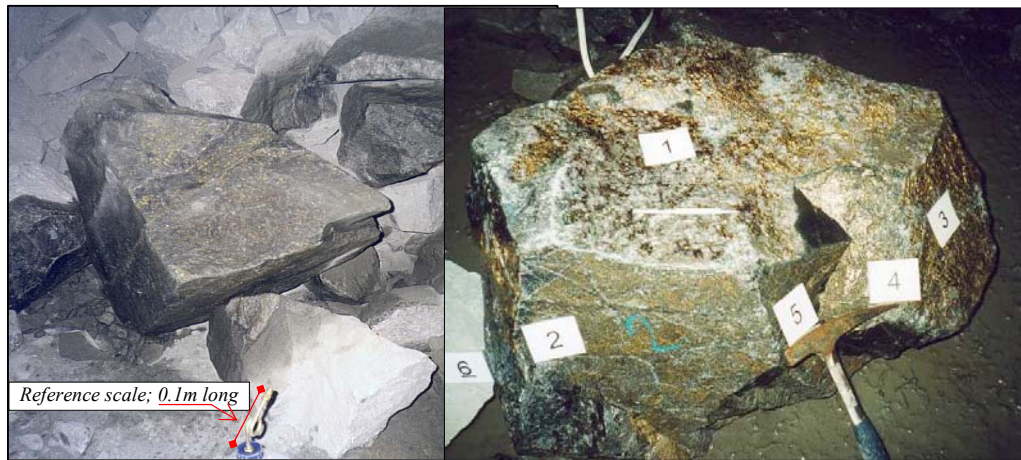


Figure 4.1.- Veins as faces of polyhedral caved rock blocks in draw points showing mineralogical infill such as chalcopyrite (yellow) and quartz (white).

The data in Table 4.1 suggests that during the entire rock mass caving process, it is easier to open or break through weakly healed discontinuities (veins) than breaking through the intact rock to create new joints or fractures.

Veins recognized as forming faces in caved rock blocks were fully characterized following the suggested method by the ISRM (Brown, 1981). The relevant characteristics of the collected information are detailed in the following sections.

4.2.2 Veins Infills

The infill observed in veins that formed caved rock block faces were studied in a method similar to the line mapping techniques. The results showed similar characteristics to the veins observed in mine drives; several infill mineral species were identified in the veins delineating caved rock block faces. The same major mineral species observed in veins the within rock mass were found to be the most abundant in the veins forming caved rock block faces (Table 4.2).

Although the four major minerals listed in Table 4.2 (namely; chlorite, anhydrite, chalcopyrite and quartz) are the same major mineral species recognized in veins within the primary copper ore, the proportion in which these mineral species were present within the rock mass (in-situ) was different compared with the results from

caved rock block faces (comparing the andesite rock type from Hw and Fw sectors in Table 3.8 or 3.9 with Table 4.2). For example, the most relevant difference was the proportion of quartz within the active, block forming veins. The proportion of quartz diminished significantly within veins found as rock block forming faces compared with veins found in-situ within the rock masses.

Table 4.2. Mean of mineral species observed as infill in veins forming caved rock block faces.

Lithology/ sectors	Mean of main infill (%)						
	Molybdenite	Chlorite*	Biotite	Anhydrite	Chalcopyrite	Quartz	Others
<i>Andesite Hw</i>	1.7	15.9	2.8	27.9	30.3	16.9	4.7
<i>Andesite Fw</i>	0.7	19.7	2.4	25.5	36.6	11.7	3.4
<i>Diorite</i>	1.0	19.3	0.9	25.0	33.0	18.4	2.4

Note *: include sericite

A general comparison of data collected from line mapping at both sectors (Table 3.8) and the caved rock block faces (Table 4.2) suggests that the mean quartz content in vein infill dropped from 56.5% to 16.9% in the *Hw* sector and from 31.5% to 11.7% at the *Fw* sector. This comparison suggests that the veins that opened up during the fragmentation process were those that had less quartz and/or more weak minerals as infill. It means that the rock mass disassembled preferentially along pre-existing veins which were mainly filled with weak mineral species as indicated by a lower quartz content.

4.2.3 Failure mode

Observed failure modes in veins forming rock block faces are presented in Table 4.3. Four main types of rock mass failure were defined based on the observations made in mine drives (Brzovic, 2001). The modes of failure are defined in Figure 2.13 (Section 2.5.2). Failure mode type *H* was considered different to failure mode type *IR*, because it occurred through the alteration halo associated with some veins.

Table 4.3. Modes of failure observed in veins forming caved rock block faces.

Lithology/Sectors	Mode of failure observed (%)		
	Mode V ₁	Mode C	Mode H
<i>Andesite Hw</i>	69.5	24.0	6.5
<i>Andesite Fw</i>	58.3	38.7	2.9
<i>Diorite</i>	56.6	39.7	3.7
Mean	61.6	34.1	4.4

Table 4.3 shows that during caving, and the subsequent fragmentation process, the rock mass fails mainly through the vein infill, irrespective of the rock type. The data also show that failure occurs at the vein-rock contacts. This failure (mode type C) may be interpreted as an extensional failure mode with little shearing, because the small asperities created through fracturing up have not suffered appreciable damage (see the highlighted ellipse in Figure 2.12). In contrast, the failure mode type V_I occurs mainly by shearing, as fewer asperities were observed. If this interpretation is correct, then shearing is the most common failure mode observed during caving and the subsequent fragmentation process.

4.2.4 Vein thickness

The thickness of veins forming caved rock block faces were observed as either an apparent or real thickness (Figure 2.13). In most cases, the apparent thickness was observed as the rock blocks separated from the rock mass through the veins. Hence, two adjacent rock blocks have one portion of the same vein, and the observations were only made for one of these rock blocks. However, in some cases, the rock block faces provided enough information to calculate the real vein thickness. This occurred when rock from both adjacent rock blocks remained attached to the observed vein (Figure 2.13d).

The failure mode type C was additionally classified by considering two limiting cases (Figuroa, 2003). Firstly, when one rock block showed almost all the vein infill (C_2 in Figure 2.13c), the apparent thickness could be almost considered the real thickness; Secondly, when one rock block showed only a small part of a vein infill (C_1 in Figure 2.13c), the apparent thickness was very thin (see also Figure 2.12).

The data analyses for the apparent thicknesses observed in veins forming caved rock block faces are summarized in Table 4.4.

Table 4.4. Apparent thickness (ae) observed in veins forming caved rock block faces.

Lithology/Sectors	Apparent thickness observed (%)		
	ae < 1mm	1mm ≤ ae < 2mm	ae ≥ 2mm
Andesite Hw	20.2	26.4	53.4
Andesite Fw	24.2	29.5	46.3
Diorite	41.8	31.5	26.6
Mean	28.8	29.2	42.0

Table 4.4 shows that on average that at least 70% of veins forming caved rock block faces have thicknesses greater than or equal to 1 mm. In addition, a total of 67 cases of real thickness were observed in veins forming rock block faces. The data are presented in Table 4.5. This table also includes the distribution of thicknesses observed in veins when the failure mode was type C_2 .

Table 4.5. Thicknesses observed in veins forming caved rock block faces.

Type	Data	Thicknesses observed (%)		
		$e < 1\text{mm}$	$1 \leq e < 2\text{mm}$	$e \geq 2\text{mm}$
Mode C_2	74	6.8	28.4	64.8
Real thickness	67	4.5	25.4	70.1

Table 4.5 shows that the observed vein thicknesses associated with failure mode C_2 were very similar to the observed real thicknesses. Hence, for practical purposes, it can be assumed that the data from this failure mode group approaches the real thicknesses of veins forming rock block faces.

The data from Table 4.5 also suggest that a low percentage of the veins activated during caving have real thicknesses of less than 1mm. Hence, veins having less than 1 mm thickness may be less relevant to the rock mass disassembly and fragmentation process. Most of the failure appears to occur in rock block faces having vein thicknesses in excess of 2mm. This is an important finding considering that such features (veins having thicknesses $\geq 2\text{mm}$) represent less than 40% of the total number of veins mapped using line mapping techniques (Table 3.12).

This finding is in agreement with the experimental behaviour exhibited by filled rock joints loaded in shear, that is, it is in accordance for the interpretation of failure mode type V_f . Joints filled with crushed mica (Goodman, 1970), kaolin (Papaliangas et al., 1990), cohesive soil (Pereira, 1990), and dry bentonite (Phien-wej et al., 1990) showed a reduction of shear strength when the thickness was almost twice the asperity amplitude regardless of the joint roughness. This behaviour occurs because at such a thickness, there is no interference between joint asperities. The strength of the discontinuity is equal to the strength of the infill (which can be weaker than the host rock).

For the failure mode type *C*, the data analyses are not conclusive with regard to explaining thicker veins defining caved rock block faces. This is also considering that the vein infill does not change with the thickness as Figure 3.27 suggests. Mine experience indicates that failure mode type *C* occurs predominantly when the vein infill is mainly chalcopyrite (Figure 2.12). The data show that when chalcopyrite exceeds 70%, the failure mode type *C* represented over 60% of the observed failure modes.

Therefore, the data from caved rock block faces at the El Teniente mine suggest that thick veins control the rock mass disassembly or failure. This is consistent with the assumption that shearing is the principal failure mechanism. Thick discontinuities are weaker, as the influence of the host rock asperities is minimized due to the nature of the wide infill.

4.3 Empirical Definition of Weak Veins

Experimental determination of stockwork vein strength has not been previously reported in the literature. Some experiments showed that is a complex problem and difficult to perform using standard approaches (Willoner 2000, p.47-48). The lack of laboratory test data is because, such discontinuities have been considered less relevant from the rock mechanics point of view. The discontinuity definitions provided by ISRM (Brown, 1981) excluded vein types, such as those present within the El Teniente primary copper ore, which have intermediate to high tensile strength. In contrast, experimental and theoretical strength determinations for rock joints are abundant in the literature (see Barton and Stephansson, 1990), as those features are considered the key to inferring the quality of a rock mass.

However, Laubscher and Jakubec (2001) have incorporated the effect of healed veins in their proposed methodology to estimate the quality of a jointed rock mass. They described veins as cemented filled joints. However, because of the lack of data regarding the mechanical properties of veins, they proposed the use of the *Mohs scale of hardness* (Hurlbut, 1941) to define their frictional properties. Thus, veins filled with chalcopyrite would be harder than veins filled with chlorite or molybdenite. The frequency of veins within a rock mass is used to adjust the rock

mass strength in order to estimate the Modified Rock Mass Rating (Laubscher and Jakubec, 2001).

That work does not specify which value should be used when a vein is filled with more than one mineral having different hardnesses, as is the case for most discontinuities recognized in the current research. An example of this would be a case when quartz, chalcopyrite, anhydrite and chlorite exist in equal proportions within a vein. Furthermore, the presence of quartz on veins has been ignored by Laubscher and Jakubec (2001), as they argued that it can be reasonably assumed that its hardness is not likely to be a significant weakness within a rock mass. The present study has shown that quartz is still an important component within veins defining caved rock block faces at the mine site (Table 4.2).

Following the discussion in Section 4.2.2, veins having chalcopyrite, anhydrite and some amount of quartz as infill can be considered weak discontinuities, as they opened during the fragmentation process. In addition, determining the critical amount (%) of quartz, or any other hard mineral within these veins, is a relevant issue in order to establish if such veins would still be considered weak discontinuities. Furthermore, determining what proportion should exist between at least two minerals having different infill hardness on a single vein, to change its strength from hard to weak or vice versa, is also a relevant research issue.

In order to define the relative strength of veins, the present study proposes to use the *Mohs scale of hardness* (Hurlbut, 1941) in combination with the abundance of infill material. The objective is to empirically define a weak discontinuity within the primary copper ore based on the amount of hard infill observed in rock faces of the rock block sampled.

4.3.1 Relative vein infill strength

The main minerals recognized as vein infill within the El Teniente primary ore are presented in Table 4.6. In this table the *Mohs scale of hardness*, H (Hurlbut, 1941) is used to classify the relative strength of these minerals.

Table 4.6. Relative strength of the minerals at the El Teniente mine.

Relative strength and its criterion	Mineral	Symbol	H
Soft $H < 3$	Molybdenite	Mo	$1-1\frac{1}{2}$
	Gypsum	Gyp	$2\frac{1}{2}$
	Chlorite	Chl	$2-2\frac{1}{2}$
	Biotite	Bt	$2\frac{1}{2}-3^*$
	Calcite	Ca	3^*
Intermediate $3 \leq H \leq 4$	Bornite	Bo	3
	Anhydrite	Anh	$3-3\frac{1}{2}$
	Ankerite	Ank	$3\frac{1}{2}$
	Chalcopyrite	Cpy	$3\frac{1}{2}-4$
Hard $H > 4$	Pyrite	Py	$6-6\frac{1}{2}$
	Quartz	Qtz	7
	Tourmaline	Tu	$7-7\frac{1}{2}$

Note *: Biotite and Calcite are microcrystalline minerals formed by alteration process, then, their H is less than when they have been crystallised.

The percentage of the minerals present as infill in veins forming caved rock block faces according to their strength properties can be assessed using Table 4.6. For instance, the example of a vein containing quartz, chalcopyrite, anhydrite and chlorite in equal proportions would be described as being filled with 25% of soft, 50% of intermediate and 25% of hard minerals.

Therefore, the hard infill distribution observed in veins forming caved rock block faces was examined using the proposed relative strength classification for those minerals.

4.3.2 Data Analysis using relative vein infill strength

The distributions of hard infill observed in veins forming caved rock block faces are shown in Figure 4.2. The data are presented by considering the two rock types, as no differences between the andesite sectors could be established.

The data show that the proportion of hard infill recognized in veins forming rock block faces drastically reduced when the proportion exceeded around 1/3 of the total infill. I.e., Veins having 1/3 or more of hard mineral as infill were not important to the caving disassembly and the subsequent fragmentation process. These veins can be considered as being hard for this particular caving process at the El Teniente.

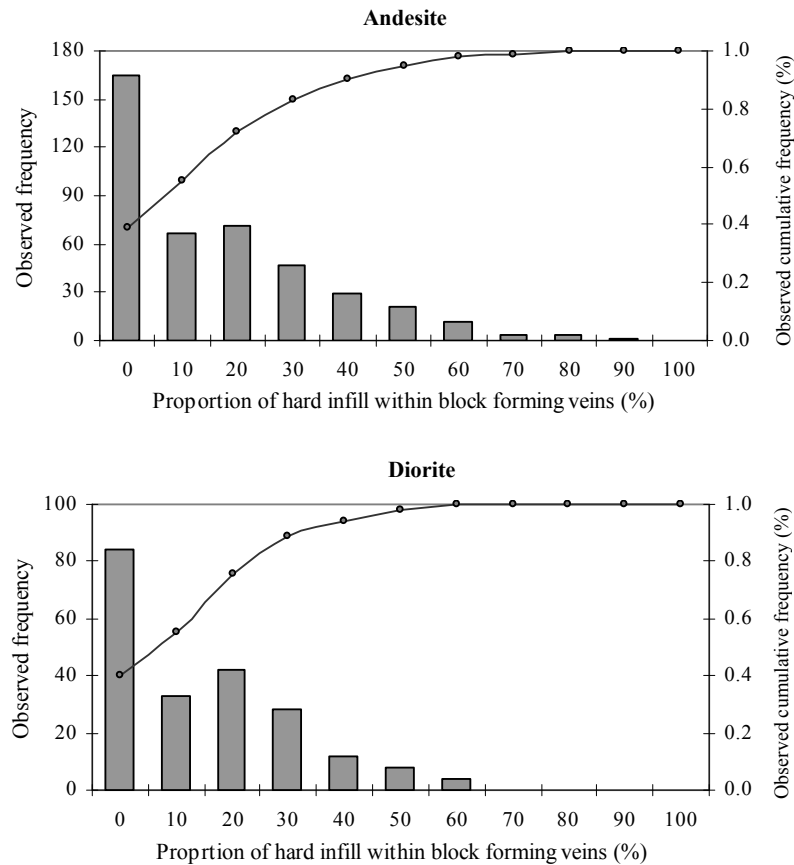


Figure 4.2.- Distribution of hard infill observed within rock block forming veins from andesite and diorite rock types.

The same data were re-analyzed, to take into consideration the failure mode, the rock block volume and the percentage of extraction within the caving draw points. The percentage of extraction represents the percentage of designed column height that has been extract through production level draw points, for instance, 60 meters of column height extracted over a 240 meters column height planed represent a percentage of extraction of a 25%. The results of the analyses are shown in Figure 4.3, Figure 4.4, and Figure 4.5.

Similarly to the results shown before, the hard infill within veins forming rock block faces dropped drastically when the proportion contained exceeded around 1/3 of the total infill, irrespective of the mode of failure, the volume of rock block, or the percentage of extraction.

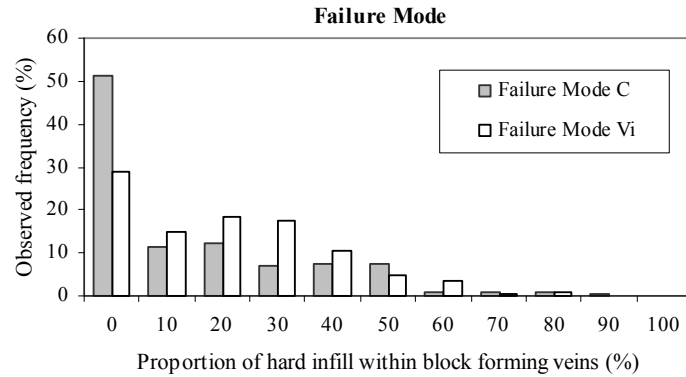


Figure 4.3.- Distribution of hard infill observed in veins considering failure mode.

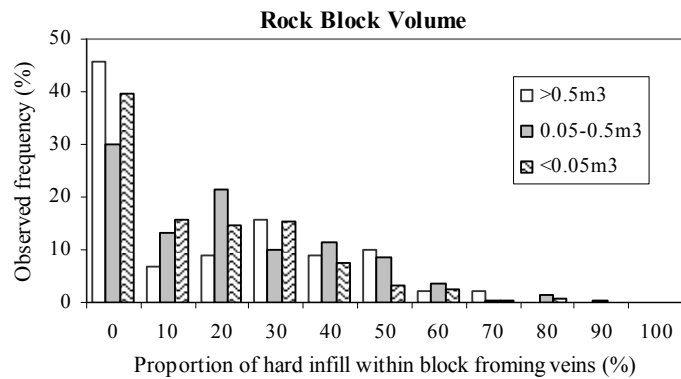


Figure 4.4.- Distribution of hard infill observed in veins considering rock block volume.

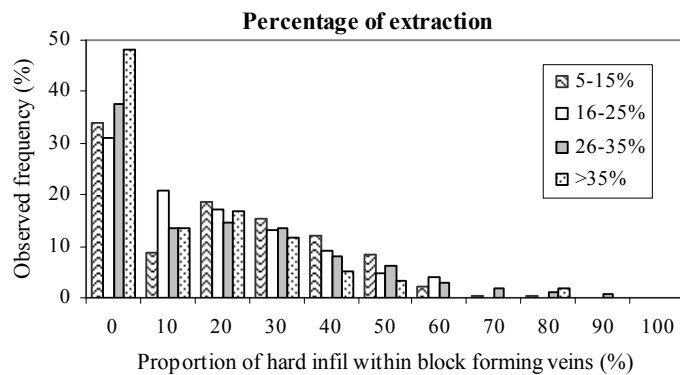


Figure 4.5.- Distribution of hard infill observed in veins considering percentage of block caved column extraction.

Additionally, Figure 4.3 shows that failure mode type *C* is observed in the majority of veins forming caved rock block faces without any hard mineral as infill, which

could be consistent with the fact that failure mode type C in the major failure mode observed for veins filled with high percentage of chalcopyrite. Figure 4.5 also shows that most of the veins that formed caved rock block faces without any hard minerals as infill, was observed for draw points when the extraction rate exceeded 35%.

4.3.3 Interpretation

Rock masses of primary copper ore are disassembled following caving initiation, propagation and subsequent comminution. Loading imposed by stress redistribution from the cave propagation opens up healed veins to form rock blocks. Subsequently, the loading imposed by the weight of the dissembled rock blocks is likely to split other rock blocks through healed veins to create new ones (comminution process).

In both cases, failure may not necessarily occur through a weak discontinuity. Rock mass failure may occur through a hard discontinuity if the shear stresses acting on the discontinuity surface exceed that the shear strength. Nevertheless, if weak discontinuities have the same orientation as hard discontinuities, and if they are present having high frequency within the rock mass (as is the case presented here in the next section), the possibility of failure through a hard discontinuity would be minimized, as in the example given in Figure 4.6.

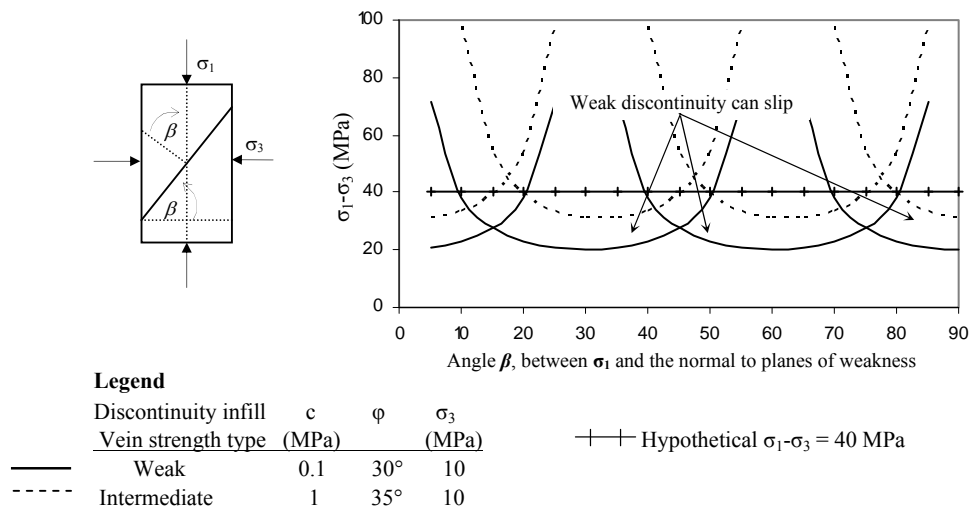


Figure 4.6.- Plane of weakness theory applied to a rock mass having three discontinuity sets (Mohr-Coulomb parameters as reference).

Figure 4.6 shows the relationship between the deviatoric stress (and/or ‘rock mass strength characteristic’) and the angle β , between σ_1 and the normal to the weaknesses plane (Jeager, 1960). It is assumed that three discontinuity sets are present and have the same azimuth but differing 30° in dip from each other (almost similar to a north south direction in Figure 3.6 from Hw sector), and that each discontinuity set has two discontinuity types in term of strengths. Now, at the El Teniente mine the major principal stress, σ_1 , may increase from 47 to 90MPa (Rojas et al., 2000b), due to the effect of increasing the abutment stress by the caving propagation (Figure 1.14). Therefore in a hypothetical case represented by Figure 4.6, having $\sigma_1 = 50$ MPa, the rock mass would always fail through a pre-existing weak discontinuity rather than through a hard one.

4.4 Conclusions

In this chapter, a rock structure characterisation of caved rock block faces has been undertaken at the production level caving draw points. The result show that during caving and the subsequent fragmentation process, rock masses of primary copper ore fail mainly through pre-existing discontinuities. These discontinuities are mainly filled veins having the following particular features:

- Less than 1/3 of hard minerals as infill.
- Thicknesses greater than or equal to 2 mm.

This phenomenon occurred irrespective of the mining method, lithology, and percentage of extraction within production level caving draw points.

Hard minerals are defined using a particular categorization of the *Mohs scale of hardness*. This approach was used since no experimental data was available on the strength properties of the vein infill minerals. According to this categorization most vein infill observed within the rock mass are intermediate and hard. These characteristics can be used as a criterion to define weak veins from the raw data.

Therefore, weak discontinuities within rock masses of primary copper ore during caving are both faults and weak veins. Weak veins are defined as these veins filled with less than 1/3 of hard minerals as infill.

CHAPTER 5 ANALYSIS OF WEAK DISCONTINUITY DATA**5.1 Introduction**

Research from previous chapters has shown that almost no open joints were found within rock masses of the El Teniente primary copper ore. However a high frequency network of small scale veins couple with widely spaced faults were present. In addition, during caving and the subsequent fragmentation process, these rock masses fail mainly through pre-existing discontinuities such as faults and thicker, healed veins filled with less than $1/3$ of hard minerals¹ as infill (weak veins). Both discontinuity types are the weaker path within primary copper ore where the competent and massive rock mass fail during caving.

In order to investigate if the application of the new established empirical definition of weak discontinuities has any control on rock mass response to mining, a re-analysis of the rock structure data is presented in this chapter

5.1.1 Goal

The main objective of this chapter is presents a re-analysis of data presented in Chapter 3, but incorporating the new-established empirical definition of weak discontinuities to investigate if it has any impact on rock mass characterization of the primary copper ore at the El Teniente mine.

A second objective carried out through this data analysis is to compare two structural domains (H_w and F_w sectors), which have historically behaved differently in terms of mining performance.

5.2 Weak Discontinuity Occurrence

Veins mapped during scanline mapping and oriented core logging were analyzed in terms of their hard infill occurrence (Figure 5.1). This figure, which present the data in term of the cumulative occurrence of hard mineral within veins as infill, shows that appreciable differences between andesite sectors (H_w and F_w) appear when the definition of weak discontinuities is adopted (veins filled up to $1/3$ of hard infill). The

data shows that up to 16.3% and 49.9% of veins mapped in cores and Scanlines are weak veins in the *Hw* and *Fw* sectors respectively. The differences still appear between andesite sectors if other threshold values of hard infill would be adopted as also suggests that figure.

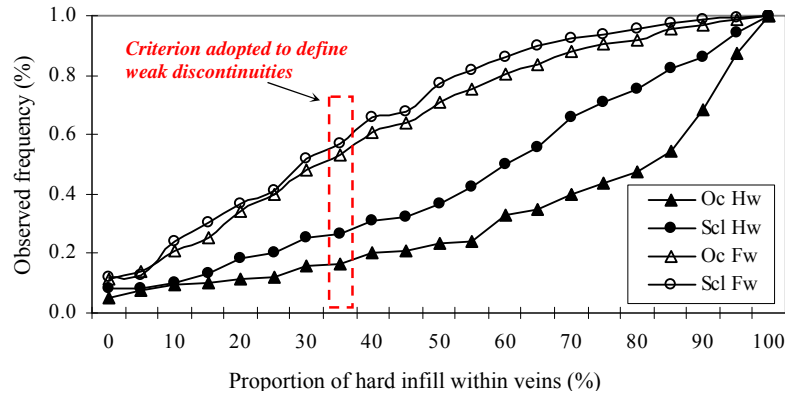


Figure 5.1.- Cumulative frequency of veins collected in small scale sampling in term of the proportion of hard infill within veins. Oc; oriented core logging, Scl; scanline mapping.

In addition, Figure 5.1 shows a very good correlation between data collected by sampling lines from *Fw* sector, and an acceptable correlation for data collected from *Hw* sector when the hard infill is less that 50%. Two main reasons that may be invoked to explain the differences observed in data from *Hw* sector when high proportion of hard infill in veins is observed. The first reason may be due to that veins filled with hard infill could be not collected during scanline sampling, i.e., these could be obscured by the effect of the covering exposure bias and/or these could have been ignored. The second reason may be due to that oriented core samples from *Hw* sector were not set up exactly in the same place as scanlines sampling (see their location in Figure 2.4), then, data in this Figure 5.1 may be suggesting some variations of the same sector.

In addition the good correlation observed between data from *Fw* sector may suggest that there was a good repeatability of the infill observation during data collection.

¹ Hard minerals defined as having Mohs' hardness number grater than or equal to 4.

5.2.1 Discontinuity type

The occurrence of weak discontinuities observed at the small sampling scales was analyzed for each discontinuity set (defined in Section 3.2.5). Data analysis is presented in Table 5.1, which include details of discontinuity type and occurrences.

Table 5.1. Weak discontinuity occurrence for discontinuity sets observed in small scale sampling.

Sector Studied	Mapping Scale	Set Number	Data Number		Individual set occurrences and percentage of weak discontinuities per discontinuity type						
					Faults	LH Veins		HP Veins		LM Veins	
			n	Weak* (%)	%	%	Weak* (%)	%	Weak* (%)	%	Weak* (%)
<i>Hw</i>	Scanline Mapping	Random	30	13%	-	-	-	-	-	100	13%
		1	178	30%	2.8	5.1	89%	5.6	90%	86.5	21%
		2	145	32%	2.1	1.4	100%	3.4	100%	93.1	27%
		3	168	20%	1.2	2.4	100%	7.7	100%	88.7	10%
		Total	521	27%	1.9	2.9	93%	5.4	96%	89.8	19%
	Oriented Core Logging	Random	57	19%	-	3.5	50%	7.0	100%	89.5	12%
		1	208	27%	0.5	11	74%	11.1	74%	77.4	13%
		2	110	10%	0.9	1.8	50%	3.6	75%	93.6	6%
		3	81	7%	-	-	-	6.2	80%	93.8	3%
		4	150	10%	-	1.3	50%	4.0	33%	94.7	8%
		Total	606	16%	0.3	4.8	69%	6.9	71%	88.0	9%
	<i>Fw</i>	Scanline Mapping	Random	19	47%	10.5	-	-	10.5	100%	78.9
1			119	58%	12.6	5.9	45%	31.9	66%	49.6	42%
2			63	51%	1.6	1.6	100%	7.9	80%	88.9	46%
3			67	60%	3.0	1.5	100%	22.4	93%	73.1	47%
4			51	51%	5.9	3.9	100%	27.5	64%	62.7	38%
Total			319	55%	7.2	3.4	64%	23.2	73%	66.1	44%
Oriented Core Logging		Random	69	42%	1.4	1.4	100%	21.7	93%	75.4	25%
		1	204	48%	2.5	3.9	75%	25.5	71%	68.1	36%
		2	221	51%	0.9	2.7	83%	23.1	84%	73.3	39%
		3	71	55%	4.2	5.6	100%	25.4	67%	64.8	43%
		Total	565	49%	1.9	3.4	84%	24.1	78%	70.6	37%

Note *: proportion of weak discontinuities from all discontinuities.

Some conclusions can be drawn from data in Table 5.1:

1. Similar to the conclusion from previous section, there is a clear difference between studied sectors (*Hw* and *Fw*). This difference may be due the infill characteristics of LM veins, which change considerably between these mine sectors.
2. The majority of the PH and LH veins can be considered as being weak veins. A high proportion of LM veins can be considered as being hard veins, particularly at the *Hw* sector.
3. Considering the data from the column 'Data Number' for each mapping scale, it can be seen that the occurrence of weak discontinuities for each set

varies little. It is practically the same to each other, being also the same to the mean of the sector. This is in agreement with the mineralogical infill as being an isotropic feature within each sector (also discussed in Section 3.5.1).

4. Considering the data from the columns '*Weak (%)*' for each veins type and for each own mapping scale, it can also be seen that the occurrence of weak discontinuities varies little between sets of the same sector or between mapping scales. This observation is also in agreement with the average mineralogical infill measured in a representative sample line as being an isotropic feature within each sector.

5.3 Spacing

Since weak discontinuities are a sub-group of all discontinuities, the mean normal weak discontinuity set spacing was estimated using the same set definition accepted for all discontinuity. I.e., set definitions for weak discontinuities were defined using the same set definition shown in Figure 3.6 and in Figure 3.7.

Because the infill characteristics of veins were only determined quantitatively in a small scale sampling (scanline and oriented core logging), for practical purposes here, it was assumed that HP and LH veins observed in drive mapping are all weak discontinuities. It was also assumed that LM veins observed in drive mapping are all hard discontinuities. These seem a reasonable assumptions considering the data showed in previous section (Table 5.1) couple with data of the discontinuity occurrence at large scale sampling (in Table 3.1).

Data analysis of normal set spacing for data collected in drive mapping, which follows the procedure discussed in Chapter 3 is presented in Table 5.2.

Table 5.2 shows that the mean normal discontinuity set spacing for weak discontinuities having observed trace length over 4.0m range from 3.4m to 15.4m. These data are consistent with observed spacing in other mine sectors as is discussed in Section 7.2.1 (data from Esmeralda mine sector in Table 7.1 under the same assumptions).

Table 5.2. Mean normal set spacing for data collected by drive mapping.

Sectors Studied	Set number	Dip / Dipdir	Discont. Type	Poles	Arithmetic		n	Max-Min (m)	Negative Exponential Distribution
					Mean (m)	S.D. (m)			Mean (m)
Hw	Set 1	74/182	All	112	4.3	3.7	103	19.3-0.2	4.53
			Weak	89	4.8	4.3	80	22.8-0.3	5.04
	Set 2	77/318	All	22	10.0	7.5	16	27.7-0.6	-
			Weak	18	12.1	8.8	12	27.7-0.6	-
	Set 3	24/228	All	37	4.5	4.9	28	18.8-0.2	3.63
			Weak	14	9.5	10.0	8	28.6-1.1	-
	Set 4	65/359	All	33	12.9	11.7	24	32.7-0.7	12.26
			Weak	24	15.4	10.7	16	32.1-1.0	16.67
Fw	Set 1	74/194	All	117	3.2	2.7	107	11.5-0.1	3.4
			Weak	112	3.4	2.8	102	11.5-0.1	3.6
	Set 2	85/125	All	39	4.9	4.2	32	15.2-0.4	5.0
			Weak	37	5.3	4.1	30	15.2-0.4	5.6
	Set 3	41/065	All	13	5.1	2.7	6	7.8-0.6	-
			Weak	13	5.1	2.7	6	7.8-0.6	-
	Set 4	75/022	All	22	10.9	11.9	15	32.1-0.5	7.2
			Weak	22	10.9	11.9	15	32.1-0.5	7.2

Notes: S.D.; standard deviation.

Data analysis of normal set spacing for data collected in small scale sampling is presented in Table 5.3.

Table 5.3. Mean normal set spacing for weak discontinuities observed in small scale sampling.

Sectors Studied	Mapping scale	Sets	Poles	Arithmetic		Poles used	Max-Min (m)	Poles vertic. lines *	Negative Exponential Distribution
				Mean (m)	S.D. (m)				Mean (m)
Hw	Scanline Mapping	Set 1	54	1.254	1.545	47	7.059-0.048	-	1.040
		Set 2	47	0.880	1.115	43	6.127-0.031	-	0.795
		Set 3	34	1.401	1.152	19	1.890-0.007	6	0.241
	Oriented Core Logging	Set 1	56	0.224	0.244	53	1.046-0.004	-	0.204
		Set 2	11	0.751	0.839	8	2.537-0.026	-	-
		Set 3	6	2.454	0.784	4	3.682-2.004	-	-
Fw	Scanline Mapping	Set 1	69	0.592	0.686	57	3.740-0.018	3	0.522
		Set 2	32	0.696	0.668	26	2.593-0.021	1	0.665
		Set 3	40	0.549	0.504	28	2.184-0.029	20	0.542
		Set 4	26	0.555	0.559	17	1.694-0.029	-	-
	Oriented Core Logging	Set 1	98	0.119	0.127	92	0.722-0.007	-	0.115
		Set 2	113	0.126	0.142	102	0.807-0.008	-	0.116
		Set 3	39	0.239	0.418	35	2.040-0.008	-	0.135

Notes *: poles used from vertical lines. S.D.; standard deviation.

Table 5.3 reveals that less spacing data is observed in these sampling techniques. If the Sen and Kazi's rule to obtain normal set spacing with enough accuracy (Sen and Kazi, 1984) is followed (line sampling short than 20 times then mean spacing in section 3.3.3), some estimates from Hw sector and vertical sets may be considered as not having enough accuracy.

In addition, using the proposed discontinuity frequency diagram (in section 3.3.4), the three-dimensional loci (Hudson and Priest, 1983), the global maxima and minima and their orientations for discontinuity frequencies were estimated for both sectors (Table 5.4). This table also includes the mean discontinuity frequency as the average values obtained from more than 8000 equidistant directions. This mean value would represent the discontinuity frequency normalized with respect to the orientation at this location. The true three-dimensional loci diagram using data collected in scanline mapping from *Fw* sector is presented in Figure 5.2.

Table 5.4. Extreme values of discontinuity frequency and their orientations of weak discontinuities.

Sampling method	Global type	Andesite Hw		Andesite Fw	
		Discontinuity frequency (m^{-1})	Trend/Plunge	Discontinuity frequency (m^{-1})	Trend/Plunge
Line mapping	Maxima	3.29	066/47	4.88	062/36
	Minima	0.80	197/07	1.41	257/68
	Mean	2.44		3.24	
	Coef. of variation	23%		24%	
Oriented Core logging	Maxima	5.62	027/06	15.40	340/00
	Minima	1.04	280/05	2.88	225/65
	Mean	3.46		9.11	
	Coef. of variation	35%		31%	

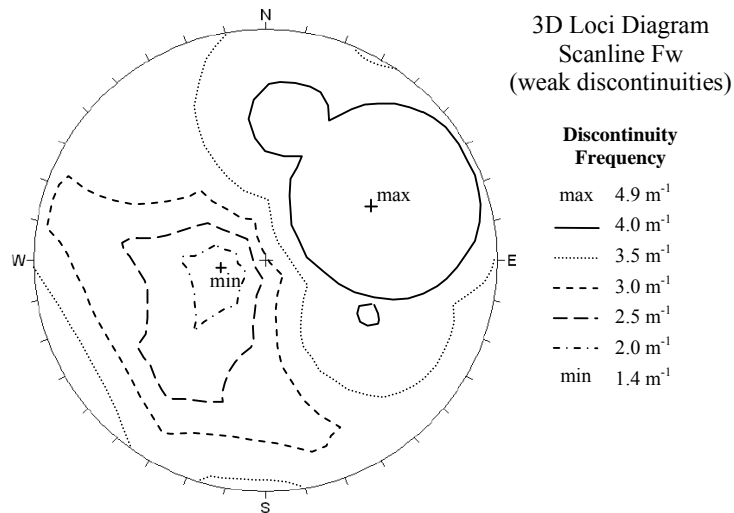


Figure 5.2.- 3D loci of discontinuity frequency diagram for weak discontinuities (scanline Fw sector).

No appreciable difference in structural anisotropy can be determined when only weak discontinuities are considered (Table 5.4 and Figure 5.2) compared to when all discontinuities are considered (Table 3.5 and Figure 3.14). This conclusion reveals two important things. First, they confirm the isotropic characteristic of the average

vein infill within the rock mass. Secondly, the different thickness distributions observed at both mapping scales do not affect the vein infill characteristics, as was also suggested Figure 3.26. But what is most relevant from Table 5.4, is that at any mapping scale the andesite rock type from the Fw sector has a larger frequency of weak discontinuities. According to data from oriented core logging, the normalised frequency of weak discontinuities within the Fw sector is nearly three times that of the Hw sector.

These results are in agreement with the appreciable differences of ground behaviour observed within these two typical andesite sectors (see also Figure 1.18 and Figure 1.19 discussed in Section 1.6.3 and 1.6.4 respectively). Therefore, the empirical definition of weak discontinuities is a good indicator to represent real, appreciable differences of rock mass response to mining activities, particularly in term of fragmentation at Reno mine sector.

5.4 Persistence

The observed trace length distribution and the observed arithmetic mean for each set of weak discontinuities are presented in Table 5.5. In this table, the individual data set distributions are similar to each other, and similar to the mean of the sector. The average observed trace length of weak discontinuities are similar between andesite sectors, and similar to when all discontinuities are considered (Figure 5.3).

Assuming that all discontinuities are flat circular disc of negligible thickness, parallel to each other with centre locations randomly and independently distributed in the space (Warburton, 1980), the data seem to exhibit an isotropic size distribution for weak and all discontinuities (see also what is discussed in Section 3.4.2).

5.5 Roughness

Following the procedure described in Section 3.5 (Chapter 3), the roughness of weak discontinuity sets was characterised, with the results presented in Table 5.6 and in Figure 5.4.

Data from Table 5.6 confirms that weak discontinuities are a subgroup of all discontinuities, i.e., the same roughness characteristics for all discontinuities observed at any roughness scale are observed in weak discontinuities.

5.6 Thickness

The distribution of thicknesses of weak discontinuities was estimated for each set, for all sectors, and all mapping scales. The results are presented in Table 5.7. This table shows that at each mapping scale, only slight differences in thickness distribution can be observed between sets and between sectors as well.

The thickness distributions for weak discontinuities are practically the same to when all discontinuities are considered (comparing Table 3.11 and Table 3.12).

As was discussed in section 3.6.1, important differences in thickness distribution are observed when comparisons are made between different mapping scales. These comparisons confirm the influence of truncation bias on the abundance of thin discontinuities either for weak or for all discontinuities, as can be seen in Figure 5.5.

In this Figure 5.5, the mean thickness of each weak discontinuity set at any mapping scale is plotted against to the truncation bias length used during data collection. The main tendency can be described as fractal relationship between these parameters.

In summary, the data show that similar to trace length and roughness, the thickness distributions observed within weak discontinuities do not change at any orientation regardless of the truncation bias. Therefore, assuming a representative sample size the thickness distributions can be considered a statistically isotropic feature within the rock mass, i.e., a linear sampling will collect the same thickness distribution at any orientation.

Table 5.5. Observed trace length of weak discontinuity at the El Teniente mine.

Sectors Studied	Set number	Dip / Dipdir	Number of data	Observed trace length of weak discontinuities											Arithmetic mean	
				Size distribution (%)											Mean (m)	S.D. (m)
				0.5m<	1.0m	1.5m	2.0m	2.5m	3.0m	3.5m	4.0m	>4.5m				
Hw	Set 1	86/182	52	3.8	23.1	15.4	11.5	21.2	3.8	7.7	5.8	3.8	1.91	1.48		
	Set 2	83/282	44	4.5	15.9	29.5	18.2	11.4	6.8	2.3	2.3	0.0	1.86	1.90		
	Set 3	24/193	34	5.9	8.8	14.7	17.6	11.8	2.9	8.8	11.8	0.0	2.71	2.04		
	Total & Mean		134	4.5	17.2	20.1	15.7	15.7	4.5	6.0	6.0	1.5	2.07	1.79		
Fw	Set 1	83/192	67	1.5	14.9	10.4	23.9	16.4	7.5	11.9	7.5	3.0	2.12	1.40		
	Set 2	68/251	32	3.1	25.0	25.0	28.1	6.3	3.1	6.3	-	3.1	1.49	0.80		
	Set 3	25/212	40	-	35.0	10.0	15.0	15.0	7.5	10.0	5.0	-	1.74	1.05		
	Set 4	74/301	26	7.7	23.1	19.2	3.8	30.8	3.8	3.8	3.8	-	1.85	1.78		
	Total & Mean		175	2.9	23.4	13.7	19.4	15.4	6.3	9.7	5.1	1.7	1.86	1.30		

Note: Scanlines use a cut-off by 0.3 meters long

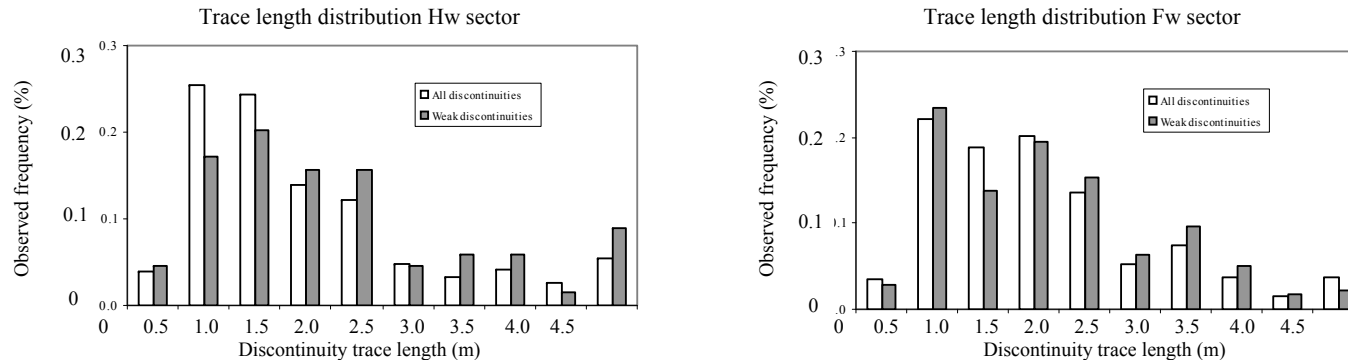


Figure 5.3.- Observed trace length in scanlines mapping, mean distribution for all sets.

Table 5.6. Roughness of weak discontinuity sets observed in scanlines mapping.

Sectors Studied	Set number	Dip / Dipdir	Number of data	Small Scale Roughness by ISRM (Brown, 1981), in term of percentage of observations									Large Scale Roughness (Laubscher 1993), %				
				Planar			Undulating			Stepped			Planar	Slight undulation	Curved	Wavy	
				Polished	Smooth	Rough	Polished	Smooth	Rough	Polished	Smooth	Rough				One-dir.	All-dir.
Hw	Set 1	86/182	52	0.0	1.9	17.3	38.5	13.5	23.1	1.9	1.9	1.9	13.0	48.1	27.8	9.3	1.9
	Set 2	83/282	44	4.5	11.4	13.6	13.6	18.2	25.0	11.4	2.3	0.0	8.7	37.0	41.3	10.9	2.2
	Set 3	12/251	32	0.0	3.1	12.5	25.0	15.6	28.1	6.3	6.3	3.1	6.1	39.4	39.4	9.1	6.1
	Total & Mean		132	1.5	5.3	14.4	25.8	15.9	25.8	6.1	3.8	1.5	9.5	41.6	35.8	10.2	2.9
Fw	Set 1	83/192	67	1.5	-	19.4	38.8	11.9	17.9	7.5	-	3.0	19.1	38.2	32.4	8.8	1.5
	Set 2	68/251	32	-	-	18.8	40.6	6.3	12.5	12.5	-	9.4	19.4	29.0	25.8	19.4	6.5
	Set 3	25/212	40	-	-	15.0	37.5	5.0	27.5	12.5	2.5	-	17.5	40.0	30.0	12.5	
	Set 4	74/301	26	-	-	3.8	76.9	7.7	11.5	-	-	-	4.2	41.7	54.2		
	Total & Mean		175	0.6	-	14.9	45.1	8.6	19.4	8.0	0.6	2.9	15.6	38.7	34.1	9.8	1.7

Note: The term polished has been used instead slickenside in the roughness profile, as ISRM (Brown 1981) recommend. The term slickenside have to be used only when evidence of previous shear displacement has been observed.

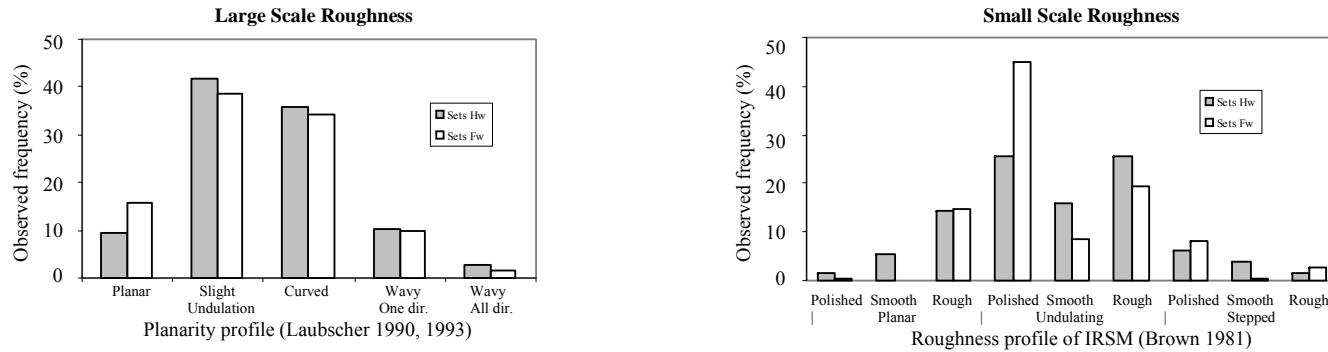


Figure 5.4.- Mean distributions of roughness profiles observed in weak discontinuities collected by scanline mapping.

Table 5.7. Thickness of weak discontinuity sets.

Sectors Studied	Mapping Scale	Set number	Dip / Dipdir	Number of data	Observed Thickness (%)											Mean (mm)	S.D. (mm)
					<1mm	1mm	2mm	3mm	4mm	5mm	6mm	7mm	8mm	9mm	≥ 10mm		
Hw	Drive Mapping	Set 1	74/182	89	-	4.5	13.5	18.0	13.5	15.7	3.4	4.5	3.4	-	23.6	6.1	4.8
		Set 2	77/318	18	-	11.1	11.1	5.6	5.6	33.3	-	5.6	5.6	-	22.2	6.0	4.2
		Set 3	24/228	14	-	7.1	21.4	21.4	21.4	7.1	-	7.1	-	-	14.3	4.3	2.8
		Set 4	65/359	24	-	12.5	12.5	16.7	8.3	16.7	-	-	12.5	-	20.8	7.5	8.3
	Total & Mean		167	-	7.8	14.4	18.6	11.4	16.2	1.8	3.6	5.4	-	21.0	6.0	5.3	
	Scanline Mapping	Set 1	86/182	53	13.2	35.8	24.5	11.3	1.9	5.7	1.9	0.0	1.9	-	3.8	3.2	5.3
		Set 2	83/282	46	4.3	65.2	17.4	8.7	-	-	-	-	-	-	4.3	2.4	3.5
		Set 3	12/251	20	-	30.0	30.0	15.0	10.0	5.0	-	5.0	-	-	5.0	3.9	5.2
		Total & Mean		136	9.6	46.3	22.1	10.3	2.9	2.9	0.7	0.7	0.7	-	3.7	2.8	4.4
	Oriented Drill Core Logging	Set 1	81/359	56	41.1	41.1	5.4	5.4	-	3.6	1.8	-	-	-	1.8	1.5	1.9
		Set 2	89/270	11	36.4	45.5	9.1	-	9.1	-	-	-	-	-	-	1.4	1.0
		Set 3	55/180	6	16.7	66.7	-	16.7	-	-	-	-	-	-	-	1.6	1.0
		Set 4	52/260	14	14.3	28.6	21.4	14.3	-	7.1	-	-	-	-	14.3	3.9	5.1
Total & Mean		98	32.7	38.8	10.2	9.2	1.0	3.1	2.0	-	-	-	3.1	1.9	2.6		
Fw	Drive Mapping	Set 1	72/194	112	-	6.3	11.6	21.4	9.8	16.1	6.3	2.7	7.1	0.9	17.9	6.0	4.8
		Set 2	85/125	37	-	15.4	38.5	23.1	7.7	7.7	-	-	-	-	7.7	14.6	24.0
		Set 3	41/065	13	-	13.6	18.2	13.6	9.1	27.3	4.5	-	4.5	-	9.1	3.1	2.4
		Set 4	75/022	22	-	2.7	8.1	16.2	16.2	13.5	2.7	5.4	5.4	-	29.7	4.2	2.6
	Total & Mean		197	-	6.6	14.2	20.8	10.7	15.7	4.6	2.5	5.6	0.5	18.8	7.1	12.3	
	Scanline Mapping	Set 1	83/192	68	13.2	51.5	14.7	8.8	4.4	2.9	-	1.5	1.5	-	1.5	2.1	1.8
		Set 2	68/251	32	18.8	50.0	15.6	12.5	3.1	-	-	-	-	-	-	1.6	1.0
		Set 3	25/212	40	2.5	65.0	20.0	5.0	2.5	2.5	-	-	-	2.5	-	1.9	1.5
		Set 4	74/301	26	19.2	30.8	19.2	19.2	7.7	-	-	-	-	-	3.8	3.1	5.6
	Total & Mean		176	12.5	51.7	17.0	9.7	4.0	1.7	-	0.6	0.6	0.6	1.7	2.1	2.8	
	Oriented Drill Core Logging	Set 1	68/192	91	28.6	35.2	15.4	5.5	2.2	4.4	3.3	1.1	1.1	0.0	3.3	2.3	2.9
		Set 2	80/293	112	15.2	58.0	12.5	6.3	1.8	3.6	0.9	0.0	0.0	0.0	1.8	1.8	1.9
		Set 3	66/005	37	29.7	54.1	10.8	5.4	0.0	0.0	0.0	0.0	0.0	0.0	0.0	1.3	0.7
Total & Mean		269	22.0	49.6	13.4	6.0	1.9	3.0	1.5	0.4	0.4	0.4	-	1.9	1.8	2.1	

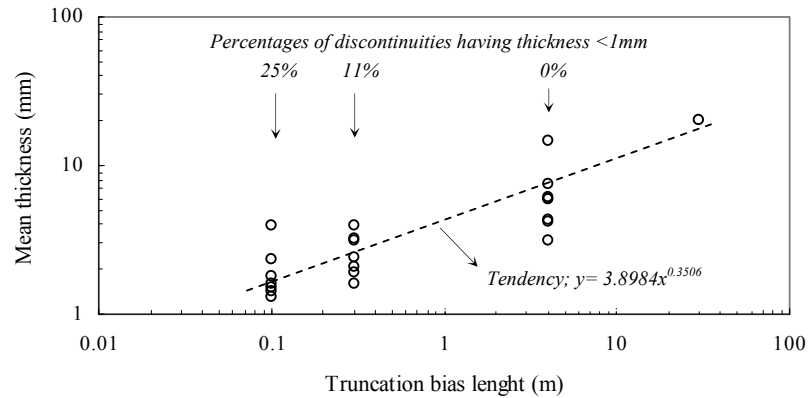


Figure 5.5.- Relationship between average thickness of discontinuity sets and truncation bias.

5.7 Block Size

Data of weak discontinuities set were used to stochastically simulate the rock structure and to determine in situ block size distributions as in section 3.8.2. The results for data collected in small scale sampling are presented in Figure 5.6.

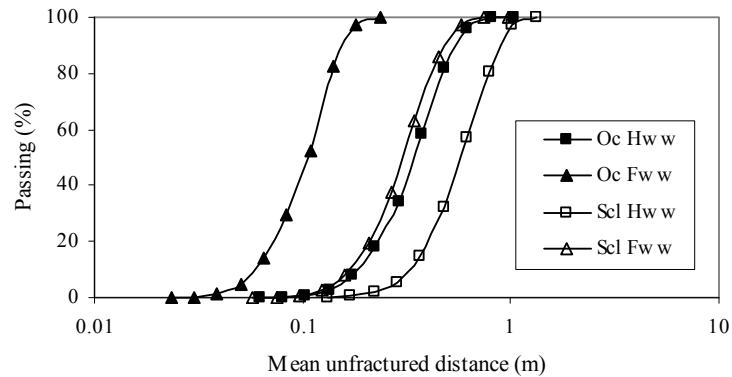


Figure 5.6.- Simulations of the mean unfractured distance for weak discontinuities. Scl; scanline mapping, Oc; oriented core logging, w; weak discontinuities.

This Figure 5.6 clearly shows that when empirical definition of weak discontinuities is adopted the andesite rock type from the *Hw* sector has a coarser in situ rock block size distribution than the *Fw* sector. These predicted differences shown in Figure 5.6 are in accordance with the observed behaviour at the studied mine sector (Villegas, 2006, Rojas, 2006). These predicted differences can not be well represented by the

rock mass quality index currently used at the mine site, where the andesite rock type is considered as having practically the same rating mine wide (see Table 1.2).

It is important to notice that the simulation assumed infinite trace length, which may be sub estimating block size definition where grater spacing is observed. This is the case observed at *Hw* sector, therefore andesite from this mine sector may have even coarser in situ block size distribution. These calculations did not include the vein thicknesses neither, which have been found as relevant factor during rock mass disassembly, i.e, these simulation should include only weak veins having thickness ≥ 2 mm. But additional problem with data collection would be encountered, which are discussed in the following section.

5.7.1 Block Size Distribution for Fragmentation

Data analyses of discontinuity spacing based on the thickness characteristics of veins are presented in Figure 5.7. In this figure the normal set spacing was estimated for all veins having thickness greater than or equal to $x = 0, 1, 2, 3$ mm. This procedure was repeated considering the case for weak veins only. Results from discontinuity set 1 (S1) identified in sampling data from the *Fw* sector are illustrated in this figure. Additional data set are presented in Figure 5.8.

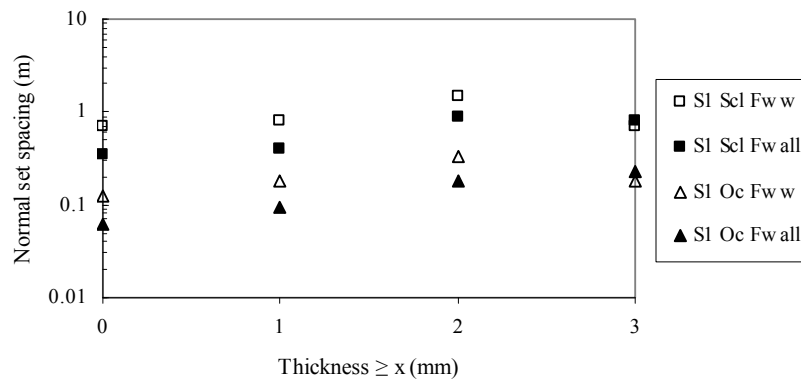


Figure 5.7.- Discontinuity spacing and thickness of discontinuities. Scl; scanline mapping, Oc; oriented core logging, w; weak discontinuities, all; all discontinuities.

Figure 5.7 and Figure 5.8 show that normal set spacing increase as the thickness threshold values increase. The observed spacing follows a clear trend, which is slightly different for vein thickness ≥ 3 mm in Figure 5.7. However, normal set

spacing estimates for veins having thickness $\geq 3\text{mm}$ may be inaccurate (Priest, 1993), because the sample length is not long enough to collect all possible spacing values as suggested Sen and Kazi (1984)². Data in this figure is also in agreement with the fact that discontinuity thickness correlated to the discontinuity size as shown Figure 3.25. It is expected that longer discontinuities are widely spaced and vice versa (scaling law property) for these parameters.

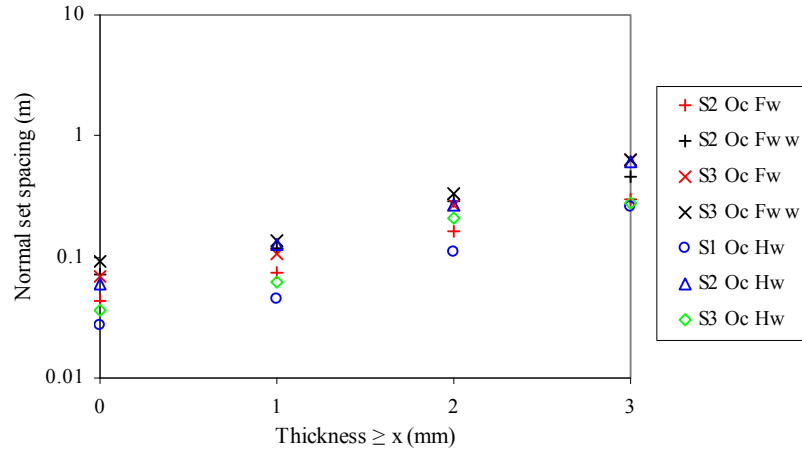


Figure 5.8.- Additional data points of the relationship between discontinuity spacing and thickness of discontinuities. Scl; scanline mapping, Oc; oriented core logging, w; weak discontinuities.

For practical purposes in rock mass characterization at the mine site, it is important to recognize that increasing the vein thickness as threshold value during data collection will require longer sampling lengths, which may constrain discontinuity surveys.

Another practical approach to obtain spacing values, for only veins having thickness greater than certain values from a limited sampling length, is by using the spacing ratio between weak and all veins of the same set. This ratio is called here as the 'incremental spacing' $\Delta S_{n,i}$. The incremental spacing is the ratio between weak and all discontinuities for each thickness threshold values, which can be estimated as follows:

² The values in Figure 5.7 are in logarithmic scale. In addition, poles used in spacing calculations decreased significantly by increasing thickness threshold, for example for S1 Oc Fw all; it was 146; 92; 42, 19. For S1 Oc Fw w; it was 89; 58; 25; 12.

$$\Delta S_{n,i} = \frac{|S_{n_{i,all}} - S_{n_{i,weak}}|}{S_{n_{i,all}}} \quad [\%] \quad (5.1)$$

where $S_{n_{i,all}}$ represent the normal set spacing of set i when all veins are included, $S_{n_{i,weak}}$ represent the normal set spacing of set i when only weak veins are included.

The spacing ratio between weak and all discontinuities for the data presented in Figure 5.7 is investigated by applying equation 5.1, but only until the vein thickness threshold value of 2mm. The results from data analysis are shown in Figure 5.9.

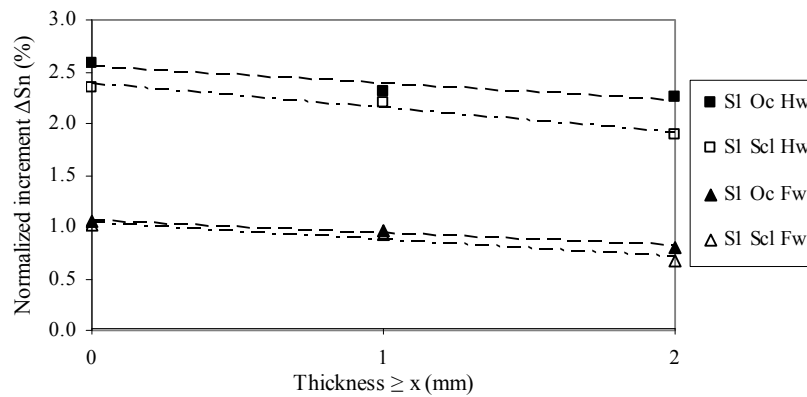


Figure 5.9.- Normalised increment of the discontinuity spacing and thickness of discontinuities. Scl; scanline mapping, Oc; oriented core logging.

Figure 5.9 shows that the incremental spacing decreases linearly with respect to the vein thickness threshold value. This figure also shows a good correlation between sampling techniques. The same data analysis undertaken for different sets, for example S2 and S3, found similar correlations.

Therefore, when only limited data is available, the normal set discontinuity spacing can be determined using the ‘incremental spacing approach’. I.e, given $\Delta S_{n,i}$ for $i=0$ (from Table 3.4 and Table 5.3), $S_{n_{i+1,weak}}$ can be determined assuming a similar tendency observed in Figure 5.9.

This procedure was used to obtain normal set spacing of thick weak veins for some data sets, particularly from Hw sector. Then, the rock structure was stochastically simulated again. In these new simulations, only weak veins having thickness ≥ 2 mm collected from oriented core logging were used, and the results are presented in

Figure 5.10. In order to assess the impact of incorporating these criteria on the total raw data, original simulations from Figure 3.32 are also included in this figure. As a comparison, this figure also includes the observed sizes of the caved rock block samples studied at the production level draw points (Chapter 4).

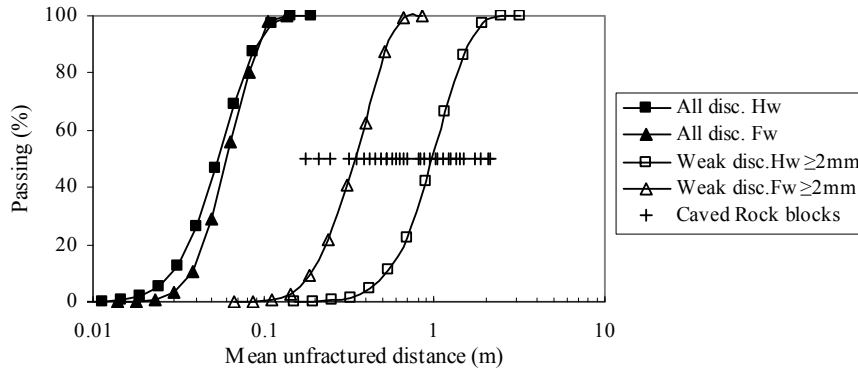


Figure 5.10.- Rock structure simulations for data collected in oriented core logging, considering all discontinuities and only weak ones having thickness ≥ 2 mm.

Data in Figure 5.10 still show that andesite Fw is more *'fractured'* (by thicker weak veins) than the andesite Hw. This figure also shows that the simulated sizes of rock block are in accordance with the observed rock block size in production level caving draw points. Therefore, despite of the assumption involved in these calculations, the result are more in agreement with what has been observed at the mine site.

5.7.2 Fragmentation Model

Figure 5.10 reveals an important concept of the primary copper ore fragmentation at the El Teniente mine. This concept is outlined in Figure 5.11, and differs from the traditional view (Hudson and Harrison, 1997, p.241). The in situ block size distribution defined by considering only weak discontinuities represents the *'potential fragmentation'* of the rock mass. These discontinuities need to be broken (mobilised, opened) to define either a removable rock block face or a removable rock block. In other words, the rock block assembly that comprise the rock mass is cemented, consequently the in situ rock block distribution is that one that the loading condition imposed by cave propagation can create. However, it is not expected that every single weak discontinuity will be opened during the caving process. The

cavability and the fragmentation of primary copper ore will depend, as suggested by Duplancic (2002), on the geological structures, the rock mass strength and the in situ field stresses.

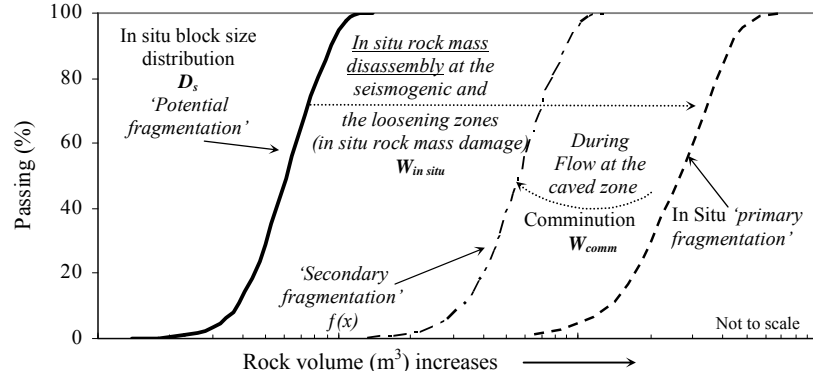


Figure 5.11.- Conceptual framework of the fragmentation in the primary copper ore at the El Teniente mine.

The duration of the loading conditions imposed by stress redistribution from the cave propagation or the intensity of the seismogenic zone (Duplancic, 2002), will likely determine the degree of the in situ rock mass disassembly. This phenomenon is referred as in situ '*primary fragmentation*' in Figure 5.11. The '*secondary fragmentation*' will then result from the *comminution process* (Laubscher, 2001) or *excavation process* (Hudson and Harrison, 1997) that occurs during flow at the caved zone.

Therefore, in order to predict the in situ primary fragmentation (called as *is situ fragmentation* by Laubscher 2001, among others) of the primary copper ore at the El Teniente mine or perhaps, in another rock mass of primary ore with stockwork veins, it is required to characterize the three-dimensional nature of the rock structure as well as to quantify the in situ disassembly of the rock mass at the *seismogenic* and the *loosening zones* (Duplancic, 2002).

The expected rock mass fragmentation at any draw point, $f(x)$, is given by:

$$f(x) = (D_s; W_{in-situ}; W_{comm}) \quad (5.2)$$

where $f(x)$, is a function of; D_s , the in situ rock block distribution (the potential fragmentation), $W_{in\ situ}$, the rock damage reached at the seismogenic zone, and W_{comm} , the comminution process³.

5.8 Conclusions

Similar to previous chapter, the geometrical and strength characteristics of discontinuities were analysed considering only for weak discontinuities, data analysis indicates the following:

It has been found that weak discontinuities have the same average characteristic as all mapped discontinuities combined. For example, the observed trace length, discontinuity roughness and thickness present almost the same mean values and distribution shapes for both the weak as well as the whole discontinuity population.

The occurrence of weak discontinuities varies throughout the rock masses. It was found more abundance of weak discontinuities and finer in situ rock block distribution at the andesite Fw sector compared to the andesite Hw sector. This also correlates with the geological division of hydrothermal alteration zones, where the PH hydrothermal alteration zone presents more abundance of weak veins. This rock structure characteristics agree with fragmentation performance during caving (Villegas, 2006, Rojas, 2006).

The new-established empirical definition of weak discontinuities proves to be a good criterion to be used to discriminate rock mass quality between the two studied areas of Reno mine sector.

Taking into account these rock structure characteristics a fragmentation model of primary copper ore is formulated through this chapter. This model differ from the traditional model (Hudson and Harrison, 1997) only because the rock block ensemble that comprise the rock mass are cemented. Then in strict sense, there is not an in situ rock block distribution defined by joints. The in situ rock block distribution or *in situ fragmentation* occurs after the loading conditions have been imposed by cave propagation.

³ In this concept, natural features of the rock mass flow such as fine migration it is also included.

CHAPTER 6 ROCK MASS CLASSIFICATION SYSTEMS

6.1 Introduction

Rock mass classification (RMC) systems have been developed and used since the 1950's as design tools in civil and mining projects. Initially developed for tunnelling reinforcement (Terzaghi, 1946), these have been extended to multiple civil engineering applications (Barton et al., 1974, Hoek et al., 1995, Laubscher, 1993). One of the main purposes of these RMC schemes is to determine rock mass quality and to predict their rock mass behaviour under particular excavation conditions. These RMC systems are used at the world wide mining industry, being part of every mining project.

The RMC schemes are based on the parameterization of the geological features of a rock mass. These systems simplify the rock mass into two main components; the properties of the intact rock material and the geological discontinuities. Numerical values are assigned to the intact rock properties and to the discontinuity parameters that most likely influence the rock mass behaviour into one overall rating of a rock mass. Some schemes have included the stress condition surrounding excavation in this assessment. The overall rating of the rock mass is correlated with observed experiences to provide estimates of the strength and deformation properties of the rock mass, as well as support requirements and cavability. As more case histories became available over the years most RMC systems were modified or updated to account for different behaviours.

6.1.1 Goal

The main objective of this chapter is to describe the application of the current rock mass classification systems to rock masses of primary copper ore. In order to achieve this objective, a literature review for main RMC systems used by the mine industry was undertaken. Using the rock structure data obtained through previous Chapters 3 and 5, these current RMC schemes were utilized to evaluate the rock mass quality within the two sectors of Reno mine (*H_w* and *F_w*). The applicability of RMC systems was tested using the definition of weak discontinuities.

6.2 Rock Quality Designation, RQD

The rock quality designation (*RQD*) is a quantitative index of rock quality developed for drill cores (Deere, 1964). For a 50mm core, it is defined as the percentage of core-recovery that incorporates pieces of core longer than 100 millimeters. In other words, it is the percentage of intact rock length or un-fractured distance along the core axis longer than 100 millimeters.

For *RQD* determination, the ISRM has suggested a core size of at least NX diameter (54.7 millimeters) drilled with double tube core barrels (Brown, 1981). Deere (1968) has proposed a relationship between the *RQD* index and the rock mass quality for engineering purposes (in Figure 6.1). In this figure the procedure to measure the *RQD* index is explained in a detailed example.

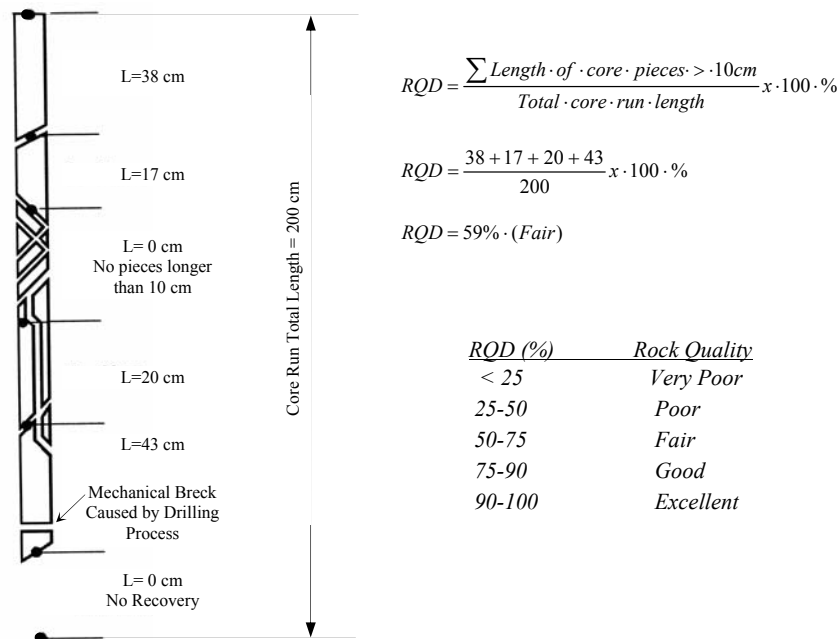


Figure 6.1.- Procedure for measurement and calculation of RQD (Deere, 1968).

Hence, *RQD* is an indirect measurement of rock mass fracturing. Some researches have established a relationship between *RQD* and the discontinuity¹ frequency λ . An example of this, is equation 3.26 given in Section 3.8.1.

¹ In this case, discontinuities are defined as suggested ISRM (Brown, 1981).

In addition, for a discontinuity spacing that follow a negative exponential distribution, Priest and Hudson (1976) has suggested the following formula:

$$RQD^* = 100(0.1\lambda + 1)e^{-0.1\lambda} \quad (6.1)$$

where RQD^* represent the theoretical RQD determined from the distribution of spacing values. Equation 6.1 is approximately linear in the range $6 < \lambda < 16$, which gives:

$$RQD^* = 110.4 - 3.68\lambda \quad (6.2)$$

Equation 6.1 is most sensitive for spacing values ranging from 0 to 0.3m (Priest and Hudson, 1976). Therefore, a general equation to overcome the lack of sensitivity for large mean spacing values is proposed by Priest and Hudson (1976) as follows:

$$RQD^* = 100(\lambda t + 1)e^{-\lambda t} \quad (6.3)$$

where t represent any threshold value, i.e., t could be the conventional value of 0.1m or a higher threshold, say of 1.0m.

Because the discontinuity frequency varies with the direction of the sampling line (represented as the three dimensional loci in Section 3.3.4 and Figure 3.14), RQD also varies with direction. Therefore, RQD is only representative of the direction in which it has been measured.

6.2.1 Applying RQD to the El Teniente Primary Copper Ore

As discussed in previous chapters, almost no joints have been found within primary copper ore and the main faults appear widely spaced. Hence, by definition, the measurements of RQD at the El Teniente mine are always close to 100% (Figure 6.2). Therefore, it can be concluded that RQD is not an adequate index to discriminate the quality of these rock masses. Un example of this is the following;

Figure 6.2 shows photography of a drill core sample extracted from a pillar in the production level of the Reno mine sector. The core sample was recovered after the pillar was loaded by stress redistribution due to cave propagation, i.e., the cave front has already passed above the pillar before core extraction (see Figure 1.15). This particular core section in andesite rock type shows a RQD over 90%, but borehole

camera records within the pillar did not find any fracture in the same core section (Brzovic et al., 1998). Therefore, fractures observed in this photography may be related to fracturing during either drill coring or core transportation. It is important to note that most of this new fracturing occurs through veins.

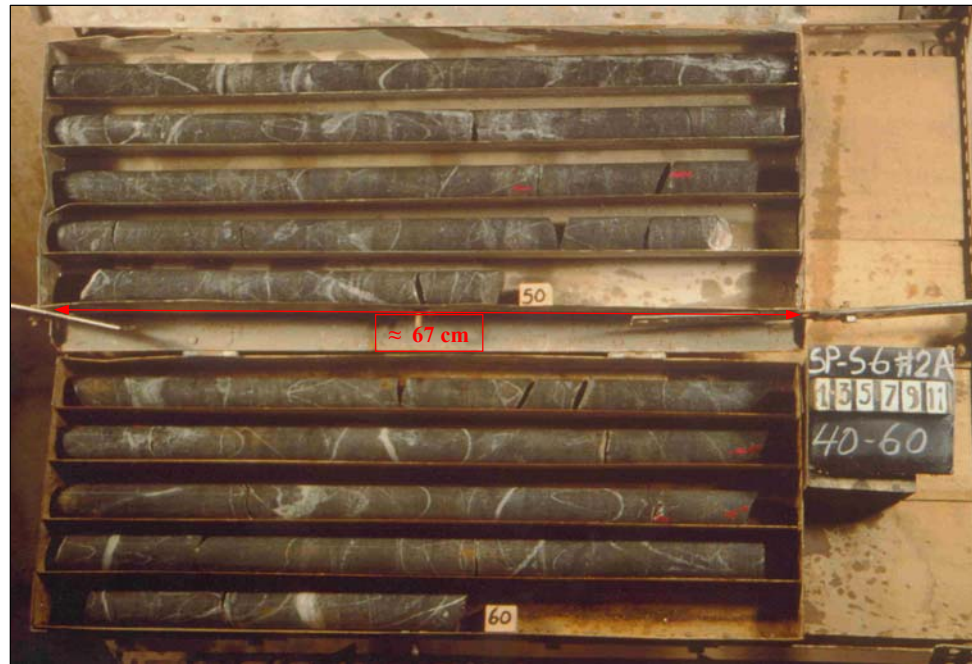


Figure 6.2.- Typical core-recovery on core tray for andesite rock type at the El Teniente mine (Brzovic et al., 1998).

6.3 Geomechanics Classification, RMR

The Geomechanics Classification or the Rock Mass Rating (*RMR*) system was developed by Bieniawski (1973). As more case histories were made available over the years, this scheme was upgraded several times (Bieniaswki, 1973, Bieniaswki, 1976, Bieniaswki, 1989). Although, this *RMR* index was originally developed for estimation of tunnelling support, its application has been modified and extended to mining applications as the case of the mining rock mass rating (Laubscher, 1973). Hereafter, this index is denoted as *RMR_B*.

The Geomechanics Classification utilises six parameters to classify a rock mass. These are as follow (in Table 6.1):

1. Uniaxial Compressive Strength (UCS) of rock material.

Table 6.1. The Rock Mass Rating System (after Bieniawski 1989).

A. CLASSIFICATION PARAMETERES AND THEIR RATINGS									
Parameter		Range of values							
1	Strength of intact rock material	Point-load strength index	>10 MPa	4-10 Mpa	2-4 MPa	1-2 MPa	For this low range-uniaxial compressive test is preferred		
		Uniaxial comp. strength	>250 MPa	100-250 Mpa	50-100 MPa	25-50 MPa	5-25 MPa	1-5 MPa	<1 MPa
	Rating	15	12	7	4	2	1	0	
2	Drill core Quality RQD	90%-100%	75%-90%	50%-75%	25%-50%	<25%			
	Rating	20	17	13	8	3			
3	Spacing of discontinuities	>2 m	0.6-2.m	200-600 mm	60-200 mm	<60mm			
	Rating	20	15	10	8	5			
4	Condition of discontinuities (see E)	Very rough surfaces Not continuous No separation Unweathered wall rock	Slightly rough surfaces Separation <1mm Slightly weathered walls	Slightly rough surfaces Separation <1mm Highly weathered walls	Slickensided surfaces, or Gouge < 5 mm thick, or Separation 1-5mm Continuous	Soft gouge > 5 mm thick or Separation > 5 mm Continuous			
		Rating	30	25	20	10	0		
5	Ground water	Inflow per 10m tunnel length (l/m)	None	<10	10-25	25-125	>125		
		(Joint water press)/ (Major Principal Stress)	0	<0.1	0.1-0.2	0.2-0.5	>0.5		
	General conditions	Completely dry	Damp	Wet	Dripping	Flowing			
	Rating	15	10	7	4	0			
B. RATING ADJUSTMENT FOR DISCONTINUITY ORIENTATIONS (See F)									
Strike and dip orientations		Very favourable	Favourable	Fair	Unfavourable	Very Unfavourable			
Ratings	Tunnels	0	-2	-5	-10	-12			
	Foundations	0	-2	-7	-15	-25			
	Slopes	0	-5	-25	-50	-60			
C. ROCK MASS CLASSES DETERMINED FROM TOTAL RATINGS									
Rating	100 ← 81		80 ← 61		60 ← 41		40 ← 21		< 20
Class number	I		II		III		IV		V
Description	Very good rock		Good rock		Fair rock		Poor rock		Very poor rock
D. MEANING OF ROCK CLASSES									
Class number	I		II		III		IV		V
Average stand-up time	20 years for 15 m span		1 year for 10 m span		1 week for 5 m span		10 hrs for 2.5 m span		30 min for 1 m span
Cohesion of rock mass	> 400		300-400		200-300		100-200		<100
Friction angle of rock mass (deg)	> 45		35-45		25-35		15-25		<15
E. GUIDELINESS FOR CLASSIFICATION OF DISCONTINUITY CONDITIONS*									
Discontinuity length (persistence)	< 1 m		1 - 3 m		3 - 10 m		10 - 20 m		> 20 m
Rating	6		4		2		1		0
Separation (aperture)	None		< 0.1 mm		0.1-1.0 mm		1 - 5 mm		> 5 mm
Rating	6		5		4		1		0
Roughness	Very rough		Rough		Slightly rough		Smooth		Slickenside
Rating	6		5		3		1		0
Infilling (gouge)	None		Hard filling <5mm		Hard filling > 5mm		Soft filling <5mm		Soft filling > 5mm
Rating	6		4		2		2		0
Weathering	Unweathered		Slightly weathered		Moderately weathered		Highly weathered		Decomposed
Rating	6		5		3		1		0
F. EFFECT OF DISCONTINUITY STRIKE AND DIP ORIENTATION IN TUNNELING									
Strike perpendicular to tunnel axis				Strike parallel to tunnel axis					
Drive with dip-Dip 45-90°		Drive with dip-Dip 20-45°		Dip 45-90°		Dip 20-45°			
Very favourable		Favourable		Very Unfavourable		Fair			
Drive against dip-Dip 45-90°		Drive against dip-Dip 20-45°		Dip 0-20° Irrespective of Strike					
Fair		Unfavourable		Unfavourable					

*Note: Some conditions are mutually exclusive. For example, if infill is present, it is irrelevant what the roughness may be used, since its effect will be overshadowed by the influence of the gouge, in this case use A.4 directly.

2. Rock quality designation (*RQD*).
3. Spacing of discontinuities.
4. Condition of discontinuities.
5. Groundwater conditions.
6. Orientation of discontinuities.

The calculations of the parameters involved in the geomechanics classification system (RMR_B) of rock masses are presented in Table 6.1.

The first five parameters are grouped into five ranges values, and these parameters are not equally important to classify the rock mass behaviour. Therefore, ‘importance ratings are allocated to the different value range of the parameters’ (Bieniaswki 1989, p.53), where an overall higher rating indicating better rock mass conditions.

The sums of these five parameters determine the rock mass rating, which is adjusted according to the predominant discontinuity orientation (part B in Table 6.1). The total rock mass rating can lineally range from 9 to 100. The rock mass is classified into five rock mass class according to the resulting rating, from very poor to very good (part C in Table 6.1). The rock mass classes can then be related to specific engineering problems, such as stand-up time and maximum stable rock span, or rock reinforcement for tunnels.

6.3.1 RMR_B Application to the El Teniente Primary Copper Ore

Table 6.2 summaries the application of RMR_B to the structural data observed within primary copper ore.

Table 6.2. Applicability of RMR_B to the El Teniente primary copper ore.

Parameters	Parameters description	Andesite <i>Hw</i> Sector Rating	Andesite <i>Fw</i> Sector Rating
UCS	120 MPa for andesite rock type (from Table 1.2)	11	11
RQD	RQD is 100% and the same at any case	20	20
Spacing	Considering weak discontinuities data from scanlines (or from oriented core logging)	14 (8)	11 (7)
Joint Condition	Weak veins (3;2;3;4;6 from part E in Table 6.1)	18	18
Ground Water	Completely dry prior mining	15	15
RMR_B		78-72	75-71
		Good	Good

The analysis shows that the RMR_B fails to determine rock mass quality of the primary copper ore, mainly due to its inability to incorporate healed veins as a rock mass failure controlling parameter. In this respect, the only discontinuity infill characteristic included in this scheme is either hard or soft gouge (part E in Table 6.1), and the actual observed joint conditions was forced to fit within these infill parameter description. In other words, by arbitrarily setting the joint condition, it is

assumed that a hard gouge has the same strength properties to the mineralogical infill that define a weak vein (which is not necessarily true).

In addition, spacing is the only parameter that really shows differences between the clearly different mine sectors. It is important to note that the RMR_B scheme does not specify how the data must be collected or if a specific truncation bias length should be adopted during data collection. In the example of Table 6.2, the discontinuity spacing was arbitrarily chosen from line mapping in mine drives, but it may vary considerably if data collected from a small diameter core samples is used (see discussion in Section 3.3.4).

6.4 Q-System

Barton, Lien and Lunde have developed the Q-system of rock mass classification in 1974, with focus on tunnel and cavern support selection (Barton et al., 1974). This system was based on data analysis of 212 tunnels case histories from Scandinavia. The Q-System uses six different parameters to assess a numerical value that can be used to represent the rock mass quality. These parameters are grouped in three quotients as following:

$$Q = \left(\frac{RQD}{J_n} \right) \times \left(\frac{J_r}{J_a} \right) \times \left(\frac{J_w}{SRF} \right) \quad (6.4)$$

where,

1. RQD is rock quality designation.
2. J_n is the joint set number.
3. J_r is the joint roughness number.
4. J_a is the joint alteration number.
5. J_w is the joint water reduction factor.
6. SRF is the stress reduction factor.

The values of each parameter are estimated from Table 6.3. Calculation of Q results on a logarithmic rock mass quality scale, which can range from 0.001 to 1000. Grimstad and Barton (1993) have updated the Q-System to incorporate a modified stress reduction factor.

Table 6.3. Current Q-System description after Barton et al. (1974).

PARAMETERS DESCRIPTION	VALUE	NOTES
1. ROCK QUALITY DESIGNATION	RQD	
A. Very poor	0-25%	(i) Where RQD is reported or measured as ≤ 10 (including 0), a nominal of 10 is used to evaluate Q
B. Poor	25-50%	(ii) RQD intervals of 5, i.e. 100, 95, 90 etc. are sufficiently accurate.
C. Fair	50-75%	
D. Good	75-90%	
E. Excellent	90-100%	
2. JOINT SET NUMBER	Jn	
A. Massive, no or few joints	0.5-1	(i) For intersections use (3.0 x Jn).
B. One joint set	2	(ii) For portals use (2.0 x Jn).
C. One joint set plus random	3	
D. Two joint sets	4	
E. Two joint sets plus random	6	
F. Three joint sets	9	
G. Three joint sets plus random	12	
H. Four or more joint sets, random, heavily jointed, "sugar cube", etc.	15	
J. Crushed rock, earth-like	20	
3. JOINT ROUGHNESS NUMBER	Jr	
(a) Rock wall contact		
(b) Rock wall contact before 10 cms shear		
A. Discontinuous joints	4	(i) Descriptions refer to small-scale features to intermediate scale features, in that order.
B. Rough and irregular, undulating	3	(ii) Add 1.0 if the mean spacing of the relevant joint set is greater than 3 m.
C. Smooth undulating	2	(iii) Jr = 0.5 can be used for planar, slickensided joints having lineations, provided that the lineations are oriented for minimum strength.
D. Slickenside undulating	1.5	
E. Rough or irregular, planar	1.5	
F. Smooth, planar	1	
G. Slickenside, planar	0.5	
(c) No rock wall contact when sheared		
H. Zones containing clay minerals thick enough to prevent rock wall contact	1.0 (nominal)	
J. Sandy, gravely or crushed zone thick enough to prevent rock wall contact	1.0 (nominal)	
Notes Continuation: (iv) Jr and Ja classification is applied to the joint set or discontinuity that is least favourable for stability both from the point of view of orientation and shear resistance, τ (where $\tau \approx \sigma_n \tan^{-1}(Jr/Ja)$).		
4. JOINT ALTERATION NUMBER	Ja	ϕ_r (approx.)
(a) Rock wall contact (no mineral filling, only coating)		
A. Tightly healed, hard, non-softening, impermeable filling	0.75	(i) Values of ϕ_r , the residual friction angle, are intended as an approximate guide to the mineralogical properties of the alteration products, if present.
B. Unaltered joint walls, surface staining only	1	25°-35°
C. Slightly altered joint walls, non-softening mineral coatings, sandy particles, clay-free disintegrated rock, etc.	2	25°-30°
D. Silty-, or sandy-clay coatings, small clay-fraction (non-softening)	3	20°-25°
E. Softening or low-friction clay mineral coatings, i.e. kaolinite, mica. Also chlorite, talc, gypsum and graphite etc., and small quantities of swelling clays. (Discontinuous coatings, 1-2 mm or less in thickness)	4	8°-16°
(b) Rock wall contact before 10cm shear (thin mineral filling)		
F. Sandy particles, clay-free, disintegrating rock etc.	4	25°-30°
G. Strongly over-consolidated, non-softening clay mineral fillings (continuous <5 mm thick)	6	16°-24°
H. Medium or low over-consolidation, softening clay mineral fillings (continuous < 5 mm thick)	8	12°-16°
J. Swelling clay fillings, i.e., montmorillonite, (continuous < 5mm thick). Values of Ja depend on percent of swelling clay-size particles, and access to water etc.	8-12	6°-12°
(c) No rock wall contact when sheared (thick mineral fillings)		
K, L, M. Zones or bands of disintegrated or crushed rock and clay (see G, H and J for clay condition)	6, 8 or 8-12	(6°-24°)
N. Zones or bands of silty – or sandy-clay, small clay fraction, non-softening	5	
O, P, R. Thick continuous zones or bands of clay (see G.H and J for clay conditions)	10, 13 or 13-20	(6°-24°)
5. JOINT WATER REDUCTION	Jw	Approx. water pressure (kg/cm ²)
A. Dry exaction or minor inflow i.e. <5 l/m locally	1	<1
B. Medium inflow or pressure, occasional outwash or joint fillings	0.66	1.-2.5
C. Large inflow or high pressure in competent rock with unfilled joints	0.5	2.5-10
D. Large inflow or high pressure	0.33	2.5-10
E. Exceptionally high inflow or pressure at blasting, decaying with time	0.2-0.1	>10
F. Exceptionally high inflow or pressure	0.1- 0.05	>10
Notes Continuation: (iii) For general characterisation of rock masses distant from excavations influences, the use of Jw = 1.0, 0.66, 0.5, 0.3, etc. as depth increases from say 0-5, 5-25, 25-250 to >250 m is recommended, assuming that RQD/Jn is low enough (e.g. 0.5-25) for goog hydraulic connectivity. This will help to adjust Q for some of the effective stress and water softening effects, in combination with appropriate characterization values of SRF. Correlations with depth-dependent static deformation modulus and seismic velocity will then follow the practice used when these were developed.		

Continuation of **Table 6.3**. Current Q-System description after Barton et al. (1974).

PARAMETERS DESCRIPTION	VALUE	NOTES	
6. STRESS REDUCTION FACTOR	SRF		
(a) <i>Weakness zones intersecting excavation, which may cause loosening of rock mass when tunnel is excavated</i>		(i) Reduce these values of SRF by 25-50% if the relevant shear zones only influence but do not intersect the excavation. This will also be relevant for characterisation.	
A. Multiple occurrences of weakness zones containing clay or chemically disintegrated rock, very loose surrounding rock (any depth).	10		
B. Single weakness zones containing clay, or chemically disintegrated rock (excavation depth ≤ 50 m).	5		
C. Single weakness zones containing clay, or chemically disintegrated rock (excavation depth >50 m).	2.5	(ii) For strongly anisotropic virgin stress field (if measured):	
D. Multiple shear zones in competent rock (clay free), loose surrounding rock (any depth).	7.5	When $5 \leq \sigma_1/\sigma_3 \leq 10$, reduce σ_c and σ_t to $0.8\sigma_c$ and $0.8\sigma_t$. When $\sigma_1/\sigma_3 > 10$, reduce σ_c and σ_t to $0.6\sigma_c$ and $0.6\sigma_t$, where σ_c is the unconfined compression strength, σ_t is the tensile strength, and σ_1 and σ_3 are the major and minor principal stresses.	
E. Single shear zone in competent rock (clay free) (Depth of excavation ≤ 50 m).	5	(iii) Few case records available where depth of crown below surface is less than span width, suggest an SRF increase from 2.5 to 5 for such cases (see H).	
F. Single shear zone in competent rock (clay free) (Depth of excavation >50 m).	2.5	(iv) Cases L, and M are usually most relevant for support design of deep tunnels excavations in hard massive rock masses, with RQD/J_n ratios from about 50-200.	
G. Loose open joints, heavily jointed or "sugar cube" etc. (any depth).	5		
(b) <i>Competent rock, rock stress problems</i>			
H. Low stress, near surface	$\sigma_c / \sigma_1 > 200$	$\sigma_1 / \sigma_3 < 13$	2.5
J. Medium stress	200-10	13-0.66	1
K. High stress, very tight structure (usually favourable to stability, may be unfavourable to wall stability)	10-5	0.66-0.33	0.5-2
L. Mild rockburst (massive rock)	5-2.5	0.33-0.16	5-10
M. Heavy rockburst (massive rock)	< 2.5	0.16	10-20
(c) <i>Squeezing rock, plastic flow of incompetent rock under influence of high rock pressure</i>			
N. Mild squeezing rock pressure			5-10
O. Heavy squeezing rock pressure			10-20
(d) <i>Swelling rock, chemical swelling activity depending on presence of water</i>			
P. Mild squeezing rock pressure			5-10
R. Heavy squeezing rock pressure			10-15
Notes (v) For general characterisation of rock masses distant from excavations influences, the use of $SRF = 5, 2.5, 1$, and 0.5 is recommended as depth increases from say 0-5, 5-25, 25-250 to >250 m.. This will help to adjust Q for some of the effective stress and water softening effects, in combination with appropriate characterization values of SRF .			

Notes, some useful notes which are not included in the original paper (Barton et al. 1974) were added from notes presented in Barton (2002).

According to Barton et al. (1974) these 3 quotients represent different aspects of the principal properties controlling tunnel stability in rock masses. The overall structure of rock mass is representing by the first quotient (RQD/J_n), and it is 'a crude measure of the relative block size'.

The second quotient (J_r/J_a) represents the shear strength of joints or filling materials, which control the inter-block behaviour. The third quotient (J_w/SRF) represents the active stress affecting the rock mass by water pressure and natural/induced loading/unloading conditions.

The Q-System is classified into nine-rock mass class according to the resulting rating, from exceptionally poor, to exceptionally good. Furthermore, those values are classified into different support categories (Figure 6.3).

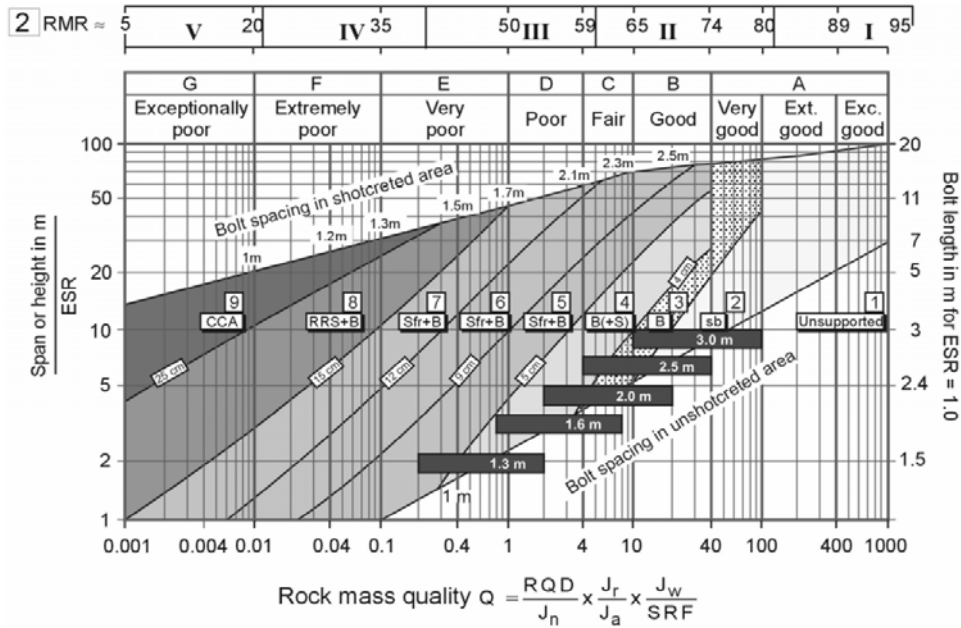


Figure 6.3.- The Q-support chart update for Sfr (instead of Smr), after Grimstad and Barton (1993). ESR= excavation support ratio, [2] $RMR_b = 15LnQ + 50$.

6.4.1 Q-System Application to the El Teniente Primary Copper Ore

Table 6.4 summaries the application of Q-System to the structural data observed within primary copper ore. In this table two cases were considered, when only faults or when only weak veins are considered to be the weaker path controlling failure within these rock masses.

The results shown in Table 6.4 for the application of the Q-System are, in some respect, meaningless. The primary copper ore is definitely not a very poor to poor rock mass under stress condition, and even a ‘good quality’ only for characterisation seems to underestimate its competent features. A number of problems were encountered when this system was applied using the structural data. These are as follow:

Although the first quotient RQD/J_n is a crude measure of block size (Barton et al., 1974), it cannot reflect the differences observed between andesite sectors as shown Figure 5.6. This is mainly due to two reasons. Firstly, existing weak veins cannot be adequately represented by RQD . Secondly, this classification scheme does not incorporate and rate discontinuity spacing as an independent parameter, which is the

main observed difference between the andesite sectors. Discontinuity spacing should be included within RQD estimates, but this cannot be done with healed veins.

Table 6.4. Q -System for the El Teniente primary copper ore.

Parameters	Parameters description	Andesite Hw Sector Values/Rating		Andesite Fw Sector Values/Rating	
		Faults	Weak Veins	Faults	Weak Veins
RQD	100% at any case or orientation	100%		100%	
J_n	Considering few joints (two fault sets*) OR at least 3 semi-orthogonal sets plus random of weak discontinuities	4	12	4	12
$Quotient RQD/J_n$		25	8.3	25	8.3
J_r	Slickensided to smooth undulating for both discontinuity types (3C-D in Table 6.3, data from Figure 3.31) + 1.0 for sparse fault	3	1.5	3	1.5
J_a	Medium and low over-consolidation gouge in faults OR healed and impermeable filling in weak veins	8.0	0.75	8.0	0.75
$Quotient J_r/J_a$		0.38	2.0	0.38	2.0
$\Phi = \tan^{-1}(J_r/J_a)$		20°	63°	20°	63°
J_w	Dry excavations	1.0		1.0	
SRF^{\ddagger}	Competent and massive rock mass with rock stress problem (rockburst) and $\sigma_c/\sigma_1 = 120\text{MPa}/(46 \text{ or } 30\text{MPa}) \approx 2.6 \text{ or } 4.0$ (from Table 1.2 and Figure 1.15). [for characterisation only, SRF can be used as 0.5]	10 [‡] [0.5]		5 [0.5]	
$Quotient J_w/SRF$ [with SRF as 0.5]		0.1 [2]		0.2 [2]	
Q		0.95	1.66	1.9	3.32
		V.Poor	Poor		
[Q for characterisation (Grimstad and Barton, 1993)]		[19]	[33.2]	[19]	[33.2]
		[good]			

Note*: Fault sets present spacing over 3 meters. ‡: Hw sector is assumed with less σ_1 because of the less overburden (see Figure 1.3). †: Considering the updated SFR (Grimstad and Barton, 1993) these values may change by 50 and 10 respectively, nevertheless for characterisation purposes (far from excavations) a value of 0.5 is recommended for depth >250m as the case studied here.

In addition, because discontinuity spacing is not included as an independent parameter, it would not be matter how the data collection was conducted; in term of truncation bias. The scale of the problem to be analysed is not appropriately specified.

The value of 0.75 for parameter J_a (part 4.A in Table 6.3) does not represent adequately a weak vein infill, because 'rock wall contact' or 'coating' represent a very thin infill. A better value would be of 8 (part 4.L in Table 6.3) since there is 'not rock wall contact when sheared (thick mineral infill)' as found Section 4.2.4. However infill minerals described in this part 4.L are; clay, sandy, gravely and crushed minerals (not applicable at the El Teniente). Nevertheless, using 0.75 for parameter J_a , the $\tan^{-1}(J_r/J_a)$ becomes 63° ($\approx \Phi$), which is a better representation of a vein shear strength compared to $\Phi \approx 12^\circ$ when J_a assumes a value of 8.

Using Q' as the result of the two first quotients, both andesite sectors are practically the same for each case in Table 6.4. Considering the case for characterisation, i.e., assuming rock mass distant from excavations; for a depth greater than 250m, a value of 0.5 is recommended for SRF (Grimstad and Barton, 1993). In this case the values of Q' are in agreement to these shown in Table 1.2, but the observed differences between andesite sectors cannot be replicated by Q-system. Therefore, the Q -system is also unable to adequately determine the quality of rock masses of primary copper ore. The geological features observed within these rock masses cannot be represented by the parameters that Q-system uses to estimate rock mass quality.

6.5 Geological Strength Index, GSI

Hoek (1994) and Hoek et al. (1995) have introduced the Geological Strength Index (GSI) to overcome limitations with RMR_B (Bieniaswki, 1989) system when the Hoek-Brown failure criterion (Hoek et al. 1995) is applied. The GSI is mainly used to determine rock mass properties based on this failure criterion. Marinis and Hoek (2000) have extended this index for heterogeneous rock masses.

The GSI index utilises two main parameters to classify a rock mass; the overall rock block structure and the surface condition (interlocking) separating these rock blocks (Figure 6.4). The GSI values range from 10 to 100, from extremely poor rock mass to massive rock mass and/or intact rock.

6.5.1 GSI Application to the El Teniente Primary Copper Ore

The term 'Blocky' in Figure 6.4 is would better represent the rock structure characteristics at the El Teniente mine, but the surface condition of discontinuities are far from the observed features within primary copper ore. Therefore, it is clear that GSI index cannot be applied to determine rock mass quality to these rock masses. Any attempt to used GSI to represent rock mass quality will be as the case of RMR_B , i.e., forcing observed discontinuity parameters to fit these with 'similar characteristic' described in the classification scheme.







<p>GEOLOGICAL STRENGTH INDEX FOR JOINTED ROCKS (Hoek and Marinos, 2000)</p> <p>From the lithology, structure and surface conditions of the discontinuities, estimate the average value of GSI. Do not try to be too precise. Quoting a range from 33 to 37 is more realistic than stating that GSI = 35. <u>Note that the table does not apply to structurally controlled failures.</u> Where weak planar structural planes are present in an unfavourable orientation with respect to the excavation face, these will dominate the rock mass behaviour. The shear strength of surfaces in rocks that are prone to deterioration as a result of changes in moisture content will be reduced if water is present. When working with rocks in the fair to very poor categories, a shift to the right may be made for wet conditions. Water pressure is dealt with by effective stress analysis.</p>		<p>SURFACE CONDITIONS</p> <p>VERY GOOD Very rough, fresh unweathered surfaces</p> <p>GOOD Rough, slightly weathered, iron stained surfaces</p> <p>FAIR Smooth, moderately weathered and altered surfaces</p> <p>POOR Slacksided, highly weathered surfaces with compact coatings or fillings or angular fragments</p> <p>VERY POOR Slacksided, highly weathered surfaces with soft clay coatings or fillings</p>				
<p>STRUCTURE</p>		<p>DECREASING SURFACE QUALITY →</p>				
 <p>INTACT OR MASSIVE - intact rock specimens or massive in situ rock with few widely spaced discontinuities</p>	90			N/A	N/A	
 <p>BLOCKY - well interlocked undisturbed rock mass consisting of cubical blocks formed by three intersecting discontinuity sets</p>	80	70				
 <p>VERY BLOCKY- interlocked, partially disturbed mass with multi-faceted angular blocks formed by 4 or more joint sets</p>		60	50			
 <p>BLOCKY/DISTURBED/SEAMY - folded with angular blocks formed by many intersecting discontinuity sets. Persistence of bedding planes or schistosity</p>			40	30		
 <p>DISINTEGRATED - poorly interlocked, heavily broken rock mass with mixture of angular and rounded rock pieces</p>				20		
 <p>LAMINATED/SHEARED - Lack of blockiness due to close spacing of weak schistosity or shear planes</p>	N/A	N/A			10	
<p>DECREASING INTERLOCKING OF ROCK PIECES ↓</p>						

Figure 6.4.- Geological strength index base on geological description (Marinos and Hoek, 2000).

6.6 Mining Rock Mass Rating, MRMR

Based on modifications to the RMR_B (Bieniaswki, 1973), D. Laubscher introduced the Mining Rock Mass Rating ($MRMR$) system in 1973 for mining applications (Laubscher, 1973). The fundamental difference with respect to the RMR_B was the recognition that RMR represent the in situ rock mass condition (hereafter denoted as $MRMR_L$), which had to be adjusted to the particular mining environment (Laubscher,

1993). The adjusted mining rock mass rating (*MRMR*) could then be used for mine design.

Over the years this classification system was updated several times (Laubscher and Taylor, 1976, Laubscher, 1990, Laubscher, 1993). In these versions, veins and cemented joints were not included because they were assumed as part of the intact rock properties (see Laubscher 1993, p.555). However, veins and cemented joints, referred as cemented filled joint have been included in the latest version (Laubscher and Jakubec, 2001), being the unique scheme that so far has included specifically the effect of veins on rock mass behaviour.

The main change introduced is the concept of Rock Block Strength (*RBS*), which account for the effect of veins and cemented joints. The *RBS* plus discontinuity spacing and joint condition define the in-situ rock mass rating (*IRMR*), which is modified later by adjustments to determine the final *MRMR*. A flow sheet for this procedure is summarised in Figure 6.5 with the main concepts explained in following paragraphs. Other notations used in this classification scheme are; Intact Rock Strength (IRS) or Unconfined Compressive Strength (UCS), and Rock Mass Strength (RMS).

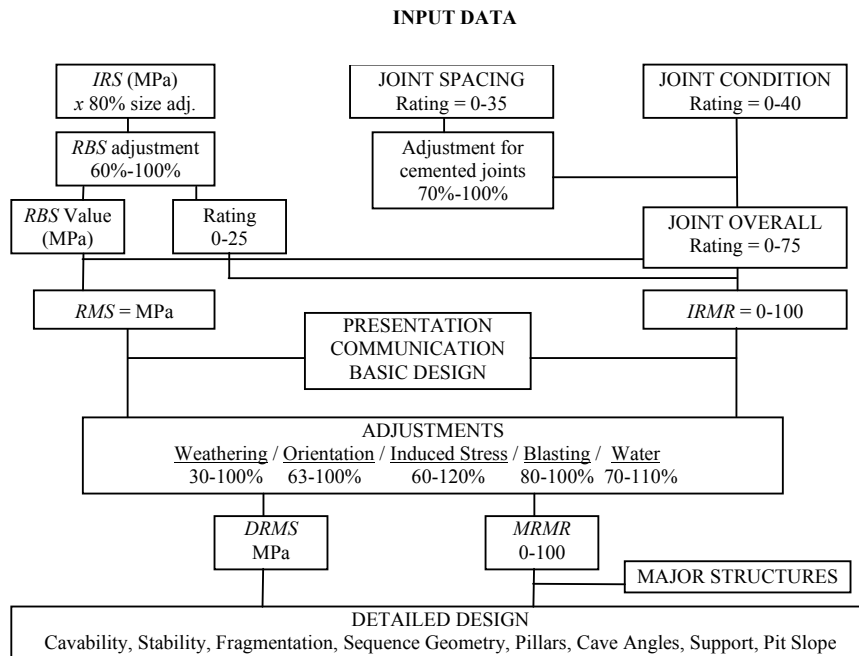


Figure 6.5.- Flow sheet of the MRMR procedure (after Laubscher and Jakubec 2000).

Some structural definitions have been provided in this classification scheme. Open joint is defined as a structural discontinuity that define the rock block (Laubscher and Jakubec, 2001), the term fracture represent the same, but it is conceived with less persistence (shorter) than open joints. Fractures are contained within the rock block (in Figure 6.6). These authors have also distinguished between veins and cemented filled joints by their size. A cemented filled joint has ‘continuity with the wall’, i.e., it may also define a rock block, veins are ‘low continuities that can occur within a rock block’ instead (Laubscher and Jakubec, 2001).

Figure 6.6 presents the general small-scale rock mass conception. There is not a rule scale for this figure in the original paper (Laubscher and Jakubec, 2001). An assemblage of these rock blocks defines a large-scale rock mass.

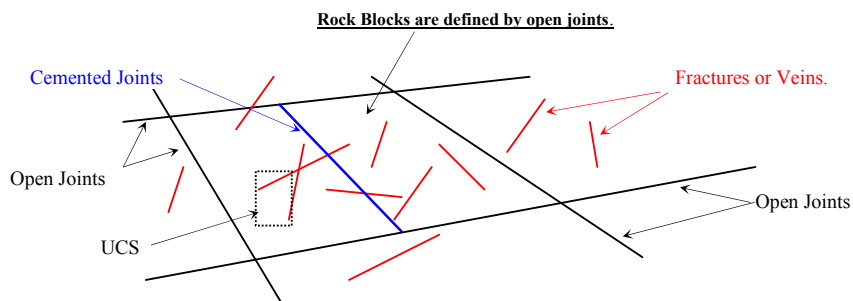


Figure 6.6.- Structural definitions in IRMR/MRMR (Laubscher and Jakubec, 2001).

6.6.1 In-situ Rock Mass Rating, IRMR

The in situ rock mass rating, *IRMR* is determined as following:

$$IRMR = RBS (25\%) + JS (35\%) + JC (40\%) \quad (6.5)$$

where,

1. **RBS** is rock block strength, which is obtained from the corrected intact rock strength (*IRS*) and/or the unconfined compressive strength (*UCS*).
2. **JS** is the joint spacing.
3. **JC** is the joint condition.

The overall *IRMR* range for 0 to 100 and each component contributes as is indicated between brackets in equation 6.5.

The *UCS* is adjusted depending on whether the intact rock specimens are homogeneous within rock mass or contain intercalations of weak material. For intercalations of weak rock mass, the *IRS* should be corrected as Figure 6.7 indicates.

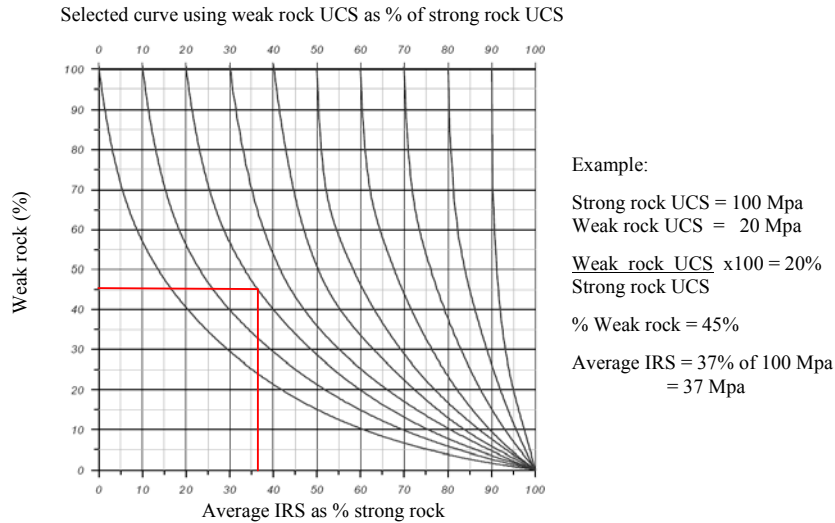


Figure 6.7.- Monogram for determining the corrected *IRS* value (Laubscher and Jakubec, 2001).

In determining the *RBS* from the corrected *IRS*, different factors can be applied depending upon whether the rock block is homogeneous or contain fractures or veins. If rock blocks are homogeneous or do not contain fractures or veins, the *RBS* will be the *IRS* value reduced by 80% to adjust for small-to-large scale specimen effects;

$$RBS = 0.8 \times \text{corrected } IRS \quad [\text{MPa}] \quad (6.6)$$

If rock blocks are inhomogeneous or containing fractures or veins, then the number and frictional properties of these discontinuities would reduce their strength. The frictional properties are defined using the Mohs' hardness number (Hurlbut, 1941). In this case, the product of the inverse hardness and the fracture/vein frequency will be the adjustment to the *RBS*, as follows:

$$RBS = 0.8 \times \text{corrected } IRS \times \text{fracture/vein adjustment} \quad [\text{MPa}] \quad (6.7)$$

where the fracture/vein adjustment is obtained from Figure 6.8, or it is given by:

$$\text{Fracture/vein adj.} = \text{fracture/vein frequency} \times \text{Inverse hardness} \quad (6.8)$$

Mohs hardness scale						
Index	1	1	2	3	4	5
Mineral as infill	Open Fractures	Talc, Molybdenite	Gypsum, Chlorite	Calcite, Anhydrite	Fluorite, Chalcocopyrite	Apatite
Inverse	1	1	0.5	0.33	0.25	0.2

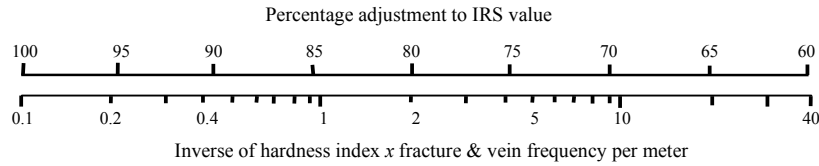


Figure 6.8.- The nomogram relating the *IRS* adjustment factor to the hardness index and vein frequency (Laubscher and Jakubec, 2001).

To illustrate the previous calculations, consider the following example. A rock mass having $IRS = 100$ MPa, and 8.0 ff/m of gypsum veins. Using equation 6.8 results in:

$$\text{Fracture/vein frequency} \times \text{Inverse hardness} = 8.0 \times 0.5 = 4.0$$

And from Figure 6.8, the adjustment found is 0.75, then equation 6.4 results in:

$$RBS = 100 \times 0.8 \times 0.75 = 60 \text{ MPa}$$

Finally, the overall rating for the *RBS* is directly read from Figure 6.9.

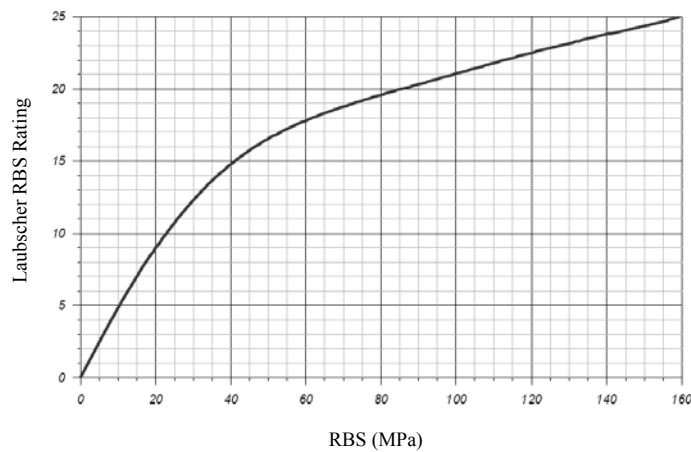


Figure 6.9.- RBS rating as a function of rock block strength (Laubscher and Jakubec, 2001).

JS is firstly determined using the open joint spacing, which is then adjusted for the number of sets to determine its rating (in Figure 6.10). Because cemented joints may influence rock mass strength when their infill strength is less than the host rock

strength, *JS* rating is adjusted for cemented joints, but only when cemented joints are forming sets within rock mass as Figure 6.11 indicates.

The *JS* rating is given by:

$$JS = \text{Open Joints rating} \times \text{cemented joint adjustment} \tag{6.9}$$

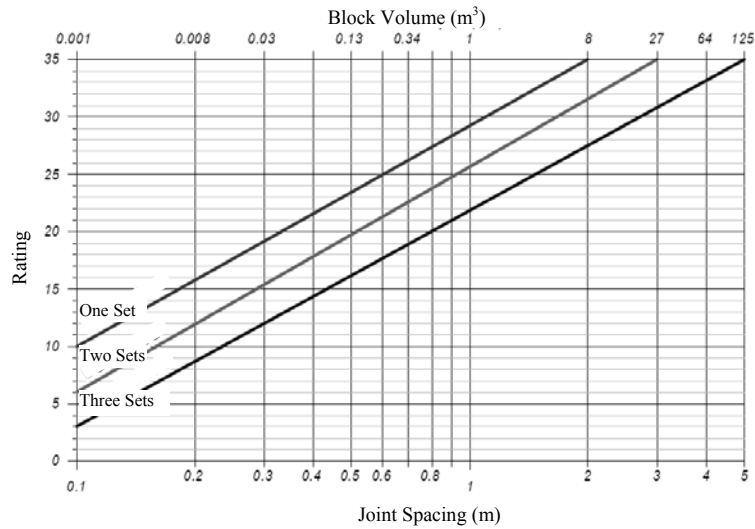


Figure 6.10.- Joints spacing rating (Laubscher and Jakubec, 2001).

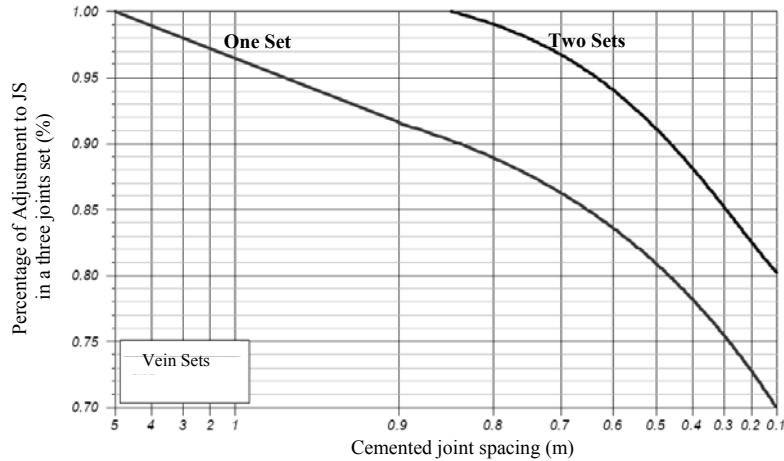


Figure 6.11.- Adjustment factor for cemented joints (Laubscher and Jakubec, 2001).

For example, a rock mass having 3 joint sets defining a mean rock volume of 1.0m³ is containing only one cemented joint set with spacing of 0.8m, then:

$$JS (\text{rating}) = 26 \times 0.89 = 23$$

Average of JC ratings is required for determining rock mass rating values. Table 6.5 provides JC adjustments for a single or multiple joint sets.

Table 6.5. Joints conditions adjustments (Laubscher and Jakubec, 2001).

A	Large-Scale joint expression	Adjustment % of 40
	Wavy-multidirectional	100
	Wavy- unidirectional	95
	Curved	90
	Straight, slight undulation	85
B	Small-Scale joint expression (200 mm x 200 mm)	
	Rough stepped/irregular	95
	Smooth stepped	90
	Slickenside stepped	85
	Rough undulating	80
	Smooth undulating	75
	Slickenside undulating	70
	Rough planar	65
	Smooth planar	60
	Polished	55
C	Joints wall alteration weaker than sidewall and filling	75
D	Gouge	
	Thickness < amplitude	60
	Thickness > amplitude	30
E	Cemented/filled joints –cement weaker than wall rock.	
	Hardness 5	95
	Hardness 4	90
	Hardness 3	85
	Hardness 2	80
	Hardness 1	75

For single open joint set, JC is calculated from Table 6.5 as follows:

$$JC = 40 \times A \times B \times C \times D \quad (6.10)$$

And, for single cemented joints set, JC rating is given by:

$$JC = 40 \times E \quad (6.11)$$

For multiple open joint sets, Laubscher and Jakubec (2001) have recommended determining an average JC rating as illustrates Figure 6.12.

6.6.2 Rock Mass Values

Laubscher and Jakubec (2001) have defined the rock mass rating (RMR_L) as follows:

$$RMR_L = RBS [\text{rating}] + \text{Overall joint rating} \quad (6.12)$$

Although it has not been specified, $IRMR$ and RMR_L are the same.

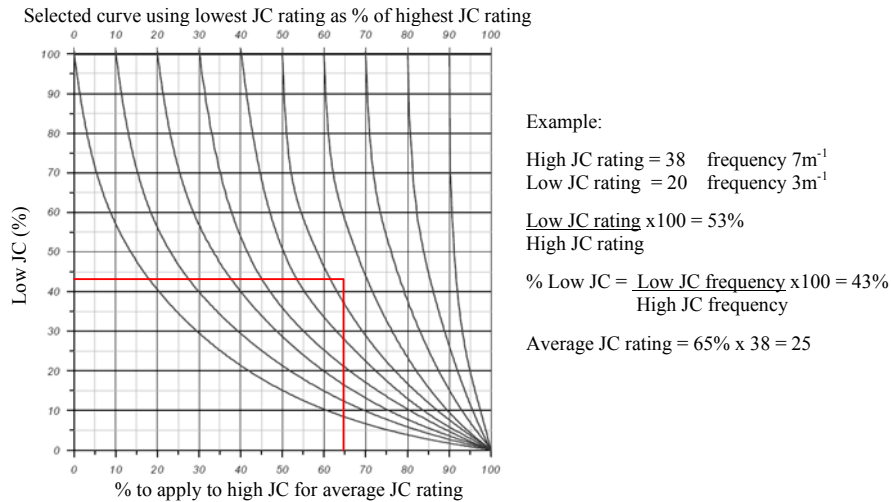


Figure 6.12.- Joints condition adjustment for multiple joint sets (Laubscher and Jakubec, 2001).

In addition, the rock mass strength (*RMS*) is defined as:

$$RMS = \frac{(RMR_L - RBS[\text{rating}])}{70} \times RBS[\text{MPa}] \quad (6.13)$$

Substituting equation 6.12 in 6.13:

$$RMS = \frac{(JS + JC)}{70} \times RBS[\text{MPa}] \quad (6.14)$$

In other words, the rock mass strength is defined by the overall discontinuity characteristic within rock mass plus the rock block strength.

Finally, the rock mass rating is multiplied by an adjustment factors to determine the *MRMR*, as follows:

$$MRMR = RMR_L \times \text{adjustment factors} \quad (6.15)$$

where the adjustment factors are weathering, joint orientation, mining induced stress, blasting, and water/ice adjustments.

Laubscher and Jakubec (2001) have recommended that one adjustment can supersede another depending on the problem analysed. Moreover, the total adjustment is not likely a multiplication of all the adjustments, carefully examining of the problem will determine which adjustments factor must be used. The total adjustment should not

exceed two classes. How these adjustment factors are determined are not explained here.

Similar to the RMR_B (Bieniaswki, 1989), the total rock mass rating can range lineally from 0 to 100. The rock mass is classified into five rock mass class according to the resulting rating, from very poor to very good. Using these $IRMR/MRMR$ values, practical applications to mass mining operations are suggested by Laubscher (1993), such as cavability diagrams, pillar design, slope stability, as well other applications.

6.6.3 Scale Effects

Laubscher and Jakubec (2001) have considered the scale effect as relevant factor during the rock mass behaviour, particularly examining mass-mining methods. For instance, assessing cavability of the deposit cannot be based on measurement from a drive assessment alone. This is due to the fact that widely spaced major structures, which may play a significant role on cavability, would have a marginal effect on the $IRMR$ estimation based on assessment made at the drive scale. The authors have proposed an adjustment to hydraulic radius (HR) for the influence of major structures when cavability is assessed. The adjustment number should be obtained by estimating the rating values for each major structure set (up to three sets), as Table 6.6 indicates. In other word, the hydraulic radius required to assess cavability is adjusted by the effect of major structure and principal stresses orientation.

Table 6.6. Parameters and rating values to major structures adjustments (Laubscher and Jakubec, 2001).

Influence of Major Structures Parameters								
A.- Dip	Value	0°-20°	21°-30°	31°-40°	41°-60°	>61°		
	Rating	6	4	2	1	0		
B.- Spacing	Value	0-9m	10-15m	16-21m	22-27m	>27m		
	Rating	6	4	3	1	0		
C.- Joint Condition	Value	0-10	10-15	15-20	20-25	>25		
	Rating	6	4	2	1	0		
D.-Stress/structure orientation	Value	0°-20°	21°-30°	31°-40°	41°-50°	51°-60°	41°-50°	>71°
	Rating	7	9	6	3	2	1	0
E.-Distance of major structures from undercut boundaries	Value	0-9m	10-20m	21-30m	>31m			
	Rating	12	8	2	0			
F.-Stress values, σ_1 as % of RMS	Value	>100%	80-99%	60-79%	40-59%	20-39%	<20%	
	Rating	14	12	8	4	2	0	

The rating values obtained from each major structure sets (up to three sets) are summed. The highest likely ranking from these three sets is 100. The number

obtained is plotted in Figure 6.13 to indicate whether the *HR* should be adjusted up or down.

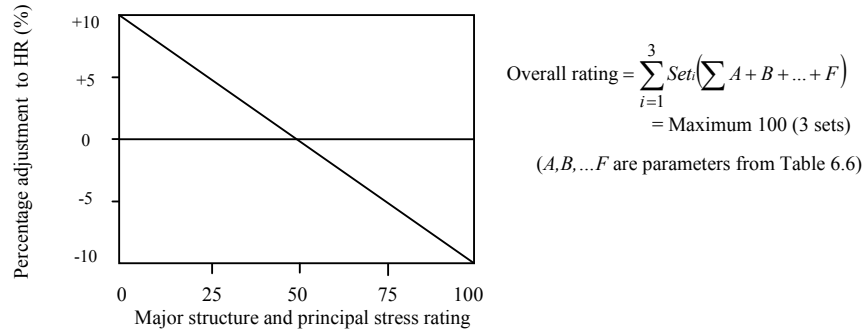


Figure 6.13.- Adjustment factor for major structure to *HR* (Laubscher and Jakubec, 2001)

6.6.4 MRMR Application to the El Teniente Primary Copper Ore

Following the procedure described previously, the *IRMR/MRMR* was estimated using the rock structure data observed within primary copper ore. In order to simplify some calculations, it was assumed that UCS rock specimen does not contain weak intercalations, i.e., it is homogeneous throughout. In addition, data collected using scanline mapping and oriented core logging were analysed separately. The calculations are presented in detail in Table 6.7.

Table 6.7 shows that several steps are required to apply the *IRMR/MRMR* index. Based on results for andesite rock type from any sector, the rock mass quality seem to be overestimated when is compared to the traditional values used for mine design at the mine site (in Table 1.2).

Although this system has included the geological features found within the primary copper ore, which established clearly differences between two studied sectors, the calculations do not significantly reflect these differences. The calculations are showing almost the same overall rock mass rating between andesite sectors.

A number of problems were encountered when this system was applied using the current structural data, which are discussed as follows:

Table 6.7. Applying IRMR/RMRM to the El Teniente primary copper ore.

(steps) Parameter/features	Andesite Hw	Andesite Fw	Commentary
(1) Average UCS (IRS)	120 Mpa	120 Mpa	Data from Table 1.2, rock mass is assumed homogenous.
(2) 80% of IRS	96 Mpa	96 Mpa	
(3) Inverse hardness	0.28	0.28	From Figure 6.8 using main vein infill as chalcopyrite-anhydrite
(4) Weak vein frequency	4.6 m ⁻¹	8.4 m ⁻¹	Highest set frequency from oriented core logging data (Table 5.3), because likely shorter discontinuities were collected
(5) Inverse x Vein freq.	1.3	2.4	Using Equation 6.8 with (3) and (4)
(6) IRS adjustment	83%	78%	Using (5) in Figure 6.8
(7) RBS	80 MPa	75 MPa	Using Equation 6.7 with (2) and (6)
(8) RBS rating	19.5	19	Using (7) in Figure 6.9
(9) Open joints spacing	3.0 m	5.6 m	Data from Table 3.4, lowest fault set spacing in drive mapping
(10) Open joints rating	35	35	Using (9) and two faults sets in Figure 6.10
(11) Weak veins spacing	0.88 m	0.55 m	Lowest set spacing from scanlines data (Table 5.3), because likely longer weak veins (cemented joint) were collected
(12) Cemented joints adjustment	1.0	0.93	Using (11) and two sets in Figure 6.11, in reality 3 and 4 sets were found, but Figure 6.11 does not offer more possibilities
(13) (Cemented joints adjustment)	(0.83)	(0.80)	Using two sets in Figure 6.11, but using (4) rather than (11)
(14) JS rating	35	33	Using Equation 6.9 with (10) and (12)
(15) (JS rating)	(29)	(29)	Using Equation 6.9 with (10) and (13)
(16) Open joints JC rating	16	16	Using faults in equation 6.10 (A=0.87, B=0.75, C=1, D=0.60)
(17) Hardness adjustment	87%	87%	From Table 6.5 part E, considering vein infill between hardness 3 and 4
(18) Weak veins JC rating	35	35	Using Equation 6.11 with E=0.87
(19) Low JC/High JC	45%	45%	Using Figure 6.12 with (16) and (18)
(20) % Low JC	6%	8%	Using Figure 6.12 with (11) and mean faults spacing
(21) (% Low JC)	(2%)	(2%)	Using Figure 6.12 with (4) and mean faults spacing
(22) Average JC rating	32	31	Using (19) and (20) in Figure 6.12 result 88% (Hw) and 87% (Fw) of adjustments.
(23) (Average JC rating)	(34)	(34)	Using (19) and (21) in Figure 6.12 result 90% (Hw) and 97% (Fw) of adjustments
(24) IRMR / RMR_I	87	82	Using either Equation 6.5 or 6.12 with (7), (14) and (22)
(25) (IRMR / RMR _I)	(82)	(82)	Using either Equation 6.5 or 6.12 with (7), (15) and (23)
(26) RMS	76 MPa	68 MPa	Using Equation 6.13 with (8), (14) and (22)
(27) (RMS)	(71 MPa)	(67 MPa)	Using Equation 6.13 with (8), (15) and (23)
(28) MRMR	69 MPa	66 MPa	Using Equation 6.15 with (24) and 80% induce stress adjustment.
(29) (MRMR)	(66 MPa)	(65 MPa)	Using Equation 6.15 with (25) and 80% induce stress adjustment.

The discontinuity size proposed by these authors is not very specific. It must be remembered that geological discontinuities (joints or fractures, veins and faults) generally display a distribution of discontinuity sizes within a rock mass. Because, the effect of sizes bias has not been considered in the proposed definition, the differences between either veins or cemented joints or between open joint and fractures cannot readily be determined.

When the *RBS* component is adjusted by fracture/vein frequency to determine its strength, only one fracture/vein set can be used. However, it is expected that a weak path within a rock block may involve two or more fracture/vein sets. In addition, if 2 or 3 vein sets exist, the method does not clearly specified which one must be used in calculations? The calculations in Table 6.7 show that both sectors have the same *RBS*, which is clearly not the case with the observed data.

Also, the system assumes that veins have only one mineral as infill, which is not the case for the El Teniente. The methodology does not specify the approach when several mineral species are presented as vein infill to estimate its hardness.

In the present case, faults treated as open joints, however; the open joint spacing was outside the scale in Figure 6.10. The minimum faults mean spacing observed was 3.0m, which is the largest value for the case of two sets in this figure. Therefore, the open joint spacing and Figure 6.10 are not suitable parameters to characterise rock masses of primary copper ore at the El Teniente. This may explain why the estimated *JS* rating is almost the same between the different sectors.

The resulting *RMR_L* indicates very good rock mass quality with an overall rating greater than 80 in both sectors for any case. Additionally, using 80% of adjustment by induced stresses², *MRMR* estimates gives an overall rating greater than 65 in all cases. Both sets of values can be considered extremely high in comparison with observed cavability at the mine site (in Figure 1.17). Caving has been reached with hydraulic radius around 25 at the Reno and Esmeralda mine sectors (discussed in detail in Section 7.3.1), which may be indicating less rock mass quality than estimated in Table 6.7.

In summary, although the *IRMR/MRMR* system incorporates the effect of weak veins during rock mass quality estimation, this system does not adequately reflect the observed differences between sectors. This may be because the *IRMR/MRMR* system still gives a high importance to open joints rather than to weak veins during calculations.

6.7 Conclusion

For rock mass classification systems were applied to the structural data observed within andesite rock masses of primary copper ore of the El Teniente. These were; *RMR_B* (Bieniaswki, 1989), *Q-System* (Barton et al., 1974), *GSI* index (Marinos and Hoek, 2000), and *RMR_L* (Laubscher and Jakubec, 2001).

² This adjustment value is commonly used at the mine site (see Table 1.2 and Figure 1.17)

None of these classification systems appears to adequately characterise the rock masses. This is mainly due to the fact that none of these schemes have properly included vein characteristic as discontinuity parameter. They treat open joints as the main feature controlling rock mass behaviour, as suggested by ISRM (Brown, 1981). However, this research has found that weak veins are the main feature controlling rock mass disassembly during caving.

In addition, the method to collect discontinuity from the field is not clearly specified by any of these schemes. Data in this research show that is key point to consider, because discontinuity spacing may vary significantly with the truncation bias chosen during data collection.

CHAPTER 7 ESMERALDA MINE SECTOR

7.1 Introduction

The Esmeralda mine sector, located in the central part of the El Teniente ore body at the East part of Braden pipe (Figure 1.6), introduced the pre-undercutting caving method at the El Teniente mine in 1997. This mine sector included a production plan of 350Mtons of ore with 1% of Cu and a life span over 35 years (Barraza and Crorkan, 2000).

The undercutting was initiated in October 1996, and caving initiation started one year later triggered by ore drawing at the production level. The breakthrough to the upper mine level was estimated to occur between April and May 1999, when the hydraulic radius reached a value of 26m. The effective mined area¹ at this time was 16,800m² (Rojas et al., 2001). Caving initiation was located only 100 meters below the old Teniente 4 South mine level to reduce the seismic risk level (Barraza and Crorkan, 2000).

The main geological features within the area of interest² are; two main rock types, andesite and diorite; two hydrothermal alteration zones, late (LH) and principal (PH); one major fault system named Fault B (Seguel, 2005). The hydrothermal alteration zones coincide with the principal orientation reference at the mine such as the hangingwall (*Hw*) and the footwall (*Fw*) sectors (Figure 7.1).

During the first years of mine production (until year 2000) moderate damage to the mining infrastructure occurred, which was mainly related to both; dynamics failures and stress concentration at the undercut mine level.

7.1.1 Goal

This chapter describes and discusses the results of the rock structure characterisation undertaken at this mine sector, which included the application of the concept of weak discontinuities (faults and veins) to be evaluated. Rock structure characterization

¹ Effective area mined considered only working draw points (detailed in Section 7.3.1).

² It extends, in the mine coordinate system, between 300 and 700 north coordinate; and between 900 and 1450 east coordinate.

included two mapping scales; re-analysis of data collected using drive mapping, and new data collected on available large diameter oriented core samples drilled at the production mine level.

This chapter also reviews some relevant information about the rock mass response to mining during caving initiation and propagation to be back analyzed in the following chapter.

7.2 Rock Mass Characterisation

Rock structure has been characterised based on the occurrence of intermediate structures mapped in mine drives at the production and the undercut mine levels, and from small discontinuities collected using large diameter oriented core samples.

In the area of interest (Figure 7.1), five major structural domains has been defined (Seguel, 2005) based on major structural features that influence the ‘*occurrence and/or nature*’ of intermediate structures. These major structural features were; orientation trends, main lithologies and hydrothermal alterations zones. In this study, these structural domains were named, from east to west, as; *Cmet Fw1*, *Cmet Fw2*, *Diorite*, *Cmet Hw1*, and *Cmet Hw2*. Under such definition, current structural data (intermediate structures) were re-analysed to determine the main discontinuity features in each domain. Sample lines chosen for re-analysis were chosen to give similar mapping lengths between the two availability horizontal directions (Figure 7.2). These selected sample lines, from both undercut and production level, included general descriptions of intermediate structures such as location, orientation, genetic, infill thicknesses, and qualitative mineralogical infill description, among others. More than 1870 intermediate structures were assessed for the structural data analysis. Sets definition and their spacing features have been determined following the procedure previously discussed in Chapter 3.

It is interesting to note that few major faults were observed within the diorite rock shown in Figure 7.1.

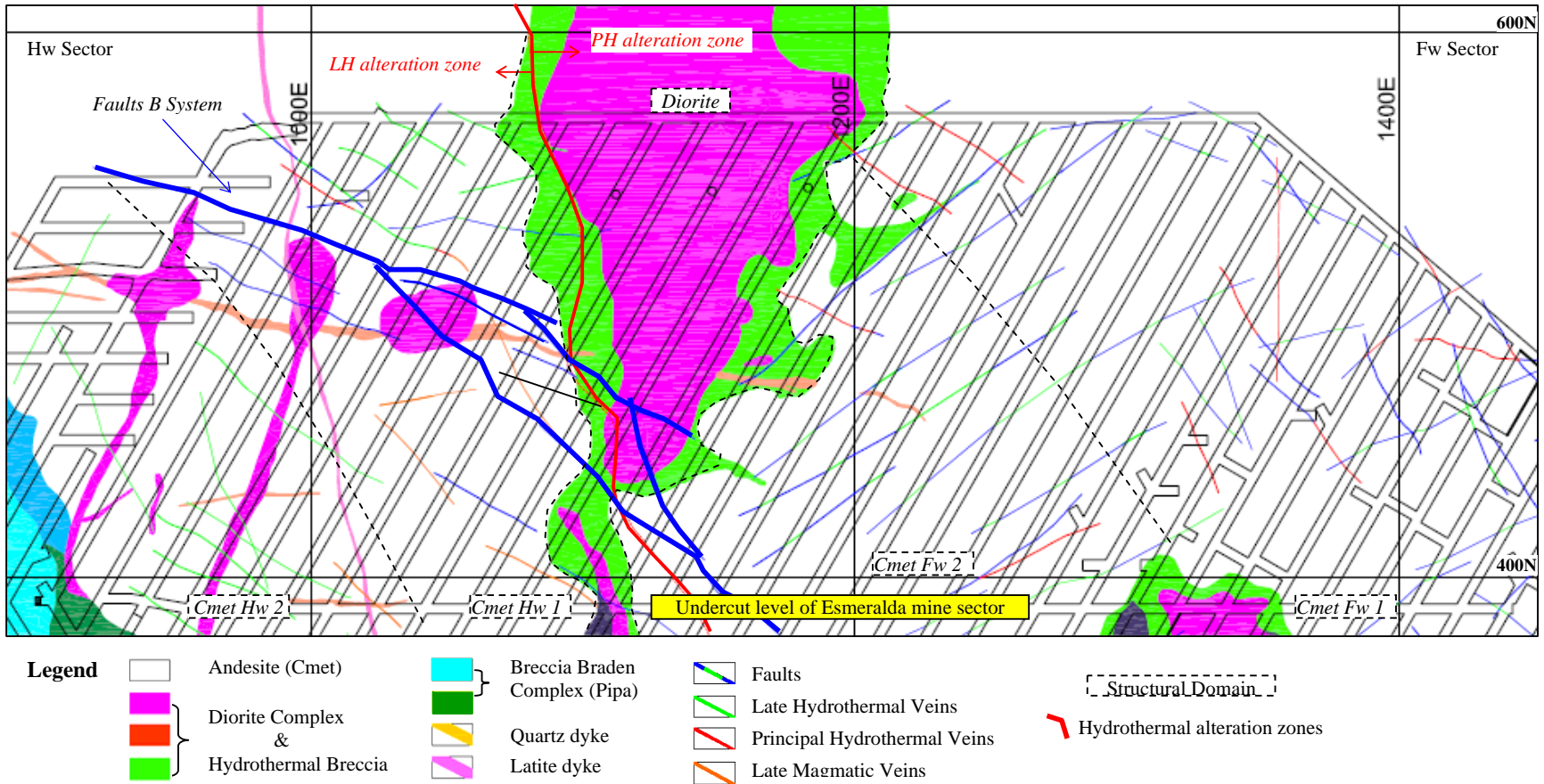


Figure 7.1.- Main geological features of the Esmeralda mine sector (modified from Seguel 2005).

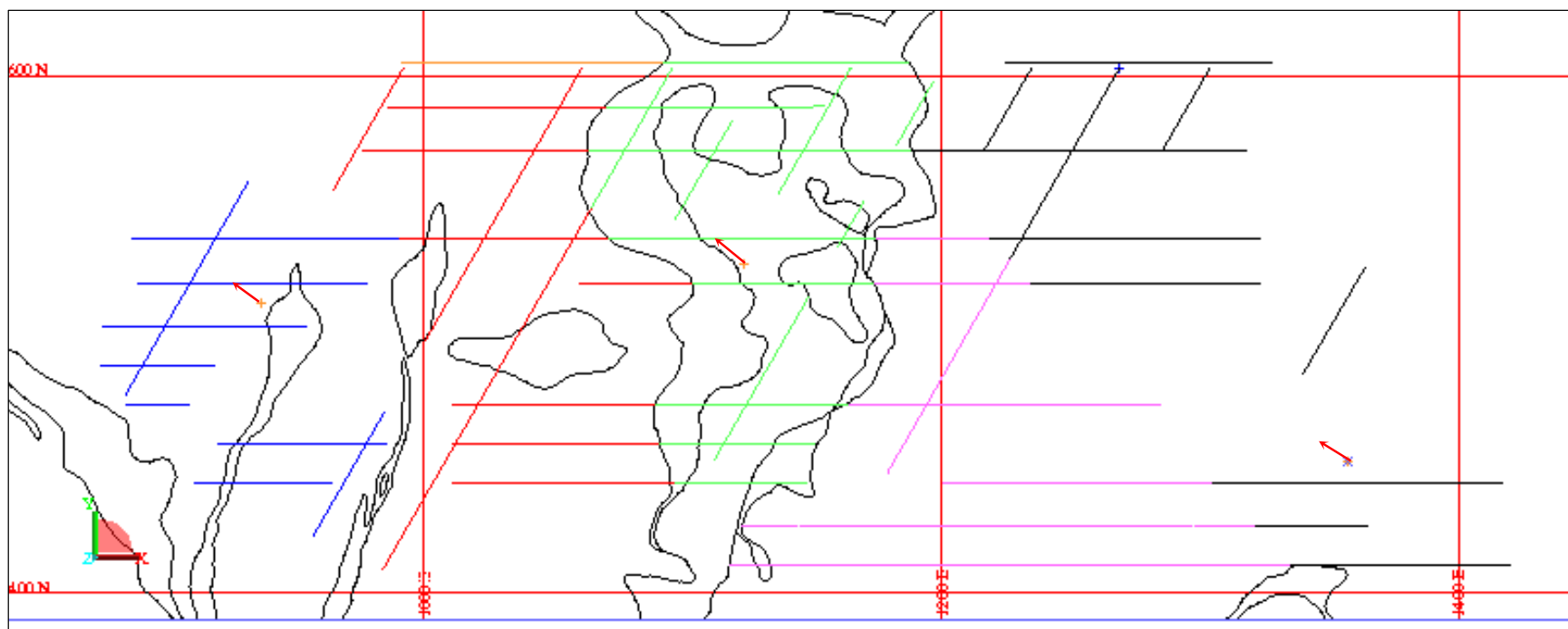


Figure 7.2.- Plan view of production level at the Esmeralda mine sector showing drive mapping line samples chosen for re-analysis of data according to different structural domain selection (different colours), and oriented drill core location (red arrows).

7.2.1 Drive Mapping

Drive mapping characterised the discontinuity infill only in qualitative terms (see Section 2.6.1), for example, being *majority*, *abundant*, *moderate*, or *rare*. According to the infill features of vein types observed in scanline mapping and oriented core logging at the Reno mine sector (see Table 5.1 in Section 5.2.1 and its draw conclusion), only PH and LH veins were assumed as being weak veins at drive mapping scale in Section 5.2 and 5.3. Data analysis of the qualitative infill description collected at drive mapping scale in Esmeralda mine sector agreed with that “*initial assumption*”. In fact, using the strength mineral definition proposed in Chapter 4 (in Table 4.6), soft and intermediate strength minerals were largely present in the PH and LH veins. These mineral types were described as either ‘*majority*’ or ‘*abundant*’ in over 90% of data (761 and 526 veins respectively) throughout all this mine sector. On the contrary, hard strength minerals were presented in LM veins describing as ‘*majority*’ or ‘*abundant*’ in over 85% of the data (119 veins). Therefore, the “initial assumption” made to define weak veins for drive mapping data in Reno mine sector can be considered appropriated.

An example of the weak veins and fault orientation observed at drive mapping scale is presented in the following Figure 7.3. Data in this figure are from the *Cmet Fw1* structural domain, which is plotted in the lower hemispheric projection. Although bias to sub-horizontal discontinuities is expected since only horizontal sample lines were used, it can be said that weak veins tend to describe three semi-orthogonal set orientations since some vein concentration having dip >45 degrees appeared in the stereonet (Figure 7.3a). Faults, on the other hand, can be considered to describe up to two sub-vertical set orientations (Figure 7.3b). The data also shows a similarity in orientations between weak veins and faults.

In addition, the orientation analysis for all structural domains was undertaken and the results are summarized in Figure 7.4. The criterion to define each set is discussed in Section 3.2.3. Figure 7.4 present the mean set orientations determined for veins and faults in each structural domain, which were clustered (red windows in that figure) considering their main trend orientations.

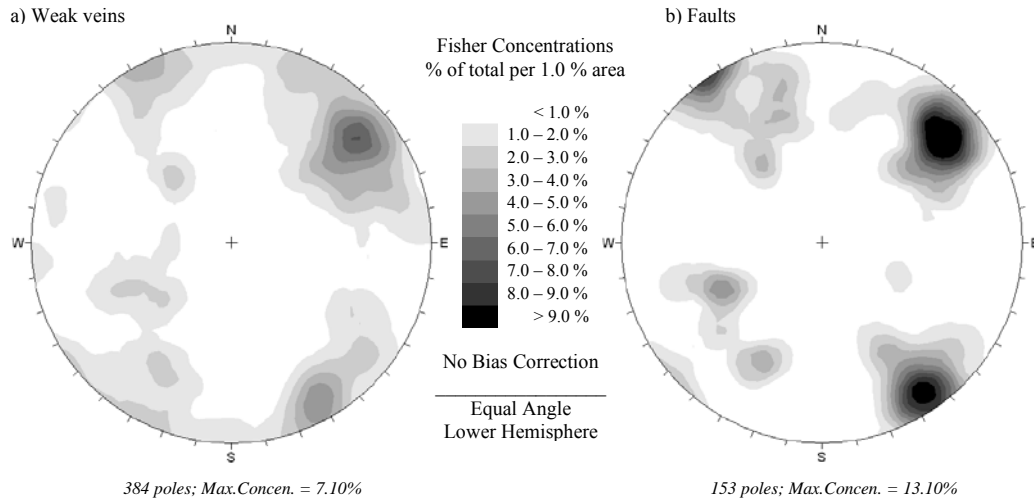


Figure 7.3.- Stereonets showing weak vein and fault orientations from *Cmet Fw1* structural domain.

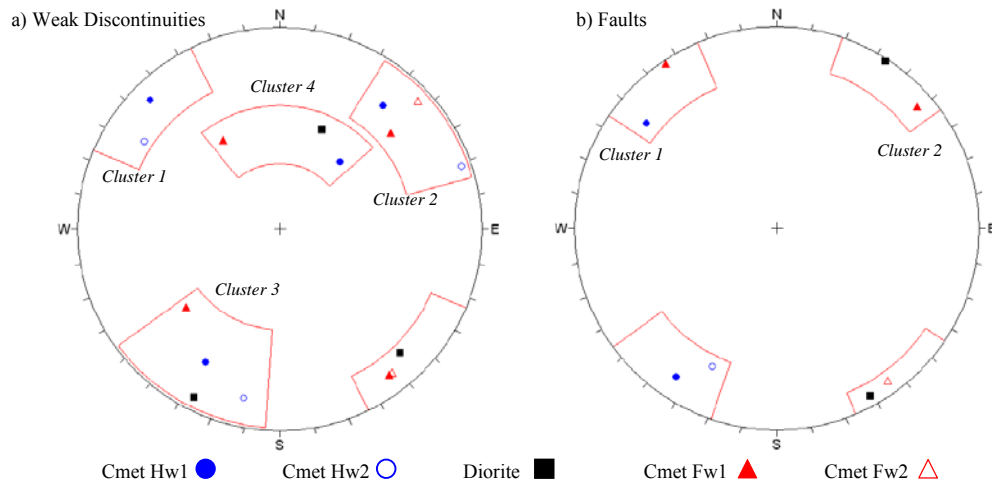


Figure 7.4.- Set definition for weak veins and faults collected at mine drives according to structural domain selection (red windows are only to identify main cluster, it is not the windows definition).

Figure 7.4 shows that almost the same pattern of discontinuity orientations (structural anisotropy) throughout different structural domains. Two main structural trends are observed for both discontinuity types; north-east and north-west. In this figure it is clearer that weak veins tend to describe three semi-orthogonal set orientations and faults tend to define only sub-vertical set orientations. Appendix II.A also shows fault orientation data recently collected at the mine site using sub-vertical small diameter oriented cores placed at the *Fw* sector, but under the Esmeralda undercut level (Harrison, 2008). The data shown in Appendix II.A agree with Figure 7.4b and

that conclusion. Therefore, data suggest that Faults orientations at the Esmeralda mine sector tend to define only sub-vertical set orientations, which is also consistent to what discussed Section 3.2.4.

Taken into account to the set definition presented in Figure 7.4, spacing for all weak discontinuities were estimated and the result are presented in Table 7.1. Data in this table shows that fault spacings are similar to the fault spacings found in data from Reno mine sector (see Table 3.4), i.e., fault spacing in drive mapping has a mean values between 5 to 10 meters throughout the El Teniente ore body.

Table 7.1. Normal set spacing for weak discontinuities and faults from drive mapping at Esmeralda mine sector.

Discontinuity type	Cluster ⁺ /DipDir		Normal set spacing (m)				
			Structural Domain				
			<i>Cmet Hw2</i>	<i>Cmet Hw1</i>	<i>Diorite</i>	<i>Cmet Fw2</i>	<i>Cmet Fw1</i>
Weak discontinuities	1	90/316	7.4*	5.2	5.8	3.2	5.3
	2	80/232	8.6†	9.3		9.5	5.3
	3	75/029	5.8	7.6	6.0		8.1
	4	49/191		9.9†	9.0		6.8†
Faults	1	89/143		7.2‡	5.5‡	6.7†	8.0
	2	86/035	8.7*	8.8	5.2†		8.8

Note; obtained from less than 40 (†), 20 (*), and 10 (‡) spacing data, respectively. †; Shown in Figure 7.4.

Following the example of *Cmet Fw1* structural domain, the infill thickness distributions for veins considering each set are presented in Table 7.2.

Table 7.2. Vein thickness distribution per family sets observed at *Cmet Fw1* using drive mapping.

Family Sets	Data	Thickness distribution observed (%)						Mean (mm)
		<1mm	1- <2mm	2- <3mm	3- <5mm	5- <10mm	≥ 10mm	
Set 1	144	-	4.2	38.2	31.9	2.8	22.9	4.5
Set 2	69	-	4.3	43.5	30.4	5.9	15.9	4.1
Set 3	129	-	1.6	52.7	37.2	2.3	6.2	3.3
Set 4	32	-	6.3	59.4	21.9	6.2	6.2	3.2
Total & mean	358	-	3.6	45.5	32.1	3.4	15.4	4.0

Table 7.2 shows that the individual set thickness distribution observed does not vary significantly between each other, which are also similar to the mean of the structural domain. A consistent vein thickness distribution was also observed for veins at the Reno mine sector.

7.2.2 Oriented Core Logging

A new data collection campaign was implemented to collect small features using large diameter oriented drill cores (100mm core diameter) in the area of interest. Unfortunately, since Esmeralda mine sector is currently in production with the undercut level caved, only three large core samples could be recovered to perform this task. These three samples were obtained from the production level, and represent three main unit/rock/structural domains; one in diorite rock, and two in andesite rock type from each alteration zones (Figure 7.2).

From these core samples, 861 new discontinuities and their features were described according to the procedure described in Section 2.6.1. All core samples have the same orientation (S75°E in Figure 7.5). Because one sample orientation per unit type is used, greater biases to discontinuity orientation is expected due to the blind zones effect (Terzaghi, 1965). Despite of this fact, veins tend to define at least three semi-orthogonal set orientations as data from *Cmet Hw1* shows in Figure 7.5. The data for veins orientation shown in Appendix II.A confirm that veins define at least three semi-orthogonal set orientations.

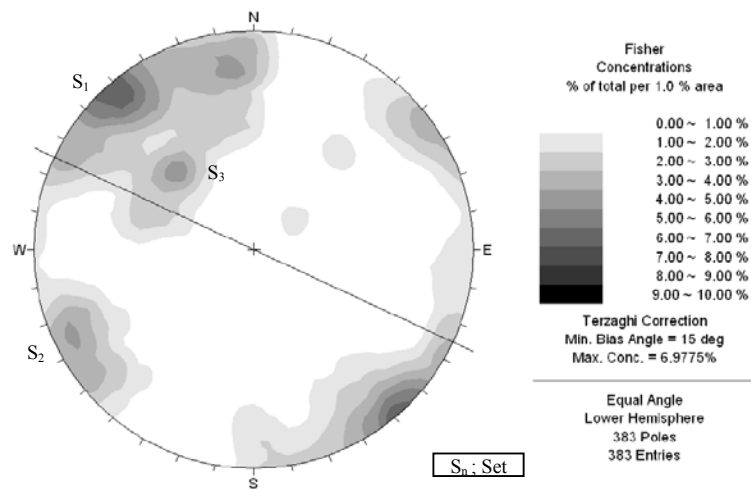


Figure 7.5.- Veins orientation, set definition (S_n) from the *Cmet Hw1* and core sample orientation (black line). Few structures are observed to the perpendicular of sample line (blind zone effect).

In addition, veins collected by mine geologists using traditional scanline mapping techniques at the same mine sector, which included vertical sample lines, are

presented in Figure 7.6. These traditional scanlines were located 100 meters above the undercut level at the central part of the Esmeralda mine (*Fw* sector). This figure also confirms clearly that veins comprise at least three semi-orthogonal set orientations at the studied sector.

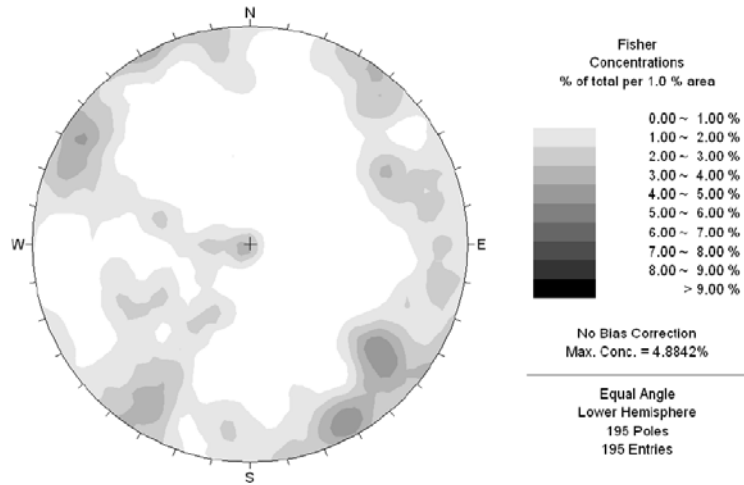


Figure 7.6.- Plot contour of veins collected by mine geologist using traditional scanline techniques in the Esmeralda mine sector (*Fw*).

Despite sampling constrains by using only one sampling orientation, at least three semi orthogonal sets were defined for each sampled data set. The normal set spacing was calculated for each family set and the results for weak discontinuities are presented in Table 7.3.

Table 7.3. Main set orientation and spacing for weak discontinuities using oriented drill core logging.

Family Sets	<i>Cmet Hw2</i>			<i>Diorite</i>			<i>Cmet Fw1</i>		
	Dip/Dir	Poles	Spacing (m)	Dip/dir	Poles	Spacing (m)	Dip/dir	Poles	Spacing (m)
Set 1	89/145	27	0.19	90/248	14	0.23	89/322	90	0.06
Set 2	86/060	3	0.15	89/294	17	0.33	80/76	62	0.07
Set 3	53/135	13	0.28	72/347	7	0.46	58/148	44	0.09
Set 4	-	-	-	50/247	12	0.17	-	-	-

From Table 7.3 it clears that andesite from *Fw* sector presents a major degree of ‘fracturing by weak veins’ or abundance of weak veins than the other two sectors, particularly with respect to andesite rock type from *Hw* sector. Similar results were observed in data from Reno mine sector in Chapter 5 (section 5.3).

The thickness distributions when only weak discontinuities were included are presented in Table 7.4. This table shows a case example of data sets, which were observed in andesite rock type within *Cmet FwI* structural domain.

Table 7.4. Weak vein thickness distribution per family sets observed at *Cmet FwI* using oriented core logging.

Family Sets	Dip/Dir	Data	Thickness distribution observed (%)						Mean (mm)
			<1mm	1- <2mm	2- <3mm	3- <5mm	5- <10mm	≥ 10mm	
Set 1	89/332	90	36.7	40.0	18.9	6.1	0.7	0.0	1.2
Set 2	80/076	62	38.7	38.7	9.7	16.3	1.0	1.9	1.4
Set 3	50/148	44	20.5	38.6	22.7	15.9	0.0	0.0	1.5
Total & mean		203	32.5	40.4	16.7	12.0	0.6	0.6	1.3

Comparison between data from Table 7.2 and Table 7.4 confirm that vein thickness may be considered to be an isotropic feature within primary copper ore. This vein thickness characteristic was also observed in other structural domains, and when all discontinuity was included in data analysis. Moreover, the same relationship between vein thickness and vein sizes observed in data from Reno mine sector is observed in data from Esmeralda mine sector, i.e., additional thin discontinuity appear as the truncation threshold value decrease during data collection. In other words, data from the Esmeralda mine sector also suggest that longer discontinuities are statistically thick.

7.2.3 Potential Fragmentation

The in situ rock block distribution or the '*potential fragmentation*' according to the fragmentation model discussed in Chapter 5 was determined by a stochastic simulation of the rock structure (Thompson, 2002). The results, when only weak discontinuities were included, are presented in Figure 7.7. The same data were re-analysed considering only thick veins as discussed Section 5.7.1. The results for the case when only weak veins having thickness greater than or equal to 2mm were included are presented in Figure 7.8. As a comparison, Figure 7.8 includes data from Reno mine sector collected using the same procedure.

Figure 7.7 shows clearly that andesite rock type from Fw sector has finer in situ block size distribution in comparison with diorite rock and andesite from the other hydrothermal alteration zone (*Hw*).

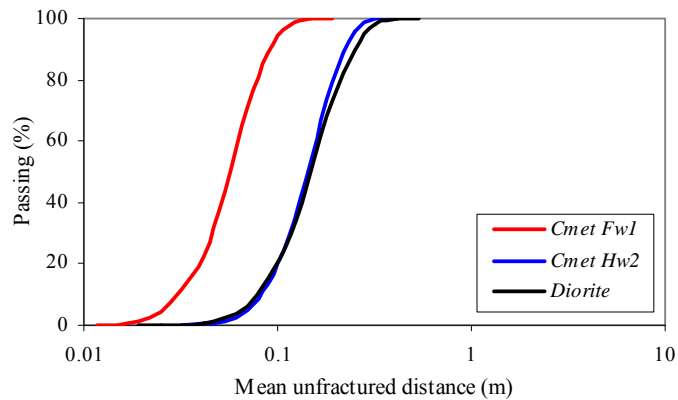


Figure 7.7.- In situ rock block size distribution for weak discontinuities.

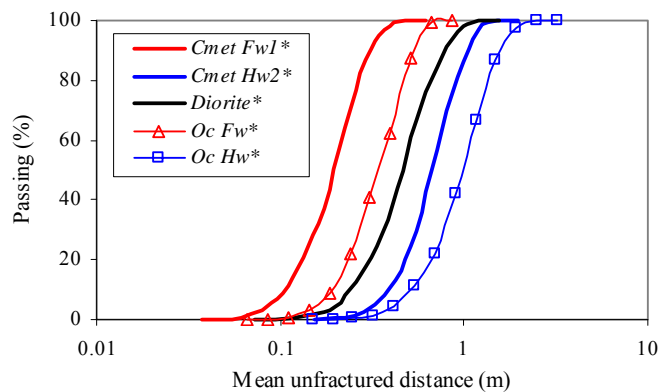


Figure 7.8.- In situ rock block size distributions for weak discontinuities considering vein thicknesses $\geq 2\text{mm}$ (with * in the chart). Oc; small diameter oriented cores from both sectors within Reno mine.

Similar results are observed in Figure 7.8 when comparisons are made for weak discontinuities having thicknesses greater than or equal to 2mm. Andesite rock type within PH alteration zone (*Fw sector*) in both mine sectors present similar rock structure characteristics, having finer potential fragmentation with respect to the other alteration zones (*Hw sector*). Therefore, for the case of Esmeralda mine sector,

diorite rock type can be considered a *stiffer* rock mass being surrounded by a *weaker* andesite rock mass.

It is important to note, that these rock structure simulation assumed infinite trace length for discontinuities, which may underestimate block size distribution, particularly where higher discontinuity spacing is observed (*Hw sector*).

Additionally, in terms of fragmentation, it also expected that the andesite rock type within the principal hydrothermal alteration zone will present finer fragmentation at the production level draw points than the LH alteration zone.

7.3 Rock Mass Response

Rock mass response due to mining activities has been observed in several aspect at this particular mine sector. The major observations discussed hereafter were; the hydraulic radius of the footprint during caving propagation; fragmentation performance; rock damage in pillar located ahead of the front cave at the undercut level, and mine induced seismicity. The record of induced seismicity during caving propagation at the seismogenic zone in this mine sector is discussed with more detail in next chapter.

7.3.1 Hydraulic Radius during Caving Propagation

In the pre-undercut caving method, the caving propagation is controlled by draw strategies at the production level. At the mine site the extraction rate is used to control the cave growth in order to control the seismic response at the seismogenic zone (Rojas et al., 2000). The undercut level, which is developed prior the production level, is being blasted at least 80m ahead from the active draw points in all direction as shown Figure 1.21 (Rojas et al., 2001). In this respect, two hydraulic radius of caving can be distinguish; one related with the undercut area, and the other related to the effective caving area defined by the active (working) production level draw points as shown Figure 1.21. The effective caving area is also called the active footprint.

An example of that particularly can be seen in detail with the case of Reno mine sector. Mining activities at this mine sector stopped in 1992 with less than 1 million tonnes of extracted ore (Rojas et al., 2000). The undercut area at this time was of 27,000 m² with a hydraulic radius of 36. The mine sector was closed due to uncontrolled induced seismicity (Dunlop and Gaete, 1997), which affected considerable areas of mine infrastructure. Mining activities was reinitiated experimentally in 1994, but with a controlled draw strategy in a limited area of 11,000 m² at the west part of the mine (active footprint in Figure 7.9). Breakthrough to upper old mine levels was achieved in the middle of 1998 without increasing that effective drawing area. Consequently, the active hydraulic radius estimated in this case was of 25m.

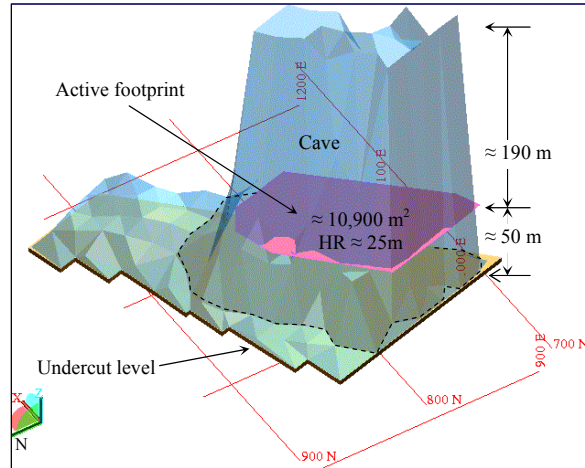


Figure 7.9.- Isometric view of the cave of Reno mine sector at the time of breakthrough to upper mine levels.

At the Esmeralda mine sector, the breakthrough to upper mine level was estimated to occur between April and May 1999, when the hydraulic radius reached a value of 26m (Figure 7.10). The effective mined area at this time was 16,800m² (Rojas et al., 2001), whereas the undercutting area at this time was of 54,470m² with a hydraulic radius of 38m.

Based on cave propagation observations, an empirical relationship was established between the extracted rock column height and the cave back height. The extracted rock column height is converted in meters from the total recorded production at each

draw point. The relationship between these two heights was found as 3, this means, for example, that after 10 meters of extraction at any draw points, is expected that the cave back has reached 30 meters over the same draw point. This relationship was also tested with drill core samples in September 1988 (Seguel and Morales, 1988), and correlated with subsidence observations (Parraguez and Campos, 2007). It is now commonly accepted to estimate the cave front geometries at any place and at any time within the mine site (Rojas et al., 2000). This relationship was used to create the cave geometry volumes in the numerical modeling (Chapter 8).

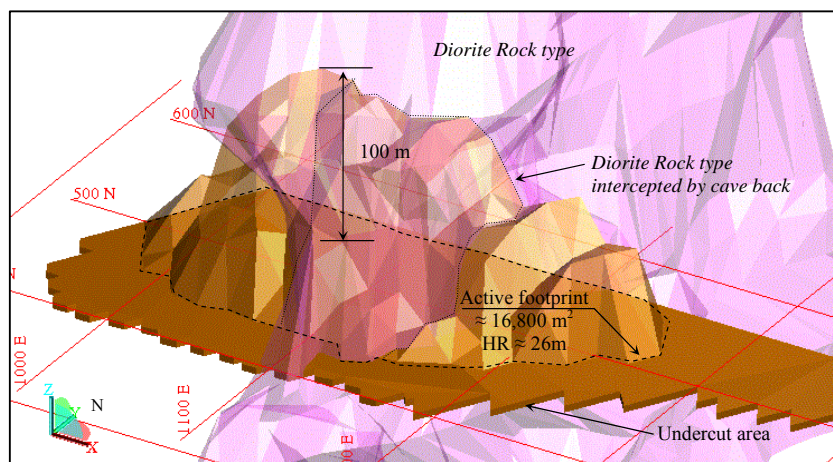


Figure 7.10.- Isometric view of the cave of the Esmeralda mine sector at the time of breakthrough to upper mine levels.

It also is important to note that rock masses of secondary ore, which are usually heavily fractured, have achieved caving with a hydraulic radius of around 22m (see Figure 1.17). That antecedent is indicating a suggestion that the rock masses of primary copper ore may also fails readily when are subjected to stress.

7.3.2 Fragmentation

Two back analysis studies on the fragmentation performance have been completed at this mine sector. The first one was implemented between May and August 1999 and included digital imaging process (DIP) of photos taken in draw points and ore passes (Pereira and Zamora, 1999). The second study was a statistical analysis of the standard observations (visual inspection) undertaken from draw points made routinely by the worker of control production. Data used in those calculations ranged

from January 1999 and July 2004 (NCL, 2004). A summary of the first study is presented in Table 7.5, which included fragmentation predictions made during feasibility studies of the mine sector.

Table 7.5. Fragmentation back analysis of Esmeralda mine sector (Pereira and Zamora, 1999).

Unit Type	Oversize predicted and measured (%)					
	In draw points				In ore passes	
	Measured		Feasibility studies		Measured	
	>1m ³	>2m ³	>1m ³	>2m ³	>1m ³	>2m ³
Andesite Hw (Cmet Hw1)	43	33	14	8	38	23
Diorite	47	39	34	25	37	21
Andesite Fw (Cmet Fw2)	40	26	5	2	38	22

Note; rock block size reduction by secondary blasting are included only at the ore passes measurements.

The results present in Table 7.5 are in good agreement to what is shown in the previous chapter, i.e., rock masses from *Cmet Fw2* structural domain (*Fw* sector and/or PH alteration zone) have rock structure characteristic that may result in finer fragmentation. The hang-up data of this study, which showed major frequency of event than other structural domains, was also in agreement with diorite rock type as the unit type with expected coarser fragmentation (Pereira and Zamora, 1999).

The results from the study that used visual inspections were found similar to these shown in Table 7.5. In addition, a comparison between the predicted in situ fragmentation using weak discontinuities (from Figure 7.8) and from feasibility studies (in Table 7.5) are shown in Figure 7.11. This figure also includes the observed fragmentation in Table 7.5.

Some conclusions can be draw from Figure 7.11; larger differences in the in situ fragmentation can be expected between *Fw* and *Hw* mine sector when the concept of weak discontinuities is applied compared to the methodology used during feasibility studies. As it was outline in Section 5.7.2 (Fragmentation Model for primary copper ore at the El Teniente mine), fragmentation in the draw points curve is located at the right of the potential fragmentation curve. Next, it seems that secondary blasting is not needed for caved rock block of *Fw* sector.

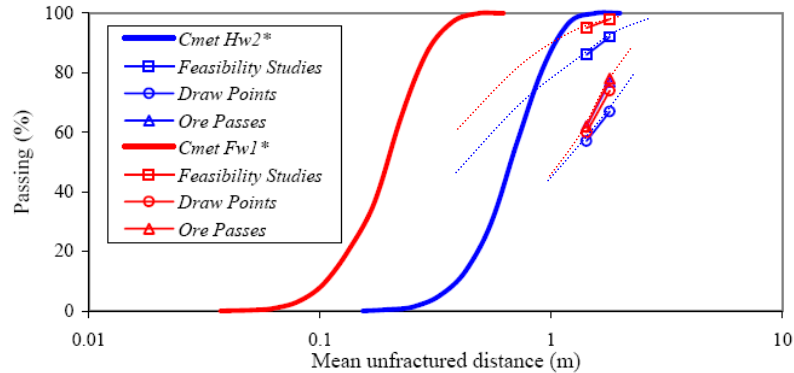


Figure 7.11.- Comparison between predicted (potential, feasibility studies) and observed (draw points and ore passes) fragmentation (adapted from Figure 7.8 and Table 7.5).

7.3.3 Rock Damage in Mine Drives of the Undercut Level

Major rock damage in mine drives has been observed and measured at the undercut level ahead of the cave front. This rock damage, which was observed as mine drive over brake, may be due to abutment stress caused by stress redistribution from major cave geometries. This kind of rock damage has been characterized in a general form of two damaged zones; high and low zone of mine over brake as shown Figure 7.12 (adapted from Gaete et al., 2005). The exactly picture of general mine conditions in June of 1999 is present in this figure, the main features shown are; a) The active footprint delimited by active draw points. b) The cave front geometry and/or the complete undercut area, c) Two zones in which pillar geometries can be considered similar; pillar areas equal to and greater than 250m^2 , as yellow and green colors respectively. d) Control points for stress analysis related to each structural domains used in the numerical model discussed in the next chapter. e) Rock damage areas located ahead of the undercutting front, high drive over brake (red zone) and low drive over brake (blue zone), which can be associated to the attached picture in that figure. The following figures, from 7.13 to 7.21, the picture of general mine condition at different times between 1999 and 2002. Rock damage zones as would be expected moved accordingly to the advancing cave front. A summary of the rock damage in term of the total damage area (m^2) between 1999 and 2004 for *Hw* and *Fw* sectors is shown in Figure 7.22.

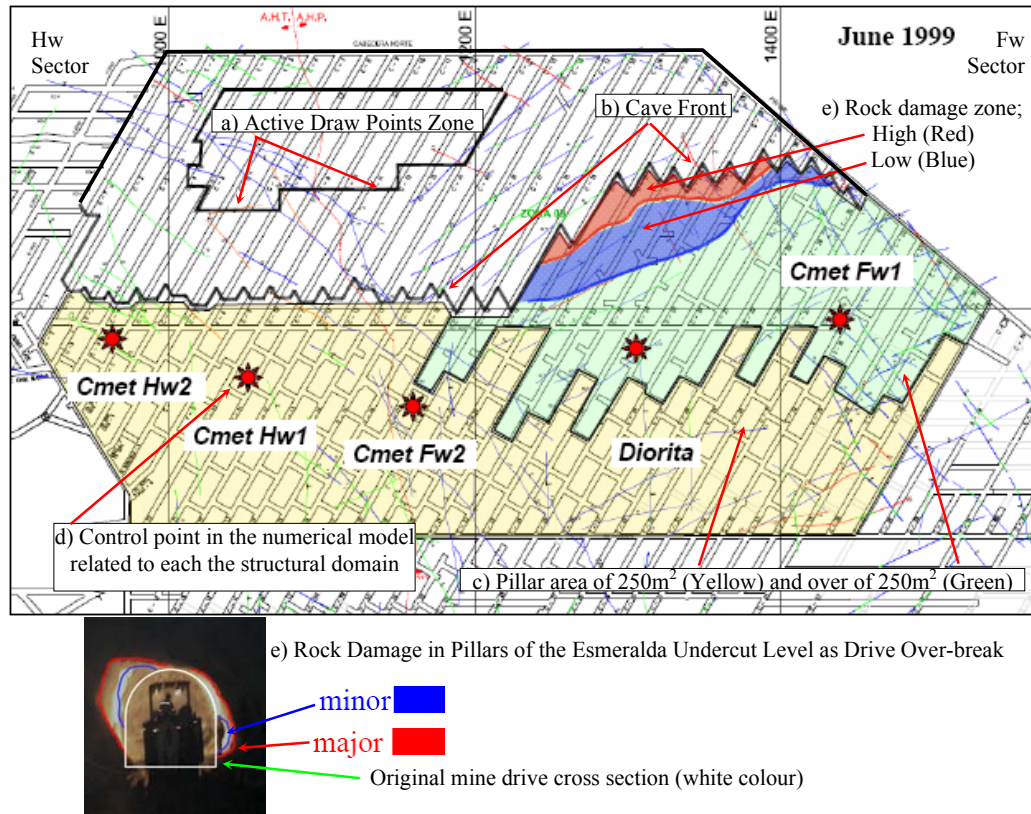


Figure 7.12.- Observed rock damage in mine drives as areas of high and low mine over-brake at the undercut level in June 1999 (adapted from Gaete et al., 2005).

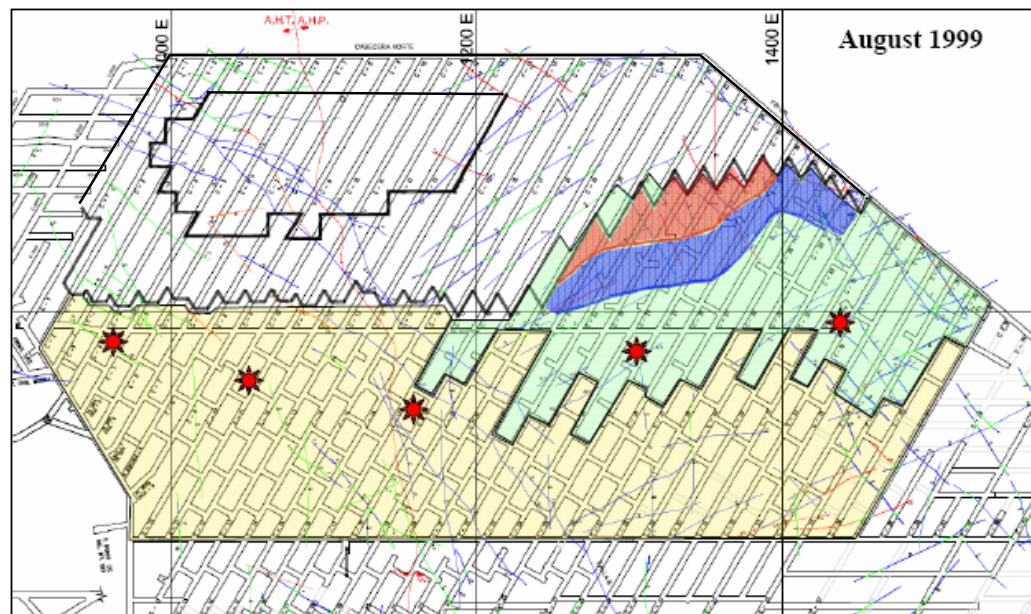


Figure 7.13.- Observed rock damage in mine drives of the undercut level in August 1999 (adapted from Gaete et al., 2005).

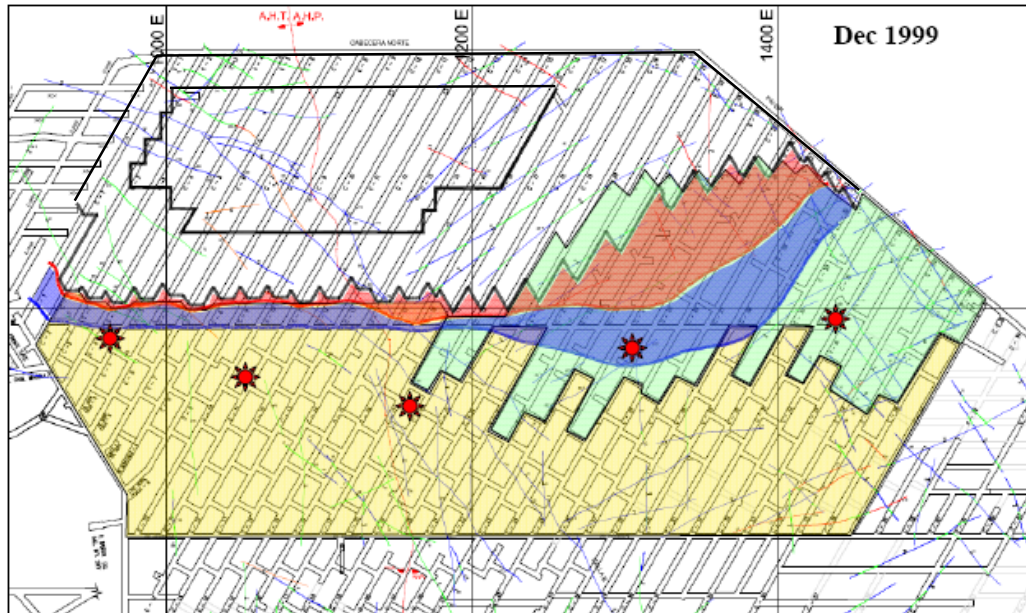


Figure 7.14.- Observed rock damage in mine drives of the undercut level in December 1999 (adapted from Gaete et al., 2005).

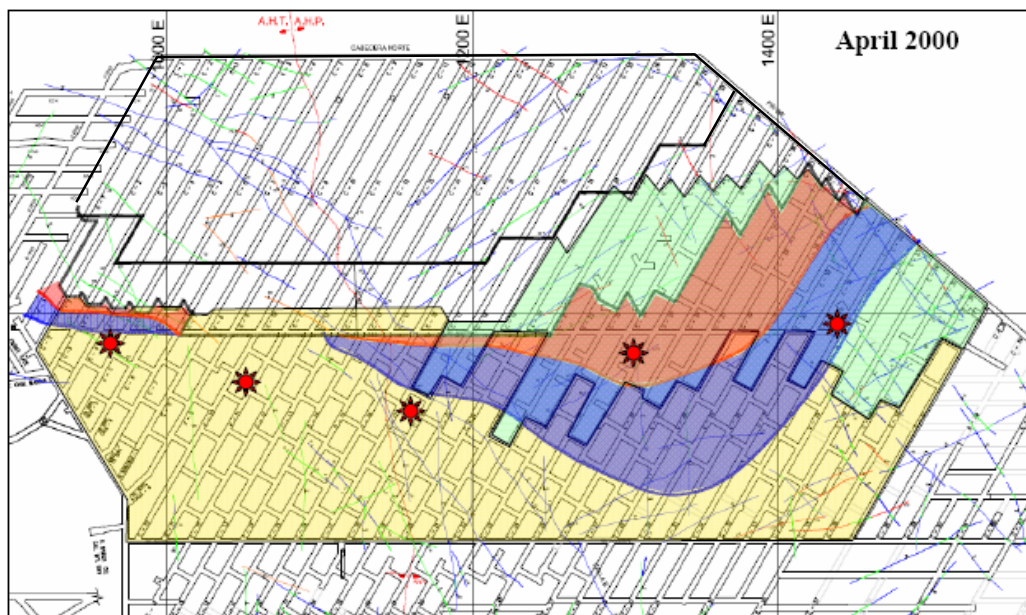


Figure 7.15.- Observed rock damage in mine drives of the undercut level in April 2000 (adapted from Gaete et al., 2005).

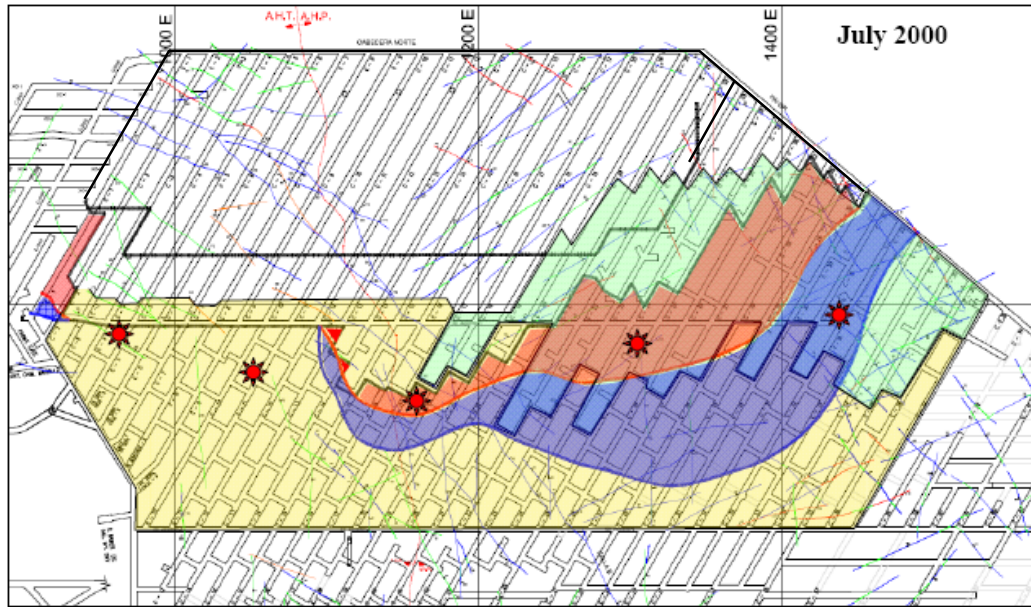


Figure 7.16.- Observed rock damage in mine drives of the undercut level in July 2000 (adapted from Gaete et al., 2005).

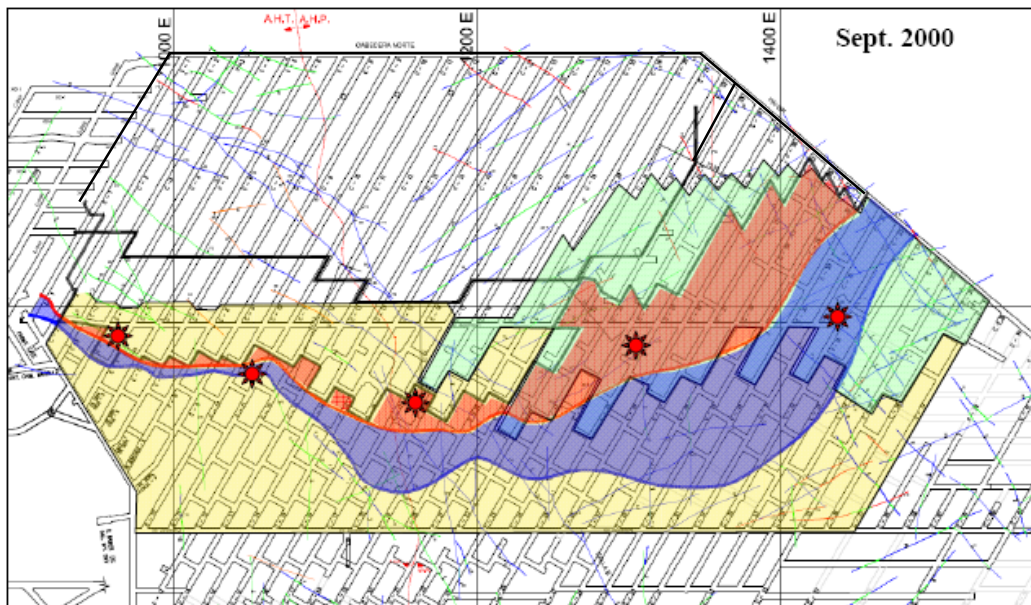


Figure 7.17.- Observed rock damage in mine drives of the undercut level in September 2000 (adapted from Gaete et al., 2005).

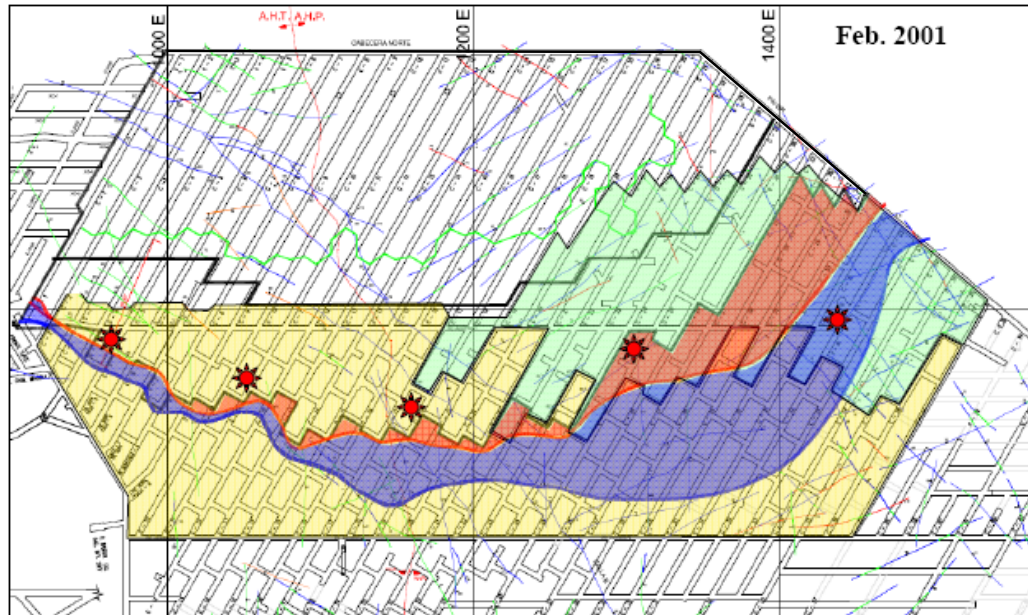


Figure 7.18.- Observed rock damage in mine drives of the undercut level in February 2001 (adapted from Gaete et al., 2005).

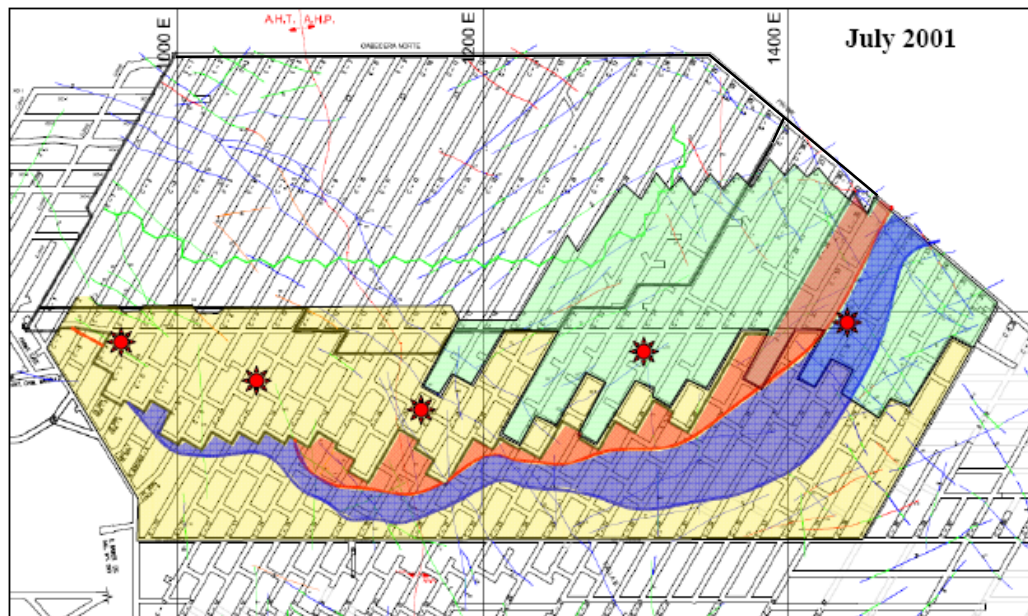


Figure 7.19.- Observed rock damage in mine drives of the undercut level in July 2001 (adapted from Gaete et al., 2005).

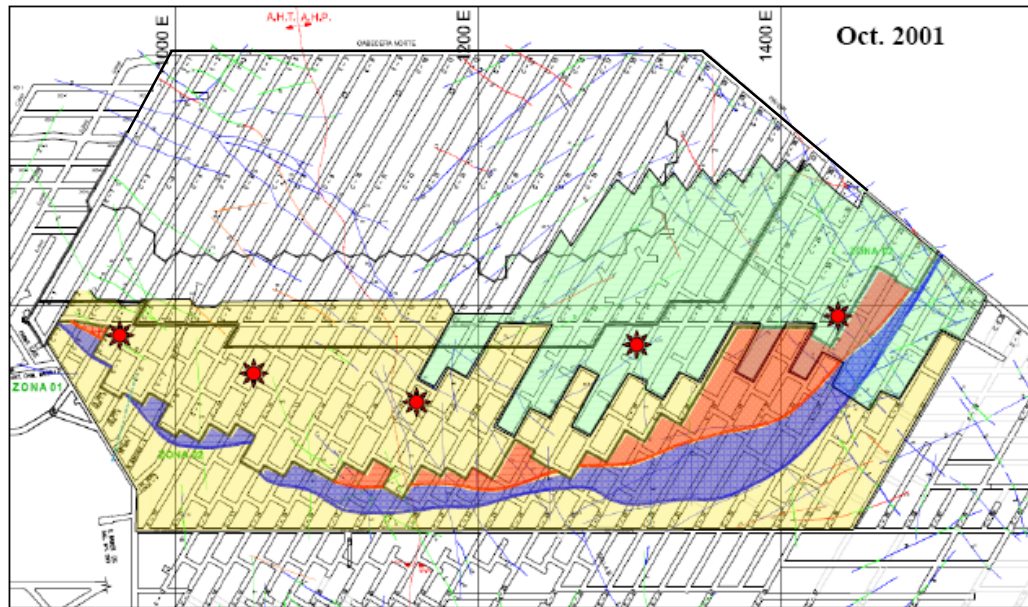


Figure 7.20.- Observed rock damage in mine drives of the undercut level in October 2001 (adapted from Gaete et al., 2005)

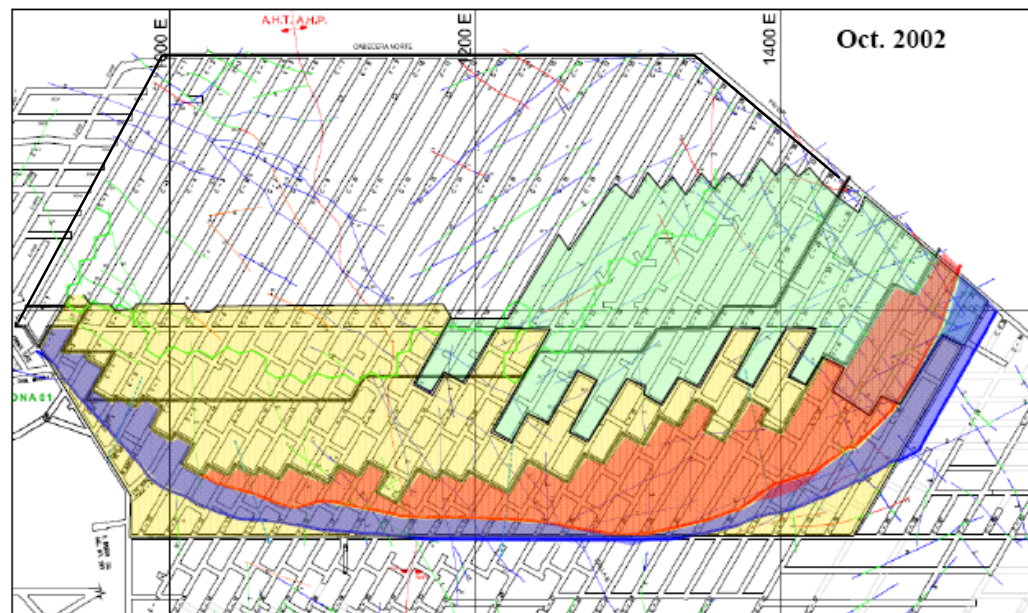


Figure 7.21.- Observed rock damage in mine drives of the undercut level in October 2002 (adapted from Gaete et al., 2005)

The data shown in Figure 7.22 indicates that grater zones of drive over brake has always been observed at the F_w sector compared to the H_w sector, even though the analysis considered to normalize the F_w sector by a factor of 2. This because, the F_w

sector area for the analysis almost duplicates the *Hw* sector area. Similar result can be seen for case when data are split in high and low rock damage (Figure 7.23). It interest to note that until February 2001 high mine over brake took place in pillar to be considered more robust (larger pillar areas in *Fw* sector) compared to the rest of the mine sector studied³. Based on the information presented in all these figures, it seems that the rock mass at the *Fw* sector maybe weaker than the one at the *Hw* sector.

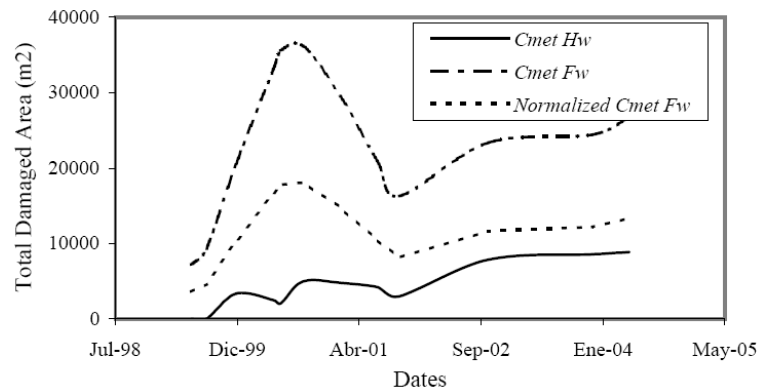


Figure 7.22.- Total rock damage observed at the undercut level of Esmeralda mine sector between 1999 and 2004 for *Hw* and *Fw* sectors. *Fw* sector has also being normalized by a factor of 2.

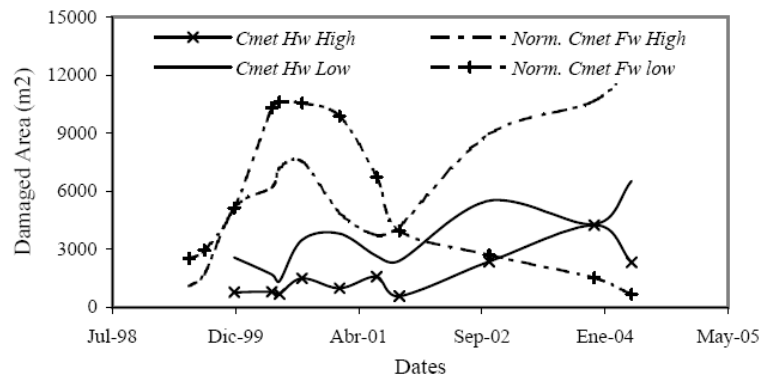


Figure 7.23.- Total rock damage observed in the undercut level of Esmeralda mine sector between 1999 and 2004 for *Hw* and *Fw* (normalised) sectors considering high and low rock damage.

The major rock damage observed at the undercut mine level is preferentially located at the *Fw* sector, it has been interpreted as the results of higher stress concentration due to stress redistribution by cave propagation (Gaete et al., 2005), which is

³ Maybe drive mine over brake does not correlate with pillar wide, but to weak discontinuity occurrence.

consistent with the higher over burden observed also at the *Fw* sector (see Figure 1.3). The stress concentration in the undercut level mine drives caused rock damage inside several pillars. Consequently, the normal blasting operations to increase the undercut area have been affected and consequently sometimes poorly performed. No relevant conclusion has been obtained from this phenomenon since no back analysis studies have been undertaken.

7.4 Conclusions

A new rock structure characterisation has been performed at the Esmeralda mine sector following the methodology developed in Chapter 5. This included a new data collection campaign and re-analysis of the standard data collected at the mine site. It was found similar results to what was found in data from the Reno mine sector, which are detailed as follow;

Weak veins, which are mainly filled with intermediate infill strength minerals, comprise at least three semi orthogonal discontinuity set orientations. These structures were found in high frequency within the rock mass, but describing different abundance between structural domains.

Faults were found widely spaced within the rock mass, comprising at least two sub-vertical sets trending north-east and north-west. The structural anisotropy defined by the fault occurrence does not change significantly through the structural domains in the area of study.

The in situ rock block distribution simulated for the case when only thick weak discontinuities were considered, shows that the andesite rock from *Fw* sector as the rock mass with finer potential fragmentation. This characteristic is in agreement with the fact that at the principal hydrothermal alteration zone (*Fw* sector) is more likely to find grater amount of weak discontinuities.

The thickness distributions have been found to have an isotropic characteristic within the rock mass, and it has also been confirmed that long discontinuities are statistically thicker than the short ones.

The application of the proposed rock structure characterization methodology to the new data demonstrated that comparable differences between unit types can be obtained when the infill strength features of veins is taken into account.

The preliminary analyses of the rock mass response to mining activities correlate with the fact that rock masses with grater abundance of weak discontinuities tend to determine weaker rock masses. In fact, it is clear that very finer fragmentation correlated with greater abundance of weak discontinuities. In addition, mayor drive mine over brake correlated apparently to a weaker rock mass as the one observed at the *F_w* sector.

CHAPTER 8 BACK ANALYSIS STUDIES

8.1 Introduction

During previous chapters it has been shown that the fragmentation observed during caving at Reno mine sector of the El Teniente occurred mainly through weak discontinuities (Chapter 4). It can also be say that the finer fragmentation observed in the production level at the *Fw* sector of the Esmeralda mine (Villegas, 2006, Pereira and Zamora, 1999) was associated with the large abundance of weak discontinuities observed within the rock mass, compared to those ones observed at the *Hw* sector (Chapter 7). Hence, data suggest that weak discontinuities defined in this study truly represent the weak path where the massive and competent rock mass of primary copper ore fail under stress conditions.

Consequently, it is expected that the weak discontinuities also play a relevant role in the overall geotechnical behavior of primary copper ore. In other words, it could be states that *“the strength of the massive and competent rock mass at the El Teniente mine would depend of the occurrence of weak discontinuities within such rock masses”*. Although the proper way to prove such statement would be through performing a controlled experiment (for instance, a triaxial compressive test of the rock mass in the laboratory), both the scale and the nature of the problems studied here does not allow performing such kind of experiments. However, it would be possible to back analyses some observed experiences during caving performance at the El Teniente mine to investigate the validity of such statement, which is the hypothesis research.

In this study, recorded mine seismicity and rock damage observed during caving initiation and propagation at the Esmeralda mine sector were back analysed to investigate the importance of the weak discontinuities in the overall geotechnical behavior of rock masses of the primary copper ore. Additionally, in order to complete the back analysis loop; *stress* applied lead to observe *strain* which would depend of the *rock mass strength*, a mine scale numerical model was performed to assess the state of stress around excavations during caving initiation and propagation at the studied mine sector.

8.1.1 Goal

The main objective of this chapter is to investigate the validity of the hypothesis research through back analyses studies. In other words, to investigate the importance of weak discontinuities in the overall geotechnical behavior of rock masses of the El Teniente primary copper ore.

Induced seismicity, which included moment tensor estimates, and rock damage response to mining activities at the Esmeralda mine sector (from section 7.3.3) were the data used to perform the back analyses studies. In order to assess the state of stress around excavation during caving operations, a mine scale numerical model was performed. The back analyses studies also included a review of mine seismology and seismic monitoring at the mine site.

8.2 Background of Mine Seismology and Seismic Monitoring at the El Teniente Mine

Mining activities, such as block caving, disturb the near field stress within the rock mass surrounding excavations (cave). This may result in stress levels exceeding the rock mass strength. If this is the case, rock failure may occur and the potential energy accumulated in the rock mass may be released (unloaded) gradually or suddenly. The rock failure may occur through the intact rock material (fracturing) or through a pre-existing discontinuity (slip). A mining induced seismic event corresponds to the radiated energy during a sudden rock mass failure.

The energy is released in form of seismic waves, which propagate through a *medium* and then are recorded by the seismic sensor at a seismic station. Seismic sensors essentially record the ground motion as a time function, and it is represented as a seismogram (Figure 8.1). Waveform characteristics from the seismograms recorded in several seismic stations provide valuable information of the source, such as location (hypocentral distance from sites) and source parameters like the overall size of the event (Magnitude), seismic moment and radiated energy, among others seismic parameters. In general, the characteristic of the induced seismic event will depend of the strength of the rock mass, the state of stress, the size of the source of

the seismic radiation, and on the rate at which the rock mass is deformed during rock mass failure (Mendecki, 1997).

At the El Teniente mine, seismicity has been noticeable since the primary copper ore exploitation started in the 80's (Rojas et al., 2000). The experimental primary copper ore Ten-4 Fw mine sector was closed in 1987 after severe damage in the production level caused by some large magnitude dynamic failures from stress redistribution. The Reno mine sector suffered a similar situation; it was closed in 1992, and was experimentally re-opened between 1994 and 1998. After gained experience in controlling mine induced seismicity, Reno mine sector was again incorporated to the production plan in 1998 (Rojas et al., 2000).

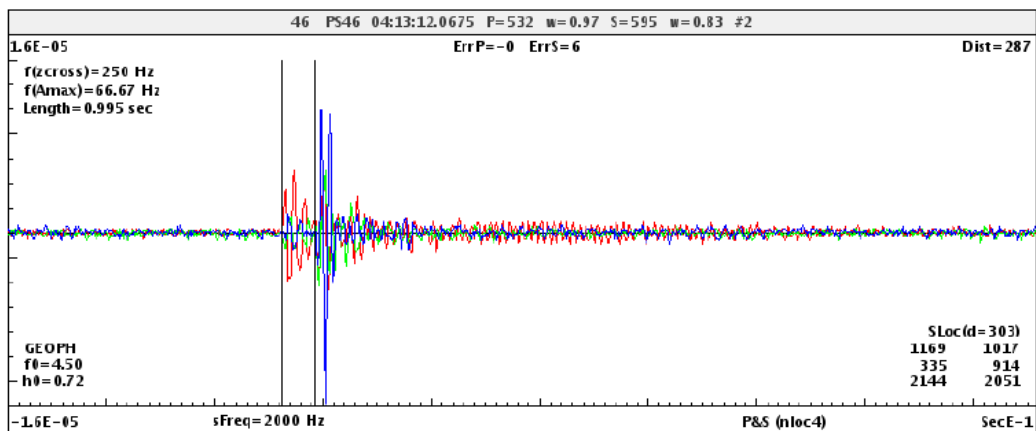


Figure 8.1.- Seismogram recorded by a triaxial sensor at the El Teniente mine.

Initially at the El Teniente mine, three different analogue monitoring systems were installed aiming to cover only the primary ore exploitation (Dunlop and Gaete, 1997). From 1992 a fully digital seismic monitoring system has been operating to cover the entire mine, since then this system has been supported and maintained by ISS International Limited (ISS, 2007). During caving initiation at the Esmeralda mine sector, around 29 remote seismic stations were operating. Each seismic station included a 4.5Hz triaxial geophone (Dunlop and Gaete, 2001). Evidence of seismicity at the Esmeralda mine sector started after the undercutting initiation in October 1996 (Dunlop and Gaete, 2001). Caving initiation started one year later, and the breakthrough to the upper level was estimated to occur in April-May 1999. Until

2003 more than 80,000 events were processed by the monitoring system in that mine sector (Figure 8.2). Seismicity due to blasting is not included in this number.

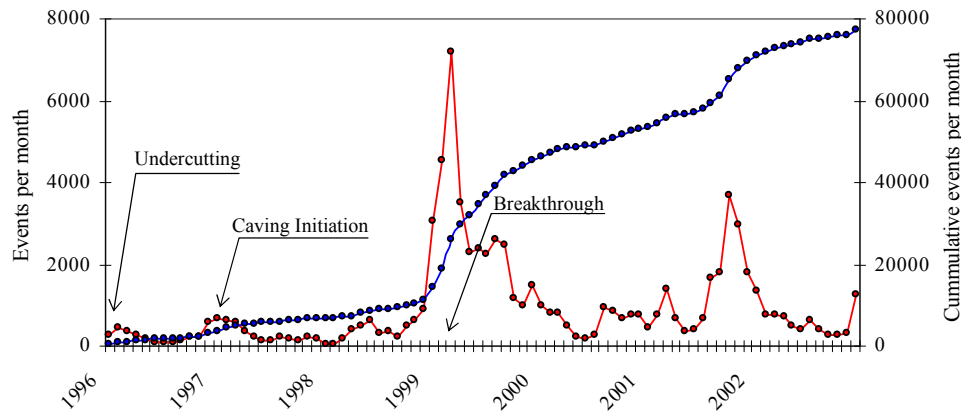


Figure 8.2.- Seismic events recorded per months at Esmeralda mine sector between 1996 and 2003.

The seismic events at the El Teniente mine are automatically processed using the commercial JMTS-ISS software package, and the seismic source parameters including the event location, time, radiated seismic energy, seismic moment (measure of the strength of the seismic event), Magnitude (overall size of the seismic event) are automatically calculated. Detailed descriptions of seismic source parameters are presented in Appendix III.A. A more detailed technical description of the ISS software package calculations is also described by Mendecki (1997).

The quality and the integrity of the seismic data at the El Teniente mine has been recently assessed by ISS International Limited as part of a seismological back analysis study of large seismic events at the Reno mine sector (ISS, 2007). The assessment shown that the monitoring system was in good condition and seismic source parameter have been well estimated (ISS, 2007).

Main seismic parameters recorded at the El Teniente mine range as follow;

Scalar Seismic Moment: $10^7 \leftrightarrow 10^{13}$ (Nm)

Radiated Energy: $0.2 \leftrightarrow 10^8$ (J)

Moment Magnitude scale: $-1.5 \leftrightarrow 2.7$ (used as local magnitude scale)

The media or medium for seismic calculation is defined as isotropic and homogeneous at the mine site. The currently velocity model assumes the following values;

$$V_p = 5600 \text{ m/s} \quad V_s = 3500 \text{ m/s} \quad \text{Density } \rho = 2700 \text{ kg/m}^3$$

An example of the recorded seismicity at the Esmeralda mine sector between 1997 and 1999 is shown in Figure 8.3. In this figure, the majority of the induced seismic events are located surrounding the cave, which has been described as the seismogenic zone around the cave (Duplancic, 2002).

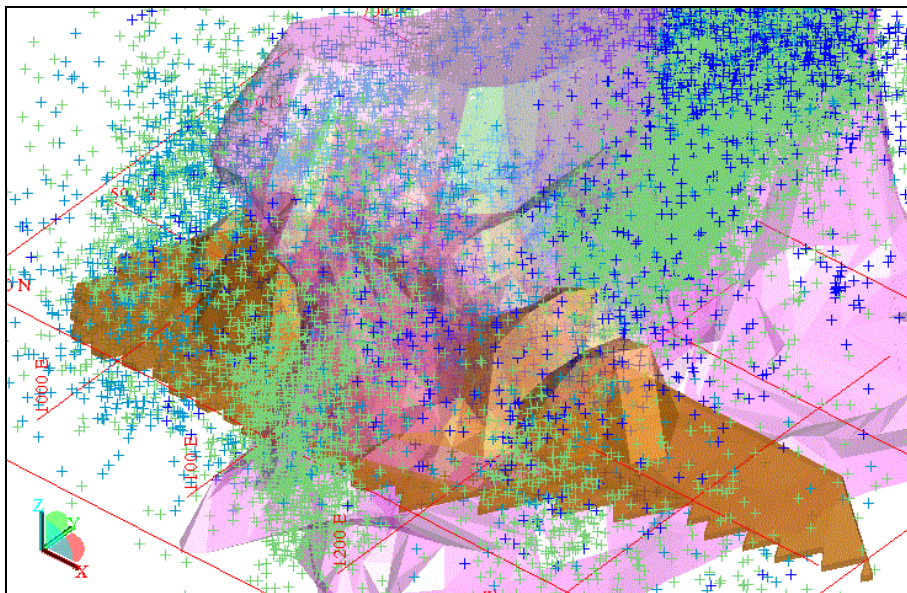


Figure 8.3.- Isometric view of Esmeralda mine sector showing cave geometry, diorite rock and the recorded seismicity (crosses green and blues) between 1997 and 1999. For details see Figure 7.10.

8.2.1 Seismic Moment and Moment Magnitude

The seismic moment also called the *scalar moment*, M_o , is a measure of the strength of the seismic event¹. It is defined assuming a double-coupled point model or a pure shear dislocation mechanism (Figure 8.4). M_o is expressed as (Aki and Richards, 1980):

$$M_o = \mu A D \quad [\text{Nm}] \quad (8.1)$$

¹ Originally defined for earthquakes, is also a measure of the size of the induced seismic events.

where μ is the shear modulus at the source, A is the area over which the dislocation occurred, and D is the average slip over the area A .

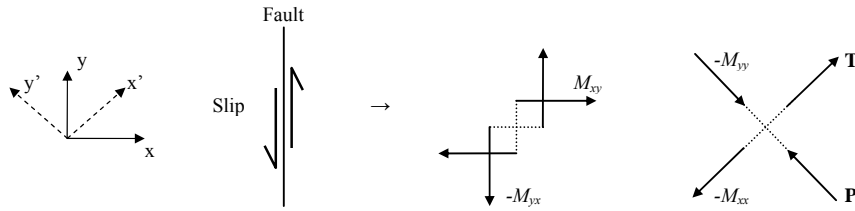


Figure 8.4.- Equivalent body force description. Fault slip can be described by the superposition of either force couples M_{xy} and M_{yx} or force dipoles M_{xx} and $-M_{yy}$. (Modified after Stein & Wysession 2003).

A force couple consists of two forces acting together, in opposite direction. The net force or torque is annulled when two force couples (double couple) are simultaneously acting at the source, allowing only shear failure to occur.

Magnitude was the first measure of the size of an earthquake. It is based on the amplitude of the resulting waves recorded on a seismogram (Figure 8.1). The first magnitude scale was introduced by Charles Richter (Richter, 1935), which is known as *local magnitude scale*, M_L . It is defined as;

$$M_L = \log A(\Delta) - \log A_0(\Delta) \quad [\text{dimensionless}] \quad (8.2)$$

where

A is the maximum trace amplitude at distance Δ

A_0 is the maximum amplitude

Moment magnitude scale, M_w (Hanks and Kanomori, 1979) used as local magnitude at the El Teniente mine is based on the seismic moment, which is derived from the spectra domain² (in appendix III.A). It is estimated as follow.

$$M_w = \frac{2}{3} \log M_o - 6.0 \quad [\text{dimensionless}] \quad (8.3)$$

where M_o is the scalar seismic moment.

² See Figure III.A4 in Appendix III.A for more details.

8.2.2 The Gutenberg-Richter Distribution and Seismic Potential

Seismicity that occurs in a certain period of time within a particular seismogenic zone varies with magnitude, with successively smaller seismic events being more common. This natural occurrence of seismicity has been quantified by Gutenberg–Richter power law seismic event *frequency-magnitude* relation. This empirical distribution for events, has been observed at different range scales; from earthquakes to laboratory experiments, including mine induced seismicity (Scholz, 2002). Figure 8.5 presents an example of the Gutenberg–Richter plots of the observed mine induced seismicity in different years at the Esmeralda sector.

Based on that empirical distribution for induced seismic events, seismic potential or event probability can be assessed as follow;

$$\text{Log } N(\geq m) = a - bm \quad (8.4)$$

where $N(\geq m)$ is the expected number of events not smaller than magnitude m , and a , b are constant obtained from the Gutenberg–Richter plot (Figure 8.5).

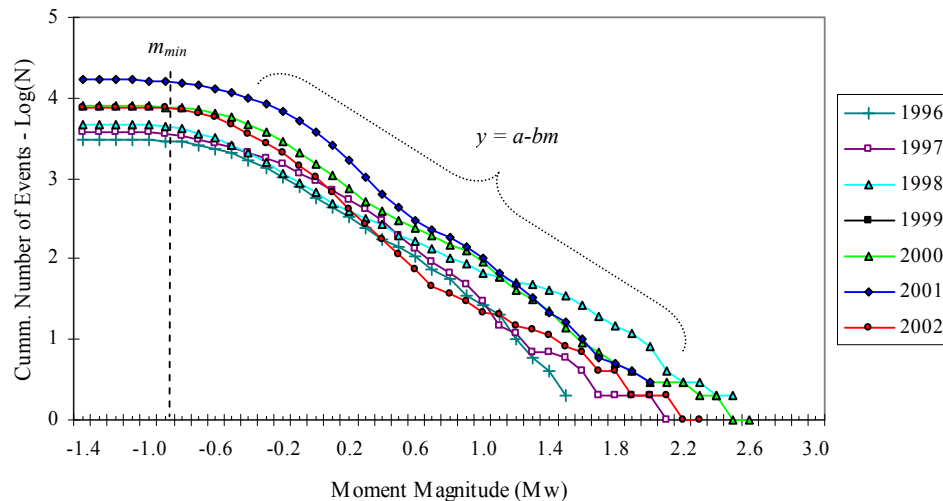


Figure 8.5.- The Gutenberg-Richter seismic event frequency-magnitude relation for different years at the studied mine sector.

The array or the monitoring system sensitivity can also be determined from the Gutenberg–Richter plot. The minimum moment-magnitude above which the system records all the events with sufficient signal to noise ratio is defined as m_{min} , which is

determined where the slope changes in the cumulative event-magnitude distribution (dashed line in graphs of Figure 8.5). In Figure 8.5, it can be seen the array sensitivity operating at the Esmeralda mine sector as the same from 1996 to 2002.

8.2.3 *Mine Production and Control of the Induced Seismicity*

Various rules, based on mining activities, have been established to control induced seismicity at the El Teniente mine (Dunlop and Gaete, 1997, Rojas et al., 2000, Dunlop and Gaete, 2001). Mining parameters such as the undercutting advance rate (increment of the hydraulic radius) and the extraction rates (draw) modify the size and geometry of the cave, which control induced stresses that cause induced seismicity. Therefore, management the induced seismicity can be based on controlling the rate of these mining parameters, as used the Esmeralda mine production (Rojas et al., 2000, Dunlop and Gaete, 2001).

One of the main concepts gained through Esmeralda's experience is the "30% of the column height extraction" (applied only to primary copper ore). It has been observed, particularly in this mine sector during caving propagation (1998-9), that for 1 meter high of ore extraction at the production level draw points, the broken rock mass in the caveback grew up to 3 meter high, therefore the caveback may breakthrough (reach the top of extracted rock column) after the ore extraction reach 30% of the column height. It is expected that most of the induced seismicity occurs before the ore extraction reaches this 30% of the primary ore column height, therefore, extraction rate is only constrained to this column height (Rojas et al., 2000, Dunlop and Gaete, 2001).

8.2.4 *Moment Tensor*

A major research in seismology is the description of the physics of the seismic source; a common approach is the approximation by a model of equivalent forces acting in a point that cause the physical dislocation and displacements during a seismic event. The body force representing the seismic point source can be modelled by nine possible combinations of force and arm directions, as is shown in Figure 8.6. The equivalent forces are determined from observed seismograms correcting by instrument and path.

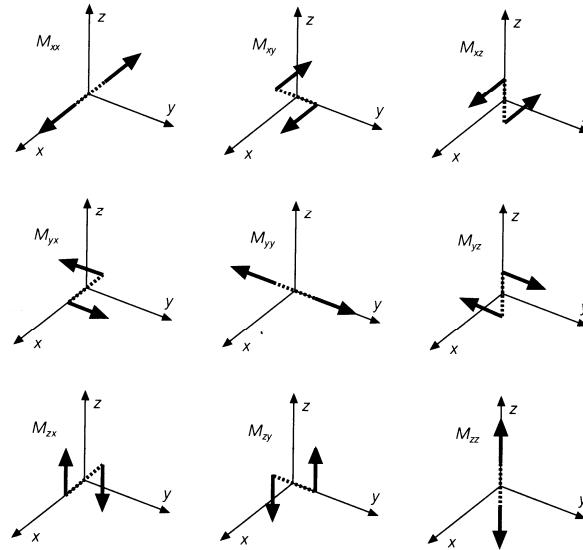


Figure 8.6.- Nine possible force couples M_{ij} of a moment tensor (after Aki & Richardson, 1980).

The set of nine terms M_{ij} (forces couples) is known as the moment tensor, M , which is a symmetrical second order tensor with six independent components. The subindices i and j denote the directions of the forces and the arm of the couple, respectively. Then, the moment tensor is denoted as;

$$M = \begin{pmatrix} M_{xx} & M_{xy} & M_{xz} \\ M_{yx} & M_{yy} & M_{yz} \\ M_{zx} & M_{zy} & M_{zz} \end{pmatrix} \quad [\text{Nm}] \quad (8.5)$$

A double couple source or shear mechanism is only one of these possible force combinations, which may be represented as;

$$M = \begin{pmatrix} 0 & M_o & 0 \\ M_o & 0 & 0 \\ 0 & 0 & 0 \end{pmatrix} = M_o \begin{pmatrix} 0 & 1 & 0 \\ 1 & 0 & 0 \\ 0 & 0 & 0 \end{pmatrix} = M_o(M_{xy} + M_{yx}) \quad (8.6)$$

where M_o is the scalar seismic moment or magnitude of the equivalent body force.

The eigenvectors of the moment tensor give the directions of the principal stress axes acting on the source (neglecting gravity). The eigenvalues provide their magnitude (Gibowicz, 1990).

Let m_1, m_2, m_3 define the eigenvalues and their corresponding eigenvectors a_1, a_2, a_3 of a moment tensor M . Then, the moment tensor can be decomposed into three major parts; the compensated linear vector dipole (*CLVD*), the isotropic (*ISO*) and the double-couple (*DC*) components according to the rule (Gibowicz and Kijko, 1994):

$$M = \frac{1}{3}(m_1+m_2+m_3)\mathbf{I} + m_3^d F (2a_3a_3-a_2a_2-a_1a_1) + m_3^d (1-F)(a_3a_3-a_2a_2)$$

$$M = \text{ISOI} + \text{CLVD}(2a_3a_3-a_2a_2-a_1a_1) + \text{DC}(a_3a_3-a_2a_2) \quad (8.7)$$

where \mathbf{I} represents the unity matrix, $m_i^d = m_i - (m_1+m_2+m_3)/3$ with $|m_3^d| \geq |m_2^d| \geq |m_1^d|$, and $F = -m_1^d / m_3^d$.

The isotropic or the volumetric component represents a volume change at the source. An explosive source such as a mining blast is an example of pure isotropic mechanism (non zero trace³). Two primary explanations have been offered for *CLVD* mechanism (zero trace); a crack opening under tension⁴ and/or due to near-simultaneous faults of different geometries (Stein and Wysession, 2003). Several reported cases of mine tremors showing evidence of non-double couple mechanism have been compiled by Gibowicz (1990). For instance, it was found that the ratio between tensile/shear component ranged from 1 to 13 percent for shallow earthquakes (Sileny et al., 1986). The waviness of a fault and/or the occurrence of two sub-events occurring on fault planes of different geometries and separated in time may explain non-double couple mechanism at the source (Gibowicz, 1990). Figure 8.7 illustrates these possible explanations, where for instance, a fault slip (shear mechanism) can be associated with traction failure (the top illustrations in that Figure 8.7).

8.2.5 Focal Mechanism

The study of the geometry of faulting during earthquakes is known as the focal mechanism. Seismograms recorded at various distances and azimuths are used for this purpose. This concept assumes a double couple source mechanism and the pattern of radiated seismic waves depends on fault geometries (Figure 8.8), i.e., the

³ Trace is defined as $m_1+m_2+m_3$

⁴ An inflating magma dike modelled as crack in tension.

first motion or polarity of P wave arrivals are related to the sensor location. This figure illustrates a strike slip earthquake on a vertical fault, the first motion is in compression (P wave up) for stations located where the fault move *'toward'* the station. Where the motion is *'away from'* the stations, the first motion is in dilatation (P wave down).

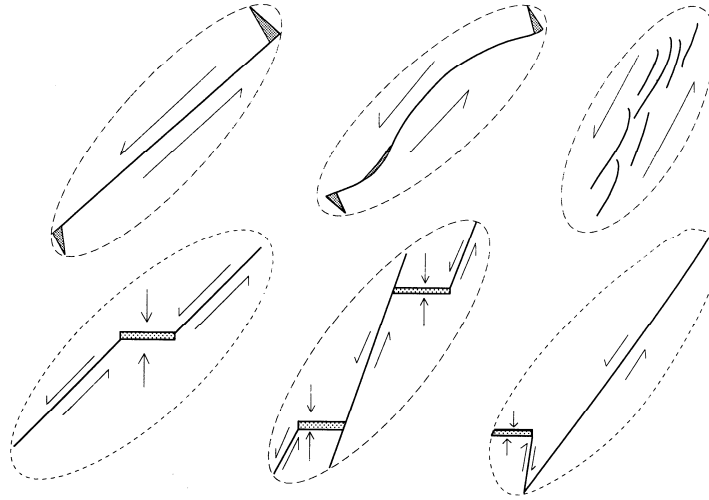


Figure 8.7.- Several possible source explanations for simultaneous non-double couple and double couple source mechanisms (from Mendecki, 1997).

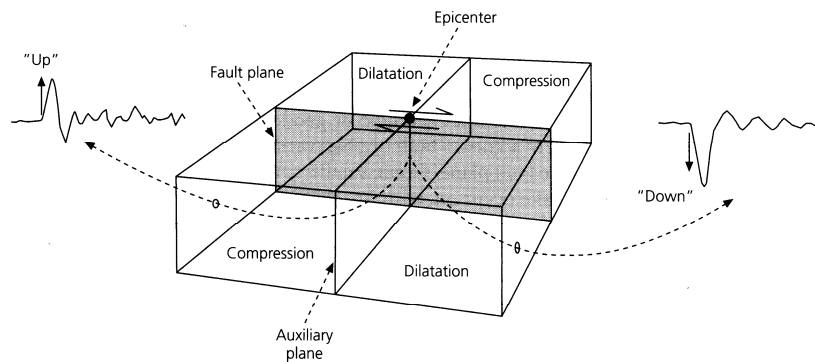


Figure 8.8.- Focal mechanism and first motion (after Stein & Wysession 2003).

The first motion divides the space or the focal sphere in four quadrants, two compressional and two dilatational. These occur along the fault plane and a plane perpendicular (auxiliary plane) to it, both are called *'nodal planes'*. The same pattern of first motion can be detected as result of slip occurring at either of the two nodal

planes, and then the first motion cannot be solved without additional geological or geodetic information.

First motion solutions (also known as fault plane solutions) relate the focal mechanism to the ambient of state stress by the equivalent representation of body forces. The two force couples acting at the source are: the pressure P axes and the tension T axes (see also Figure 8.4), while the null motion axes B is represented by the intersection of the two nodal planes. The P, T, and B axes are considered to be close to the maximum, minimum and intermediate principal stresses within the rock mass during failure, respectively (Gibowicz 1990). Closer solution of the principal stress orientation can be obtained through cluster analysis of the P, T, and B axes for a set of events spatially and temporally related (Gephart and Forsyth, 1984, Urbancic and Young, 1993, Mendecki, 1997).

Focal mechanism can be determined either by geometrical data analysis by knowing the source and station locations or directly by moment tensor using the inversion procedure. The second one has the advantage to analyse the seismograms without assuming a determined source mechanism.

8.2.6 Moment Tensor Inversion

The method consists in finding the moment tensor that best matches the observed and the synthetic seismograms.

The displacement field, $u_i(x,f)$, generated by the nine possible combinations of body forces (Figure 8.6), which can be modelled as a linear functions of the component of moment tensor in the frequency domain (Gibowicz and Kijko, 1994);

$$u_k(x,f) = M_{ij}(f) G_{ki,j}(f), \quad (8.8)$$

where $M_{ij}(f)$ is a vector that represents the source, which contains the 6 independent component of the moment tensor⁵ (Equation 8.5). f represent each frequency, and $G_{ki,j}(f)$ is the Green's function that represents the medium response to the motion. The Green's function includes the seismometer effects, and the earth structure along the path from the source to this seismometer.

⁵ 6 because it is a symmetric matrix

Then, a synthetic seismogram, u , at the i^{th} station is defined as the sum of the Green's function weighted by the each moment tensor component:

$$u_i(t) = \sum_{j=1}^6 G_{ij}(t)m_j \quad [m_i = M_{ij}] \quad (8.9)$$

Since we have many seismograms, equation 8.9 can be written as a vector matrix equation:

$$\mathbf{u} = \mathbf{Gm} \quad \text{or} \quad \begin{pmatrix} u_1 \\ u_2 \\ \cdot \\ \cdot \\ u_n \end{pmatrix} = \begin{pmatrix} G_{11} & G_{12} & G_{13} & G_{14} & G_{15} & G_{16} \\ G_{21} & G_{22} & G_{23} & G_{24} & G_{25} & G_{26} \\ \cdot & \cdot & \cdot & \cdot & \cdot & \cdot \\ \cdot & \cdot & \cdot & \cdot & \cdot & \cdot \\ G_{n1} & G_{n2} & G_{n3} & G_{n4} & G_{n5} & G_{n6} \end{pmatrix} \begin{pmatrix} m_1 \\ m_2 \\ m_3 \\ m_4 \\ m_5 \\ m_6 \end{pmatrix} \quad (8.10)$$

This represents a system of linear equations with more equations (n) than unknowns (6). Because \mathbf{G} is not a square matrix, it cannot be inverted to solve the system of linear equations. Instead, the moment tensor that best matches the observed seismograms is found by applying what is called the *generalized inverse* of \mathbf{G} as (Stein and Wysession, 2003):

$$\mathbf{m} = (\mathbf{G}^T \mathbf{G})^{-1} \mathbf{G}^T \mathbf{u} \quad (8.11)$$

The quality of the inversion is quantified by a mean coefficient of correlation, \bar{C}_c , between the observed and the synthetic seismograms (Mendeki, 1993). The \bar{C}_c ranges from 1 to -1: 1 is a perfect match, 0 implies no correlation and -1 is the perfect anti correlation.

8.3 Analysis of Recorded Seismic Data during Caving Propagation

Seismicity is one of the best records of rock mass response to mining activities at the mine site; therefore, its analysis was used to validate the hypothesis research. Two different approaches were undertaken to perform this task. The first approach is related to the focal mechanism studies, because this seismic analysis technique may provide information of the discontinuity orientation being mobilised during the development of seismicity. In this section re-analysis of focal mechanism studies

were undertaken to correlate the discontinuities being mobilized (damage orientation) at the seismogenic zone, where caving will propagate, with the structural data collected in previous chapters. The second approach is related to seismicity at the seismogenic zone itself. In general, the characteristic of the induced seismic event will depend of the strength of the rock mass, the state of stress, and on the rate at which the rock mass is deformed during rock mass failure (Mendecki, 1997). Therefore, seismicity may be correlated to the rock mass strength by assessing and analyzing all these parameters.

8.3.1 *Focal Mechanism at Reno Mine Sector*

Two different studies based on moment tensor inversion methodology have been carried out to determine focal mechanism for major dynamic failures that occurred at the East sector (hanging wall) of the Reno mine sector.

The first study assessed the temporal seismicity spatially related to the $M_w = 3.0$ event that occurred on April 22nd, 2003 (Dunlop and Belmonte, 2005). Hence, seismicity recorded between January 2002 and May 2003 were analysed for events having $M_w > 0.0$. Only 26 stable solutions were obtained. According to the motion of the upper side of the faults, only 22 events were identified having reverse mechanism. The original data was re-analysed and plotted using pole vector representation (stereographic projection, Figure 8.9). In this figure only events $M_w \geq 0.6$ are plotted: a) shows the fault plane solutions, and in b) the cluster of P, T and B axes are plotted. No information of the inversion quality is provided in this work.

The second study included all seven major dynamic failures and their aftershock that occurred between 2000 and 2005 at the same sector (ISS, 2007). Only event magnitude ranging from -0.4 to 3.0 were included. In this case a more accurate procedure, which included sensor orientation corrections, was applied. Again, the original data (38 events) was re-analysed and plotted using pole vector representation (Figure 8.10).

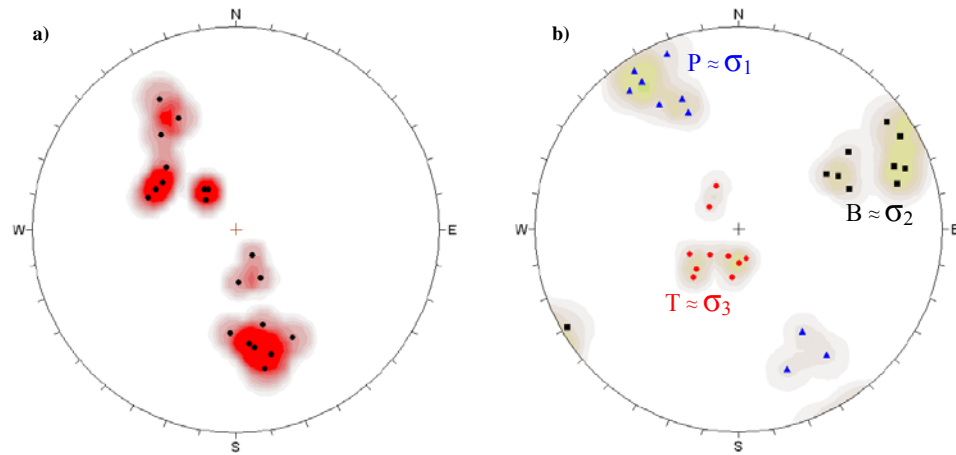


Figure 8.9.- Faults plane solution and orientation of T, P and B axes for seismicity associated to the April 22nd, 2003 event plotted in lower hemispheric projection (modified from Dunlop and Belmonte, 2005).

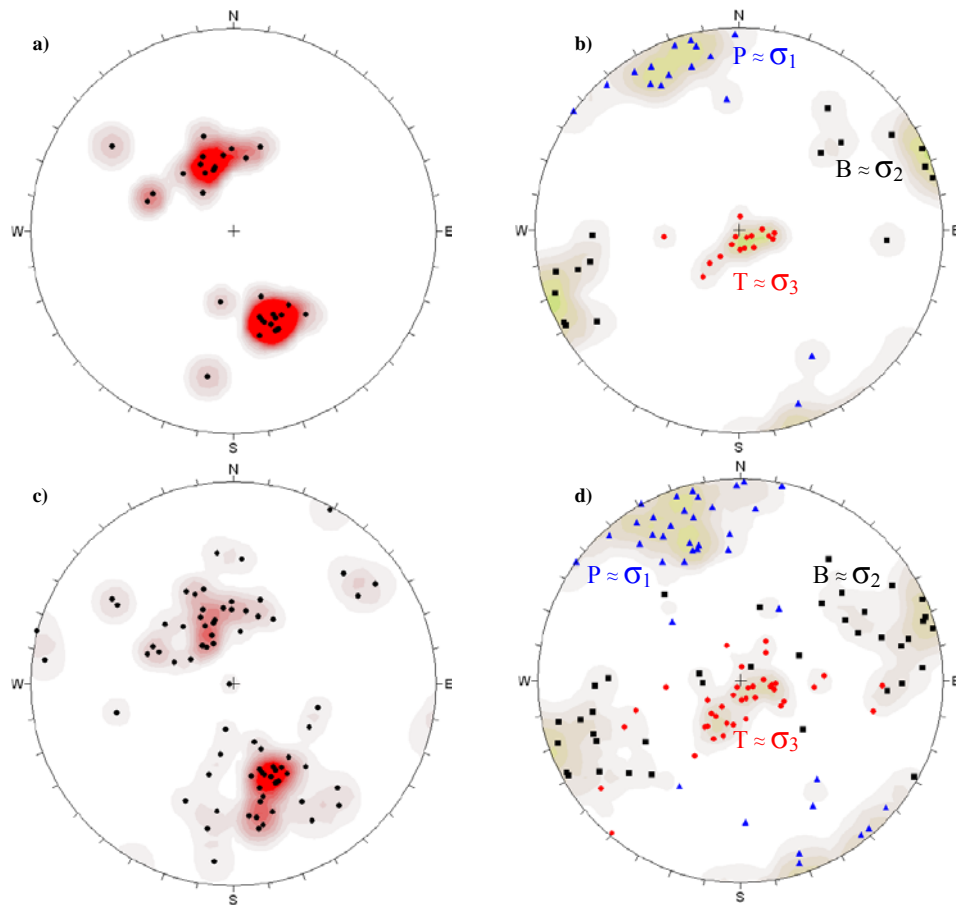


Figure 8.10.- Faults plane solution and orientation of T, P and B axes for major failures occurring between 2000-2005 plotted in lower hemispheric projection (modified after ISS, 2007)

Different illustrations are presented in Figure 8.10; in a) is shown all fault plane solutions for events $M_w \geq 0.7$. In b) Cluster of P, T and B axes as principal stresses orientation for events $M_w \geq 0.7$ are plotted. In c) all 76 fault plane solutions are shown. In d) Cluster of P, T and B axes for all events are illustrated. The inversion quality estimated for most data investigated is over 0.5.

The following can be concluded based upon the data shown in Figure 8.9 and Figure 8.10;

1. The same source mechanism for major dynamic failures has been operating at the *Hw* sector of the Reno mine between 2000 and 2005. In practically all cases only a reverse mechanism has occurred.
2. The discontinuities which were the most likely to be mobilized are faults. This interpretation is based in two main arguments; faults as open discontinuities are weaker than veins, and faults have also larger sizes.
3. From Figure 8.9a and Figure 8.10a, the discontinuity orientation 50/340 (Dip/Dipdir) was the most likely to be mobilized. This result was reached after a comparison between faults and veins orientations from the same sector (see also Figure 3.5 and Figure 3.6 from *Hw* sector where those seismic event were located).
4. Similar to what has been found in other mine environments under high confining pressure (Gibowicz, 1990), the tensile component of source mechanism was up to 20% for most mobilized discontinuities (Figure 8.11). Low values of the isotropic component of moment tensor can be inferred from higher confining pressure during failure, and that agree with the interpretation that most of these events have been re-located below and far from mine level (ISS, 2007).
5. The principal stress orientations obtained from cluster analysis of P, T, and B axes are showing similar orientation to the in situ principal stresses obtained from the WASM acoustic emission stress measurements (compared with Figure 1.14). These results are in agreement with major events location below and far from current mine levels, where stress redistribution by caving

geometries may have occurred only in terms of magnitude changes. Similar results have been obtained in other seismological field and mine environments (Gephart and Forsyth, 1984, Urbancic and Young, 1993, Mendecki, 1997).

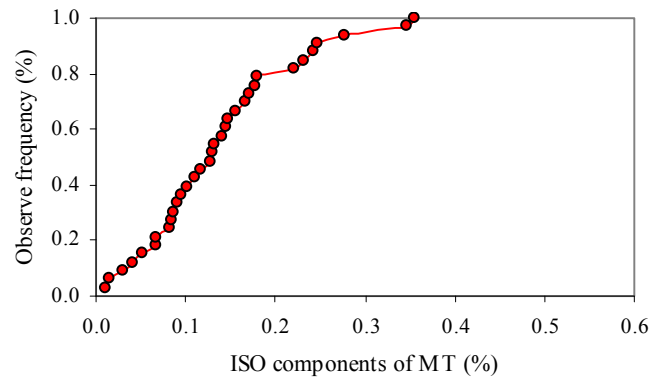


Figure 8.11.- Source mechanism for major dynamic failures at the Reno mine sector.

6. Data of moment tensor by the inversion procedure have not been significantly affected by location errors (ISS, 2007), even for data processed without sensor orientation corrections⁶. This increases the confidence in the moment tensor estimates used in this study, despite any location errors that may exist.

8.3.2 Focal Mechanism at Esmeralda Mine Sector

A special data collection program for this research was designed to obtain moment tensors during April 2007. Moment tensor estimates were determined using the inversion procedure at the JMTS-ISS software package at the mine site⁷ (Belmonte 2007, written communication). The main criteria to select the mine section to be studied were;

⁶ The ISS' assessment of the monitoring system mentioned error in both seismic event location and sensor orientation that did not affect moment tensor estimates, for details see Appendix III.A.

⁷ This is a standard procedure of the software undertaken from seismic database.

- Seismicity recorded between October 1997 and December 1999 and having $M_w > 0.0$. This mine section represents caving initiation, propagation and breakthrough to upper mine levels.
- The volume studied considered mainly the diorite rock type above the undercut level and close to cave propagation as the central part of the mine sector (Figure 8.12).

Several moment tensor estimates were used to investigate numerical model calibration (in Brzovic et al., 2008). In general terms, moment tensor estimates included re-calculation of shear and compressional wave arrivals. Some waveform data was rejected when either unclear arrival phases or large gaps were obtained. Over 8 stations were used to obtain stable fault solution (Belmonte 2007, written communication). Unfortunately, no information of the inversion quality was provided.

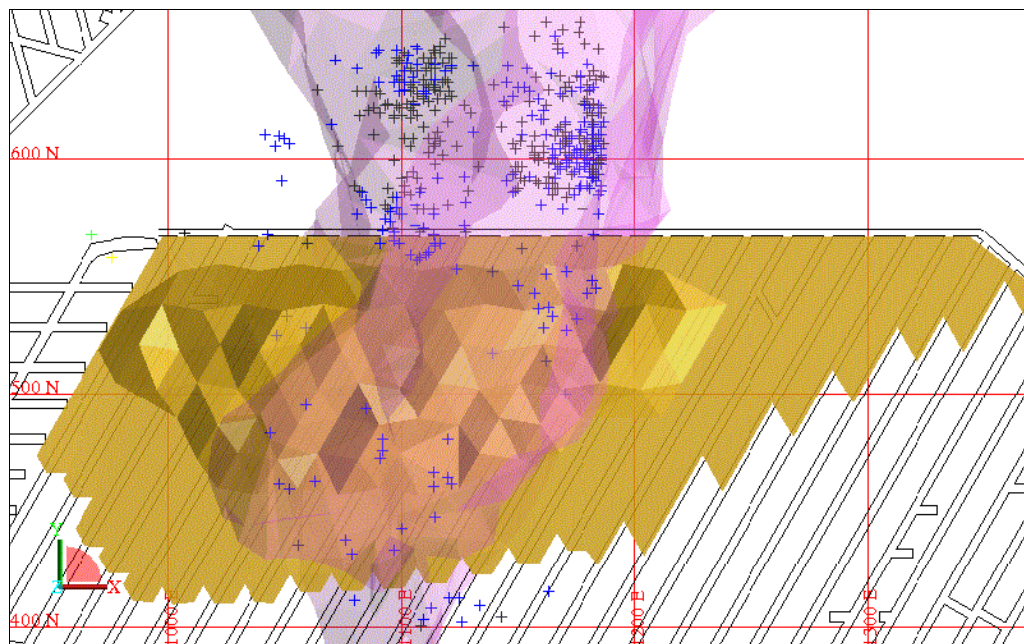


Figure 8.12.- Plan view of Esmeralda mine sector showing event with moment tensor estimates (+; events. Blue coloured events were recorded prior to breakthrough to the upper levels and black ones after that).

A small sample of these data, which represent a reduced window of time and space were compared with structural data from the same place. Focal plane solutions of

142 events recorded between February and April 1999 were analysed. These data were located within the rock volume defined by mine coordinates; 580-660 North, 1100-1200 East, and 2240-2300 mine level. This mine section also represents caving propagation just prior to breakthrough to the upper level as shown Figure 8.13.

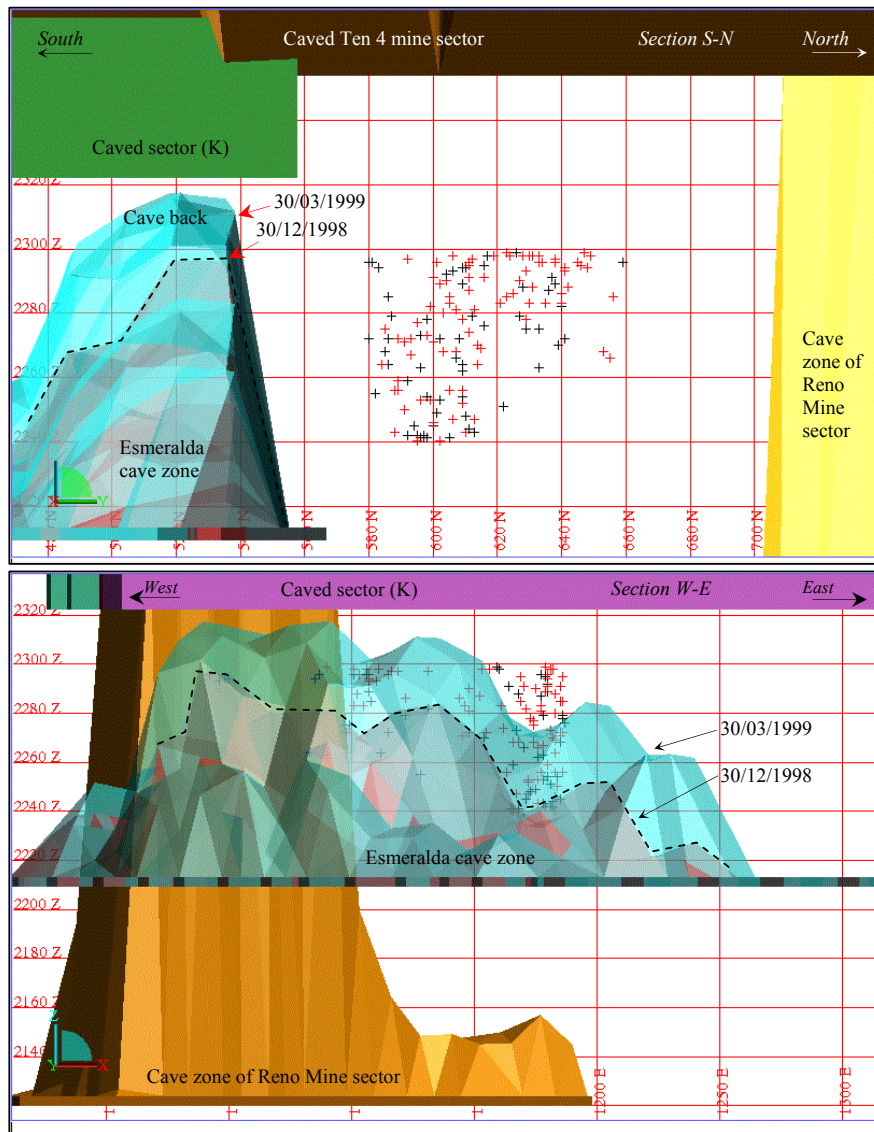


Figure 8.13.- Location of events with plane focal solution recorded from February to April 1999 indicating fault mechanisms; inverse-strike slip (red), normal-strike slip (black).

Based on the direction of the motion given by the slip vector in the plane, faults mechanisms are included in Figure 8.13 as well. When the motion of the upper side of the fault goes in an upward direction the faults can be classified as either inverse

or strike slip⁸. When the motion goes in a downward direction the faults can be classified as either normal or strike slip.

The 284 pairs of focal plane solutions obtained were compared against fault orientation data from the same area (Figure 8.14). Assuming that sampling bias against sub-horizontal discontinuities is not significant (as discussed in Section 3.2.4 and 7.2.1), this information can be used to assess whether every pair of plane solutions is likely to be a fault or another discontinuity such as weak veins. The stereographic projection shows that mostly steeply-dipping faults collected in mine drives are present in this structural domain (Figure 8.14a). If most of the seismic events occurred due to slip on pre-existing discontinuities as found in Chapter 4, therefore, for orientations where no faults have been identified, slipping is likely to correspond to weak veins as shown Figure 8.14b. In this figure, blue dots represent the cases where either one or both plane solutions are assigned as being a fault, with the black asterisks represent the case when the second plane solution is assessed as being a vein (with less probability to fail due its harder infill as discuses Section 4.3.3 shown in Figure 4.6). Finally, red dots represent the case where neither of both plane solutions can be assigned as being a fault, i.e., these solutions can be assigned as being weak veins. This interpretation is plausible since veins observed within the rock mass have been found comprising at least 3 semi-orthogonal directions.

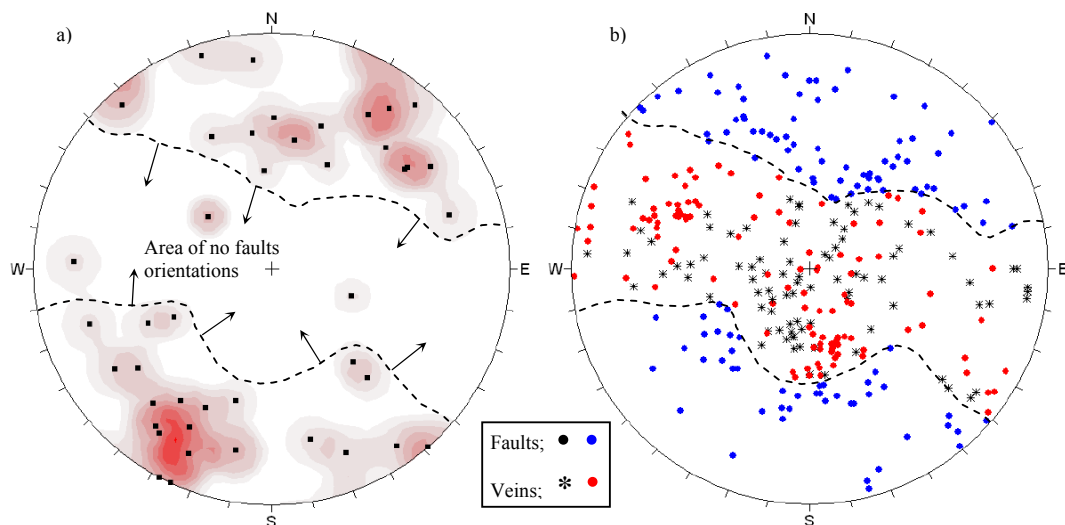


Figure 8.14.- Fault orientation from data collected by drive mapping (a) and fault plane solutions (b), both from diorite rock type at the Esmeralda mine sector.

⁸ If the bearing of the slip vector is below 30°, a major component of the fault motion will be by strike slip.

The results of this analysis infers that rock masses of primary copper ore offer multiple options to accommodate strain caused by stress redistribution. However, it seems that the more abundant the options (i.e., more fault and weak veins), the less likely potential energy will be stored in the rock mass, and therefore be available to be released as seismic events.

A similar analysis was again undertaken just for those seismic events with lower location residual ($R \leq 20$, that comprised 134 pair of focal plane solutions) and the results obtained were exactly the same (Brzovic, 2009).

From the same whole data base but incorporating the type of discontinuity, the tensile component of the failure for events having only reverse mechanism (107 events) and occurring prior to breakthrough were analyzed to compare with data from Reno mine sector (Figure 8.11), the results are presented in Figure 8.15. This figure illustrates that faults being mobilised at the Esmeralda mine sector exhibit a major tensile component during failure than events occurred at the Reno mine sector. These differences can be explained as result of different confining pressures, where the seismic events have occurred. Less confining pressure is expected at Esmeralda mine sector due to the proximity of the existing caves (see Figure 8.13), and high confining pressure is expected at Reno mine sector if the location of these events are below the production level and far from the existed caves as their re-location suggested by ISS are true (ISS, 2007).

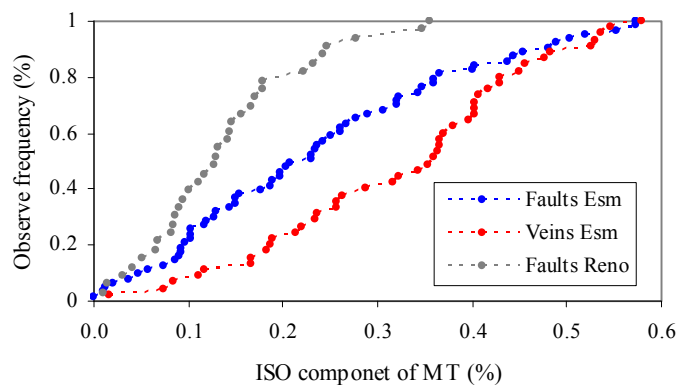


Figure 8.15.- Isotropic component of moment tensor from interpreted discontinuities at the Reno mine sector (from Figure 8.11) and at the Esmeralda mine sector.

The P, B and T axes of the events studied in Figure 8.13 are presented in Figure 8.16. This figure includes all source mechanisms, which can be compared to those presented in Figure 8.10d. It is clear that at the Esmeralda mine sector the principal force moments acting on the discontinuity planes scatter more in comparison with what is observed at the Reno mine sector.

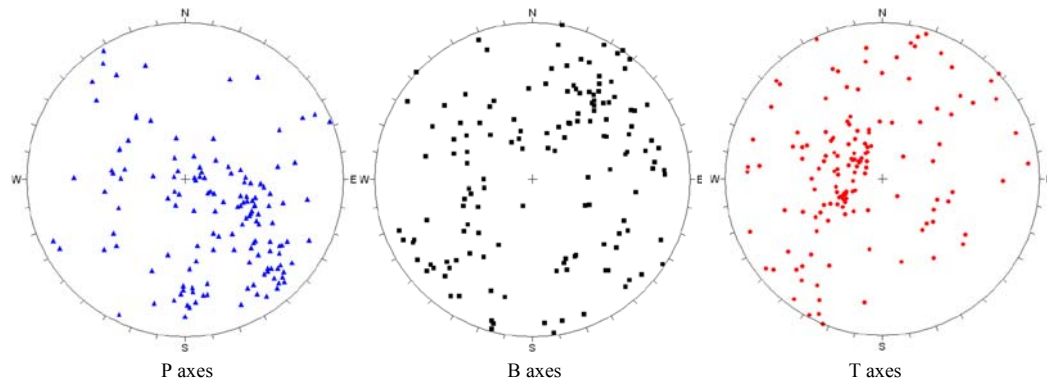


Figure 8.16.- Orientation of P, B and T axes for focal solutions interpreted in Figure 9.20b.

These observed differences between the studied seismicity at both mine sectors (Figure 8.10d and Figure 8.16) may be interpreted as following;

1. Seismicity from the mine section studied at the Esmeralda mine sector can be related to what occur at the seismogenic zone (Duplancic, 2002). In this zone major changes in the stress field are experienced due the proximity of a growing cave, leading to the occurrence of rock failure, which mainly occurs through pre-existing discontinuities. Mobilised discontinuities also affect the local stress field as largely discussed the literature (Pollard and Segal, 1987, Scholz, 2002). The changing stress condition can lead to failure occurring through different source mechanisms, therefore, scatter force moments acting on the discontinuity planes may occur.
2. Seismicity studied by ISS (2007) at the Reno mine sector may correspond to the second type of mine seismicity described by Gibowicz & Kijko (1994). Although this type of mine seismicity is related to major discontinuities triggered by mine operation, it cannot be directly related to the seismogenic zone in the sense as discussed in the previous paragraph. In other words, less stress changes are experienced where these seismic events occurred. The re-

location of seismic event by (ISS, 2007), values of the isotropic component of moment tensor, the scalar characteristics of moment tensor in relation to the in situ stresses are arguments that seem to confirm this interpretation.

The results of this analysis infers that rock masses of primary copper ore offer multiple options to accommodate strain caused by stress redistribution. In other word, the discontinuity network characteristic coupled with stress redistribution at the seismogenic zone may result in cave propagation through the mobilisation of faults and weak veins.

8.3.3 *Seismicity during Caving Propagation*

Three similar rock volumes within Esmeralda mine sector were studied through the present back analysis. These volumes represent three rock/unit types; *Cmet Hw1*, *Diorite*, and *Cmet Fw(1-2)* as shown Figure 8.17 (grey colour areas). Each volume encompasses the area shown in that figure, and the column height goes from 2210m(z) to 2250m(z). Figure 8.17 also shows the area delimited by the 30% of the column high extraction by year (extraction front), including when breakthrough occurred (April 1999). Most of the areas of *Cmet Hw* and *Diorite* units were extracted before Dec-1999, and *Cmet Fw* before Dec-2001 (Rojas et al., 2000, Dunlop and Gaete, 2001)

The same Figure 8.17 includes the undercutting area affecting these studied sectors (undercutting front). Again, most of the areas of the column base of *Cmet Hw* and *Diorite* units were completely cut before Dec-1998, and *Cmet Fw* before Dec-1999.

The whole seismicity recorded within the three studied rock volumes between 1996 and 2003 is presented in Figure 8.18. Three important increments of seismic intensity are shown this figure; the first one was during caving initiation, the second one correlated when the caveback reached (breakthrough) the broken rock located in the Ten-4 upper level (see also Figure 8.13), and the last one was during 2001. During breakthrough, undercutting had taken place in most of the area including the three studied sectors. The remaining induced seismicity occurred after breakthrough, which maybe interpreted to correlate to both the advancing cave and extraction front. The last increase of seismic activity which occurred during 2001 and beginning of

2002 is not discussed here. However, this last jump of seismicity maybe related to the continue movement of extraction front close to the studied sectors as shown Figure 8.17.

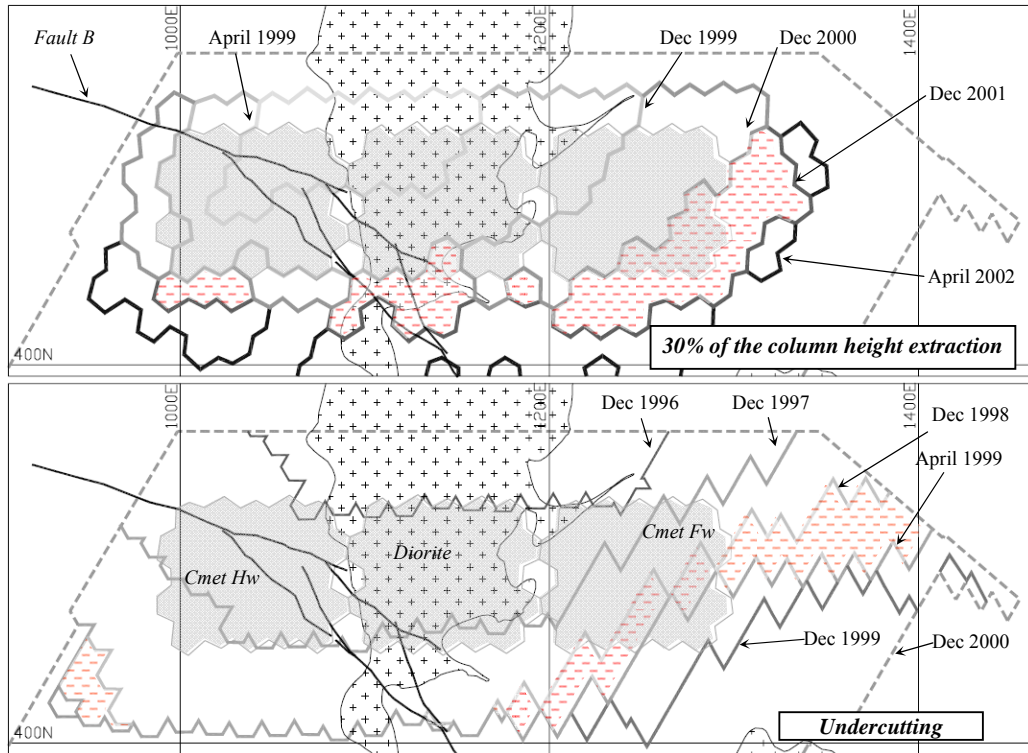


Figure 8.17.- Studied areas at the Esmeralda mine sector showing the extraction front (30% of primary ore column height) and the undercutting by years.

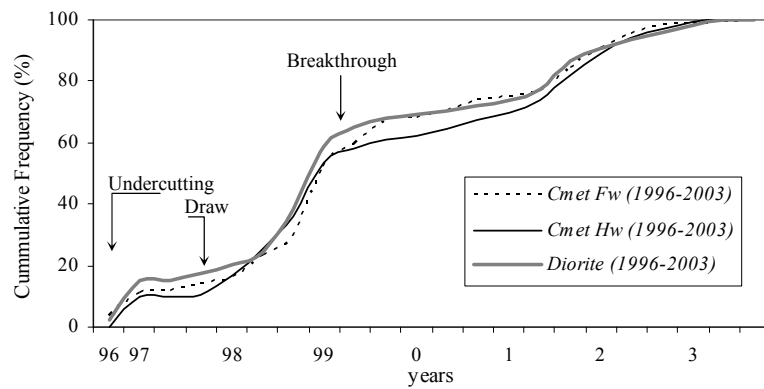


Figure 8.18.- Proportion of the cumulative seismicity recorded in Esmeralda mine sector per each location.

The recorded seismicity within each sector of *Cmet* rock type, and the Gutenberg - Richter curve for each studied rock volume are illustrated in Figure 8.19. The

Gutenberg –Richter curves show that the system sensitivity ($M_{w_{min}}$) is the same in each of the studied sector within Esmeralda mine sector. This plot also shows that *Cmet* rock masses of the *Fw* sector have recorded considerably fewer seismic events and lower local magnitude than other unit types. It seems to be that *Cmet* rock masses of the *Fw* sector tend to fail more in an aseismic way compared to the other unit types. This important feature of seismicity between the two *Cmet* sectors is discussed latter in Sections 8.6.1 and 8.7.

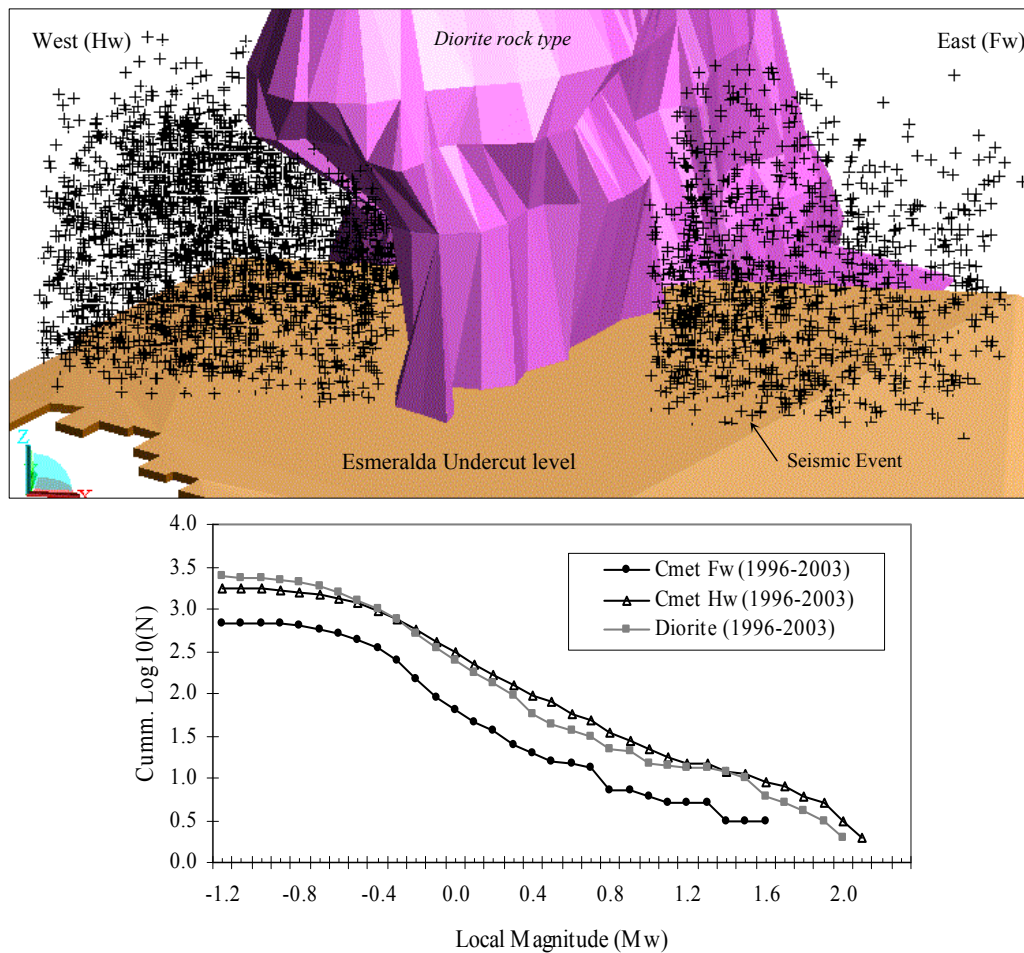


Figure 8.19.- Isometric view of Esmeralda mine sector showing the recorded seismicity within *Cmet* rock type (above). Gutenberg-Richter curve for each studied unit type (below).

In addition, the extraction rates applied in these three studied volumes, considering only up to 30% of the extraction rate, in terms of cumulative tonnes extracted per month are shown in Figure 8.20. As it could be expected, due to the draw strategies motioned in section 8.2.3, the three sectors were practically exploited at the same extraction rate. The extraction rate can be considered to influence the rate in which

the rock mass was load, because draw allow space for the broken rock, and caving can propagate, however, it is not guaranteed that caving will propagate after drawing (e.g. air-gaps). Therefore, extraction rate cannot be considered a major factor explaining such differences in the recorded seismicity between at least *Cmet* rock types from *Hw* and *Fw* sector.

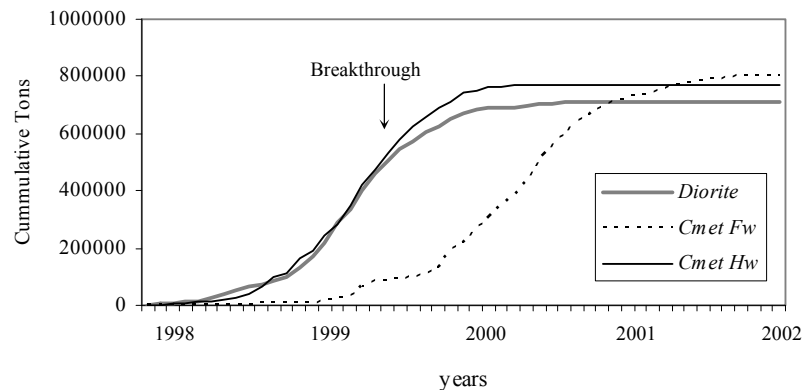


Figure 8.20.- Cumulative production (tonnes) for different mine sector considering up to 30% of primary ore column high.

Since the rock mass encompassed in each of the studied volume was completely caved (failed), it could be expected, that the whole seismicity recorded was the result of two main factors; the rock mass strength (rock structure features) and the stated of stress (stress path) during caving propagation (Mendecki, 1997), which is discussed in the following section. This interpretation is plausible since the extraction rate applied in each sector was similar (Figure 8.20), i.e., the average mining activities were undertaken in a similar fashion.

8.4 Mine Scale Numerical Model

Assessing the rock mass strength through back analysis studies of some observed rock mass damage due to mining activities require to know the stresses affecting the rock mass prior and during failure, and this requirement can only be possible to achieve by performing a mine scale numerical model.

A common research interest was established between the author through the WASM and Beck & Arndt Engineering Pty. Ltd. (BAE) to simulate the El Teniente mine history focusing in to the Esmeralda cave experience using ABAQUS numerical

model software. The agreement contemplated the numerical modelling by BAE with WASM providing the model geometry and seismic data for numerical model calibration.

The main objective of the numerical model was to assess the stress state around excavation such as; the Esmeralda undercut level both ahead of the front cave and in the seismogenic zone during caving propagation, to be back analyzed with the observed rock damage and the recorded induced seismicity.

8.5 Model Characteristics

The entire mine excavation history was simulated, from its initial stage prior to 1917 until the recent period of 2002. Luckily, records of mine geometries and production record have been kept at the mine site. This included several surface surveys, which have been used to build the model geometry. The main characteristics of the modelling process are detailed, as follows.

8.5.1 Model Package

The modelling package used here was ABAQUS Explicit with prolific BEA geotechnical enhancements (Beck, 2007). ABAQUS is a specialist-oriented, general purpose, 3-D, non linear, Finite Element (FE), continuum and discontinuum analysis product. It is a product designed specially for advanced problems where there is high plasticity and large amount of deformation (Beck et al., 2006).

ABAQUS uses quadratic tetrahedral elements as model discretisation. It has been analysed that for the same level of precision, the high order element used in ABAQUS require 30% to 40% less elements than in distinct element package. The reason quadratic elements provide better precision is that derived quantities, such as strain vary throughout the element, whereas for linear elements these values are constant throughout the element.

8.5.2 Material Assumptions

Mohr-Coulomb strain softening, dilatant material models for material behaviour were used in the model. The inelastic constitutive model for continuum material

assumes that each material has peak and residual strength and elastic properties. In the model, yield results in dilation, and once the peak strength is exceeded, residual properties are introduced. Cohesion, friction angle, stiffness and compressive strength are all reduced as a result of yield, then a dilation angle for yielded materials is calibrated using BEA's data base and expertise (Beck et al., 2006). Three major rock types were used in the model, andesite, diorite and breccia Braden (pipe), their peak rock mass properties used here are presented in Table 1.2 (in Section 1.6.3).

8.5.3 *In situ Stress Field*

In situ stress field incorporated at the model is described in Section 1.6.2, which has been estimated using the WASM acoustic emission technique (Villaescusa and Machuca, 2007)⁹. These measurements have been reconciled with the strain, the structures and the stresses within the mine region (Windsor et al., 2006a). The in situ stress field used in the model also agreed principal stress orientation obtained from cluster analysis of P, T and B axes of a set of related seismic events located away from cave influence as discussed Section 8.3.1.

During the initial modelling step, in situ stress field, main rock types, and initial surface topology (without mining excavations) were all setup to reach geological equilibrium. A hypothetical erosion of the Andes region surface as far as 20km wide from mine site was simulated in this process (Figure 8.21) to reach in situ stress field at the mine site used in the model.

8.5.4 *Model Geometry, Size and Model Steps*

The model geometry is based on electronic mesh and wireframes that were converted to FE meshes, containing higher-order tetrahedral elements. The electronic CAD meshes containing pre- and post-mining activity regional and local surfaces, subsidence or fracture cone geometries, secondary ore surfaces, and some 3D rock type geometries were collected from the mine site. Specific 3D rock geometries (diorite), and cave geometries from several mine sectors including Reno and Esmeralda were all specially built using Surpac 3D software package. Several

⁹ This includes stress measurement in more than 10 underground sites.

modelled mine sectors, one fracture cone geometry (year 1990), and the initial surface topology used in the model are shown in Figure 8.22.

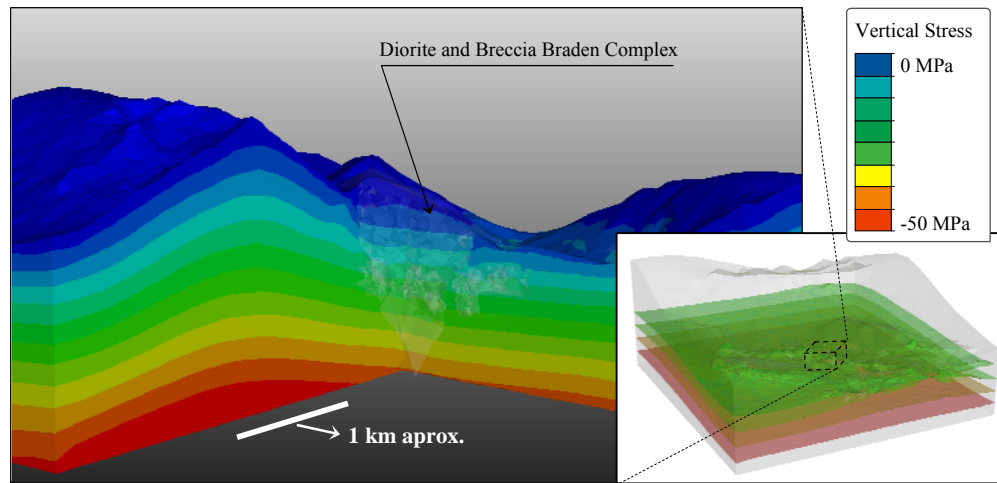


Figure 8.21.- Initial geological equilibrium with the stress field and initial surface topology after hypothetical ranges erosion.

The model boundary condition for stress-strain analysis considered an original volume of 75.6km^3 (Figure 8.22a), but the initial geological equilibrium used a bigger volume. The original volume contains more than 200,000 model elements; however a refined volume for model calibration considered more than 130,000 model elements (Pink Square in Figure 8.22b). The Esmeralda and Reno mine sector are contained within this refined volume. In addition, greater resolution was considered within a second refined volume used for moment tensor comparison as the calibration process, which is showed as red parallelepiped within the pink square in Figure 8.22b. In the second refined volume, mesh points considered to be 12.5m apart.

The total model sequence included 82 mining steps. Some particular features of model geometries built (model steps), which includes descriptions, geometries, and dates are presented in Table 8.1 and in Figure 8.23.

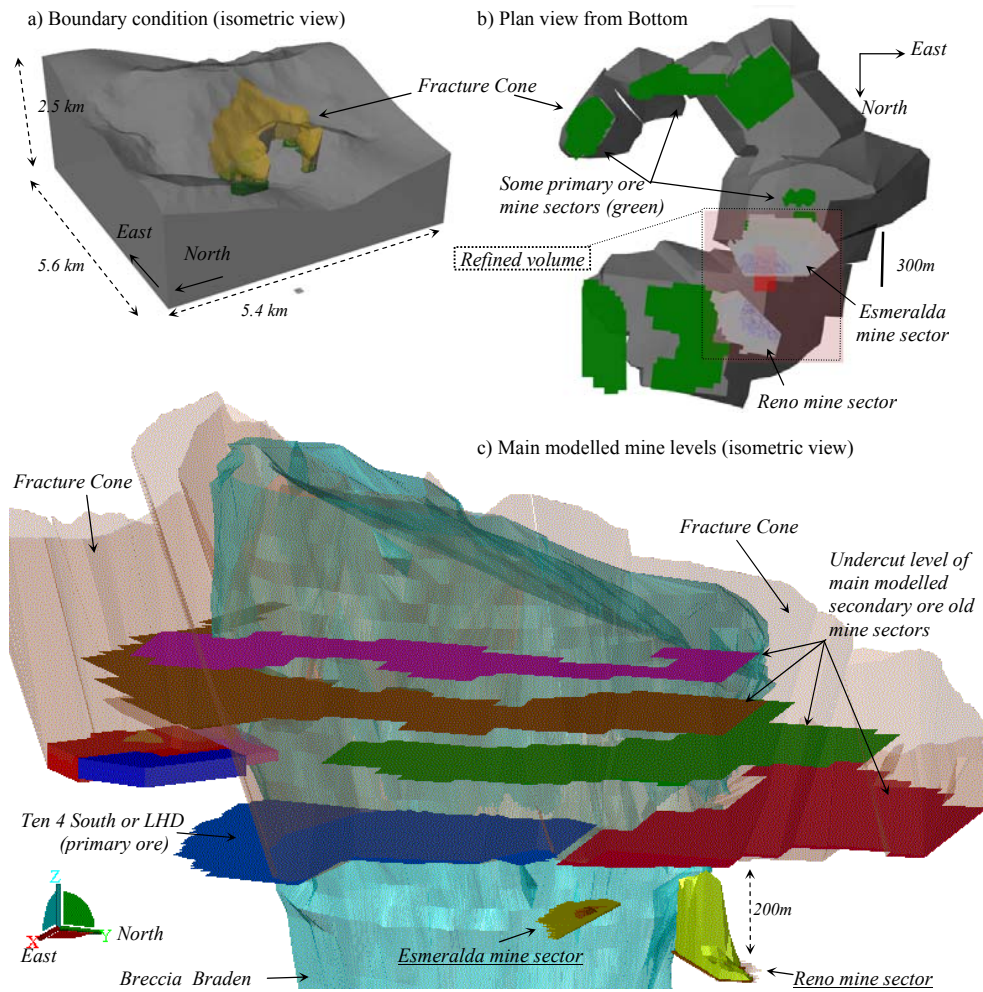


Figure 8.22.- Model size, boundary condition, and modelled mine levels.

Table 8.1. Main mine model steps and their descriptions.

Steps	Dates	Mine sector / Comment
1-6		Geological equilibrium
7-34	1917-1970	Secondary ore exploitation, general mine sequence from up to down, and north to south
40	1990	Reno mine sector started using panel caving mining method
47	31/12/1996	2 months of undercutting at Esmeralda mine sector
50	31/12/1997	2 months of drawing generate the first modelled cave volume at Esmeralda mine sector
56	30/08/1998	Reno mine sector breakthrough to upper mine level
59	31/12/1998	Caving propagation at Esmeralda and Reno mine sectors
63	30/03/1999	Caving propagation prior breakthrough to upper mine level at Esmeralda mine sector
67	30/05/1999	Caving propagation just after breakthrough to upper mine level at Esmeralda mine sector
71	31/12/1999	Caving propagation at Esmeralda and Reno mine sectors
75	31/12/2000	Caving propagation at Esmeralda and Reno mine sectors
79	31/12/2001	Caving propagation at Esmeralda and Reno mine sectors
82	31/12/2002	Caving propagation at Esmeralda and Reno mine sectors

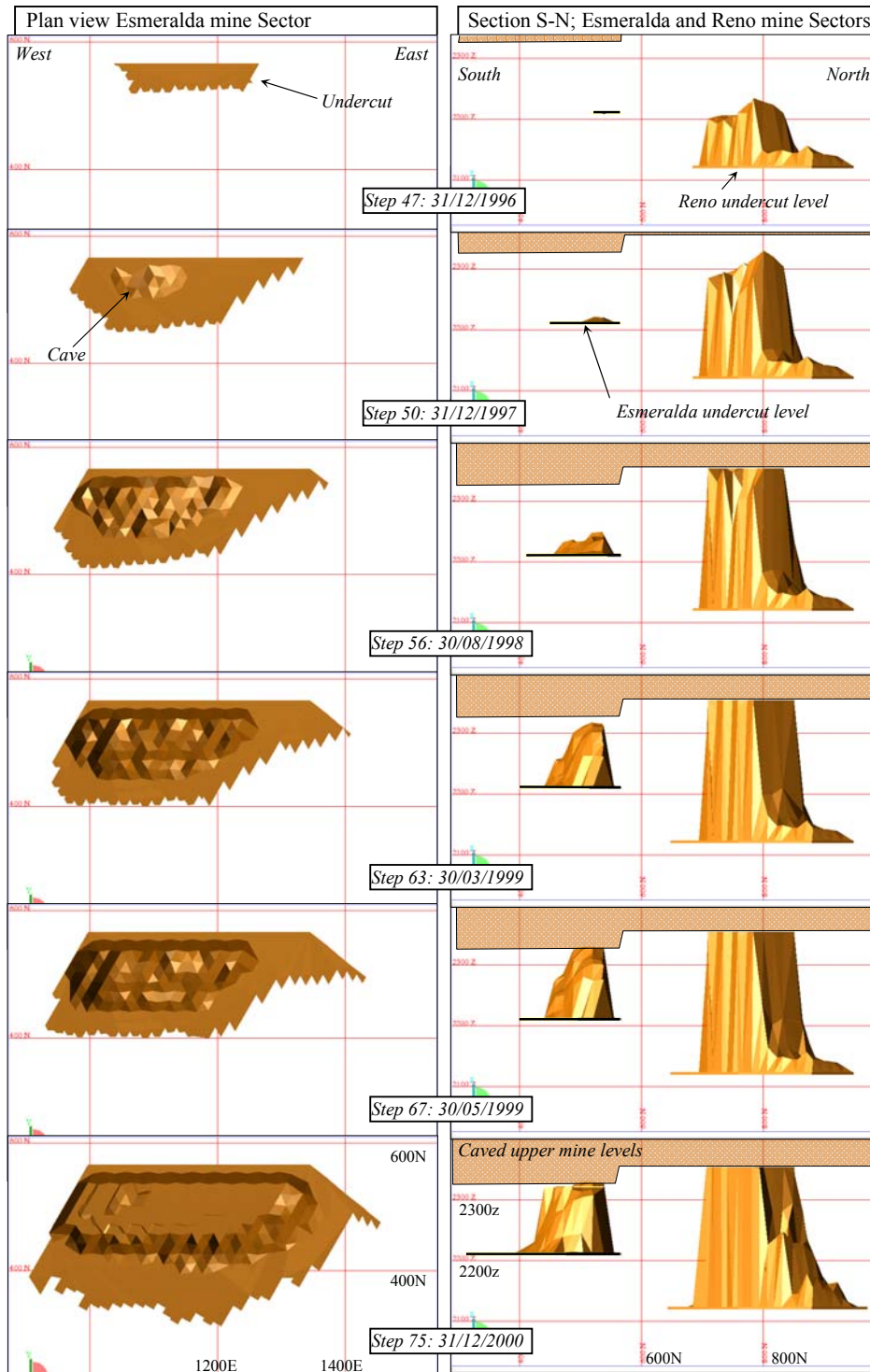


Figure 8.23.- Detailed geometries of some mine model step in the numerical model.

The undercut volume for Esmeralda and Reno mine sectors were built based on mine survey data. Caves geometries anywhere at the mine site may be considered an

unknown parameter since these have not been properly measured; however the empirical relationship discussed in Section 8.3.1, which was validated at least in the Esmeralda mine sector, was used to build the cave geometries. The model does not include mine drives, infrastructure opening, and excavations at any level, only caved zones and the undercut volumes were included.

8.5.5 Model Calibration

The aim of any model calibration is to match modelled and observed behaviour. Due to the limited budget for modeling¹⁰, in the present case, model calibration was only based on a methodology that qualitatively correlates the dissipated plastic energy (Joule/m³) and an observed seismic event probability (described in detail in Beck et al., 2006).

The dissipated plastic energy of DPE is a concept developed by Beck et al. (2006), it is defined as the energy in joules dissipated as the results of yield in a particular mining step. In other words it is the work (W) done by the rock mass due to a rock mass failure, which is calculated from the seismic radiated energy E , as;

$$DPE = W = E/\eta \quad [J] \quad (8.12)$$

where η is the *seismic efficiency*¹¹. This concept means that high cluster of seismicity should be appearing where high values of DPE are observed in a particular model step.

An example of the model calibration is shown in Figure 8.24 and Figure 8.25. In Figure 8.24, three model steps that represented cave propagation during January and February 1999 are plotted against seismicity recorded during the same period of time at the Esmeralda sector. An encouraging correlation is shown in this figure, which is particularly good around the cave where low DPE values correlate with scarce seismic events. That correlation can be considered good despite of one important fact about the model calibration process; there is not a precise seismic event location involved in the correlation DPE-event probability. This means that the model is able to reproduce cluster of seismicity rather than to reproduce a single event location.

¹⁰ The low budget constrained the model calibration process, therefore calibration was undertaken in qualitative terms only.

¹¹ More details in Appendix III.A

Another example to evaluate the model calibration is presented from Figure 8.26 to Figure 8.28. These figures illustrate the modeled plastic strain where rock mass was yielding above the undercut level of Esmeralda mine (2240z). The plastic strain may be or may be not correlated with seismicity, because either the aseismic rock mass behaviour or the lack of pressure confinement during failure. But it is clear that seismicity should be correlated to where plastic strain occurred. In other words, where seismicity was recorded, the modeled plastic strain should be high. In Figure 8.28 there are two areas with a particular of good correlation, pillar north and west (highlighted as red areas), which represent two wall cave of Esmeralda cave. In these two highlighted sectors, the high and low recorded seismicity agreed with high and low modeled plastic strain respectively.

Additionally, in terms of the state of stress in the rock mass around excavation, the results of this particular model agrees with the state of the stress (similar magnitude of the in situ stress) of the current numerical model used at the mine site for mining planning and rock mechanics purposes (Pardo, 2007). All these antecedents suggest that the model calibration may be considered good enough for the purpose of this back analysis.

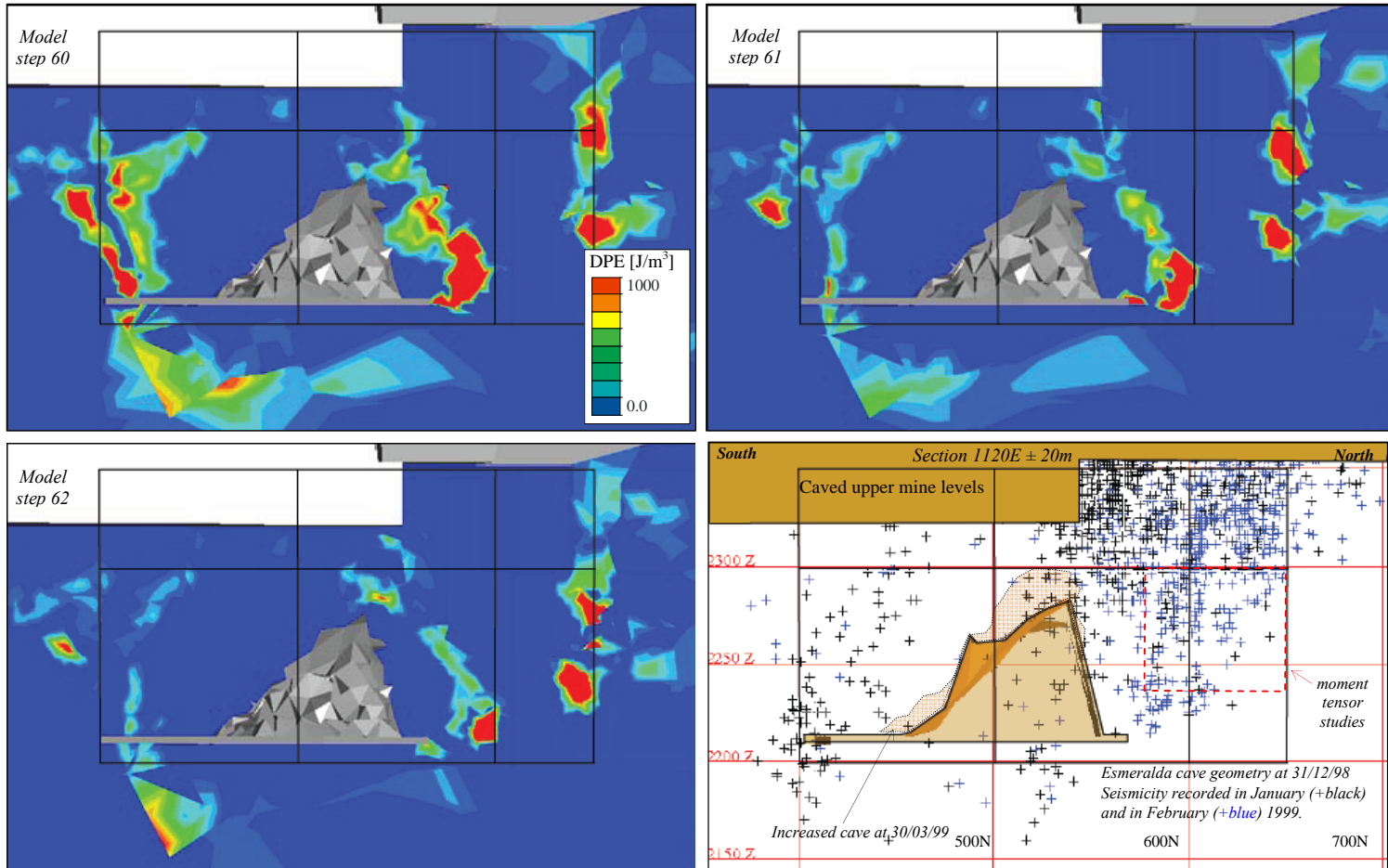


Figure 8.24.- DPE plots and seismicity at the Esmeralda mine sector (Section 1120E).

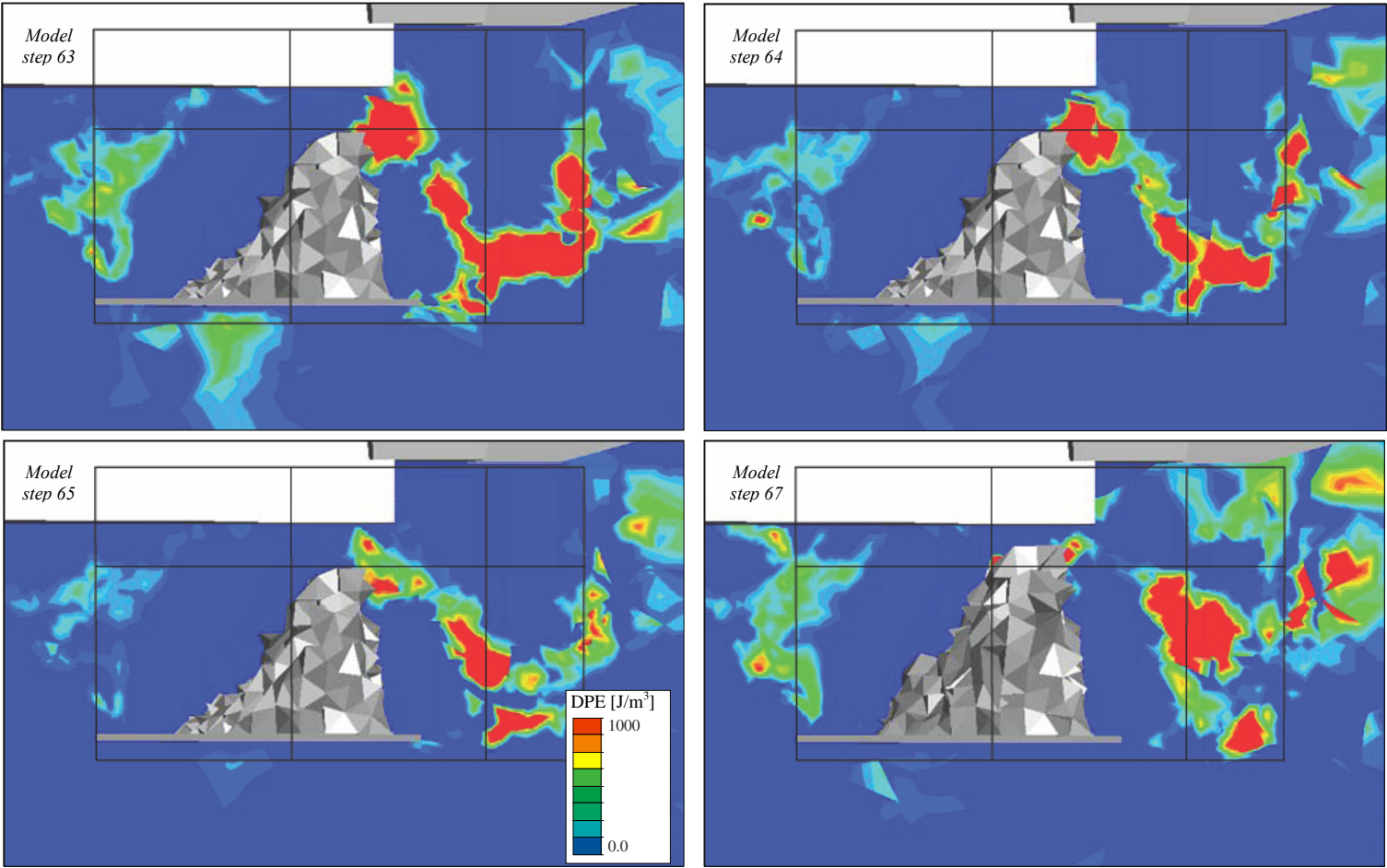


Figure 8.25.- DPE plots at the Esmeralda mine sector during breakthrough to upper mine levels (Section 1120E).

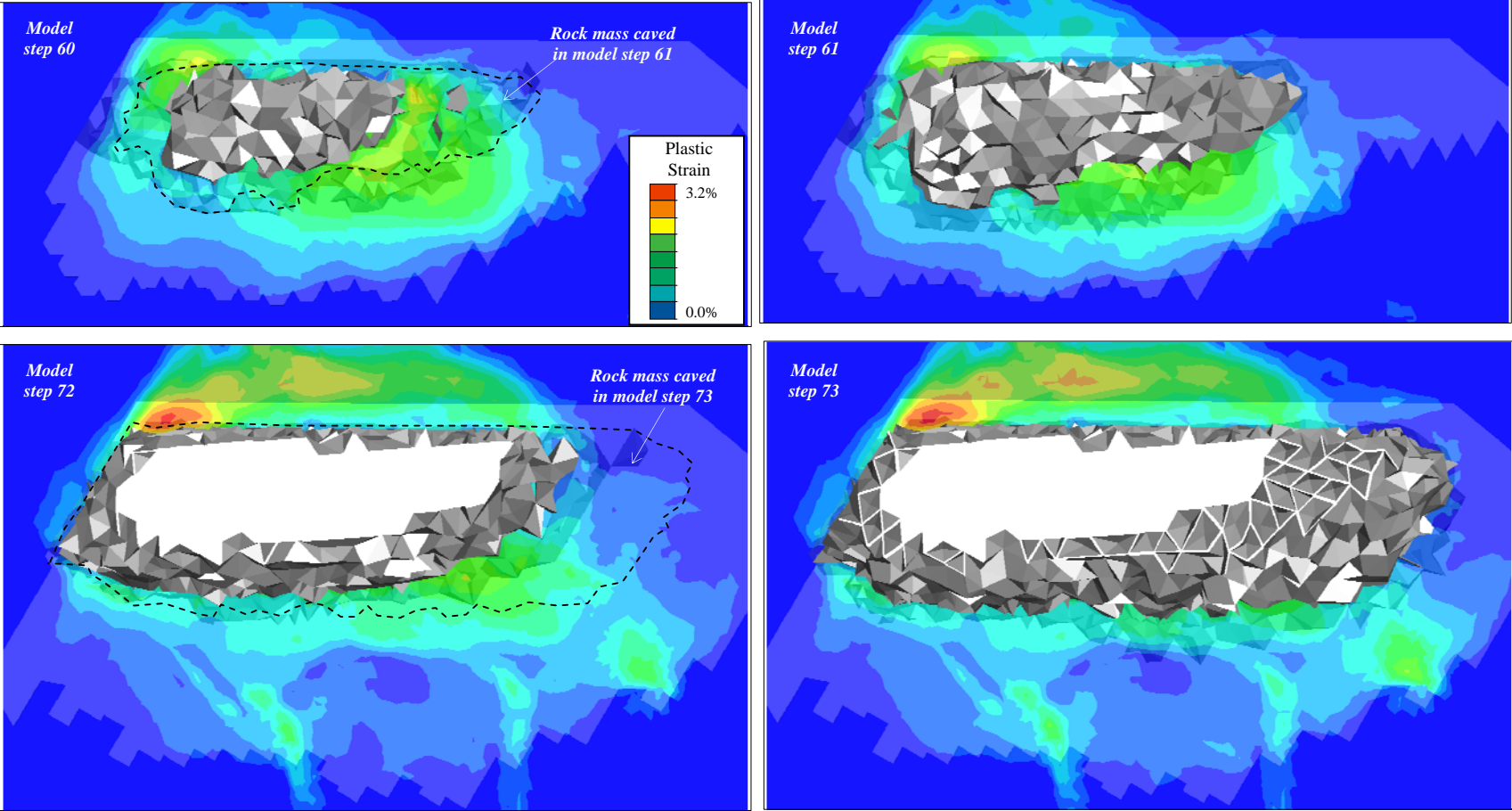


Figure 8.26.- Different plan views (2240z) showing cumulative plastic strain reached for the rock mass at the model step before it is caved.

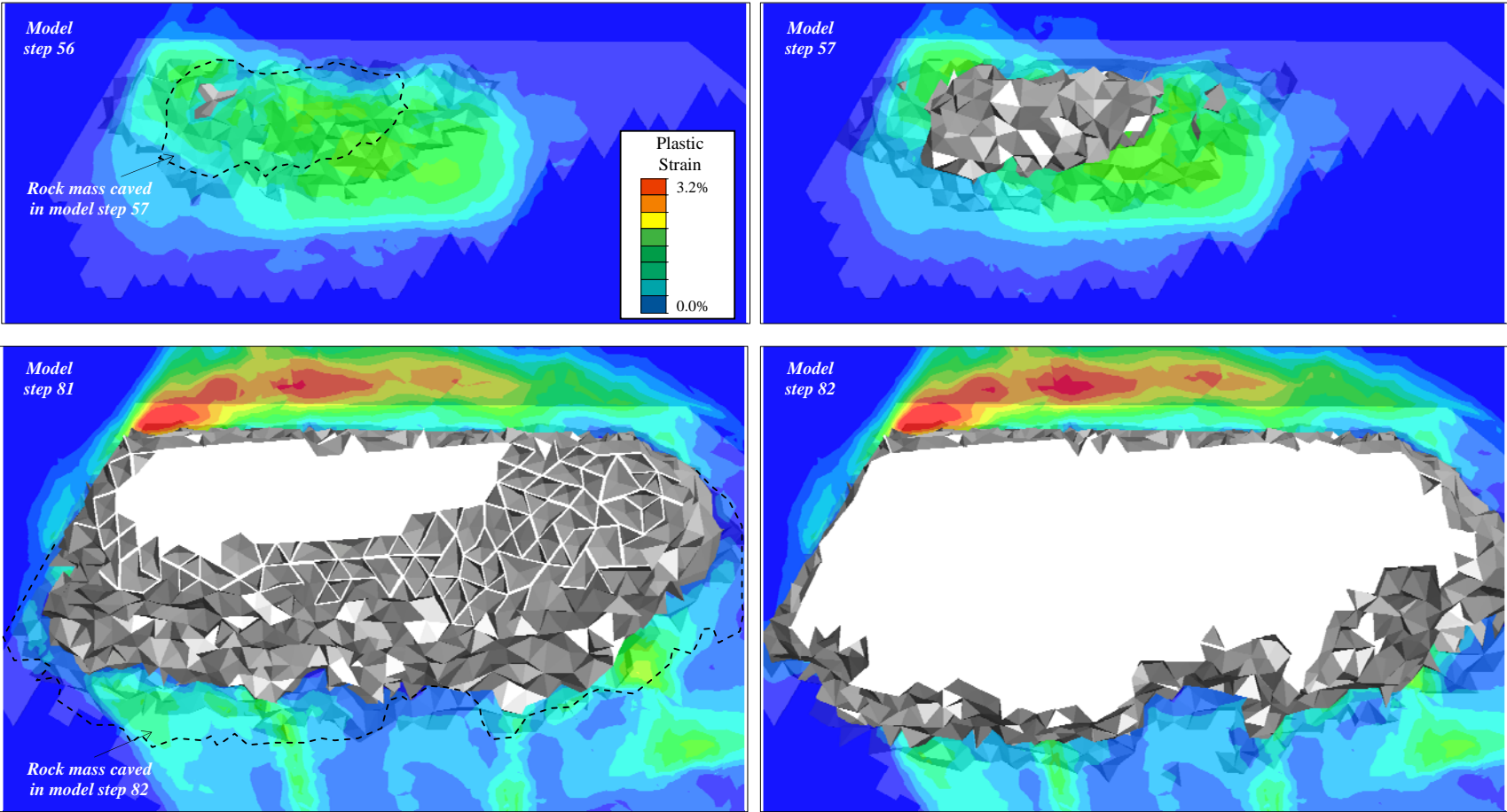


Figure 8.27.- Additional plan views (2240z) showing cumulative plastic strain reached for the rock mass at the model step before it is caved.

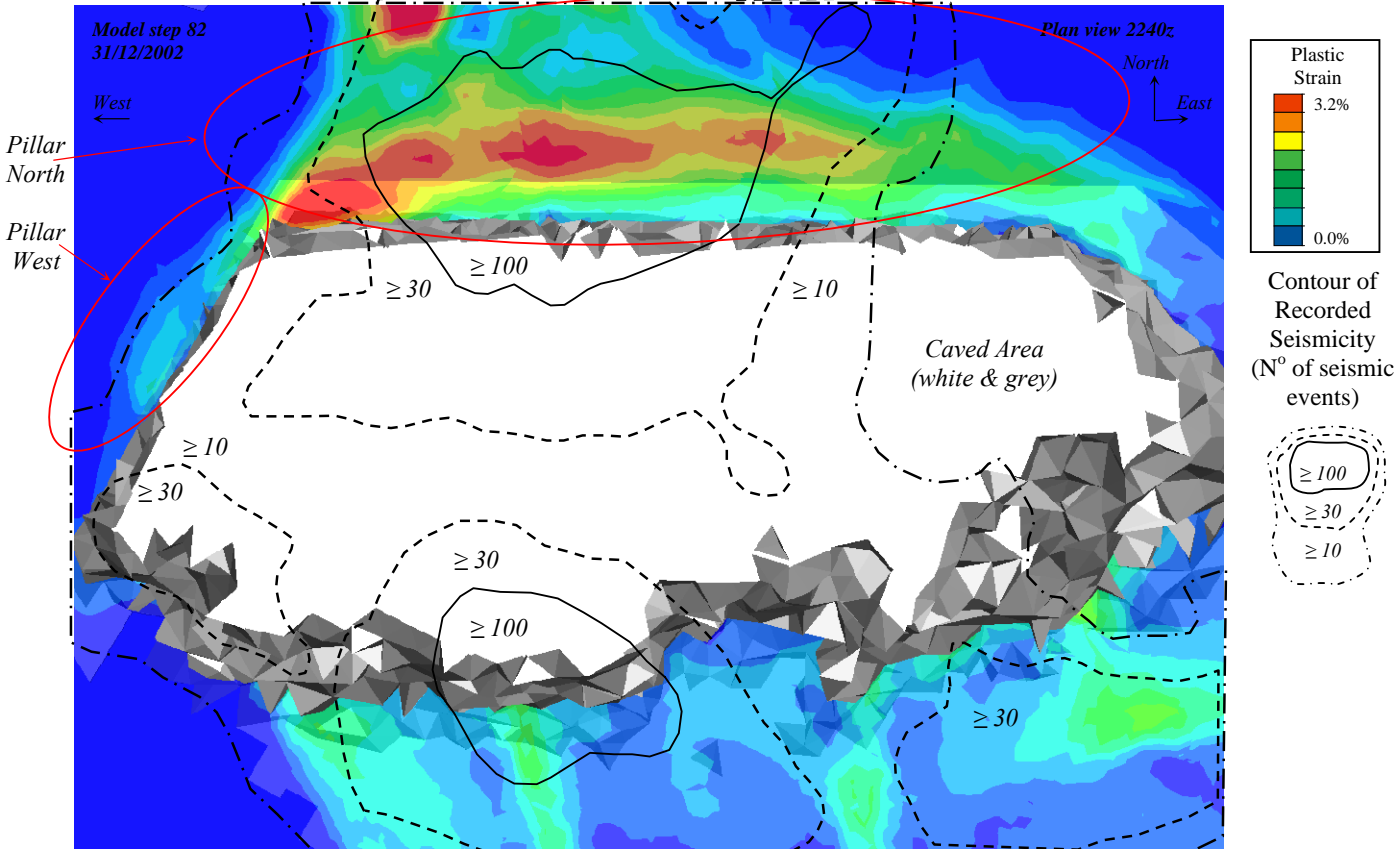


Figure 8.28.- Cumulative plastic strain at the plan view 2240z and the recorded seismicity between 1996 and 2002.

8.6 Model Results

The model results were conducted to obtain the stress path in different location around the Esmeralda cave during caving propagation to be correlated with rock mass response to mining activities. The results are detailed in the following sections.

8.6.1 Modelled Stress Path and Seismicity during Caving Propagation

Several points in the numerical model, as shown in Figure 8.29, were used to assess the state of the stress in the rock mass around excavation during caving propagation. These points represent different location and heights within the three volumes studied in Section 8.3.3 (see Figure 8.17). The model results are presented in Figure 8.30.

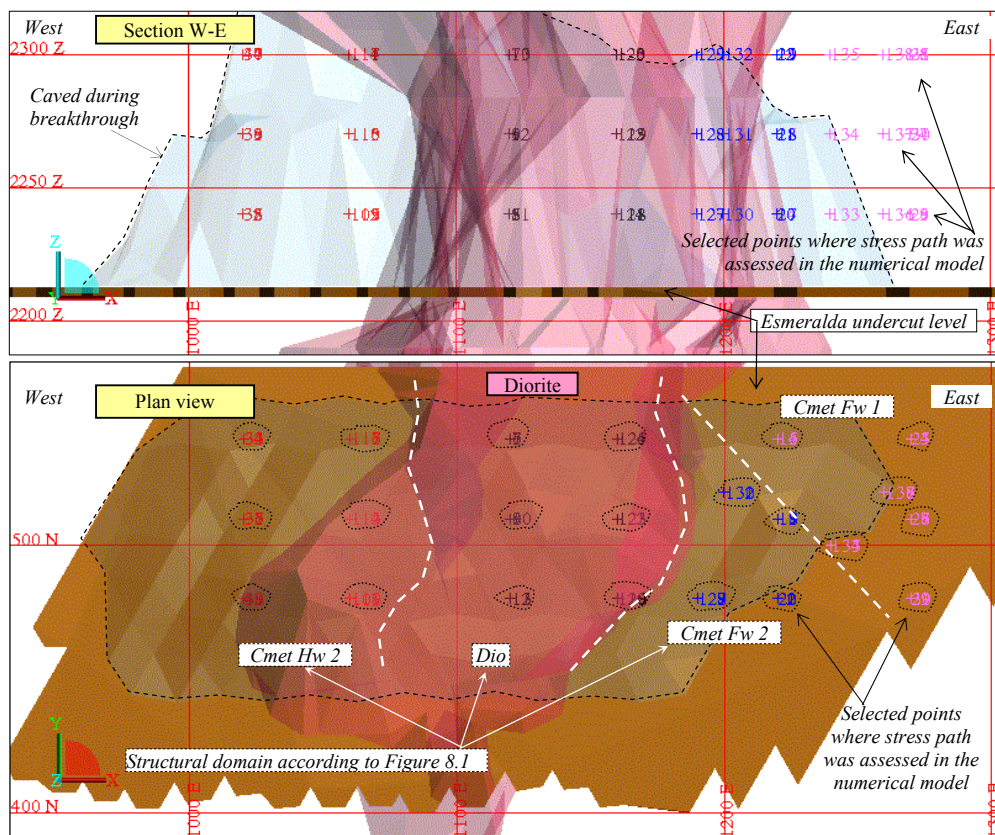


Figure 8.29.- Location of selected points where the stress path were analysed.

The initial state of stress at each structural domain within the three volume studied is shown as circles in Figure 8.30. It shows that higher initial stress level predominates at the *Fw* sector, which agrees with the major overburden observed in this place (see also Figure 1.3). The stress level before the rock mass reaches the peak strength (as the *Mohr-Coulomb* failure criterion in these graphs) moves (blue arrows in this figure) toward the confinement reduction in the *Hw* sector (diorite and *Cmet Hw2*), whereas at the *Fw* sector (*Cmet Fw1-2*) it moves not only toward the confinement reduction, but also toward high confining pressure levels. Increasing σ_1 at constant high σ_3 level may result in high stress release, i.e., a large seismic event may occurs.

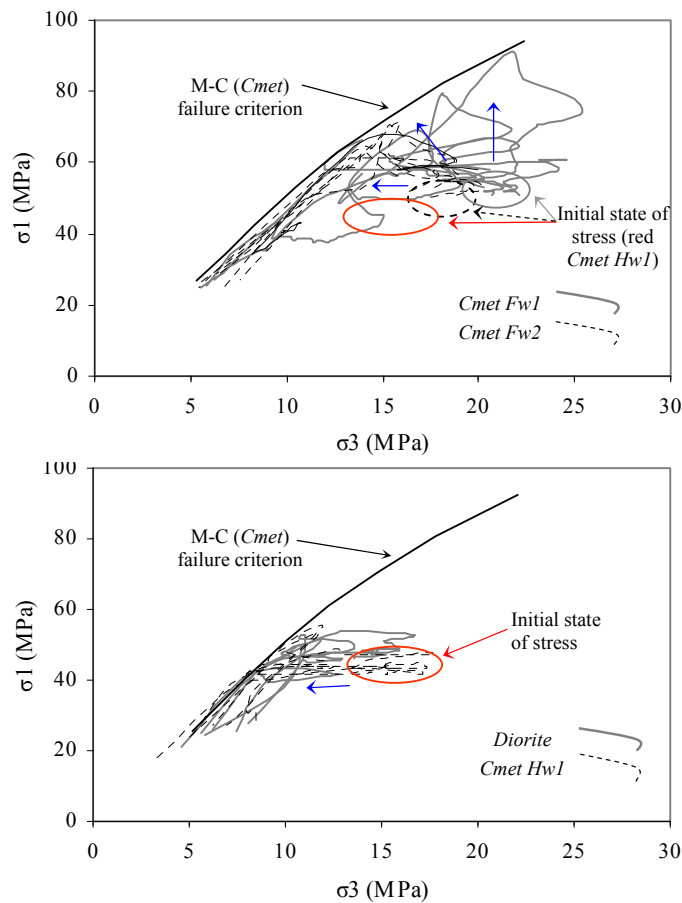


Figure 8.30.- Modelled Stress paths (lines and arrows) at different structural domains as the result of cave geometries during caving propagation at the Esmeralda mine sector. Small circles indicate initial state of stresses (red circle from *Diorite* and *Cmet Hw1* in both graphs).

Data in Figure 8.30 indicate that severe seismicity should be expected at the *Fw* sector of the Esmeralda mine compared to the *Hw* sector, but it did not happen as shown Figure 8.19. This is further discussed in the following section 8.7.

8.6.2 Modelled Stress Path and Rock Damage ahead of the Front Cave

Five points in the numerical model, as shown in Figure 7.12 were used to assess the state of the stress at the Esmeralda undercut level ahead of the front cave during caving propagation. These points represent the five structural domains of the mine sector studied (in Figure 8.1). The model results with the modeled stress path of these points are presented in Figure 8.31 as both, the maximum shear stress ($\tau_{max}=[\sigma_1+\sigma_3]/2$) and the mayor principal stress (σ_1) against the distance to the cave front. This figure also includes when the low and high over brake was observed in mine drives and the time in months this damage level held in place.

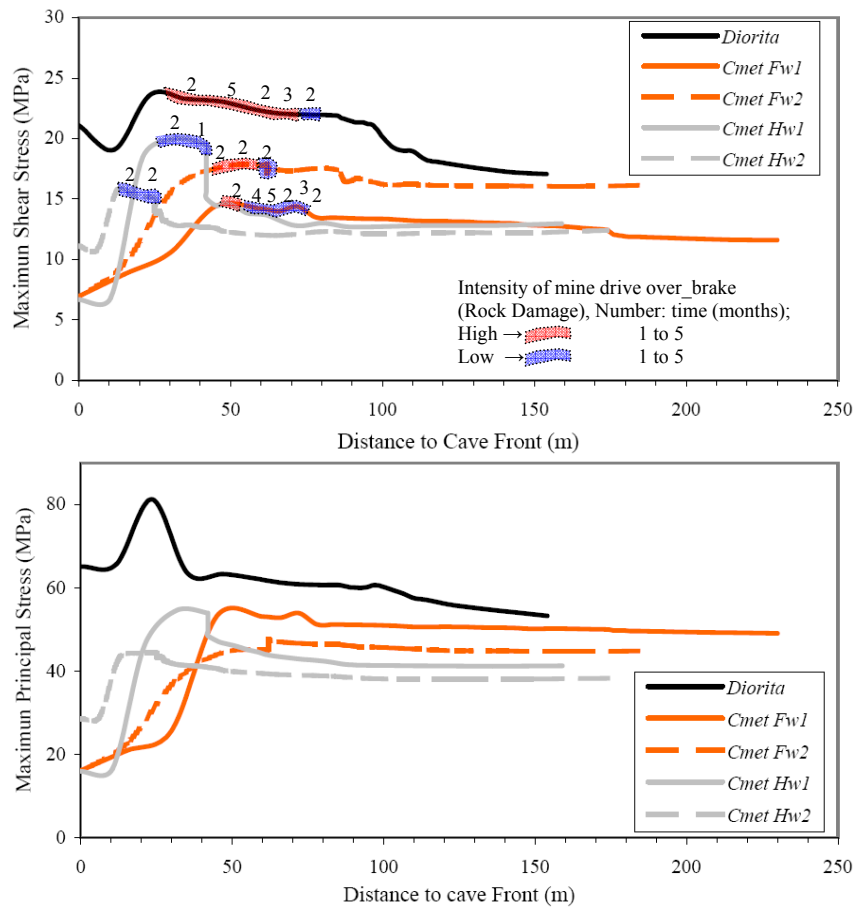


Figure 8.31.- Rock damage observed in mine drives at the undercut level, and shear stress path from the numerical model.

The interpretation of the model result presented in Figure 8.31 is discussed in the following section.

8.7 Discussion

The present chapter attempts to demonstrate the relationship between rock mass strength, rock damage and seismicity at the El Teniente mine, which was undertaken through the back analysis studies of the Esmeralda caving experience occurred between 1997 and 2003.

The back analysis studies relating to the rock mass characterization indicates that the rock structure at the Esmeralda mine sector differ between sectors and rock types. There is one major fault system (fault B), which is only present in the *Cmet Hw1* unit type. Considering to the large scale observations of structural data in *Cmet* rock type (drive mapping from Table 7.1), there is more appreciable differences between nearby structural domains (*Hw1- Hw2* or *Fw1- Fw2*) than between major *Hw* or *Fw* sectors. For example, there is more faulting (and large scale weak veins as well) in *Cmet Fw1* than in *Cmet Fw2*, but it looks the same between *Cmet Hw1* and *Cmet Fw1* (Table 7.1). Now, considering to the small scale observation of structural data in *Cmet* rock type (oriented drill core logging from Table 7.3), the differences are substantially clearer between rock/unit types when the infill strength of discontinuities is taken into account (see also Figure 7.7 and Figure 7.8. It is important to note that existing rock mass classification systems fail to discriminate differences between sectors/units as discussed Charter 6.

It has been shown that the three sectors studied were mined out in a very similar rate (Figure 8.20), consequently, extraction rate's factor can be disregarded as an important contribution to explain the differences on the recorded seismicity between them (Figure 8.19). However, it is also necessary to mention that the relationships between drawing and cave propagation (caveback grows up 3m for 1m of draw) has been well validated only in rock masses of *Cmet Hw1* structural domain [discussed in section 7.3.1 and at the mine site (Parraguez and Campos, 2007)], and major fault B could have been played a relevant role in that process. This rule is considered relevant to cave propagation in upward direction, however no rules have been established with regard to the advancing front direction. In addition, although drawing is necessary for caving propagation (i.e., allowing space for the broken rock), it is not guaranteed that caving will propagate after drawing (e.g. air-gaps), other factors regarding to the rock structure and state of stress need to be considered

in this phenomenon. It is very clear that more research is needed to understand this important mine parameter used widely in mining planning.

The recorded seismicity was completely different between the three studied unit types as shown Figure 8.19, particularly between *Cmet* rock masses from *Hw* and *Fw* sectors. The same observed differences (seismic intensity and magnitude) were also observed again after several years in the same mine sector (period 2002-2007), but under different cave geometries (Parraguez and Zepeda, 2007), which confirm that the features of the rock structure are a relevant factor in the seismicity at the El Teniente mine.

The cave geometry is one of the key factors that control induced stress. The relationships between drawing and cave propagation have been used to build the cave geometry in the model. Assuming that a rock mass with more abundant weak discontinuities has less strength, the cave should have propagated faster in *Cmet* rock masses of *Fw* sector. If this is the case, the cave geometry could have been different to what was used in model for the *Fw* sector. Although, this has not been properly evaluated (run a different cave geometry in the model), it seems to be less relevant in the model result because the general geometry and shape of the cave will change only slightly.

The model results shown in Figure 8.30 indicate that the stress path in *Cmet* rock masses of *Fw* sector goes in a direction where a severe seismicity should be expected in comparison to the rock masses of the *Hw* sectors. Since all mine sectors were stimulated by draw in a similar fashion, only the rock mass strength appears to be the most important factor that explains such differences in the recorded seismic intensity, in other word, rock masses with less abundance of weak discontinuities behave as a weaker rock mass compare to when weak discontinuities are scarce. This situation has also been stated by Araneda and Sougarret (2007). Considering the features of rock structure at different scales, this back analysis strongly suggests that not only large scale faults, but also the small scale weaker veins accommodate strain when the rock mass is loaded, and therefore all these structures play a major role in the seismicity at the El Teniente mine. It can also be inferred that when there is a less abundance of small scale weak veins (usually in the *Hw* sector of Esmeralda and Reno mine sector), the rock mass not only tends to store more potential energy

(allowing major seismic event to occurs), but also constrains caving propagation. This last means that more column height extraction would be needed for a rock mass with less abundance of weak discontinuities to the caveback to reach the top of the extracted ore column.

This back analysis strongly suggests that any seismic risk analysis undertaken at the mine site should incorporate a proper geotechnical characterization that accounts for the occurrence of the large scale faults and of the small scale network of weak veins as well.

In addition, the rock damage as mine drive over brake indicates that at a similar stress condition (maximum shear stress and major principal stress in Figure 8.31), pillars from *Fw* sector reached high level of damage whereas pillars from *Hw* sector only reached low level of damage. This rock mass behavior is only possible for a rock mass with different strength, therefore, rock masses at the El Teniente mine with fewer occurrences of weak veins can be considered stronger than a rock mass with high abundance of weak discontinuities. This analysis is more valid considering that most pillar of the *Fw* sector at the Esmeralda undercut mine level are bigger in area (robust) than these from *Hw* sector.

8.8 Conclusions

Major factors causing seismicity and mine drive rock damage in the undercut level were analysed through back analysis studies of the Esmeralda caving experience between 1997 and 2003 to investigate the validity of the research hypothesis. These studies included; rock structure characterization, which discusses Chapter 8, data analysis of the recorded seismicity and the production records, and numerical modelling to assess the state of the stress around excavations during caving propagation.

The structural data collected in this study at different mapping scales suggest that rock masses of primary copper ore at the El Teniente mine consist of an assemblage of blocks bounded mainly by veins of different strength and widely spaced sub-vertical fault contacts. Geotechnical units can be clearly distinguished in such rock masses by the application of a novel definition of weak discontinuities, which are not

included in traditional rock mass classification systems. Data also suggest that under certain stress conditions, the rock mass fails along both the large scale faults and the small scale weak veins.

Mining parameters such as the extraction rate (and the extraction front), which help caving propagation, were found to be similar between three studied unit types (sectors). However, the recorded seismicity of a complete caved rock volume was found very different between the same three studied sectors. Therefore, that mining parameter cannot be considered important to explain observed differences in seismicity.

The stress paths followed by the rock masses within the three sectors studied during caving propagation were obtained through the numerical model. The model results indicated that the stress path in rock masses of *F_w* sector generally proceeded in a direction where severe seismicity should be expected, however the recorded seismicity was benign compared to the other studied sectors. This rock mass response is only possible for a rock mass with low strength. These results agree with the concept that the rock mass strength correlates with the abundance of weak discontinuities; therefore these particular rock structure features are an important factor to understand and to predict the seismic response during caving propagation at the El Teniente mine.

Back analysis of rock damage observed in mine drives at the undercut level due to stress redistribution from cave propagation couple with modelled stress conditions also show that rock mass behavior agree with the concept that rock mass strength correlate with the abundance of weak discontinuities.

Therefore, the back analysis studies undertaken at the Esmeralda mine sector demonstrate the research hypothesis is true, i.e., *the strength of the massive and competent rock mass at the El Teniente mine depend of the occurrence of weak discontinuities within such rock masses.*

CHAPTER 9 CONCLUSIONS

9.1 Predicting Behaviour of Rock Masses of Primary Copper Ore

Rock masses of primary copper ore at the El Teniente mine have been described as very competent and massive during caving operation (Rojas et al., 2001). This is because caving performance has resulted in larger than expected fragmentation, and these rock masses have exhibited brittle, often violent failure under a high stress conditions (Dunlop and Gaete, 1997, Rojas et al., 2000a, Araneda and Sougarret, 2007). However, significant proportion of fine fragmentation, which has allowed high rates of underground caving production, has been observed within primary copper ore production level draw points. Furthermore, such competent rock masses have achieved caving with a hydraulic radius of around 25m in two different mine sectors, which is relatively similar to the values of 21m observed in the heavily fractured rock masses of secondary ore.

Therefore, mining experience in primary copper ore has exhibited a complex rock mass behaviour during caving operation, sometimes associated with a brittle and/or dynamic failure mode, and in other cases achieving readily caving with large proportion of fine fragmentation.

This observed mining performance has not been predicted using traditional tools in rock mass characterization as stated the Geotechnical Committee Board at the El Teniente mine (Goodman et al., 2000), nor explained the vast differences in rock mass behaviour.

9.2 Achievements of the Research

The main purpose of the present study was to determine main rock structure features controlling rock mass behaviour. The hypothesis of this research said that “*the occurrence of weak healed veins may control the strength and behaviour of the rock mass of primary copper ore during the caving process*”. In order to determine the validity of this hypothesis and its implication for rock mass characterization, an extensive data collection campaign of the rock structure was conducted at the mine site, which included several caved rock block found in the production level draw

points. In addition, back analysis studies were undertaken to investigate how the hypothesis correlates with real rock mass response to mining activities.

Significant contributions were achieved in this research in the areas of the structural characterization of the primary copper ore, the importance of cemented joint as controlling rock mass behaviour, and establishing a criterion to characterise rock masses at the El Teniente mine.

9.2.1 *Structural Characterization of Primary Copper Ore*

Rock masses of primary copper ore at the El Teniente mine have practically no open joints, with the large scale fault systems being the only open discontinuities presented. Faults were found to constitute one to two sub-vertical set orientations describing a large spacing of around 5 to 10 meters. The stockwork veins were found in high frequencies describing at least three semi-orthogonal discontinuity set orientations. Therefore, rock masses at the El Teniente mine can be thought of as an assemblage of both, small intact rock blocks bounded by joints that are cemented by the mineralogical infill (mainly chalcopyrite, quartz, anhydrite and chlorite) and widely spaced faults contacts. This rock mass feature is consistent with its high grade ore resources, its strong competence and massive character prior to caving.

The discontinuity characteristics observed in mine drives have similar discontinuity features observed in others geological environments. In this respect, scaling law properties between spacing/thicknesses and length were established for veins and faults. This means that the truncation bias length applied during data collection plays a relevant role during discontinuity survey. Furthermore, longer discontinuities tend to be statistically thicker, and some discontinuity parameters, such as vein infill and thickness distribution can be considered to have an isotropic feature within rock mass. The mineralogical infill assemblage in veins is the only parameter that varies throughout rock masses, which is in agreement with the geological definition of hydrothermal alteration zones for the ore body (Cuadra, 1986).

9.2.2 *Cemented Joints as Controlling Rock Mass Failure*

A major contribution of this research was to demonstrate that joints having intermediate or high tensile strength may play a relevant role as controlling rock

mass failure during caving propagation. The output of the caving process in different rock types and alteration zones was examined through the systematic characterisation of several caved rock-block forming geological discontinuities found at the production level caving draw points of the Reno mine sector. A common denominator was found; during caving rock masses of primary copper ore fail mainly through pre-existing geological discontinuities. These discontinuities are mainly healed, filled veins having the following particular features:

- Less than 1/3 of hard minerals as infill¹.
- Thicknesses greater than or equal to 2mm.

These observations were irrespective of the mining method, mode of failure, and percentage of extraction within draw points.

The observed characteristics of caved rock block faces led to define an empirical criterion to define weak discontinuities (faults and weak veins) from all discontinuities observed within rock mass.

9.2.3 *Characterising Rock Masses at the El Teniente Mine*

The structural data collected in mine drives were re-analysed taken into account the overwhelming effect of weak discontinuities. Considerable differences in term of the in situ rock block distributions defined by weak discontinuities were then predicted (of around 60%) between the two studied structural domains at the Reno mine sector, whereas conventional rock mass classification schemes only predict a difference of less than 5% between them.

Similar results were also observed when the proposed methodology was applied in other different structural domains at the Esmeralda mine sector, confirming that weak veins are more abundant at the *F_w* sector (PH hydrothermal alteration zone) than the *H_w* sector (LH hydrothermal alteration zone). In other words, by using this empirical criterion, considerable differences in term of the abundance of weak discontinuities can be predicted within rock masses of primary copper.

¹ A hard mineral is defined as having Mohs scale of hardness ≥ 4 .

9.2.4 Correlation with Rock Mass Response

The observed characteristic of caved rock block faces has proved that weak veins may at least control the fragmentation process in Reno mine sector. Records of the mining performance (Vasquez, 2003, Villegas, 2006) and real fragmentation data collected at the production level caving draw points at the Esmeralda mine sector (Pereira and Zamora, 1999) confirms that the concept of weak discontinuities have a real impact in the fragmentation performance mine wide.

A comparison between structural data and focal plane solutions of seismic events located within the seismogenic zone at the Esmeralda mine shows that not only the large scale, weak faults, but also healed weak veins are being mobilised during caving propagation. This interpretation was plausible because faults are limited to sub-vertical orientations, whereas the mobilised discontinuity orientations occurred scattered to multiple discontinuity orientations as weak veins do.

Back analysis studies of mine induced seismicity undertaken at the Esmeralda mine sector between 1997 and 2003, which included a mine scale numerical model to assess the state of the stress around excavations during caving propagation, showed that the recorded seismicity for a complete caved block volume of the same rock type was benign (fewer seismic event and lower magnitude) in the sector with large abundance of weak discontinuities (F_w) compared to the recorded seismicity in a sector with less abundance of weak discontinuities (H_w). Then, it can be inferred that rock masses of primary copper ore offer multiple options to accommodate strain caused by stress redistribution. However, it seems that the more abundant the options (i.e., more fault and weak veins), the less likely potential energy will be stored in the rock mass, and therefore be available to be released as seismic events.

Back analysis of rock damage observed in mine drives at the undercut level due to stress redistribution from cave propagation also shown that the rock mass behavior agree with the concept that rock mass strength correlate with the abundance of weak discontinuities.

Therefore, it is demonstrated that the research hypothesis is true, i.e., *the strength of the massive and competent rock mass at the El Teniente mine depend of the occurrence of weak discontinuities within such rock masses.*

9.3 Limitations and Recommendations for Future Work

Several limitations in rock mass characterisation must be recognized. One of the main contributions in this study is the description of the infill strength of weak discontinuities. This has been assessed empirically using the *Mohs scale of hardness* coupled with the infill mineral abundance. Although this proved to be a practical approach, more laboratory testing data is needed to determine the strength properties of the vein infill. This can be done by controlled triaxial testing on rock samples contained special oriented veins to characterise the infill peak and residual strength.

Despite of the difficulties involved, improved rock mass characterization at the El Teniente Mine could be further developed through work on a number of specific issues as follows:

- a) Extend this methodology to characterize rock masses mine wide, and perform more back analyses studies to understand mining performance.
- b) The total rock mass *fracturing* (by weak veins) has been undertaken based on rock structure simulations, which have assumed infinite trace length for discontinuity sizes. A sensitivity analysis is required to establish the influence of the true discontinuity size distributions on the simulations. In this respect, the development of a more complex and complete Discrete Fracture Network (DFN) of the rock structure is required. The key problem is to determine the true discontinuity size, but data from scanline mapping may be not reliable because of the unsystematic covering exposure bias. A different approach could be to determine the discontinuity size through simulated sampling as suggested La Pointe et al. (1993).
- c) Improve the understanding of the relationship between discontinuity thicknesses and discontinuity sizes. Methodologies, such as the one applied by Vermilye and Scholz (1995), can be used on data from the El Teniente mine.
- d) Investigate how to include data from the small diameter un-oriented core logging to characterize rock masses of primary copper ore based on the propose methodology.
- e) Improve the numerical modeling by additional activities/steps to understand rock mass behaviour. Better calibrations by including the observed rock damage in mine

drives is a first step. Including more different rock types (strength) could be a second step. A third step could be to include discrete elements (discontinuities) in the way “Synthetic Rock Mass” done it (Mas Ivars et al., 2007) to understand rock mass disassembly during caving propagation.

REFERENCES

- AKI, K. & RICHARDS, P. G. (1980) *Quantitative Seismology. Theory and Methods*, San Francisco, Freeman.
- AMADEI, B. (1988) Strength of a regularly jointed rock mass under biaxial and axisymmetric loading conditions. *Int. J. Rock Mech. Min. Sci. and Geomech. Abstr.*, 25, 3-13.
- BACKUS, G. & MULCANY, M. (1976) Moment tensor and other phenomenological descriptions of the seismic source - II. Discontinuous displacement. *Geophys J. R. Soc.*, 47, 301-29.
- BAENE, R. & BODNAR, R. (1995) Hydrothermal fluids and Hydrothermal alteration in porphyry copper deposits. *Porphyry Copper Deposits of the America Cordillera*. Arizona Geol. Soc., digets Arizona.
- BANDIS, S. C. (1990) Mechanical properties of rock joints. IN BARTON, N. & STEPHANSSON, O. (Eds.) *Rock Joint*. Rotterdam, Balkena.
- BAROS, M. C. (1995) *El Teniente. Hombres del Mineral, 1905-1945*, Santiago, Grafica Andes.
- BARRAZA, M. & CRORKAN, P. (2000) Esmeralda mine exploitation project. IN CHITOMBO, G. (Ed.) *Massmin 2000*. Brisbane, AusIMM.
- BARTON, N. (1976) The shear strength of rock and rock joints. *Int. J. Rock Mech. Min. Sci.*, 13, 255-79.
- BARTON, N. (2002) Some new Q-value correlations to assist in site characterization and tunnel design. *Int. J. Rock Mech. Min. Sci. and Geomech. Abstr.*, 39, 185-216.
- BARTON, N., BANDIS, S. C. & BAKHTAR, K. (1985) Strength, deformation and conductivity coupling of rock joints. *Int. J. Rock Mech. Min. Sci. and Geomech. Abstr.*, 22, 121-40.
- BARTON, N. & CHOUBEY, V. (1977) The shear strength of rock joints in theory and practice. *Rock Mechanics*, 10, 1-54.
- BARTON, N., LIEN, R. & LUNDE, J. (1974) Engineering classification of rock masses for the design of tunnel support. *Rock Mechanic*, 6, 183-236.
- BARTON, N. & STEPHANSSON, O. (Eds.) (1990) *Proceeding of the International Symposium on Rock Joints*, Loen, Norway, AA Balkema, Rotterdam.
- BEACHER, G. B., LANNY, N. A. & EINSTEIN, H. H. (1997) Statistical description of rock properties and sampling. *18th US Symp. on Rock Mechanics*.
- BECK, D. (2007) Back Analysis of Esmeralda mine sector, Numerical Modelling Results. . IN WASM (Ed.) Excel and PowerPoint files ed. Kalgoorlie.
- BECK, D. & BRADY, B. (2002) Evaluating and application of controlling parameters for seismic events in hard-rock mines. *Int. J. Rock Mech. Min. Sci.*, 39, 633-42.
- BECK, D., REUSCH, F., ARNDT, I., THIN, I., STONE, C., HEAP, M. & TYLER, D. (2006) Numerical modelling of seismogenic development during caving initiation, propagation and breakthrough. IN HADJIGEORGIOU, J. & GRENON, M. (Eds.) *Deep and High Stress Mining*. Quebec, Canada, University of Laval.
- BELMONTE, A. (2007) Personal communication. Excel files ed. The El Teniente mine.
- BIENIASWKI, Z. T. (1973) Engineering classification of jointed rock masses. *Transactions of the South African Institution of Civil Engineers*, 15, 335-44.

- BIENIASWKI, Z. T. (1976) Rock mass classifications in rock engineering. IN BIENIASWKI, Z. T. (Ed.) *In Exploration for Rock Engineering*. Cape Town, A.A.Balkema.
- BIENIASWKI, Z. T. (Ed.) (1989) *Engineering Rock Mass Clasifications*, New York, Wiley.
- BLONDEL, J., CELHAY, F. & PEREIRA, J. (1995) Consideraciones de geologia aplicada en estudios de fragmentacion de la roca primaria, Mina El Teniente. *Revista Minerale*s, 50, 7-19.
- BOATWRIGHT, J. & FLETCHER, J. B. (1984) The partition of Radiated energy between P and S waves. *Bulletin of the Seismological Society of America*, 74, 361-76.
- BRADY, B. H. G. & BROWN, E. T. (2003) *Rock Mechanics for Underground Mining*, London, Klumer Academic Publishers.
- BRIDGES, M. C. (1975) Presentation of fracture data for rock mechanics. 2nd ANZ conf. on Geomechanics.
- BRIDGES, M. C. (1990) Identification and characterization of sets of fractures and faults in rock IN BARTON, N. & STEPHANSSON, O. (Eds.) *Rock Joint*. Rotterdam, Balkena.
- BROOKS, B. A., ALLMENDINGER, R. & GARRIDO, I. (1996) Fault spacing in the El Teniente mine, central Chile: evidence for not fractal geometry. *J. Geophy. Res.*, 101, 13633-53.
- BROWN, E. T. (Ed.) (1981) *Rock Characterization Testing and Monitoring, Suggested Methods*, London, International Society of Rock Mechanics.
- BROWN, E. T. (Ed.) (2003) *Block Caving Geomechanics*, Indooroopilly, Australia, University of Queensland, JKMRRC.
- BRUNE, J. N. (1970) Tectonic Stress and the Spectra of Seismic Shear Waves from Eearthquakes. *J. Geophy. Res.*, 75, 4997-5009.
- BRZOVIC, A. (2001) Fundamentos geológicos para un sistema de clasificación geotécnico del macizo rocoso primario, mina El Teniente. Superintendence Geology, Division El Teniente CODELCO-Chile.
- BRZOVIC, A., QUEZADA, O. & VILLEGAS, F. (1998) Geotecnia pilares Teniente Sub-6 nivel de produccion. Superintence Geology, Division El Teniente CODELCO-Chile.
- BRZOVIC, A. & VILLAESCUSA, E. (2007) Rock mass characterization and assessment of block-forming geological discontinuities during caving of primary copper ore at the El Teniente mine, Chile. *Int. J. Rock Mech. Min. Sci. and Geomech, Abstr.*, 44, 565-83.
- BRZOVIC, A., VILLAESCUSA, E. & FIGUEROA, C. (2006) Characterization of block-forming geological discontinuities during primary ore caving at the El Teniente mine, Chile. IN YALE, D., HOLTZ, S., BREEDS, S. & OZBAY, U. (Eds.) *41st US Symp. on Rock Mechanics*. Golden Colorado, ARMA.
- BURNHAM, C. W. (1979) Magmas and hydrothermal fluids IN BARNES, H. L. (Ed.) *Geochemistry of Hydrothermal Deposits*. New York, John Wiley and Sons.
- BURRIDGE, R. & KNOPOFF, L. (1964) Body force equivalent for seismic dislocations. *Bulletin of the Seismological Society of America.*, 54, 1875-1888.
- CALL, R. D., SAVELY, J. P. & NICHOLAS, D. E. (1976) Estimation of joint set characteristic from surface mapping data. IN BROWN, W. S., GREEN, S. J.

- & HUSTRULID, W. A. (Eds.) *17th US Symp. on Rock Mechanics*. New York, SME.
- CHACON, J., GOPFERT, H. & OVALLE, A. (2004) Thirty years evolution of block caving in Chile. IN KARZULOVIC, A. & ALFARO, M. (Eds.) *Massmin 2004*. Santiago, Minera Chilena.
- CHARRIER, R., BAEZA, O., ELGUETA, S., FLYNN, J. J., GANS, P., KAY, S. M., MUÑOZ, N., WYSS, A. R. & ZURITA, E. (2002) Evidence for Cenozoic extensional basin development and tectonic inversion south of the flat-slab segment, southern Central Andes, Chile (33°–36°S.L.). *J. of South Am. Earth Sciences*, 15, 117-39.
- CLADOUHOS, T. (1994) Fault kinematics near the El Teniente Mine. Rancagua, Codelco, El Teniente Division
- CLADOUHOS, T. & MARRET, R. (1996) Are fault growth and linkage models consistent with power law distributions of fault length? . *J. Struct. Geo.*, 18, 281-93.
- CLINE, J. (1995) Genesis of porphyry deposits: the behavior of water, chloride, and copper in crystallizing melts. IN PIERCE, F. W. & BOLM, J. G. (Eds.) *Porphyry Copper Deposits of the America Cordillera*. Arizona Geol. Soc., digets Arizona.
- CRUDEN, D. M. (1977) Describing the size of discontinuities. *Int. J. Rock Mech. Min. Sci. and Geomech. Abstr.*, 14, 133-7.
- CUADRA, P. (1986) Geocronologia K-Ar del yacimiento El Teniente y areas adyacentes. *Revista Geologica de Chile*, 27, 3-26.
- DAVID, G. H. (1984) *Structural Geology of Rocks and Regions*, New York, John Wiley & Sons.
- DE NICOLA, R. & FISHWICK, M. (2000) An underground airblast, Codelco Chile, Division El Salvador. IN CHITOMBO, G. (Ed.) *Massmin 2000*. Brisbane, AusIMM.
- DEERE, D. U. (1964) Technical description of rocks cores for engineering purposes. *Rock Mechanics and Rock Engineering*, 1, 17-22.
- DEERE, D. U. (1968) Geological considerations. IN STAGG, R. G. & ZIENKIEWICZ, R. G. (Eds.) *Rock Mechanics and Engineering Practices*. New York, Wiley & Son.
- DERSHOWITZ, W. S. & HERDA, H. H. (1992) Interpretation of fracture spacing and intensity. IN TILLERSON, J. R. & WAWERSIK, W. R. (Eds.) *33rd US Symp. on Rock Mechanics*. Santa Fe, New Mexico, A.A.Balkema.
- DERSHOWITZ, W. S., LEE, G., GEIER, J., FOXFORD, T. & LAPOINTE, P. (1998) FracMan, interactive discrete feature data anaylisis, geometric modeling, and exploratioin simulation. 2.6 ed. Seattle, Washington, Golder Assocites Inc.
- DUNLOP, R. & BELMONTE, A. (2005) The April 22nd, 2003 Rockburst in the sub 6 sector, El Teniente Mine-A case history. IN POTVIN, Y. & HUDYMA, M. (Eds.) *6th int. Symp. on Rockburst and Seismicity in Mines (RaSiM6)*. Perth, Australia, ACG.
- DUNLOP, R. & GAETE, S. (1997) Controlling induced seismicity at El Teniente Mine: the Sub6 case history. IN GIBOWICZ, S. J. & LASOKI, S. (Eds.) *4th Int. Symp. on Rockbursts and Seismicity in Mines (RaSiM4)*. Krakow, Poland, Balkema.
- DUNLOP, R. & GAETE, S. (2001) Induced seismicity at El Teniente mine: The Esmeralda sector case history. IN VAN ASWEGEN, G., DURRHEIM, R. J.

- & ORTLEPP, W. D. (Eds.) *5th Int. Symp. on Rockburst and Seismicity in Mines (RaSiM5)*. Johannesburg, South African Instn. Min & Metall.
- DUPLANCIC, P. (2002) Characterisation of caving mechanics through analysis of stress and seismicity. Perth, University of Western Australia.
- EINSTEIN, H. H. & BEACHER, G. B. (1983) Probabilistic and statistical methods in engineering geology. *Rock Mechanics and Rock Engineering*, 16, 39-72.
- ESTERHUIZEN, G. S. (1999) A program to predict block cave fragmentation. 3.1 ed.
- FIGUEROA, C. (2003) Caracterización geológica y geotécnica de Colpas en puntos de extracción, mina Teniente Sub-6. Concepcion, Universidad de Concepción.
- FLOODY, R. (2000) Estudio de la vulnerabilidad geologica y geotecnica de chimenea de Brecha Braden. Fase I, geologia de Brecha Braden. Superintendence Geology, Division El Teniente CODELCO-Chile.
- GAETE, S., LEIVA, E., QUIROZ, R., RUBIO, J. & SEGUEL, J. (2005) Diagnostico mina Esmerelda, grupo de trabajo proyecto Esmeralda. Division El Teniente CODELCO-Chile, Internal report SGM-I-024/2005.
- GARRIDO, I., RIVEROS, M., CLADOUHOS, T., ESPINEIRA, D. & ALLMENDINGER, R. (1994) Modelo geologico estructural yacimiento El Teniente. *VII Congreso Geologico Chileno*. Antofagasta.
- GEPHART, J. W. & FORSYTH, D. W. (1984) An improved method for determining the regional stress tensor using earthquake focal mechanism data: Application to the San Fernando earthquake sequence. *J. Geophy. Res.*, 89, 9305-20.
- GIBOWICZ, S. (1990) The mechanism of seismic events induced by mining. IN FAIRHURST, C. (Ed.) *2nd int. Symp. on Rockburst and Seismicity in Mines (RaSiM2)*. Minneapolis, A.A.Balkema, Rotterdam.
- GIBOWICZ, S. & KIJKO, A. (1994) *An Introduction to Mining Seismology*, New York, Academic Press.
- GIBOWICZ, S. J., HARJES, H. P. & SCHAFFER, M. (1990) Source parameters of seismic events at Heinrich Robert Mine, Ruhr Basin, Federal Republic of Germany: Evidence for nondouble-couple events. *Bulletin of the Seismological Society of America*, 80, 88-109.
- GILLESPIE, P. A., HOWARD, C. B., WALSH, J. J. & WATTERSON, J. (1993) Measurement and characteristic of spatial distribution of fractures. *Tectonophysics*, 226, 113-41.
- GOODMAN, R., BRADY, G. & BRADY, B. H. G. (2000) Geotechnical review board, División El Teniente CODELCO Chile. Rancagua, Division El Teniente CODELCO-Chile.
- GOODMAN, R. E. (1970) The deformability of joints. Determination of the in-situ modulus of deformation of rock. *J. Am. Soc. for Testing and Materials*, 477, 171-96.
- GOODMAN, R. E. (1976) *Methods of Geological Engineering in Discontinuity Rock*, St. Paul., West.
- GRIMSTAD, E. & BARTON, N. (1993) Updating of the Q-system for NMT support selection. *International Symposium on Sprayed Concrete*. Oslo, Norway, Norwegian Cobcrete Association.
- HADJIGEORGIOU, J., LESSARD, J. F. & FLAMENT, F. (1995) Characterizing in-situ block distribution using a stereological model. *Canadian Tunnelling J.*, 201-11.

- HAMRIN, H. (2001) Underground mining methods and applications. *Underground Mining Methods; Engineering fundamental and international case studies*. Colorado, SME.
- HANKS, T. C. & KANOMORI, H. (1979) A moment tensor magnitude scale. *J. Geophy. Res.*, 84, 2348-50.
- HARR, M. (1987) *Reliability Based Design in Civil Engineering*, New York, McGraw Hill.
- HARRISON, D. (2009) Caracterización estructural bajo el nivel Teniente 8 mediante el análisis de sondajes ortogonales orientados para el proyecto nuevo nivel mina, yacimiento El Teniente, Chile. *Geological Department*. University of Concepcion.
- HOEK, E. (1994) Strength of rock and rock masses. *ISRM News J.*, 2, 4-16.
- HOEK, E. & BROWN, E. T. (1980) *Underground Excavation in Rock*, London, IMM.
- HOEK, E., KAISER, P. K. & BAWDEN, W. F. (Eds.) (1995) *Support of Underground Excavations in Hard Rock*, Rotterdam, A.A.Balkema.
- HOOPS, B. E. (1993) The significance of structural geology in rock mechanics. IN HUDSON, J. A. (Ed.) *Comprehensive Rock Engineering*. Pergamon Press.
- HOWELL, F. H. & MOLLOY, S. (1960) Geology of the Braden orebody, Chile, South America. *Economic Geology*, 70, 863-905.
- HUDSON, J. A. & HARRISON, J. P. (1997) *Engineering Rock Mechanics, an Introduction to the Principles*, Oxford, Pergamon Press.
- HUDSON, J. A. & PRIEST, S. D. (1983) Discontinuity frequency in rock masses. *Int. J. Rock Mech. Min. Sci. and Geomech. Abstr.*, 20, 73-89.
- HURLBUT, C. (Ed.) (1941) *Dana's manual of mineralogy*, New York, John Wiley & Sons.
- ISS (2007) Seismological back analysis of large events at Reservas Norte, El Teniente. *ISS International Limited*. Codelco, El Teniente Division.
- JEAGER, J. C. (1960) Shear fracture of anisotropic rock. *Geol. Mag.*, 97, 65-72.
- JOHNSTON, J. D. & MCCAFFREY, J. W. (1996) Fractal geometries of veins systems and the variation of scaling relationship with mechanism. *J. Struct. Geo.*, 18, 249-58.
- KEMENY, J., DEVGAN, A., HAGAMAN, R. & WU, X. (1993) Analysis of rock fragmentation using digital image processing. *J. Geotech. Eng.*, 119, 1144-60.
- KIJKO, A. & SCIOCATTI, M. (1995) Optimal spatial distribution of seismic stations in mines. *Int. J. Rock Mech. Min. Sci.*, 32, 607-15.
- KULATILAKE, P. H. S. W. (1993) Application of probability and statistics in joint network modeling in three dimensions. IN LI, K. S. & LO, S.-C. R. (Eds.) *Probabilistic Methods in Geotechnical Engineering*. Camberra, Australia, A.A.Balkema, Rotterdam.
- KULATILAKE, P. H. S. W., UM, J., WANG, M., ESCANDON, R. F. & NARVAIZ, J. (2004) A case study on stochastic fracture geometry modelling in 3-D including validation for tunnelling site in USA. IN VILLAESCUSA, E. & POTVIN, Y. (Eds.) *5th Int. Symp. Ground Support in Mining and Underground Construction*. Perth, Balkema.
- KULATILAKE, P. H. S. W. & WU, T. H. (1984) Estimation of mean trace length of discontinuities. *Rock Mechanics and Rock Engineering.*, 17, 215-232.
- LASLETT, G. M. (1982) Censoring and edge effect in areal and line transect sampling of rock joint traces. *Mathematical Geology*, 14, 125-40.

- LAUBSCHER, D. (1973) Class distinction in rock masses. *Coal, Gold + Base Miner. South. Afr.*, 23.
- LAUBSCHER, D. (1990) A geomechanics classification system for the rating of rock mass in mine design. *J. South African Ins. Min. and Metallurgic.*, 90, 257-73.
- LAUBSCHER, D. (1993) Planning mass mining operations. IN HUDSON, J. A. (Ed.) *Comprehensive Rock Engineering* London, Pergamon.
- LAUBSCHER, D. (2001) Caving Mining – The state of the art. IN HUSTRULID, W. A. & BULLOCK, R. (Eds.) *Underground Mining Methods; engineering fundamental and international case studies*. Colorado, SME.
- LAUBSCHER, D. & JAKUBEC, J. (2001) The MRMR rock mass classification system for jointed rock masses. IN HUSTRULID, W. A. & BULLOCK, R. (Eds.) *Underground Mining Methods; engineering fundamental and international case studies*. Colorado, SME.
- LAUBSCHER, D. & TAYLOR, H. W. (1976) The importance of geomechanics classification of jointed rock masses in mining operations. IN BIENIAWSKI, Z. T. (Ed.) *Exploration for Rock Engineering*. Cape Town, A.A.Balkema.
- LU, P. & LHATAM, J. P. (1999) Developments in assessment of the in-situ block size distribution of rock masses. *Rock Mechanics and Rock Engineering*, 32, 29-49.
- LYNCH, R. (2006) Ray tracing at El Teniente. *ISS International Limited*. Codelco, El Teniente Division.
- MADARIAGA, R. (1976) Dynamics of an expanding circular fault. *Bulletin of the Seismological Society of America*, 66, 639-66.
- MAERZ, N. H. & GERMAIN, P. (1992) Block size determination around underground opening using simulations. IN MYER, L. E., TSANG, C. F., COOK, N. G. & GOODMAN, R. (Eds.) *Fractured and Jointed Rock Masses*. Lake Tahoe, California, A.A.Balkema.
- MAHTAB, M. A. & YEGULALP, T. M. (1982) A rejection criterion for definition of clusters in orientation data. IN GOODMAN, R. E. & HENZE, F. (Eds.) *23th US Symp. on Rock Mechanics*. New York, SME.
- MARINOS, P. & HOEK, E. (2000) GSI: a geologically friendly tool for rock mass strength estimation IN LANCASTER, P. A. (Ed.) *GeoEng 2000*. Melbourne, Australia, Technomic Publishers.
- MAS IVARS, D., DEISMAN, N., PIERCE, M. & FAIRHURST, C. (2007) The synthetic rock mass approach - A step forward in the characterization of jointed rock masses IN RIBEIRO E SOUSA, OLALLA & GROSSMAN (Eds.) *11th Congress of the ISRM*. Lisboa, Portugal, Taylor & Francis Group.
- MAULDON, M. & MAULDON, J. G. (1997) Fracture sampling on a cylinder: from scanlines to boreholes and tunnels. *Rock Mechanics and Rock Engineering*, 30, 129-44.
- McGARR, A. (1984) Some applications of some and damage source mechanism studies to assessing underground hazard. IN GAY, N. C. & WAINWRIGHT, E. H. (Eds.) *Rockbursts and Seismicity in Mines*. Johannesburg.
- McGARR, A. (1999) On relating apparent stress to the stress causing earthquake fault slip. *J. Geophys. Res.*, 104, 3003-11.
- MENDECKI, A. J. (1993) Real time quantitative seismology in mines. IN YOUNG, R. P. (Ed.) *3rd Int. Symp. Rockbursts and Seismicity in Mines (RaSim3)*. Kingston, A.A.Balkema, Rotterdam.
- MENDECKI, A. J. (1997) *Seismic Monitoring in Mines*, London Chapman & Hall.

- MENDECKI, A. J., VAN ASWEGEN, G. & MOUNTFORT, P. (1999) A guide to routine seismic monitoring in mines. IN JAGER, A. J. & RYDER, J. A. (Eds.) *A Handbook or Rock Engineering Practice for Tabular Hard Rock Mines*. Cape Town, Crede Communicatios.
- MERINO, L. (1990) Sistema Size, manual de usuario.
- MONLAR, P. (1983) Average regional strain due to slip on mumerous faults of different orientations. *J. Geophy. Res.*, 88, 6430-2.
- NCL (2004) Analisis de producion de parametros de control y planificacion. Linea base mina Esmeralda. Division El Teniente CODELCO-Chile.
- PAHL, P. J. (1981) Estimating the mean length of discontinuity traces. *Int. J. Rock Mech. Min. Sci. and Geomech. Abstr.*, 18, 221-228.
- PAPALIANGAS, T., LUMSDEN, A. C., HENCHER, S. R. & MANOLOPOULOU, S. (1990) Shear strength of modelled filled joints. IN BARTON, N. & STEPHANSSON, O. (Eds.) *Rock Joint*. Loen, Norway, AA Balkena, Rotterdam.
- PASLMTRON, A. (1985) Applications of the volumetric joint count as a measure of rock mass jointing. . *Int. Symp. on Fundamentals of Rock Joints*. Sweden, Bjorkliden.
- PEREIRA, J. (1990) Shear strength of filled discontinuities. IN BARTON, N. & STEPHANSSON, O. (Eds.) *Rock Joint*. Loan, Norway, AA Balkena, Rotterdam.
- PEREIRA, J. & ZAMORA, A. (1999) Estudio Granulometrico Mina Esmeralda. Superintendence Geology, Division El Teniente CODELCO-Chile.
- PHIEN-WEJ, N., SHRESTHA, U. B. & RANTUCCI, G. (1990) Effect of infill thickness on shear behaviour of rock joints. IN BARTON, N. & STEPHANSSON, O. (Eds.) *Rock Joint*. Loan, Norway, AA Balkena, Rotterdam.
- PINCUS, H. (1951) Statistical methods applied to the study of rock fractures. *Geological Society of American Bulletin*, 62, 81-130.
- PINCUS, H. (1953) The analysis of aggregates of orientation data in the earth sciences. *Geology*, 61, 483-509.
- POLLARD, D. D. & AYDIN, A. (1988) Progress in understanding jointing over the past century. *Geological Society of American Bulletin*, 100, 1181-204.
- POLLARD, D. D. & SEGAL, P. (1987) Theoretical displacements and stress near fractures in rock: with applications to faults, joints, veins, dikes, and solution surfaces. IN ATKINSON, B. (Ed.) *Fracture Mechanism of Rock*. London, Academins Press.
- PRIEST, S. D. (1993) *Discontinuities Analysis for Rock Engineering*, London, Chapman and Hall.
- PRIEST, S. D. & HUDSON, J. A. (1976) Discontinuity spacing in rock. *Int. J. Rock Mech. Min. Sci. and Geomech. Abstr.*, 13, 135-48.
- PRIEST, S. D. & HUDSON, J. A. (1981) Estimation of discontinuity spacing and trace lengh using scanline surveys. *Int. J. Rock Mech. Min. Sci. and Geomech. Abstr.* , 18, 183-97.
- PUSCH, R. (1995) *Rock Mechanics on a Geological Base*, Amsterdam, Elsevier.
- RAMOS, V. A. (1988) The tectonics of the Central Andes; 30° to 33°S latitude. IN CLARK, S. & BURCHFIEL, D. (Eds.) *Processes of Continental Lithosphere Deformation*. Geol. Soc. Am.
- RICHTER, C. (1935) An instrumental earthquake magnitude scale. *Bulletin of the Seismological Society of America*, 25, 1-32.

- ROCSCIENCE INC (1999) Dips version 5.02. Toronto, Canada.
- ROJAS, E., CAVIERES, P., DUNLOP, R. & GAETE, S. (2000a) Control of induced seismicity at El Teniente mine, Codelco Chile. IN G.CHITOMBO (Ed.) *Massmin 2000*. Brisbane, AusIMM.
- ROJAS, E., MOLINA, R., BONANI, A. & CONSTANZO, H. (2000b) The pre-undercut caving method at the El Teniente mine, Codelco Chile. IN G.CHITOMBO (Ed.) *Massmin 2000*. Brisbane, AusIMM.
- ROJAS, E., MOLINA, R. & CAVIERES, P. (2001) Preundercut caving in El Teniente mine, Chile. IN HUSTRULID, W. R. & BULLOCK, R. (Eds.) *Underground Mining Methods; engineering fundamental and international case studies*. Colorado, SME.
- SAVELY, J. P. (1972) Orientation and engineering properties of jointing in the Sierra pit. Tucson, University of Arizona.
- SCHOLZ, C. R. (2002) *The Mechanics of Earthquakes and Faulting* Cambridge, Cambridge University Press.
- SEGUEL, J. (2005) Antecedentes geológicos y geotécnicos al norte XC-3 ucl Esmeralda Superintendence Geology, Division El Teniente CODELCO-Chile.
- SEGUEL, J. & MORALES, A. (1988) Estimacion grado de fracturamiento del macizo en sondajes geotécnicos sg-88 al 91, Mina Esmeralda. Superintendence Geology, Division El Teniente CODELCO-Chile.
- SEN, Z. & EISSA, E. A. (1991) Rock quality charts for log-normally distributed block sizes. *Int. J. Rock Mech. Min. Sci. and Geomech. Abstr.*, 29, 1-12.
- SEN, Z. & KAZI, A. (1984) Discontinuity spacing and RQD estimates from finite length scanlines. *Int. J. Rock Mech. Min. Sci. and Geomech. Abstr.*, 21, 203-12.
- SHANLEY, R. J. & MAHTAB, M. A. (1976) Delineation and analysis of clusters in orientation data. *Mathematical Geology*, 8, 9-22.
- SILENY, J., RITSEMA, A. R., CSIKOS, I. & KOZAK, J. (1986) Do some shallow earthquakes have tensile source component? *PAGEOPH*, 124, 825-40.
- SKEWES, M. A. & AREVALO, A. (1997) Andesitas de la mina, El Teniente. *VIII Congreso Geológico Chileno*. Antofagasta.
- SKEWES, M. A., AREVALO, A., FLOODY, R., ZUNIGA, P. & STERN, C. R. (2002) The giant El Teniente breccia deposit: Hypogene copper distribution and emplacement. *Economic Geology*, 9, 299-32.
- STEIN, S. & WYSESSION, M. (2003) *An Introduction to Seismology, Earthquakes, and Earth Structure*, London, Blackwell Publishing Ltd.
- TAPPONNIER, P. & BRACE, W. F. (1976) Development of stress-induced microcracks in Westerly Granite. *Int. J. Rock Mech. Min. Sci.*, 13, 103-12.
- TERZAGHI, R. (1946) *Theoretical soil mechanics*, Jonh Wiles&Sons.
- TERZAGHI, R. (1965) Sources of error in joint surveys. *Geotechnique*, 15, 287-303.
- THOMPSON, A. (2002) Stability assessment and reinforcement of block assemblies near underground excavations IN HAMMANH, R., BAWDEN, W. F., CURRAN, J. & TELESNICKI, M. (Eds.) *NARMS-TAC*. University of Toronto press.
- URBANCIC, T. I. & YOUNG, R. P. (1993) Space-Time variations in source parameters of mining-induced seismic events with $M < 0$. *Bulletin of the Seismological Society of America.*, 83, 378-397.

- VAN AS, A. & JEFFREY, R. G. (2000) Hydraulic fracturing as a cave inducement technique at Northparkes mine.. IN G.CHITOMBO (Ed.) *Massmin 2000*. Brisbane, AusIMM.
- VASQUEZ, P. (2003) Aplicacion del sistema estandar de control de la fragmentacion (secof) al sector Ten-4Sur. Codelco El Teniente Division, internal report SPL-I-032/2003.
- VENCE, J. B., HASSANI, F. P. & MOTTAHED, P. (1988) Improved determination of microseismic source location using a complex technique. *IEEE Trans. Ind. Applic.*, 24, 666-71.
- VERGARA, M., CHARRIER, R., MUNIZAGA, F., RIVANO, S., SEPULVEDA, P., THIELE, R. & DRAKE, R. (1998) Miocene volcanism in the central Chilean Andes (31°30'S–34°35'S). *J. South Am. Earth Sciences*, 1, 199-209.
- VERMILYE, J. M. & SCHOLZ, C. R. (1995) Relation between veins and aperture. *J. Struct. Geo.*, 17, 423-34.
- VILLAESCUSA, E. (1985) Slope stability analysis at the Caridad mine, Nacazari, Sonora Mexico. Colorado, University of Colorado, Colorado School of Mines.
- VILLAESCUSA, E. (1991) A three dimensional model of rock jointing. . Brisbane., University of Queensland.
- VILLAESCUSA, E. & BROWN, E. T. (1992) Maximum likelihood estimation of joint size from trace length measurements. *Rock Mechanics and Rock Engineering*, 25, 67-87.
- VILLAESCUSA, E. & MACHUCA, L. (2007) Stress measurement from oriented core using the Acoustic Emission method, El Teniente mine. WASM, Curtin University
- VILLEGAS, F. (2006) Anecdotal experiences of Esmeralda mine sector. Personal data ed. Rancagua.
- WALLIS, P. F. & KING, M. S. (1980) Discontinuity spacing in crystalline rock. *Int. J. Rock Mech. Min. Sci. and Geomech. Abstr.*, 17, 63-6.
- WANG, L. G., YAMASHITA, S., SUGIMOTO, F., PAN, C. & TAN, G. (2003) A methodology for predicting in situ and shape distribution of rock block. *Rock Mechanics and Rock Engineering*, 36, 121-142.
- WARBURTON, P. M. (1980) A stereological interpretation of joint trace data. *Int. J. Rock Mech. Min. Sci. and Geomech. Abstr.*, 17, 181-90.
- WHITNEY, J. (1975) Vapour generation in Quartz Monzonite magma: A synthetic model with application to porphyry deposits. . *Economic Geology*, 70, 346-58.
- WILLONER, A. (2000) Characterization of rock mass quality and prediction of mass behaviour; an investigation into the parameters which influence the strength of healed joints in hypogene mineralized andesite at El Teniente copper mine, Chile. Leeds, The University of Leeds, School of Earth Sciences.
- WINDSOR, C. R. (1997) A course on structural mapping and structural analysis (Course notes for M.Eng.Sc). Kalgoorlie, Western Australian School of Mines. Rock Technology Pty Ltd.
- WINDSOR, C. R., CAVIERES, P., VILLAESCUSA, E. & PEREIRA, J. (2006a) Reconciliation fo strain, structure and stress in the El Teniente mine region, Chile. IN LU, M., LI, C., KJORHOLT, H. & DAHLE, H. (Eds.) *In-situ Rock Stress. Measurement, Interpretation and Applications*. Trondheim, Norway, Taylor&Francis.

- WINDSOR, C. R., CAVIERES, P., VILLAESCUSA, E. & PEREIRA, J. (2006b) Rock stress tensor measurements at the El Teniente mine, Chile. IN LU, M., LI, C., KJORHOLT, H. & DAHLE, H. (Eds.) *In-situ Rock Stress. Measurement, Interpretation and Application*. Trondheim, Norway, Tylor&Francis.
- ZHANG, L. & EINSTEIN, H. H. (2000) Estimating the intensity of rock discontinuities. *Int. J. Rock Mech. Min. Sci. and Geomech, Abstr.*, 37, 819-37
- ZUNIGA, P. (1982) Alteracion y mineralizacion hipogenas en el sector oeste del yacimiento El Teniente. Santiago, Universidad de Chile.

Every reasonable effort has been made to acknowledge the owners of copyright material. I would be pleased to hear from any copyright owner who has been omitted or incorrectly acknowledged.

APPENDIX I

Raw Data used in this thesis are contained in the attached CD, these are from;

- A. Major Structures
- B. Drive Mapping
- C. Line Mapping (Scanlines)
- D. Oriented Core Logging (Large Diameter Core Samples)
- E. Un-Oriented Core logging (Small Diameter Core Samples)
- F. Caved Rock Block Data

Some examples of the raw data are as follow.

Appendix I.A Major Structures

Example of data from Reno Hw mine sector;

id	id2	Dist. m	Trace Length m	Disc. Type	DIP	DIPDIR	Thickness (max-min)		Infill Features				
							mm	mm					
1	1	47	30	F LH	74	10	5	5	gouge	gyp	py	cpy	
2	1		30	F LH	73	13	8	8	ca	anh			
3	1	40	30	F LH	70	209	5	5	gyp	cpy	py		
4	1		30	F LH	60	208	5	5	anh	ca			
5	1	60	40	PH	50	233	10	10	cpy	qtz	py	anh	
6	1		40	PH	44	240	9	9	cpy	anh			
7	1	80	45	F LH	90	16	8	8	ca				
8	1		45	Fault	75	18	20	50					
9	1		20	LH	80	185	2	2	gyp				
10	1			LH	81	183	2	2	gyp				
11	1	116	45	F LH	90	192							
12	1		45	F LH	90	196							
13	1		50	LH	90	191	2	2	gyp				
14	1		50	F LH	90	198	6	6	cpy	anh			
15	1	48	45	F LH	90	190							
16	1		45	Fault	65	11	3	3	gyp				
17	1	60	45	F LH	78	23	30	30	anh	gyp	cpy		
18	1		45	F LH	76	18	20	25	cpy	anh	ca	gouge	
19	1	56	55	F PH	65	194	10	10	cpy	anh	gyp		
20	1		55	F LH	80	185							
21	1	55	50	F LH	90	214	8	8	gyp	cpy	anh		
22	1		50	F LH	87	200	12	12	anh	cpy	ca	chl	
23	1	75	60	F LH	90	210	8	8	gyp	cpy	ca		
24	1		60	F LH	86	215	10	12	anh	ca	cpy		
25	1	74	60	F LH	65	200	15	15	ca	gyp	cpy		
26	1		60	F LH	70	203	20	20	ca	anh	gyp	cpy	
27	1	56	55	F LH	86	212	4	10	cpy	anh	gyp	te	ca

Note; two discontinuity observations for each major structure have been included. The second observation is in the following row

The rest of data including data from Reno Fw mine sector is included in the attached CD.

Appendix I.B Drive Mapping

Example of data from Reno Hw mine sector;

Id	Transverse	Distance	Disc. Type	DIP	DIPDIR	Thickness (max-min)			Infill Features		
		m				mm	mm				
1	1	4.28	V PH	67	186	10	10	cpy	anh	qtz	bo
2	1	8	V LM	75	192	5	5	qtz	cpy		
3	1	19.05	V LM	90	354	4	4	qtz			
4	1	24.01	V LH	30	55	5	5				
5	1	24.5	V LH	74	172	10	10	ca	qtz	cpy	tu
6	1	27.28	V LH	85	18	15	15	ca	te	cpy	
7	1	27.75	V LH	55	338	2	2	ca	cpy	te	
8	1	30	V LM	69	308	5	5	qtz	cpy		
9	1	30.75	V LM	32	206	5	5	qtz	anh	bo	
10	1	34.35	V PH	55	206	8	8	cpy	qtz		
11	1	40.66	V LM	42	220	5	5	qtz	bo	cpy	
12	1	41.13	V PH	74	194	2	2	cpy			
13	1	46.99	V LH	68	331	15	15	ca	gyp	cpy	te
14	1	47.18	V LH	55	32	3	3	cpy	ca		
15	1	47.95	V LM	64	339	2	2	qtz	cpy		
16	1	51.19	V LM	40	233	15	15	qtz	bo	cpy	
17	1	69.37	V LH	75	306	10	10	ca	chl	cpy	te
18	2	3.86	V LM	53	32	15	15	qtz	cpy		
19	2	7.7	F LH	68	305	5	5	cs	gyp	tu	te
20	2	12.75	V LM	74	158	10	10	qtz	anh		
21	2	14.37	V LH	63	321	10	10	qtz	ca	tu	te
22	2	20.65	V LM	90	327	30	30	qtz	anh		
23	2	32.46	F LH	75	304	5	5	cpy	gyp	mo	

The rest of data including data from Reno Fw mine sector and from all structural domains at the Esmeralda mine sector are included in the attached CD.

Appendix I.C Line Mapping

Example of data from Reno Hw mine sector;

Location				Discontinuity			Geometry						Mineralogical Infill																			
Id	Transverse	Distance (m)	Endpoints	Type	DIPDIR	DIP	Roughness		T1-T2		Trace Length (m)	Face's area (cm ²)	Thickness		halo type width (mm)	Anh	Bt	Bo	Cpy	Ca	Ca*	Chl	Qtz	Mo	Py	Te	Tu	Gyp	Mt	Se		
							Large Scale	Small Scale	Above	Below			max (mm)	min (mm)																		
1	1	0.02	2	VLM	354	82	2	4	AJL	IR	0.8	375	1	0		20			5			10	65									
2	1	0.08	1	VLM	212	68	1	3	AJH	C	1.6	0	3	1				5			10	85										
3	1	0.01	2	VLM	14	88	1	3	AJL	AJL	0.2	120	0.5	0		62		5	3			10	20									
4	1	0.2	1	VLM	10	75	2	4	AJL	C	1	300	1	0.5		15			3			10	72									
5	1	0.3	1	VLM	6	56	3	6	AJL	C	2.7	180	15	1		30	5	3	5			10	47									
6	1	0.3	1	VLM	340	78	1	3	AJH	C	0.9	1050	1	0.5		10		3	5			10	72									
7	1	0.3	2	VLM	346	87	2	5	AJH	AJL	0.3	225	0.5	0		10					5	85										
8	1	0.45	2	VLM	154	82	7	4	AJH	AJL	1.9	2700	2	1		30		2	3			10	55									
9	1	0.21	2	VLM	98	84	1	3	AJL	AJL	2	56	1	0.5		5		3	15				77									
10	1	0.45	1	VLM	202	26	2	4	UN	C	2.5	0	15	2		30	5	3	5			10	47									
11	1	0.54	1	VPH	29	72	3	6	IR	C	2.2	0	2	1	qtz se chl 2	20			50			30										
12	1	0.78	2	VLM	358	81	2	4	C	AJH	2.5	750	5	2		10		3	5				82									
13	1	0.73	1	VLM	305	82	9	5	UN	C	2	200	3	2		20		3	15			10	47			5						
14	1	0.95	1	VLM	186	80	4	7	UN	AJL	1.7	1500	3	1		30			10				60									
15	1	0.9	2	VLM	296	71	3	6	AJL	AJL	1.4	240	2	1	qtz chl 2	10		5	60				25									
16	1	1	2	VLM	230	30	3	6	C	AJL	1.3	0	2	1	qtz 1		30		5			40	25									
17	1	1.47	2	VLM	5	88	1	3	AJL	AJL	0.8	160	1	0		10	10	5	3			20	52									
18	1	1.9	0	VLM	72	80	1	3	C	C	3.5	0	10	3					5				95									
19	1	1.97	1	VLM	106	80	1	3	AJH	C	2	800	2	1		10		10	20			5	55									
20	1	2.7	1	VPH	286	76	1	3	IR	C	2.1	420	0.5	0	qtz se 1	10			60				30									
21	1	2.9	2	VLM	6	86	1	3	AJL	AJH	0.5	1200	0.5	0		70			5			10	15									

The rest of data including data from Reno Fw mine sector are included in the attached CD.

Appendix I.D Oriented Core Logging

Example of data from Reno Hw mine sector;

Location				Discontinuity								Mineralogical Infill												
id	Transverse	DIST (m)	Endpoints	Type	DIPDIR	DIP	Roughness	Thickness		Halo		Anh	Bt	Bo	Cpy	Ca	Ca*	Chl	Qtz	Mo	Py	Tu	Gyp	Mt
								max (mm)	min (mm)	Type	width (mm)													
1	1	0	0	VLM	270	18	6	3	1									10	75					
2	1	0.09	2	Fault	270	20	6	2	1			20		5	10	30			45					
3	1	0.09	0	VLM	326	50	6	2	<1						5			5	90					
4	1	0.14	0	VLM	338	43	8	1						10	5				85					
5	1	0.31	0	VLM	270	40	4	2						5	3				92					
6	1	0.36	2	VLM	45	20	8	1	1					5	15				80					
7	1	0.38	2	VLM	309	25	5	4	1					3					97					
8	1	0.47	0	VLM	107	40	5	2	1			5			3			10	82					
9	1	0.51	0	VLM	248	55	9	1							5			10	85					
10	1	0.52	0	VLM	259	65	5	2	1					3					97					
11	1	0.56	0	VLH	84	25	9	10	2	qtz se chl	20				25	10			35			30		
12	1	0.57	0	VLM	0	85	6	10	4					3	3			5	89					
13	1	0.61	0	Fault	56	80	5	2	1					5	25	10		15	45					
14	1	0.65	0	VLM	84	50	5	2	1			20							80					
15	1	0.68	2	VLM	248	50	5	1							5			5	90					
16	1	0.7	2	VLH	79	10	9	2	1	se chl	8			3	40			10	47					
17	1	0.8	0	VLM	259	65	5	1.5											100					
18	1	0.81	2	VLM	23	25	9	5	1				25	3				15	57					
19	1	0.98	2	VLM	326	40	5	1.5	<1						10				90					
20	1	0.95	2	VLM	349	30	9	1.5	<1						5				95					
21	1	0.92	2	VLM	11	35	9	1	<1			10			5				85					

The rest of data including data from Reno Fw mine sector and from all structural domains at the Esmeralda mine sector are included in the attached CD.

Appendix I.E Un-Oriented Core Logging

Example of data from Reno Hw mine sector;

Core Section Location													All Discontinuity Frequency (m ⁻¹)				Weak Discontinuity Frequency (m ⁻¹)			
id1	id2	Rock Type	Core Section (ft)		Mine Coordinates						Orientation		Thickness mm	Fault	V PH	V LH	V LM	V PH	V LH	V LM
			from	To	East_j	North_j	z_j	East_f	North_f	z_f	Plunge	Trend								
1.0	DDH1054	Andesite	220	240	1091	890	2274	1096	890	2269	45	263.5	< 1	0.00	0.00	0.00	20.67	0.00	0.00	4.84
1.0	DDH1054	Andesite	220	240	1091	890	2274	1096	890	2269	45	263.5	1<=x<2	0.00	0.16	0.00	13.62	0.00	0.00	1.72
1.0	DDH1054	Andesite	220	240	1091	890	2274	1096	890	2269	45	263.5	>=2	0.00	0.66	0.00	6.73	0.33	0.00	0.57
1.0	DDH1054	Andesite	220	240	1091	890	2274	1096	890	2269	45	263.5	all	0.00	0.82	0.00	41.01	0.33	0.00	7.14
2.0	DDH1062	Andesite	360	380	949	941	2245	944	941	2241	46	83.5	< 1	0.00	1.31	0.00	33.46	0.82	0.00	4.10
2.0	DDH1062	Andesite	360	380	949	941	2245	944	941	2241	46	83.5	1<=x<2	0.00	3.12	0.16	13.12	2.95	0.16	4.18
2.0	DDH1062	Andesite	360	380	949	941	2245	944	941	2241	46	83.5	>=2	0.00	0.82	0.66	4.43	0.49	0.16	1.64
2.0	DDH1062	Andesite	360	380	949	941	2245	944	941	2241	46	83.5	all	0.00	5.25	0.82	51.02	4.27	0.33	9.92
3.0	DDH1062	Andesite	640	660	888	935	2186	883	934	2182	46	83.5	< 1	0.00	0.49	0.00	26.08	0.49	0.00	2.95
3.0	DDH1062	Andesite	640	660	888	935	2186	883	934	2182	46	83.5	1<=x<2	0.00	0.16	0.00	10.33	0.16	0.00	0.66
3.0	DDH1062	Andesite	640	660	888	935	2186	883	934	2182	46	83.5	>=2	0.00	0.00	0.00	6.73	0.00	0.00	0.33
3.0	DDH1062	Andesite	640	660	888	935	2186	883	934	2182	46	83.5	all	0.00	0.66	0.00	43.14	0.66	0.00	3.94
4.0	DDH1073	Andesite	260	280	982	1018	2276	987	1018	2272	55	263.5	< 1	0.16	0.16	0.00	22.31	0.16	0.00	3.44
4.0	DDH1073	Andesite	260	280	982	1018	2276	987	1018	2272	55	263.5	1<=x<2	0.00	0.16	0.00	6.89	0.00	0.00	0.41
4.0	DDH1073	Andesite	260	280	982	1018	2276	987	1018	2272	55	263.5	>=2	0.00	0.82	0.16	3.94	0.08	0.00	0.66
4.0	DDH1073	Andesite	260	280	982	1018	2276	987	1018	2272	55	263.5	all	0.16	1.15	0.16	33.14	0.25	0.00	4.51
5.0	DDH1073	Andesite	480	500	1037	1024	2237	1042	1025	2234	55	263.5	< 1	0.49	0.00	0.00	21.16	0.00	0.00	3.12
5.0	DDH1073	Andesite	480	500	1037	1024	2237	1042	1025	2234	55	263.5	1<=x<2	0.00	0.82	0.00	6.73	0.49	0.00	1.23
5.0	DDH1073	Andesite	480	500	1037	1024	2237	1042	1025	2234	55	263.5	>=2	0.00	0.82	0.16	6.56	0.00	0.16	0.57
5.0	DDH1073	Andesite	480	500	1037	1024	2237	1042	1025	2234	55	263.5	all	0.49	1.64	0.16	34.45	0.49	0.16	4.92
7.0	DDH1077A	Andesite	260	280	888	1007	2247	886	1007	2241	21	83.5	< 1	0.00	0.16	0.16	27.40	0.08	0.08	2.87
7.0	DDH1077A	Andesite	260	280	888	1007	2247	886	1007	2241	21	83.5	1<=x<2	0.16	0.33	1.15	13.29	0.33	0.82	3.28
7.0	DDH1077A	Andesite	260	280	888	1007	2247	886	1007	2241	21	83.5	>=2	0.00	0.16	0.98	5.58	0.16	0.16	1.56
7.0	DDH1077A	Andesite	260	280	888	1007	2247	886	1007	2241	21	83.5	all	0.16	0.66	2.30	46.26	0.57	1.07	7.71

The rest of core data are included in the attached CD.

Appendix I.F Caved Rock Block Data

Example of data from Reno Hw mine sector;

id	id Block	Block Volume	Face Id	Type	Thickness (mm)			Infill Features													Failure Mode				
					min	max	Real	qtz	cpy	anh	mo	chl	bt	tu	bo	mt	ser	ca & ca*	py	gyp					
1	C06-Z29F-01	0.298	1	VLM	<1			50	50																C1
2	C06-Z29F-01	0.298	2	VPH	1.0	3.0		15	35		10	40													C2
3	C06-Z29F-01	0.298	3	VPH	1.0	1.0		25	35	25		15													C2
4	C06-Z29F-01	0.298	4	VPH	<1	1.0		30	15	15	20	20													Vi
5	C06-Z29F-01	0.298	5	VPH	1.0	1.5	1.5	35	45	20															C2
6	C06-Z29F-01	0.298	6	VPH	1.0	1.5		30	10	35		25													C2
7	C06-Z29F-01	0.298	7	VLH	5.0	1.0		20	25	20		10						25							C2
8	C06-Z29F-01	0.298	8	VLM	<1	1.5	1.5		13	87															Vi
9	C06-Z29F-01	0.298	9	V																					-
10	C06-Z29H-02	0.022	1	VLM	<1	1.0			6			57	37												C1
11	C06-Z29H-02	0.022	2	VLM	1.0	1.5		10	20	50		20													C2
12	C06-Z29H-02	0.022	3	IR																					
13	C06-Z29H-02	0.022	4	VLM	3.0	4.0		10	15	45	5	25													C2
14	C06-Z29H-02	0.022	5	VLM	3.0	4.0		10	15	45	5	25													C2
15	C06-Z29H-02	0.022	6	VLM	3.0	4.0		10	15	45	5	25													C2
16	C06-Z29H-02	0.022	7	VLM	<1	1.0			6			57	37												C1
17	C06-Z29H-02	0.022	8	VLM	1.0	1.0			15	65								20							C2
18	C06-Z30F-01	0.043	1	VLH	3.0	7.0		33	12	22		33													C2
19	C06-Z30F-01	0.043	2	VLH	1.5	2.0		10	65	20		5													Vi

The rest of core data are included in the attached CD.

APPENDIX II

Additional data analysis;

- A. Fault and veins orientations observed in sub-vertical small diameter cores
- B. Set definition for veins type
- C. Infill of LM, PH and LH veins and Faults
- D. Thicknesses of LM, PH and LH veins and Faults

Appendix II.A Fault and Veins Orientations Observed in Sub-Vertical Cores

Additional fault orientation data collected in both Reno and Esmeralda mine sectors using sub-vertical small diameter either oriented or un-oriented cores are presented as follows.

Fault orientation data collected in cores from Reno mine sector included 3 small diameter (62 mm) oriented cores (Figure II.A1c) and 4 small diameter (62 mm) un-oriented cores (Figure II.A1d). All of them have approximately between 50 and 70 meters long.

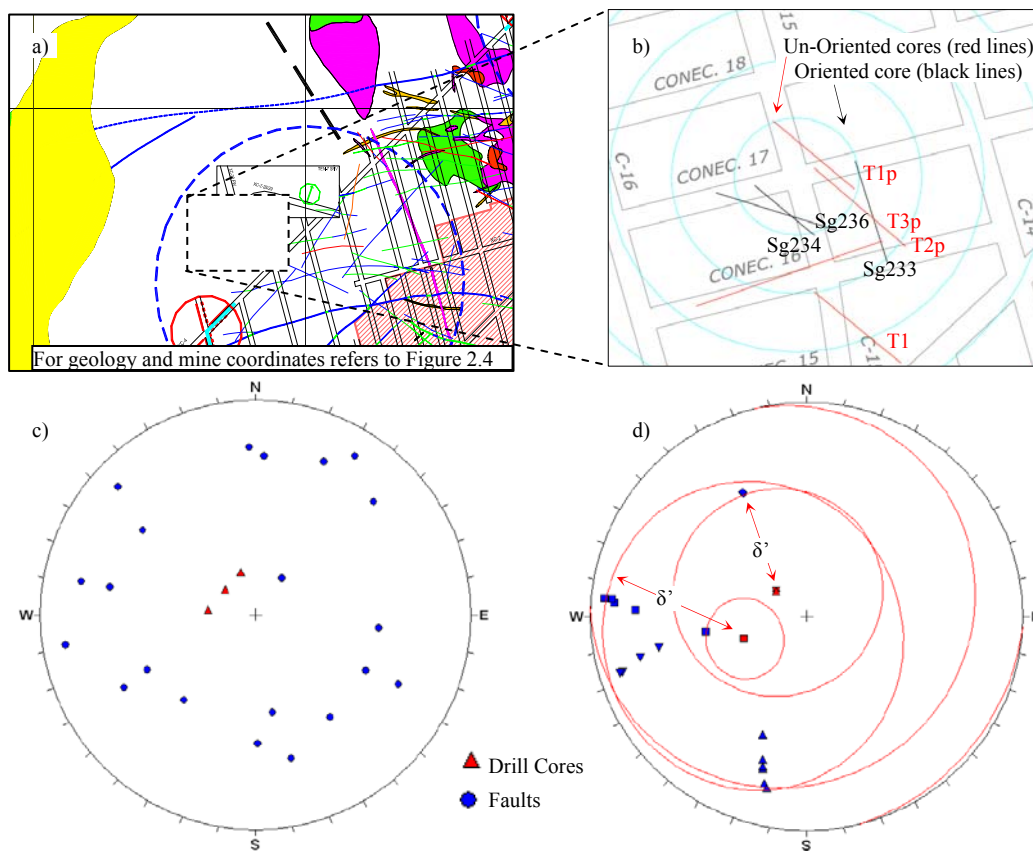


Figure II.A1. Fault orientations observed in both oriented (c) and un-oriented (d) small diameter drill cores located at the Reno mine sector (plan views a & b). Data are plotted in the lower hemispheric projection, for d) only the apparent dip angle (δ') between core orientation and vector normal to faults (pole) is shown.

Figure II.A1 is showing that sub-vertical fault orientations are the most common feature of faults at the Reno mine sector.

Table II.A1. Raw data from small diameter oriented core logging (Reno mine sector)

ID	Orient1	Orient2	Traverse	DIST(M)	TYPE
1	25	270	2	20.77	Fault
2	25	180	2	23.82	Fault
3	30	18	2	25.9	Fault
4	25	163	2	26.07	Fault
5	10	162	2	26.56	Fault
6	25	120	2	27.94	Fault
7	55	77	2	36.83	Fault
8	45	45	2	37.87	Fault
9	50	354	2	45.14	Fault
10	60	210	2	47.19	Fault
11	90	0	2		Core Sg23
12	30	138	3	8	Fault
13	29	356	3	14	Fault
14	32	32	3	15.85	Fault
15	23	257	3	16	Fault
16	27	279	3	20.5	Fault
17	48	81	3	32.55	Fault
18	36	298	3	42.3	Fault
19	40	149	3	43.35	Fault
20	16	273	3	43.85	Fault
21	50	3	3	47.4	Fault
22	90	0	3		Core Sg23
23	25	194	4	17.45	Fault
24 *	90	0	4		Core 236

Note; dip: Orient1, dipdir: Orient2

Table II.A2. Raw data from small diameter un-oriented core logging (Reno mine sector)

ID	Orient1	Orient2	Traverse	DIST(M)	TYPE
1	50	330	1	33.03	Fault T2p
2	49	330	1	33.9	Fault T2p
3	90	0	1		Core T2p
4	35	330	2	66.83	Fault T3p
5	30	330	2	66.91	Fault T3p
6	34	330	2	66.94	Fault T3p
7	45	330	2	67.01	Fault T3p
8	75	330	2	67.23	Fault T3p
9	90	0	2		Core T3p
10	20	60	1	8.1	Fault T1
11	31	60	1	16.7	Fault T1
12	40	60	1	27.23	Fault T1
13	19	60	1	58	Fault T1
14	90	0	1		Core T1
15	14	120	1	22.2	Fault T1p
16	21	120	1	27.43	Fault T1p
17	35	120	1	9.98	Fault T1p
18	12	120	1	46.21	Fault T1p
19	25	120	1	34.47	Fault T1p
20	22	120	1	41.20	Fault T1p
21	90	0	1		Core T1p

Note; dip: Orient1, dipdir: Orient2

Additional fault and veins orientation collected from core of Esmeralda mine sector included 3 small diameter (62 mm) oriented cores (Figure II.A2b) located about 200 meters below the undercut level (Harrison 2009). Each drill core has 100 meters long.

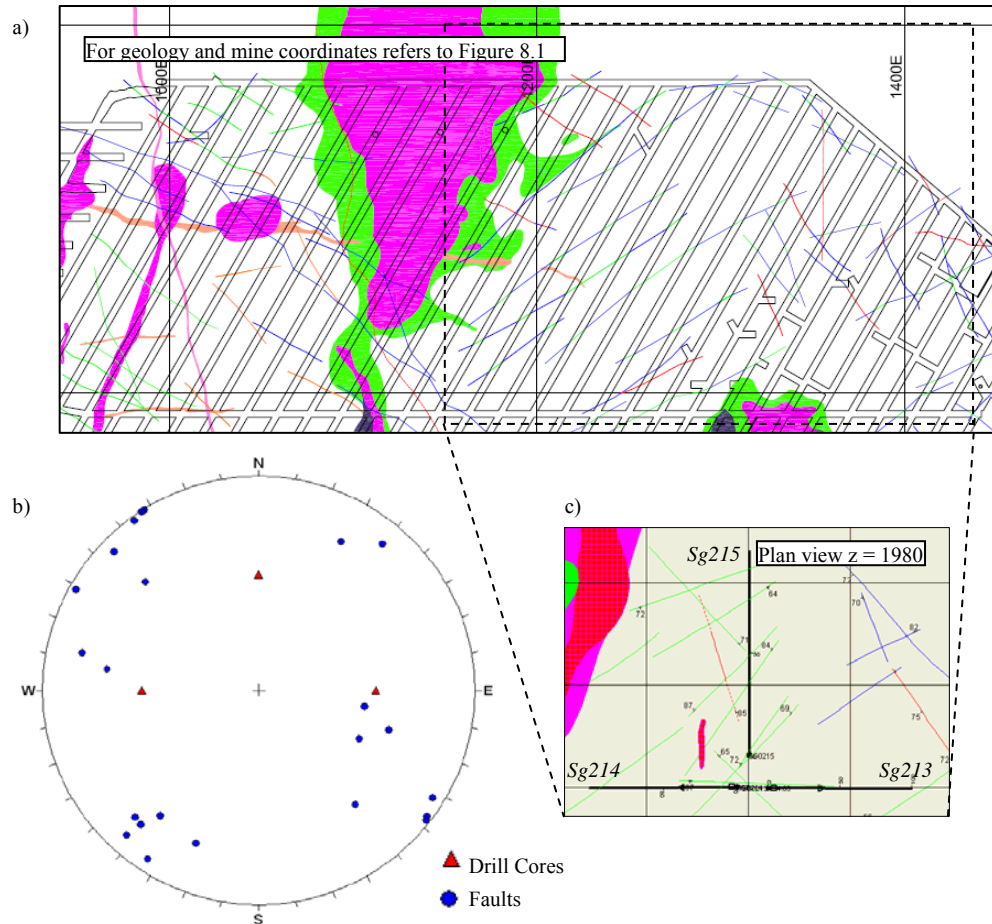


Figure II.A2. Fault orientations observed in small diameter oriented (b) cores located at the Esmeralda mine sector (a). Data from Harrison (2009) are plotted in the lower hemispheric projection.

Figure II.A2 is showing that sub-vertical fault orientations are the most common feature of faults at the Esmeralda mine sector as well.

Table II.A3. Raw data from small diameter oriented core logging (Reno mine sector)

ID	Orient1	Orient2	Traverse	DIST(M)	TYPE
1	36	273	6	17.326	Fault Sg213
2	50	87	10	29.794	Fault Sg213
3	90	0	103		Core Sg213
4	42	289	40	17.626	Fault Sg214
5	30	46	41	18.439	Fault Sg214
6	17	310	43	24.399	Fault Sg214
7	47	277	44	27.665	Fault Sg214
8	61	24	45	30.639	Fault Sg214
9	27	65	45	30.696	Fault Sg214
10	44	290	47	38.039	Fault Sg214
11	73	25	48	40.611	Fault Sg214
12	5	14	51	48.792	Fault Sg214
13	22	67	51	48.815	Fault Sg214
14	6	198	52	52.000	Fault Sg214
15	37	60	55	61.527	Fault Sg214
16	31	37	63	86.746	Fault Sg214
17	66	22	64	87.551	Fault Sg214
18	35	296	67	96.940	Fault Sg214
19	270	0	104		Core Sg214
20	41	279	69	0.265	Fault Sg215
21	56	76	74	15.170	Fault Sg215
22	57	267	79	30.672	Fault Sg215
23	37	274	93	73.315	Fault Sg215
24	38	234	93	73.366	Fault Sg215
25	28	265	96	82.345	Fault Sg215
26 *	360	0	105		Core Sg215

Note: dip: Orient1, dipdir: Orient2

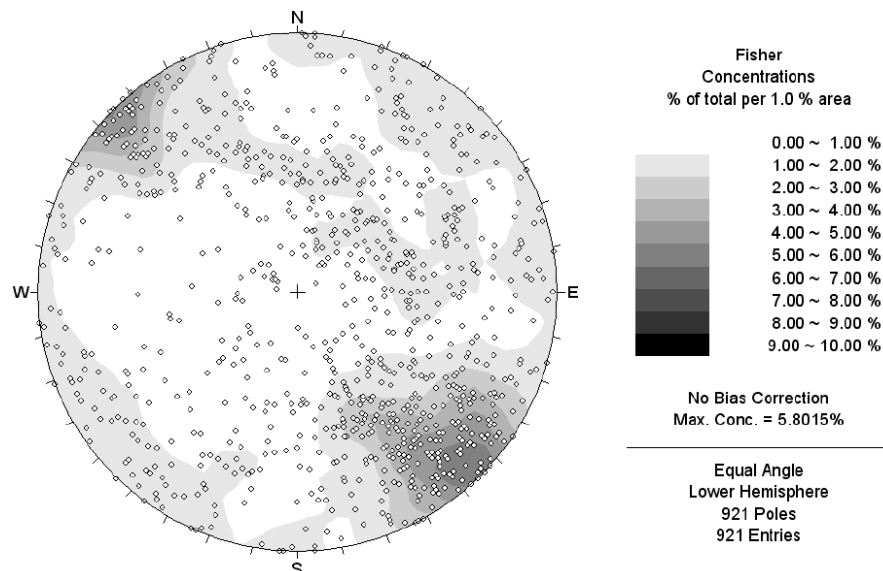


Figure II.A3. Veins orientations observed in three small diameter oriented cores located at the Esmeralda mine sector. Data from Harrison (2009) are plotted in the lower hemispheric projection.

Appendix II.B Set Definitions for Vein Types in Reno Mine Sector

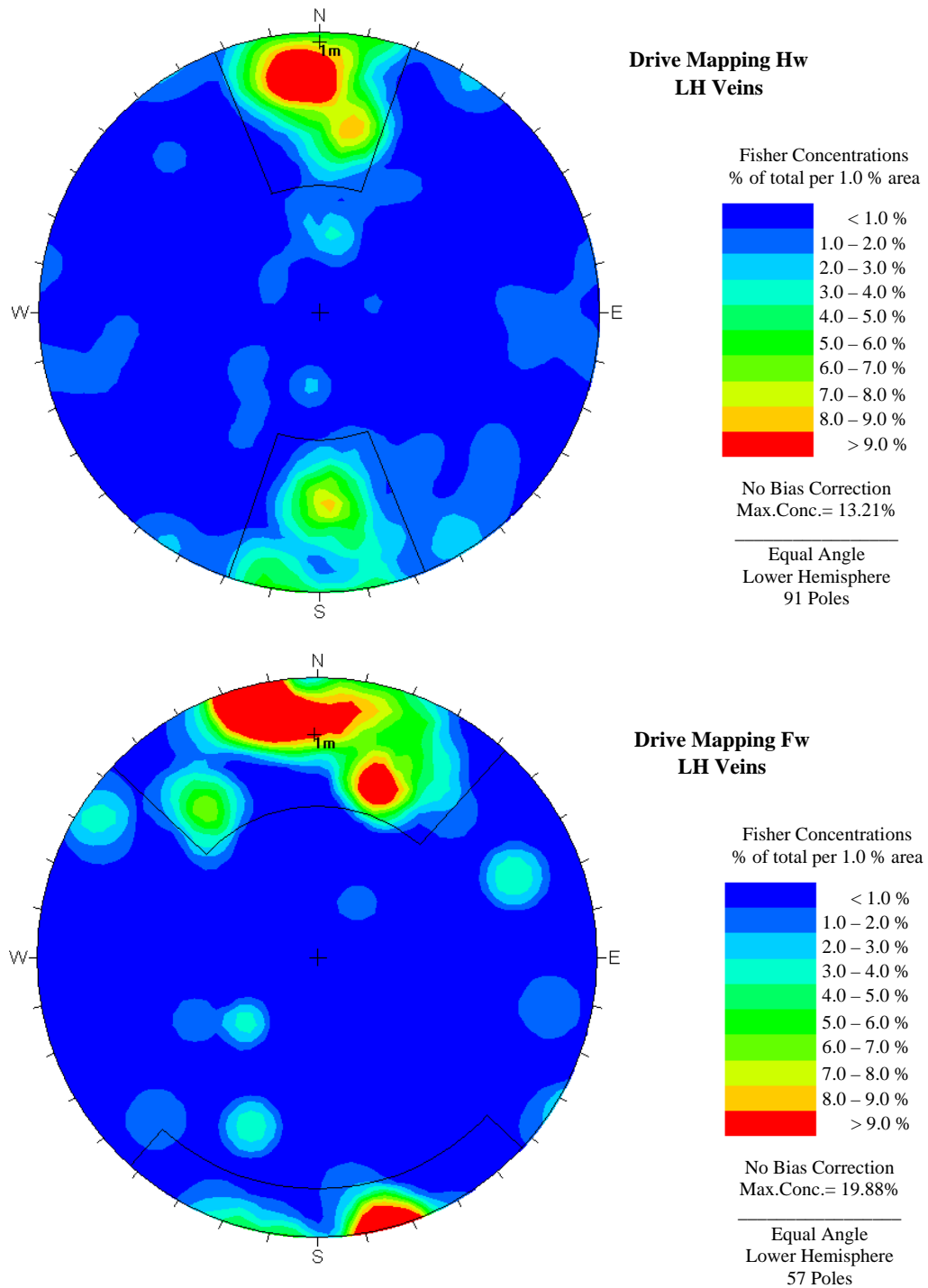


Figure B1. Plot contour and set definition using equal area lower hemispheric projection for LH veins observed in drive mapping.

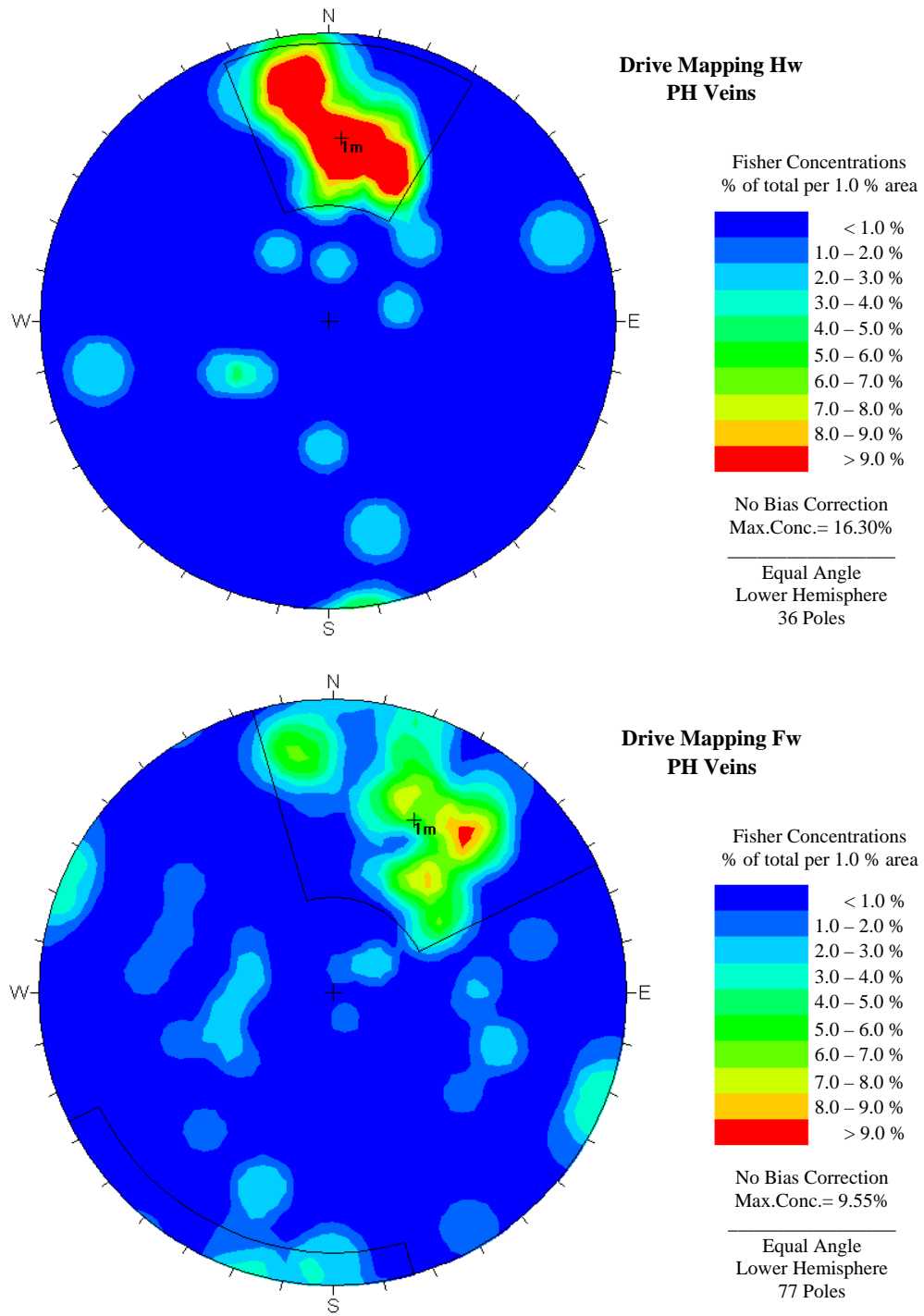


Figure B2. Plot contour and set definition using equal area lower hemispheric projection for PH veins observed in drive mapping.

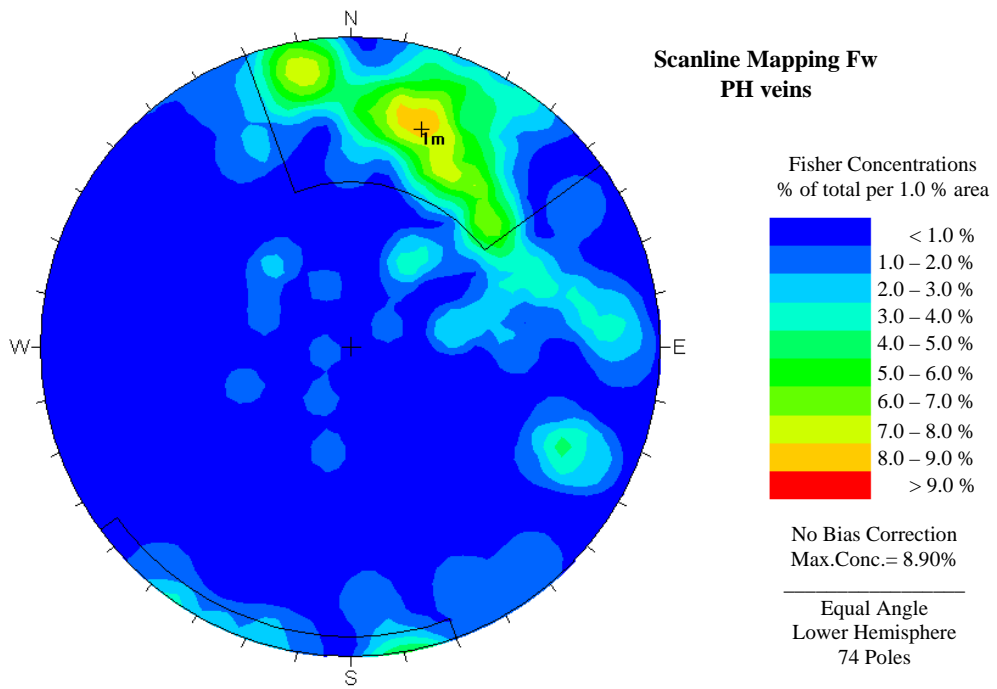


Figure B3. Plot contour and set definition using equal area lower hemispheric projection for PH veins observed in scanline mapping.

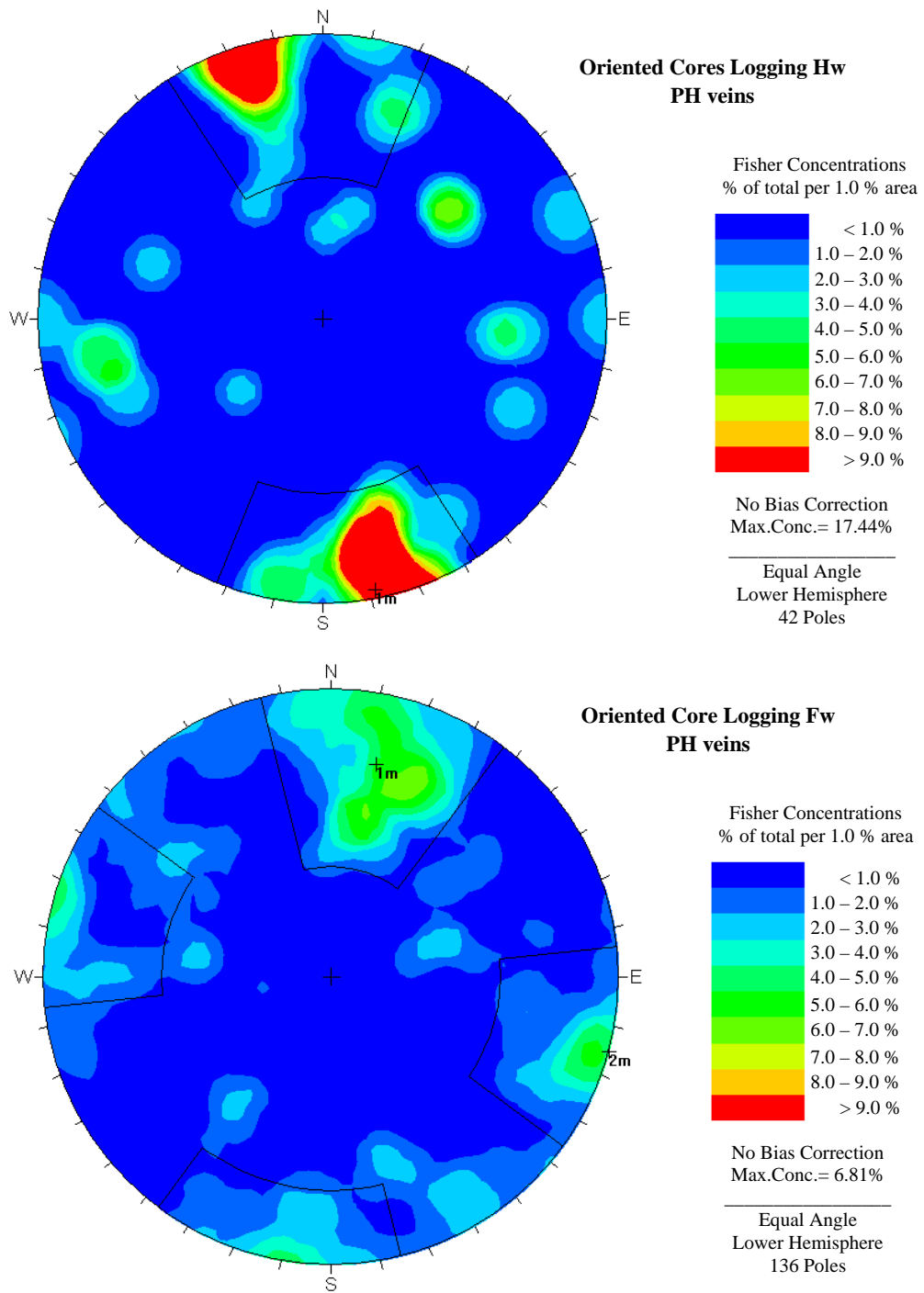


Figure B4. Plot contour and set definition using equal area lower hemispheric projection for PH veins observed in large diameter oriented core logging.

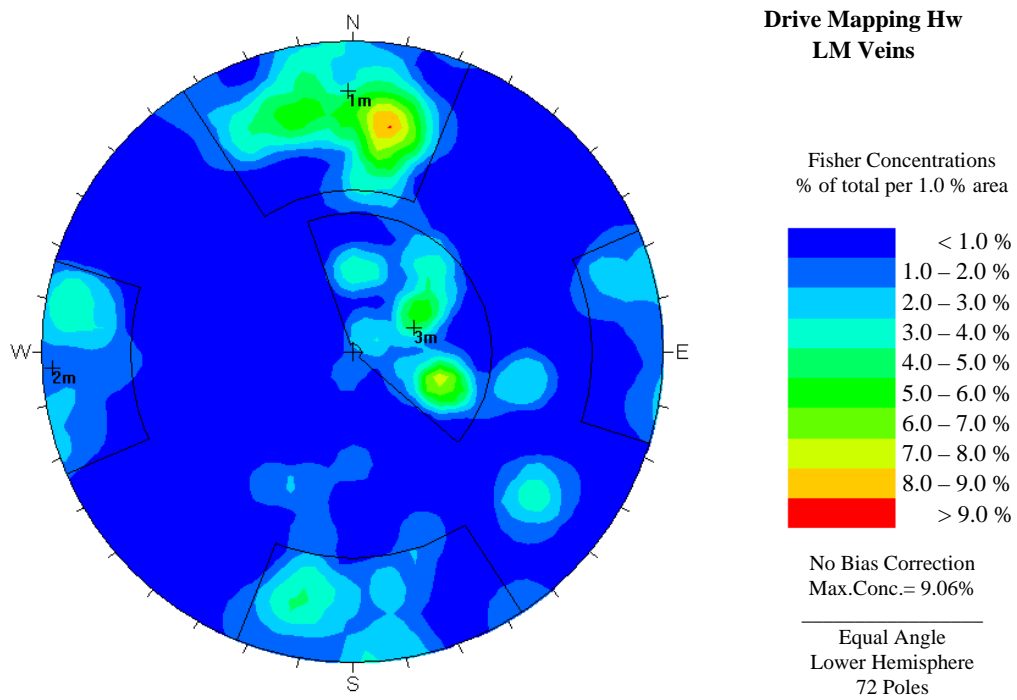


Figure B5. Plot contour and set definition using equal area lower hemispheric projection for LM veins observed in drive mapping.

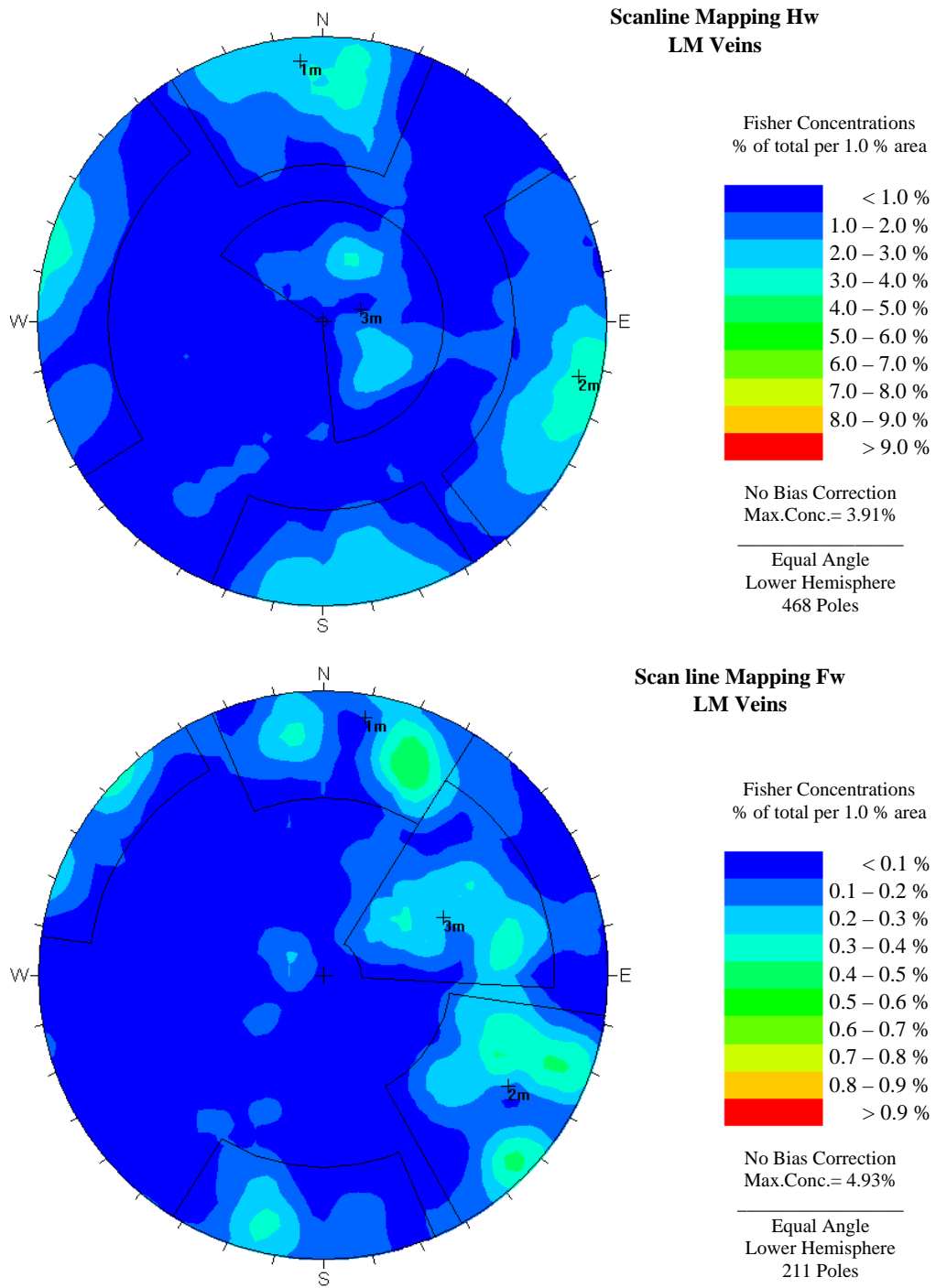


Figure B6. Plot contour and set definition using equal area lower hemispheric projection for LM veins observed in scanline mapping.

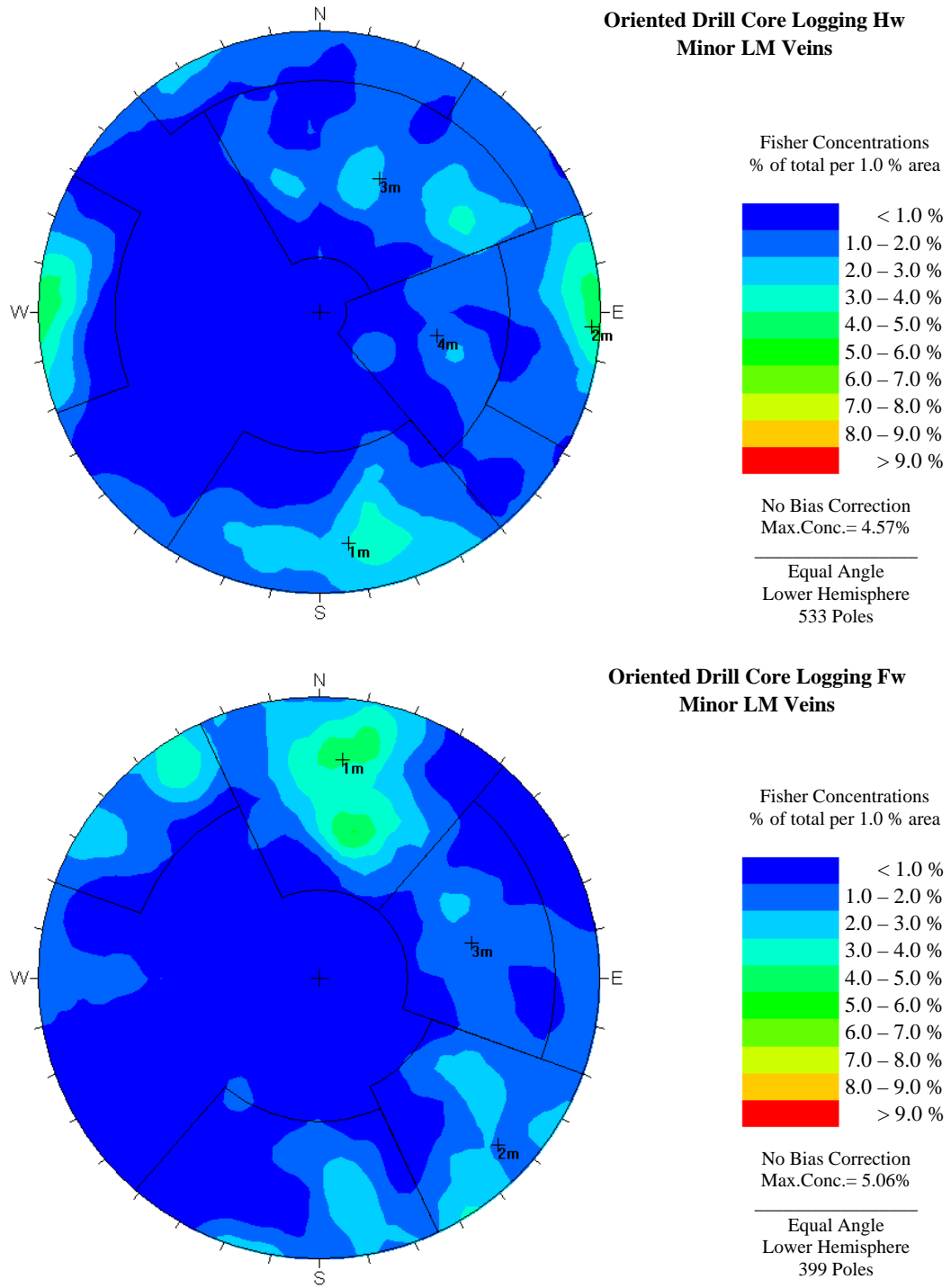


Figure B7. Plot contour and set definition using equal area lower hemispheric projection for LM veins observed in large diameter oriented core logging.

Appendix II.C Infill of Faults and LH, PH and LM veins in Reno Mine Sector

Observed discontinuity infill features as a combined number that represents the average mineral infill recognised only within veins that contain this particular mineral. For example; 27₍₄₅₎. This combined number means that 27% is the mean mineral infill contained in only 45% of some particular discontinuity set or type. The total mean discontinuity infill then result by multiplying these two numbers, 27x0.45= 12.2%.

Table II.C1. Observed infill features in LM vein type for different mapping scale in Reno mine sector

Discontinuity type	Mapping Scale	Set number	Sectors Studied	Dip / Dipdir	n	Infill of Discontinuities								
						Mineral average percentage as infill (percentage of discontinuities with this mineral)								
						Biotite	Chlorite	Anhydrite	Bornite	Chalcopyrite	Pyrite	Quartz	Other traces minerals	
LM Veins	Scanlines Mapping	Set 1	Hw	85/175	117	m	12 (51)	30 (65)	6 (53)	10 (82)	tr	68 (91)	Molybdenite	
		Set 2		85/282	123	m	15 (66)	27 (87)	6 (38)	15 (77)	tr	56 (87)	Molybdenite	
		Set 3		16/252	117	tr	12 (52)	20 (60)	6 (38)	10 (73)	tr	73 (97)	Molybdenite	
		Random			111	m	13 (55)	23 (77)	6 (46)	11 (85)	tr	63 (95)	Molybdenite	
		Total & Average				468	m	13 (57)	25 (73)	6 (44)	11 (79)	tr	65 (93)	Molybdenite
		Set 1	Fw	85/191	50	tr	17 (62)	29 (84)	tr	17 (96)	m	49 (88)	Molybdenite	
		Set 2		74/301	58	m	18 (83)	27 (95)	tr	23 (98)	m	37 (88)	Molybdenite	
		Set 3		48/244	61	tr	17 (69)	24 (75)	tr	22 (92)	m	44 (98)	Molybdenite, Sericite	
		Random			42	tr	17 (81)	33 (95)	tr	22 (90)	m	41 (79)	Molybdenite, Sericite	
		Total & Average				211	tr	17 (81)	33 (95)	tr	22 (90)	m	41 (79)	Molybdenite, Sericite
	Oriented Drill Cores Logging	Hw	Set 1	79/353	132	m	12 (35)	m	m	17 (81)	tr	75 (99)	Molybdenite, Magnetite	
			Set 2	88/273	93	m	10 (57)	16 (33)	3 (57)	8 (77)	tr	76 (99)	Molybdenite, Magnetite	
			Set 3	55/204	155	24 (39)	15 (30)	m	4 (40)	8 (74)	tr	76 (99)	Molybdenite, Magnetite	
			Set 4	46/281	69	m	11 (39)	m	m	6 (79)	tr	75 (99)	Molybdenite	
			Random		83	m	18 (36)	11 (25)	4 (54)	8 (84)	-	78 (96)	Molybdenite	
		Total & Average				532	22 (25)	13 (38)	m	4 (48)	10 (79)	tr	77 (98)	Molyb., Magnetite
		Fw	Set 1	76/186	176	16 (37)	22 (86)	22 (70)	-	17 (98)	9 (32)	41 (95)	Molyb., Tourmaline, Magnetite	
			Set 2	82/313	84	9 (27)	21 (63)	34 (58)	tr	16 (89)	m	49 (86)	Tourmaline, Magnetite	
			Set 3	58/257	58	13 (37)	19 (74)	17 (69)	-	17 (100)	6 (43)	50 (91)	Molybdenite, Magnetite	
			Random		81	16 (37)	20 (73)	30 (75)	tr	19 (97)	m	43 (83)	Molyb., Tourmaline, Magnetite	
Total & Average				399	15 (35)	21 (77)	25 (69)	tr	18 (96)	9 (27)	44 (90)	Molyb., Tour., Mag.		

Note: **m**; minor frequency (mineral infill observed in less than 25% of discontinuity set). **tr**; traces (mineral infill observed in less than 10% of discontinuity set)

Table II.C2. Observed infill features in faults, PH and LH vein types for different mapping scale in Reno mine sector

Discontinuity type	Mapping Scale	Set number	Sectors Studied	Dip / Dipdir	n	Infill of Discontinuities								
						Mineral average percentage as infill (percentage of discontinuities with this mineral)								
						Biotite	Chlorite	Anhydrite	Bornite	Chalcopyrite	Pyrite	Quartz	Other traces minerals	
PH Veins	Scanlines Mapping	Random	Hw		28	-	tr	14 (54)	-	75 (100)	tr	21 (82)		
		Set 1	Fw	73/198	39	-	m	19 (79)	-	60 (95)	24 (41)	20 (85)		
		Random			35	-	m	19 (77)	-	63 (100)	20 (29)	16 (83)		
		Total & Average				74	-	m	19 (78)	-	62 (97)	23 (35)	18 (84)	
	Oriented Cores Logging	Set 1	Hw	88/349	26	-	tr	m	-	80 (96)	tr	22 (92)		
		Random			16	-	m	m	-	74 (94)	tr	27 (94)		
		Total & Average				42	-	m	m	-	78 (94)	tr	24 (93)	
		Set 1	Fw	74/192	57	-	9 (32)	13 (79)	-	61 (98)	22 (56)	16 (91)	Molybdenite	
		Set 2		90/285	26	-	20 (42)	24 (77)	-	54 (100)	10 (38)	20 (65)	Magnetite	
		Random			53	tr	12 (40)	20 (72)	-	58 (98)	16 (45)	20 (74)	Molybdenite, Magnetite	
Total & Average				136	tr	13 (37)	18 (76)	-	59 (99)	18 (49)	18 (79)	Molyb., Magnetite		
						Calcite	Chlorite	Anhydrite	Bornite	Chalcopyrite	Ankerite	Quartz	Other minerals	
LH Veins	Scanlines Mapping	Random	Hw		15	22 (47)	14 (47)	15 (60)	19 (80)	33 (80)	26 (27)	20 (80)	Molybdenite, Gypsum	
			Fw		11	21 (73)	18 (55)	20 (91)	47 (27)	19 (82)	-	30 (64)	Molyb., Gypsum, Pyrite, Tour.	
	Oc Logging	Random	Fw		29	tr	32 (72)	m	m	23 (79)	47 (76)	42 (34)	Pyrite, Tourmaline	
			Hw		19	46 (63)	18 (84)	22 (68)	-	11 (89)	28 (32)	18 (58)	Molyb. Gypsum, Pyrite, Tour.	
						Gypsum	Chlorite	Calcite	Anhydrite	Chalcopyrite	Amkerite	Quartz	Other minerals	
Faults	Scanlines Mapping	Random	Hw		10	m	14 (70)	51 (70)	24 (60)	10 (70)	20 (20)	23 (60)	Molybdenite, Bornite	
			Fw		23	18 (26)	21 (96)	48 (35)	23 (52)	20 (83)	33 (39)	16 (30)	Molybdenite, Bornite	
	Oc. Logging	Random	Hw		2	-	-	-	-	-	-	-		
			Fw		11	17 (63)	21 (82)	26 (55)	25 (55)	13 (91)	56 (36)	15 (36)	Molybdenite, Tourmaline	

Note: **m**; minor frequency (mineral infill observed in less than 25% of discontinuity set). **tr**; traces (mineral infill observed in less than 10% of discontinuity set)

Appendix II.D Thicknesses of Faults and LH, PH and LM veins in Reno Mine Sector

Table II.D1. Observed thickness distributions in Faults and LH vein type for different mapping scale in Reno mine sector

Discontinuity type	Mapping Scale	Set's number	Sectors Studied	Dip / Dipdir	Data's Number	Observed thickness distribution (%)											
						<1mm	1mm	2mm	3mm	4mm	5mm	6mm	7mm	8mm	9mm	≥ 10mm	
Faults	Drive Mapping	Set 1	Hw	82/172	18	-	-	16.7	38.9	5.6	11.1	-	-	-	16.7	11.1	
			Fw	84/203	31	-	3.2	9.7	19.4	6.5	32.3	3.2	-	9.7	12.9	3.2	
		Set 2	Hw	76/316	11	-	18.2	9.1	9.1	9.1	36.4	-	-	9.1	9.1	-	
			Fw	88/144	22	-	-	9.1	13.6	4.5	9.1	-	9.1	9.1	18.2	27.3	
		Random	Hw		11	-	18.2	18.2	9.1	27.3	9.1	-	-	9.1	-	9.1	
			Fw		10	-	-	30.0	20.0	20.0	-	10.0	-	-	-	20.0	
	Total & Average					103	-	4.9	13.6	19.4	9.7	18.4	1.9	1.9	6.8	11.7	11.7
	Scanlines Mapping	Random	Hw		10	20.0	-	20.0	10.0	-	20.0	-	-	10.0	-	20.0	
			Fw		23	52.2	26.1	4.3	4.3	4.3	4.3	-	4.3	-	-	-	
			Total & Average					33	15.2	39.3	15.2	6.1	3.0	9.1	-	3.0	3.0
	Oc Core Logging	Random	Fw		2	-	100.0	-	-	-	-	-	-	-	-	-	
			Hw		11	17.4	52.2	13.0	4.3	-	-	-	-	-	-	-	
			Total & Average					13	15.4	53.8	15.4	15.4	-	-	-	-	-
LH Veins	Drive Mapping	Set 1	Hw	88/180	57	-	3.5	14.0	17.5	8.8	17.5	3.5	7.0	3.5	8.8	15.8	
			Fw	77/179	45	-	8.9	17.8	20.0	13.3	13.3	2.2	-	6.7	8.9	8.9	
		Random	Hw		34	-	8.8	11.8	23.5	8.8	8.8	-	2.9	2.9	20.6	11.8	
			Fw		12	-	16.7	25.0	25.0	16.7	8.3	-	8.3	-	-	-	
	Total & Average					148	-	7.4	15.5	20.3	10.8	13.5	2.0	4.1	4.1	10.8	11.5
	Scanlines Mapping	Random	Hw		15	-	13.3	20.0	33.3	20.0	6.7	-	-	-	-	6.7	
			Fw		11	9.1	36.4	18.2	9.1	9.1	9.1	-	-	9.1	-	-	
			Total & Average					26	3.8	23.1	19.3	23.1	15.4	7.7	-	-	3.8
	Oc Core Logging	Random	Hw		29	41.4	31.0	3.5	6.9	-	-	10.3	-	-	-	6.9	
			Fw		17	29.4	52.9	5.9	-	-	5.9	5.9	-	-	-	-	
			Total & Average					46	39.1	37.1	4.3	4.3	-	2.2	8.7	-	-

Table II.D2. Observed thickness distributions in PH vein type for different mapping scale in Reno mine sector

Discontinuity type	Mapping Scale	Set's number	Sectors Studied	Dip / Dipdir	Data's Number	Observed thickness distribution (%)											
						<1mm	1mm	2mm	3mm	4mm	5mm	6mm	7mm	8mm	9mm	≥ 10mm	
PH Veins	Drive Mapping	Set 1	Hw	65/184	26	-	7.7	15.4	7.7	23.1	11.5	3.8	3.8	11.5	15.4	-	
			Fw	66/205	48	-	10.4	6.3	25.0	8.3	12.5	10.4	4.2	6.3	16.7	-	
		Random	Hw		10	-	-	20.0	30.0	10.0	10.0	-	10.0	20.0	-	-	
			Fw		29	-	3.4	20.7	20.7	13.8	20.7	3.4	-	-	17.2	-	
		Total & Average					113	-	7.1	13.3	20.4	13.3	14.1	6.2	3.5	7.1	15.0
	Scanlines Mapping	Set 1	Fw	73/198	39	15.4	46.2	10.3	17.9	5.1	2.6	-	-	2.6	-	-	
		Random	Hw		27	18.5	44.4	14.8	14.8	3.7	-	-	3.7	-	-	-	
			Fw		35	14.3	40.0	22.9	14.3	5.7	2.9	-	-	-	-	-	
		Total & Average					101	15.8	43.6	15.8	15.8	5.0	2.0	-	1.0	1.0	-
	Oc Core Logging	Set 1	Hw	88/349	26	23.1	65.4	3.8	7.7	-	-	-	-	-	-	-	
			Fw	74/192	51	26.8	32.1	25.0	7.1	1.8	1.8	-	-	3.6	-	1.8	
		Set 2	Fw	90/285	26	-	80.8	11.5	3.8	-	3.8	-	-	-	-	-	
		Random	Hw		15	20.0	46.7	26.7	-	6.7	-	-	-	-	-	-	
			Fw		51	23.5	56.9	7.8	7.8	2.0	-	2.0	-	-	-	-	
		Total & Average					174	20.7	52.9	14.9	6.4	1.7	1.1	0.6	-	1.1	-

Table II.D3. Observed thickness distributions in LM vein type for different mapping scale in Reno mine sector

Discontinuity type	Mapping Scale	Set's number	Sectors Studied	Dip / Dipdir	Data's Number	Observed thickness distribution (%)											
						<1mm	1mm	2mm	3mm	4mm	5mm	6mm	7mm	8mm	9mm	≥ 10mm	
LM Veins	Drive Mapping	Set 1	Hw	80/179	29	-	-	3.4	10.3	6.9	24.1	-	-	3.4	17.2	34.5	
		Set 2		88/087	8	-	-	-	-	12.5	12.5	-	-	-	25.0	50.0	
		Set 3		24/248	23	-	-	-	-	-	13.0	-	-	-	21.7	65.2	
		Random			12	-	-	8.3	8.3	16.7	16.7	-	-	-	16.7	33.3	
			Fw		9	-	-	-	11.1	-	-	-	-	11.1	44.4	33.3	
	Total & Average					81	-	-	2.5	6.2	6.2	16.0	-	-	2.5	22.2	44.4
	Scanlines Mapping	Set 1	Hw	85/175	116	13.7	43.6	17.9	14.5	2.6	0.9	2.6	2.6	0.9	-	0.9	
			Fw	85/191	49	10.2	59.2	18.4	6.1	2.0	2.0	-	-	-	-	2.0	
		Set 2	Hw	85/282	117	10.0	63.3	9.2	6.7	1.7	0.8	2.5	-	0.8	0.8	4.2	
			Fw	74/301	59	22.0	50.8	15.3	6.8	3.4	1.7	-	-	-	-	-	
		Set 3	Hw	16/252	120	12.9	46.6	15.5	5.2	4.3	0.9	0.9	0.9	0.9	4.3	7.8	
			Fw	48/244	61	16.4	36.1	19.7	11.5	6.6	-	1.6	3.3	-	1.6	3.3	
		Random	Hw		111	13.5	46.8	17.1	8.1	3.6	2.7	2.7	-	1.8	0.9	2.7	
			Fw		42	9.5	66.7	16.7	-	2.4	-	2.4	-	-	-	2.4	
	Total & Average					675	13.3	50.6	15.7	8.0	3.3	1.2	1.8	0.9	0.7	1.2	3.3
	Oc Core Logging	Set 1	Hw	79/353	131	35.1	32.8	14.5	8.4	3.8	2.3	2.3	-	-	0.8	-	
			Fw	76/186	165	38.2	36.4	9.1	5.5	1.8	3.0	2.4	1.8	-	-	1.8	
		Set 2	Hw	88/273	88	22.7	46.6	19.3	4.5	1.1	1.1	1.1	1.1	-	-	2.3	
			Fw	82/313	82	20.7	46.3	9.8	4.9	2.4	9.8	-	1.2	-	1.2	3.7	
		Set 3	Hw	55/204	153	16.3	52.3	13.1	8.5	3.9	2.0	0.7	-	-	0.7	2.6	
			Fw	58/257	57	26.3	47.4	17.5	5.3	-	1.8	-	-	-	-	1.8	
		Set 4	Hw	46/281	66	30.3	43.9	13.6	6.1	-	1.5	-	-	-	1.5	3.0	
		Random	Hw		83	22.9	43.4	14.5	9.6	3.6	3.6	1.2	-	1.2	-	-	
			Fw		81	21.0	43.2	18.5	9.9	4.9	-	1.2	-	-	1.2	-	
Total & Average					906	26.7	42.8	13.8	7.1	2.6	2.8	1.2	0.6	0.1	0.6	1.7	

APPENDIX III

Seismic and numerical model results data used in this thesis are attached in the CD, these are;

- A. Seismic Source Parameters
- B. Recorded Seismicity at the Esmeralda Mine Sector 1994-2003
- C. Model Results Data (Control points)

APPENDIX III A SEISMIC SOURCE PARAMETERS	290
III.A1 SEISMIC MONITORING AT THE EL TENIENTE MINE.....	290
III.A2 QUALITY AND INTEGRITY OF THE SEISMIC DATA.....	291
<i>III.A2.1 Location of Seismic Events</i>	291
<i>III.A2.2 Cave Geometry and Location Error</i>	293
III.A3 SEISMIC SOURCE PARAMETERS.....	295
<i>III.A3.1 Seismic Moment</i>	295
<i>III.A3.2 Seismic Energy</i>	296
<i>III.A3.3 Size and Stress Release Estimates</i>	298

Figures

Figure III.A1.- Array of seismic stations around the Esmeralda mine sector and their distance distribution plots' as reference (the blue block volume contain the seismic data used in this study).....	290
Figure III.A2.- Conceptual velocity model around caves used for ray tracing techniques (above). An example of ray path without (a) and with ray tracing technique. Adapted from Lynch (2006).....	294
Figure III.A3.- Absolute distance between locations considering different procedure to locate 7 large seismic events (adapted form ISS, 2007).	294
Figure III.A4.- Example of a spectral analysis of body waves. A seismogram in time domain (top), and S-wave displacement spectra in the frequency domain (bottom). After McGarr (1984).	297
Figure III.A5.- Empirical relationship between radiated energy and the scalar seismic moment at the Esmeralda mine sector.	298
Figure III.A6.- Relation between resisting stress and displacement for a fault slip (after McGarr 1999)	299

APPENDIX III A SEISMIC SOURCE PARAMETERS

III.A1 Seismic Monitoring at The El Teniente Mine

Seismicity has been recorded at the mine site since 1986. Initially, three different analogue systems were installed aiming to cover only the primary ore exploitation (Dunlop and Gaete, 1997). From 1992 a fully digital seismic system has been operating to cover the entire mine. During caving initiation, propagation and breakthrough at the Esmeralda mine sector around 29 remote seismic stations were operating. Each seismic station included a 4.5Hz triaxial geophone (Dunlop and Gaete, 2001).

The array of seismic stations around the Esmeralda mine sector is shown in Figure III.A1. This figure includes straight ray paths from sites to a reference point located at the centre of the undercut level. The same figure shows the distance distribution to the seismic stations from that reference point.

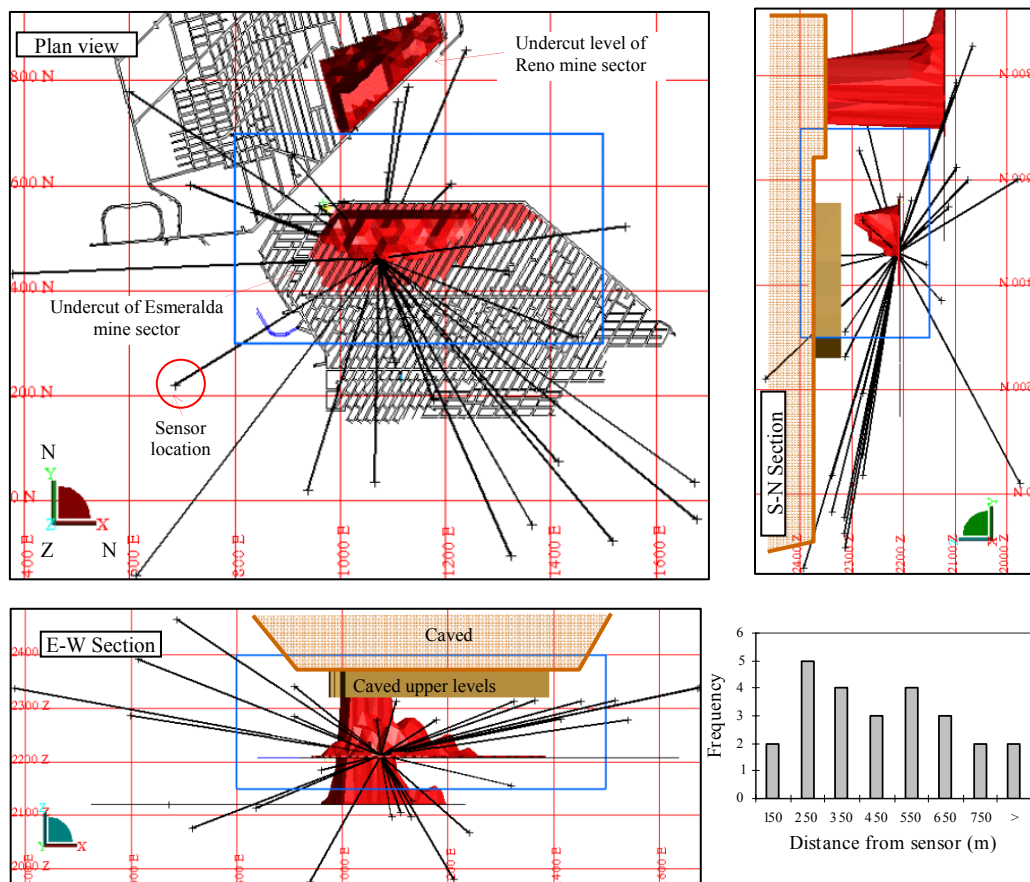


Figure III.A1.- Array of seismic stations around the Esmeralda mine sector and their distance distribution plots' as reference (the blue block volume contain the seismic data used in this study).

The seismic data used in this study comprise more than 100,000 events recorded between 1994 and 2005, blasting is excluded in this number. These data are contained in the block volume defined in mine coordinates as: 300-700 North; 800-1500 East; 2150-2400 Elevation (z), which is shown as a blue square in Figure III.A1.

III.A2 Quality and Integrity of the Seismic Data

The quality and the integrity of the seismic data at the El Teniente mine has been recently assessed by ISS International Limited as part of a seismological back analysis study of large seismic events at the Reno mine sector (ISS, 2007). Their study covered topics such as the consistency of the seismic recording, location of seismic events at Reno, estimates of the seismological source parameters and orientation of the seismic sensors.

The assessment included array sensitivity, events location, velocity model, site effects on sensors, attenuation (Q^1), and seismic source parameters. Except for the points discussed in the following sections, their main conclusions show acceptable quality and integrity of the recorded seismic data for the intended purposes according to Mendecki (1997). This also applies for the mine section being analysed in the present study².

As part of this study, a recommendation to correct sensor orientation information for some sensors was suggested (ISS, 2007). Event location determination and source parameter quantification do not require sensor orientation information. However, moment tensor estimation is only possible with accurate knowledge of a sensor orientation information (Mendecki, 1997), thus, moment tensor estimates used in this study have been determined based upon the sensor orientation corrections proposed by ISS (2007).

III.A2.1 Location of Seismic Events

The location of a seismic event is assumed to be a centre point within the seismic source, where the fracture initiates or propagates. Accurate location is of

¹ Dimensionless quantity known as Quality factor to account for natural attenuation to wave propagation through the rock mass (see Gibowicz and Kijko, 1994).

fundamental importance since, all subsequent seismological processing depend upon the location (Mendecki, 1997).

The event location can be described as vector with four unknowns as follow (Mendecki, 1997);

$$x = (h, t_0)^T = (x_0, y_0, z_0, t_0)^T \quad (\text{III.1})$$

where $h(x_0, y_0, z_0)$ is the location of the event in a coordinate system, and t_0 is the event origin time. Superscript T denotes waves travel times.

These four unknowns are retrieved from assessing the compressional wave (P-wave) and shear wave (S-wave) arrival times at the sensors in the array, plus the direction of the wave fronts. P and S waves arrival times are derived from the wave forms.

The accuracy in micro-seismic source location depends on the following main factors (Gibowick and Kijko, 1994, Mendecki, 1997):

- a. Accuracy of reading of seismic wave arrivals. Errors in arrival time determination can be originated from both automatic and manual selection. Sampling rate of instruments also introduce a lower bound of accuracy. Such form of errors cannot be entirely eliminated.
- b. Inadequate knowledge of the model velocity assumed for the media. In this respect, the general assumption of an isotropic and homogeneous media may influence the event location. In this case the existence of pre-existing voids affects the assumption of the media (discussed in next section).
- c. The numerical procedure adopted to solve the multiple systems of linear or non linear equations resulting from using several seismic stations. Several methods of solutions are discussed by Gibowicz and Kijko (1994).
- d. The spatial configurations of seismic network with respect to the event location.

With regards to the seismic data used in this study, most of these sources of errors have been assessed by ISS (2007) as discussed previously. For instance, the error

² Detailed data review included seismicity from 1998 onwards.

associated with the velocity model used was small enough to be corrected in that assessment.

The error associated to a spatial configurations of seismic network may be evaluated using a more complex statistical approach, for instance, the method that minimize the expected location error for a given network configuration (Kijko and Sciocatti, 1995). Although, no statistical approach has been performed so far, the Esmeralda mine sector has the advantage to be located at the centre of the monitoring system at the El Teniente mine (Figure III.A1). This type of configuration leads to high location accuracy as discussed by Vence et al., (1988).

III.A2.2 Cave Geometry and Location Error

At the El Teniente mine is assumed that as far as seismic wave velocities are concerned the rock mass is approximately isotropic and homogeneous. This means that seismic waves travel through the *medium* in straight rays. Voids as results of caving may lead to significant location errors, since seismic rays in reality may travel around the cave. This type of error may be corrected using ray-tracing technique to account for in-homogeneities within the medium (Mendecki, 1997). This methodology is not only applicable for voids, but also for anisotropic rock masses (i.e., layered). A ray tracing technique has been applied at the mine site to more accurately determine event location (Lynch, 2006). The technique defined an arbitrary velocity model for a particular mine section accounting for the caved zones as shown Figure III.A2.

Knowledge of cave geometries allows successful ray-tracing technique applications, but this is not exactly the case of the El Teniente mine (Lynch, 2006). There is a good quality information about cave geometries of most old abandoned mine sectors located in the upper levels of the mine, which are filled with broken rocks. However, the geometry of the active caves, such as these created at the Reno and Esmeralda mine sectors are practically unknown (see Section 8.3.1, Figures 8.8 and 8.9). These caves are also not completely filled. Therefore, even using the most appropriate velocity model, such uncertainties in cave geometries may affect the event location calculations. To justify this point Figure III.A3 is presented. This figure plots the absolute difference distance between estimated location using different procedures

for seven large events occurred at the Reno mine sector (ISS, 2007). These procedures included the original location considering straight-ray algorithm (o), re-processed by ISS expert processing with the same straight-ray algorithm (n), using ray-tracing technique (rt), the same rt but disabling P-S arrival times with large residual location (rt2), and from moment tensor³ inversion by inverting the best fit between synthetic and observed seismograms (mt).

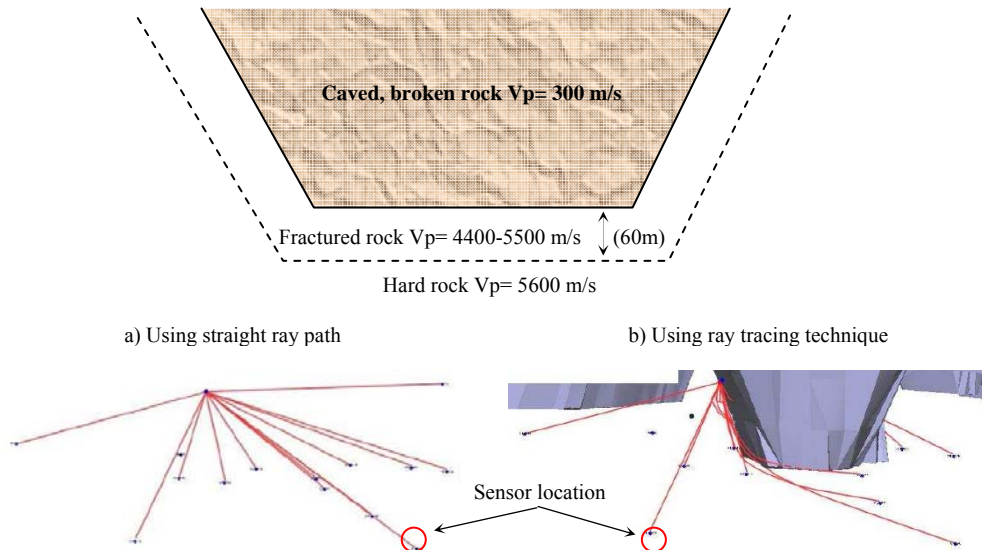


Figure III.A2.- Conceptual velocity model around caves used for ray tracing techniques (above). An example of ray path without (a) and with ray tracing technique. Adapted from Lynch (2006).

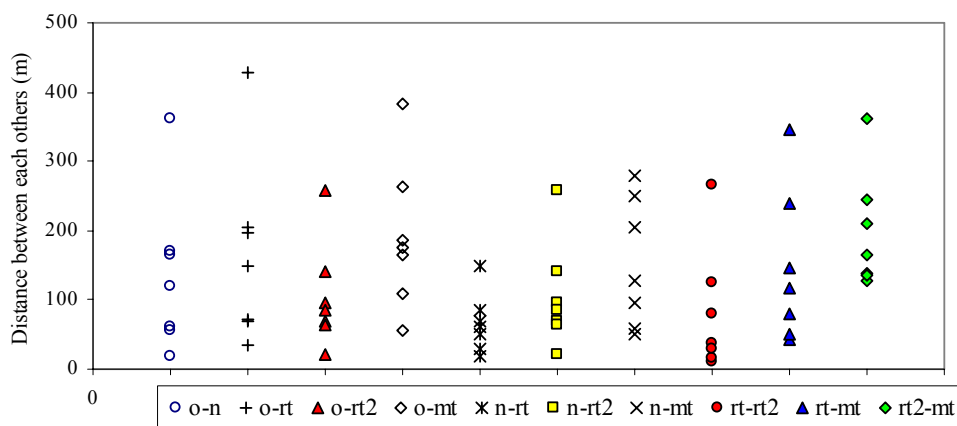


Figure III.A3.- Absolute distance between locations considering different procedure to locate 7 large seismic events (adapted form ISS, 2007).

³ Moment tensor inversion locates the point of maximum moment release of the source, which may be different from fracture initiation determined by waves arrivals in the standard seismic location procedure.

Applying ray tracing techniques may provide better results as data analysis from *rt2* shown in Figure III.A3, but uncertainties in event locations still remain. It is believed that unknown geometries of the active cave fronts play a relevant role in this problem as suggested Lynch (2006). In other words, associated error always will be present when the event location is determined automatically by the ISS system at the El Teniente mine.

III.A3 Seismic Source Parameters

Seismicity can be quantified by the following parameters derived from the recorded wave form (Mendecki, 1997);

- Time of the event, t_0 .
- Location, $h = (x_0, y_0, z_0)$.
- Seismic Moment (M_o), and Moment Tensor.
- Seismic energy radiated (E).
- Size and stress release estimates.

Time of the event and its location is routinely undertaken using the ISS software package at the mine site, as discussed previously.

III.A3.1 Seismic Moment

The seismic moment also called the *scalar moment*, M_o , is a measure of the strength of the seismic event⁴. It is defined assuming a double-coupled point model or shear dislocation mechanism. M_o is expressed as (Aki and Richards, 1980):

$$M_o = \mu A D \quad [\text{Nm}] \quad (\text{III.2})$$

where μ is the shear modulus at the source, A is the area over which the dislocation occurred, and D is the average slip over the area A .

Mine tremors have been found to have similar characteristic to natural earthquakes (McGarr, 1984), which have been successfully modelled mathematically as double-

⁴ Originally defined for earthquakes.

couple point model (Burridge and Knopoff, 1964). There is strong evidence to suggest this modelling technique can be applied for mine tremors.

The seismic moment can be estimated from the spectral analysis of body waves. The spectral analysis involves application of the Fourier transformation to the seismic waveforms, from the time domain into the frequency domain (Figure III.A4). Then, M_o is calculated as follow (Gibowicz and Kijko, 1994):

$$M_o = \frac{4\pi\rho c_o^3 R\Omega_o}{F_c R_c S_c} \quad (\text{III.3})$$

where

ρ is the density of the source material.

c_o is either the compressional or shear wave velocity.

R is the distance between the source and the receiver.

Ω_o represent the level of low-frequency plateau of the ground displacement spectrum (Figure III.A4).

F_c is a factor to account for radiation pattern of seismic waves.

R_c is a factor to account for free-surface amplification of wave amplitudes.

S_c is a site correction factor.

A double-couple point source model is an oversimplification of the forces acting at the source (McGarr, 1984, Gibowicz, 1990). A more general description of the event point source is provided by the moment tensor (described in Section 8.2.4).

III.A3.2 Seismic Energy

The radiated seismic energy, E , is only a small portion of the energy released at the source during fracture and frictional sliding. It represents the total elastic energy radiated by the seismic event. Seismic energy can be derived from recorded waveform as follow (Boatwright and Fletcher, 1984);

$$E_c = 4\pi\rho c_o F_c^2 \left(\frac{R}{F_c R_c} \right) J_c \quad [\text{J}] \quad (\text{III.4})$$

where

ρ is the density of the source material

c_o is either the compressional or shear wave velocity

F_c is the mean squared radiation pattern coefficients for either P and S waves

R is the distance between the source and the receiver

R_c is a factor to account for free-surface amplification of wave amplitudes

J_c is the Energy Flux of either the P and S waves

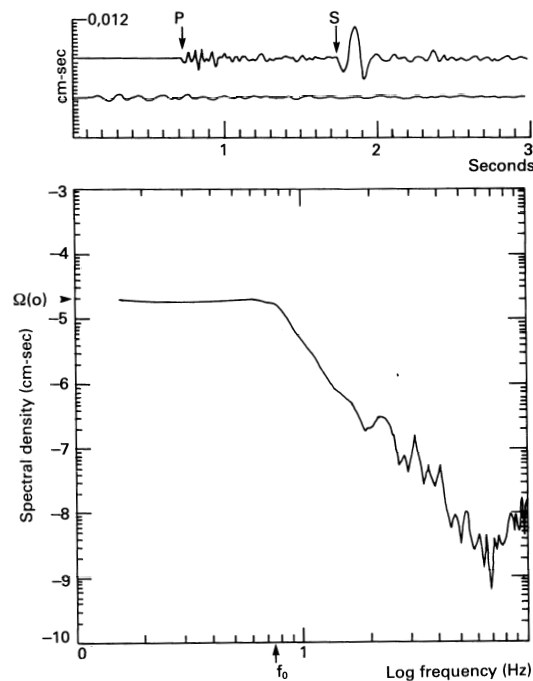


Figure III.A4.- Example of a spectral analysis of body waves. A seismogram in time domain (top), and S-wave displacement spectra in the frequency domain (bottom). After McGarr (1984).

Thus, the total radiated seismic energy is;

$$E = E_s + E_p \quad [J] \quad (III.5)$$

It has been found that the Energy radiated in the P waves is only a small fraction of that in the S waves, with ratios E_s/E_p between 10 and 30 for small earthquakes (Boatwright and Fletcher, 1984). For mine tremors have been found that the ratios E_s/E_p can extend to values of 1.5, with more of the population below 10 (Gibowicz et

al., 1990, Urbancic and Young, 1993, Duplancic, 2002). These enriched P wave energy and depleted S wave energy in mine tremor has been suggested as result of a combination of non-double couple and double couple mechanisms at the source for mine events.

The empirical relationship between E and M_o for the seismic data recorded at the Esmeralda mine sector is presented in Figure III.A5. The observed trend for the mine sector is similar to that observed in the entire mine.

III.A3.3 Size and Stress Release Estimates

In the displacement spectrum (Figure III.A4), the intersection of the low-frequency plateau (Ω_0) with the high frequency asymptote is defined as the corner frequency, f_o , which is related to the stopping phase of the rupture. Assuming the dislocation as a simple circular fault (Brune, 1970), the seismic source radius, r_o , is related to the corner frequency for S waves by;

$$f_o = 2.34 c_o / 2\pi r_o \quad [\text{Hz}] \quad (\text{III.6})$$

where c_o is the shear wave velocity.

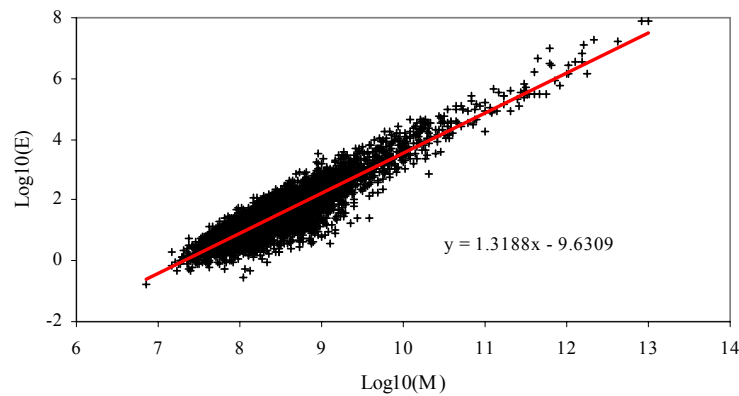


Figure III.A5.- Empirical relationship between radiated energy and the scalar seismic moment at the Esmeralda mine sector.

Gibowicz (1990) has found that the Brune's model over-estimate the source radius for mine tremors. The Madariaga's source model (Madariaga, 1976) has been proposed instead. In the equation III.6, the Madariaga's model uses a proportionality factor of 1.32, nearly a half of Brune's model.

Using equation III.1 and Figure III.A6, a seismic event will take place when a loaded fault of area A fails by an applied shear stress τ_1 . The slip increases to its final value D as the loading stress decreases from τ_1 to its final value of τ_2 . Assuming an instantaneous stress reduction for circular fault model, the stress drop, $\Delta\sigma$ ($\tau_1 - \tau_2$) is defined as the uniform reduction in shear stress. It is estimated as (Brune, 1970);

$$\Delta\sigma = (7/16) M_o / r_o^3 \quad [\text{Pa}] \quad (\text{III.7})$$

Another estimate of the stress release at the source is the apparent stress, τ_a , defined as:

$$\tau_a = \eta E / M_o = \eta \bar{\tau} \quad [\text{Pa}] \quad (\text{III.8})$$

where η is the seismic efficiency, E is the radiated seismic energy, and, $\bar{\tau}$ is $(\tau_1 + \tau_2)/2$ or the average loading stress (Figure III.A6).

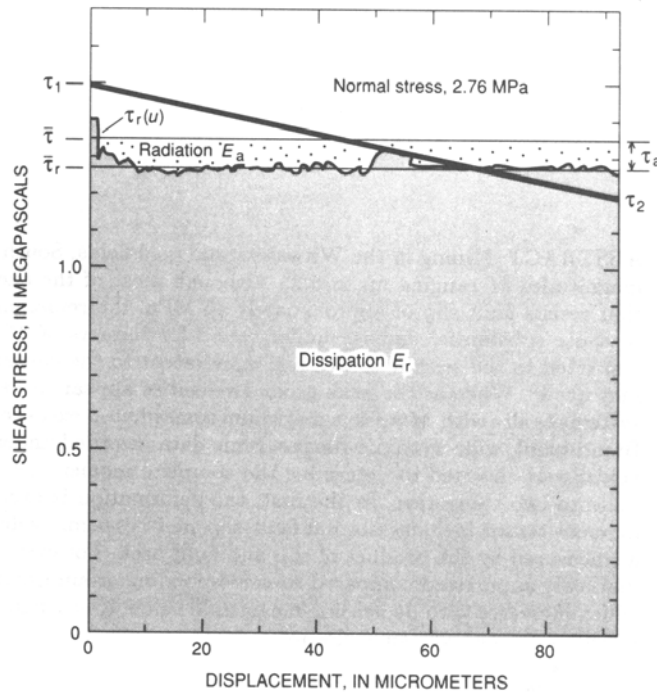


Figure III.A6.- Relation between resisting stress and displacement for a fault slip (after McGarr 1999)

Now, let W define the total work done or total energy released by the slip event (Figure III.A6). Only a small portion of that energy is radiated seismically, and described as E . Most of that energy is consumed in overcoming friction and/or

creating the fracture zone and heating the rock. The total energy released is defined as (McGarr, 1999):

$$W = \left(\frac{\tau_1 + \tau_2}{2} \right) DA = \bar{\tau} DA \quad [\text{J}] \quad (\text{III.9})$$

where τ_1 and τ_2 are the initial and final shear stress, D is the average slip over the area A (both from equation III.1).

By definition, the apparent stress, τ_a , is also the difference between the average loading stress, $\bar{\tau}$, and the average resisting stress, $\bar{\tau}_r$, (McGarr, 1999):

$$\tau_a = \bar{\tau} - \bar{\tau}_r \quad (\text{III.10})$$

and the radiated seismic energy is also defined as (McGarr, 1999):

$$E = \tau_a AD \quad (\text{III.11})$$

Accordingly, from equation 9.11 and 9.13, the seismic efficiency is defined as;

$$\eta = E/W = \tau_a / \bar{\tau} \quad (\text{III.12})$$

This ratio is not a constant value. For mine tremors located at 3km depths McGarr (1984) have estimated η of less than 1 per cent. Moreover, the same author, based on studies ranging from laboratory stick slip experiments, mining induced events in two different setting, earthquakes artificially triggered by liquid injection, and shallow tectonics earthquakes has suggested an upper bounds of 0.06 (McGarr, 1999).

Therefore, using a fixed value of $\eta = 0.06$, the total energy released by the slip event may be estimated as;

$$W = E/\eta \cong E/0.06 \quad (\text{III.13})$$

A similar equation have been used by (Beck et al., 2006) to estimate the Dissipated Plastic Energy (DPE) as the total energy dissipated due of rock mass yield.

Appendix III.B Recorded Seismicity Esmeralda Mine Sector 1994-2003

Example of data from Esmeralda mine sector;

Y (North)	X (East)	Z	DATE	TIME	STAC	MAGNITUDE	RadiatedEn	SeismicMom	EI	Enegy S/P	EventSize
m	m	m	dd/mm/yyyy	hh/mm/ss	n	Mw	J	Nm			m
506.59	1175.58	2389.5	5/01/1994	5443	5	-0.18	130.8	680347968	0.28	3.39	22.2
463.75	1080.51	2367.34	20/01/1994	43436	5	-0.77	98.8	89395840	4.09	25.54	9.1
441.95	1422.28	2315.45	18/02/1994	144810	5	-0.59	650.0	168976736	10.57	9.27	6.7
487.01	1172.01	2286.95	3/03/1994	70628	5	-0.83	91.7	73712856	5.04	4.07	5.7
657.9	1140.15	2398.8	3/03/1994	191250	11	0.25	9921.6	3099179264	2.25	4.75	14.0
436.72	1408.12	2381.27	9/03/1994	53348	6	-0.59	307.7	165263520	5.17	7.02	6.8
465.56	1143.12	2338.03	11/03/1994	140819	6	0	1721.6	1282835456	1.43	21.62	18.0
422.18	1023.69	2311.88	12/03/1994	90613	4	-0.83	61.3	72053584	3.48	12.23	6.8
530.41	958.06	2372.89	24/03/1994	142410	4	-0.9	319.2	58134664	24.85	9.71	3.6
696.3	1222.01	2248.13	24/03/1994	151315	3	-0.59	41.8	168756400	0.68	4.56	10.6
404.67	1097.73	2394.82	26/03/1994	210444	5	-0.32	719.6	420640960	3.07	3.13	11.9
404.48	1098.98	2394.41	28/03/1994	175446	5	-0.45	301.9	270341312	2.46	2.21	7.5
653.43	1203.14	2376.42	31/03/1994	181017	7	0.4	9444.5	5137592832	1.02	26.80	21.8
389.54	1121.14	2377.6	8/04/1994	83023	3	-0.69	91.3	117401320	2.53	5.79	7.2
456.27	1043.84	2321.49	8/04/1994	171203	6	-0.46	215.8	260380048	1.86	15.92	14.9
420.58	1063.26	2347.41	12/04/1994	202436	5	-0.22	75.3	595906176	0.19	2.53	19.9
419.84	1087.86	2370.01	2/05/1994	200606	4	-0.36	450.6	368003776	2.34	9.77	11.2
412.95	1073.62	2364.09	5/05/1994	152515	4	-0.42	216.6	297176960	1.54	5.22	10.2

The rest of data are included in the attached CD.

Appendix III.C Model Result Data (Control Points)

Three excel files are attached in the CD, these contain over 200 control points from the numerical model (included the modelled incremental plastic strain tensor for each measured seismic moment tensor). Each control point include; cumulative plastic strain, strain tensor, stress tensor, and incremental plastic strain tensor. An example of stress tensor data is as follow;

ID IN DATASHEET		id	Referencia-Location	Y (North)	X (East)	Z	
1	1	56	FMA	580	1180	2240	
2	2	57		PN5	580	1180	2260
3	3	58			580	1180	2280
4	4	59			580	1180	2300
5	5	60			PN1	580	1120
6	6	61		580		1120	2280
7	7	62		580		1120	2300
8	8	63		PN2	800	1120	2240
9	9	64			800	1120	2280
10	10	65			800	1120	2300
11	11	66		PN6	800	1180	2240
12	12	67			800	1180	2260
13	13	68			800	1180	2280
14	14	69			800	1180	2300

STRESS TENSOR (MPa)							
Points id in datasheet							
	STEP	S11	S22	S33	S12	S13	S23
1	38	-4.65E+07	-3.79E+07	-2.51E+07	5.09E+05	-1.04E+07	-3.40E+06
2	38	-4.72E+07	-3.86E+07	-2.43E+07	-4.97E+05	-1.05E+07	-4.01E+06
3	38	-4.83E+07	-4.00E+07	-2.34E+07	-1.85E+06	-1.02E+07	-4.57E+06
4	38	-4.86E+07	-4.19E+07	-2.16E+07	-4.05E+06	-9.48E+06	-5.40E+06
5	38	-4.70E+07	-3.83E+07	-2.03E+07	-2.28E+06	-9.18E+06	-3.07E+06
6	38	-4.74E+07	-3.89E+07	-1.91E+07	-4.13E+06	-9.06E+06	-3.70E+06
7	38	-4.79E+07	-4.14E+07	-1.81E+07	-7.04E+06	-9.29E+06	-3.96E+06
8	38	-4.68E+07	-3.81E+07	-2.24E+07	-8.21E+05	-9.97E+06	-2.68E+06
9	38	-4.80E+07	-3.91E+07	-2.06E+07	-4.30E+06	-1.05E+07	-3.76E+06
10	38	-4.85E+07	-4.10E+07	-1.94E+07	-6.99E+06	-1.15E+07	-4.73E+06
11	38	-4.63E+07	-3.80E+07	-2.62E+07	6.70E+05	-1.07E+07	-3.20E+06
12	38	-4.69E+07	-3.86E+07	-2.57E+07	-4.61E+05	-1.10E+07	-3.77E+06

CD

CD